UNIVERSITY OF CASTILLA-LA MANCHA

DOCTORAL THESIS

Mathematical models of tumor growth, response to stereotactic radiosurgery and CAR T cell immunotherapy

Author:
Odelaisy LEÓN TRIANA

Supervisor:
Prof. Víctor M.
PÉREZ-GARCÍA

A thesis submitted in fulfillment of the requirements for the degree of Doctor

in the

University of Castilla-La Mancha

December 20, 2021

Declaration of Authorship

I, Odelaisy LEÓN TRIANA, declare that this thesis titled, "Mathematical models of tumor growth, response to stereotactic radiosurgery and CAR T cell immunotherapy" and the work presented in it are my own. I confirm that:

- This work was done wholly or mainly while in candidature for a research degree at this University.
- Where any part of this thesis has previously been submitted for a degree or any other qualification at this University or any other institution, this has been clearly stated.
- Where I have consulted the published work of others, this is always clearly attributed.
- Where I have quoted from the work of others, the source is always given. With the exception of such quotations, this thesis is entirely my own work.
- I have acknowledged all main sources of help.
- Where the thesis is based on work done by myself jointly with others, I have made clear exactly what was done by others and what I have contributed myself.

Signed:

Date:

"The important thing is not to stop questioning."

Albert Einstein

UNIVERSITY OF CASTILLA-LA MANCHA

Resumen

Mathematical models of tumor growth, response to stereotactic radiosurgery and CAR T cell immunotherapy

Esta tesis exploró el uso de modelos matemáticos como herramientas para facilitar la comprensión de algunos de los procesos dinámicos del cáncer, desde la evolución de la enfermedad hasta su respuesta a terapias. El estudio se centró en tres temas clínicamente importantes: el crecimiento tumoral macroscópico, la respuesta tumoral a la radiocirugía estereotáctica y la respuesta del cáncer a la inmunoterapia con células CAR T.

El crecimiento tumoral es el resultado de la interacción de procesos biológicos complejos entre una gran cantidad de células individuales en un entorno tumoral cambiante. Utilizando un conjunto de datos recopilados de tumores no tratados de diferentes histologías, exploramos la dinámica que rige el crecimiento tumoral a nivel macroscópico y su relación con las leyes de escala universales en los cánceres humanos.

Después de estudiar el crecimiento de las metástasis cerebrales (BM) no tratadas, centramos nuestro estudio en las metástasis cerebrales tratadas. El tratamiento de los pacientes con BM que tienen una enfermedad extracraneal bien controlada y una pequeña cantidad de lesiones consiste en dosis localizadas de radiación (radiocirugía estereotáctica). Estudiamos el efecto de esta terapia sobre la dinámica volumétrica de la enfermedad y sus particularidades en presencia del tipo de respuestas inflamatorias comúnmente asociada a este tratamiento.

Finalmente, estudiamos terapias basadas en células CAR T. Estas terapias han logrado un éxito sustancial contra diferentes neoplasias hematológicas y se está investigando su uso en tumores sólidos. En esta tesis, se desarrollaron y estudiaron teórica y numéricamente una variedad de modelos matemáticos de ecuaciones diferenciales ordinarias para comprender esta terapia y proponer nuevos enfoques para su aplicación.

UNIVERSITY OF CASTILLA-LA MANCHA

Abstract

Mathematical models of tumor growth, response to stereotactic radiosurgery and CAR T cell immunotherapy

This thesis explored the use of mathematical models as tools to facilitate understanding of some of the dynamic processes in cancer, from the evolution of the disease to its response to therapies. The study focused on three clinically important subjects: macroscopic tumor growth, tumor response to stereotactic radiosurgery and cancer response to CAR T cell immunotherapy.

Tumor growth is the result of the interplay of complex biological processes between an enormous amount of individual cells in a changing tumor environment. Using a valuable dataset collected from untreated tumors of different histologies, we explored the dynamics that govern tumor growth at the macroscopic level and its relationship with universal scaling laws in human cancers.

After describing the growth of untreated brain metastases (BM), we focused our study on treated brain metastases. Treatment of BM patients who have well-controlled extracranial disease and a small number of lesions consists of localized doses of radiation (stereotactic radiosurgery). We studied the effect of this therapy on the volumetric dynamics of the disease and its particularities in the presence of the inflammatory responses type commonly associated with this treatment.

Finally, we studied CAR-T cell-based therapies. These therapies have achieved substantial success against different hematological malignancies and their use in solid tumors is being investigated. In this thesis, a variety of mathematical models of ordinary differential equations were developed and studied theoretically and numerically to understand this novel therapy and propose new approaches for its use.

Agradecimientos

Me gustaría agradecer a varias personas que sin su apoyo y colaboración no hubiese sido posible finalizar esta tesis.

Para empezar, quiero agradecer de manera especial y sincera a mi director de tesis. Primero, por darme la oportunidad de conocer el grupo de investigación Molab y mostrarme una forma diferente de hacer matemáticas. Segundo, por su confianza y apoyo en todos los momentos difíciles, tanto en la investigación como fuera de ella. Tercero, por iluminarnos con su inteligencia y guiarnos con su buen corazón, por haber sido un ejemplo a seguir, de quien he intentado aprender todo lo posible.

Agradecer a María Jesús, por abrirme su corazón desde el primer día. Por haber luchado incansablemente para que tuviera las mejores condiciones de trabajo posibles. Gracias por todos los consejos, por hacerme sentir como en casa y por hacer que la vida parezca más fácil.

Gracias a Juan por ser mi tutor, y estar ahí para responder todas mis dudas, por su gentileza y su cercanía. A Gabriel por compartir todo su conocimiento, por su comprensión y su disposición a ayudar. Gracias a ambos por haber contribuido en gran medida a mi formación como investigadora durante estos años.

Debo agradecer también a todas las personas del grupo Molab, con las que he tenido la oportunidad trabajar y aprender. A las que ya no están y a las que se han ido incorporando. También doy las gracias al grupo del café, por crear debates interesantes y hacer menos duros los días. Al resto de doctorandos por el apoyo y la solidaridad ofrecida. A los amigos de Ciudad Real, especialmente a Raquel por haber compartido su casa, la cual se convirtió en oficina durante los meses de confinamiento. Gracias a los culipardos frisbileros, por hacer de Ciudad Real un mejor lugar, donde he sido feliz y he vivido muy buenos momentos.

Gracias a las nuevas amistades que me han acompañado durante esta fase de la vida. A Justyna por mostrarme España de una forma tan cercana. A Brocs por sus lecciones de inglés y por darme muchos ánimos y hacerme sentir muy querida. A Nacho y Margarita por abrirme la puerta de su corazón y por hacerme sentir como en familia.

Gracias a mi familia por el apoyo incondicional que me han dado desde el inicio. A pesar de lo difícil que ha sido para ellos tenerme lejos, me han animado en todo momento a seguir creciendo. A mi madre por ser la heroína de mi vida, la mujer con "vara de mago", a la que nada le parece imposible. Me hubiera gustado tenerla a mi lado, pero la fuerza de su corazón ha traspasado el océano y la he sentido desde aquí. Gracias por los consejos, el optimismo y por todo el amor. A mi hermano por cuidar de mi madre, por ser ejemplo de madurez y responsabilidad y por su cariño infinito. A mi padre por toda su sabiduría, por trasmitirme su sencillez y humildad, y por enseñarme a valorar las cosas importantes de la vida.

Por último, quiero agradecer especialmente a Arturo. Por haberme hablado de la oncología matemática en aquel congreso, y trasmitirme su pasión por ayudar a los médicos con ecuaciones. Por presentarme a Molab: a Victor, a María, a Juan, ... y a todas las bellas personas que he conocido en la UCLM. Por todas las horas que hemos pasado juntos hablando de matemáticas. Por su generosidad y su empatía. Por ayudarme a ser mejor persona y por creer en mí.

Este trabajo ha sido apoyado por el Ministerio de Ciencia e Innovación, España (número de subvención PID2019-110895RB-I00), y la Junta de Comunidades de Castilla-La Mancha (número de subvención SBPLY / 17/180501/000154), la James S. Mc. Fundación Donnell (Estados Unidos) Siglo XXI Iniciativa científica en enfoques

matemáticos y de sistemas complejos para el cáncer de cerebro (colaboración premio 220020450) y por los contratos predoctorales de la UCLM [2018-PREDUCLM-8167].

Acknowledgements

I would like to thank several people without whose support and collaboration I would not have been able to finish this thesis.

To begin with, I would like to especially and sincerely thank my thesis supervisor. First, for giving me the opportunity to meet the Molab research group and showing me a different way of doing mathematics. Second, for his trust and support in all the tough moments, both in the investigation and outside of it. Third, for enlightening us with his intelligence and guiding us with his good heart, for having been an example to follow, and from whom I have tried to learn as much as possible.

Thank you María Jesús, for opening your heart to me from day one. For having fought tirelessly so that I had the best possible working conditions. Thanks for all the advice, for making me feel at home, and for making life seem easier.

Thanks to Juan for being my tutor, and being there to answer all my questions, for his kindness and his closeness. To Gabriel for sharing all his knowledge, for his understanding and his willingness to help. Thanks to both of you for having contributed greatly to my formation as a researcher during these years.

I must also thank all the people in the Molab group with whom I have had the opportunity to work and learn; both those that are no longer there and those that have recently been incorporated. I also thank the coffee group for creating interesting discussions and making brightening my days. Thanks to the rest of the Phd students for the support and solidarity offered, and to the friends of Ciudad Real, especially Raquel for having shared her house, which was converted into an office during the months of lockdown. Thanks to my Ultimate frisbee teammates, the "frisbileros culipardos", for making Ciudad Real a better place, where I have been happy, and I have had very good times.

Thanks to the new friends who have accompanied me during this phase of life. To Justyna for showing me Spain in such a special way. To Brocs for her English lessons and for encouraging me and making me feel very loved. To Nacho and Margarita for opening the doors of their hearts to me and for making me feel like family.

Thanks to my family for the unconditional support they have given me from the beginning. Despite how difficult it has been for them to be far away, they have encouraged me at all times to continue growing. To my mother for being the heroine of my life, the woman with the "magician's wand ", to whom nothing seems impossible. I would have liked to have her by my side, but the strength of her heart has crossed the ocean and I have felt it from here. Thanks for the advice, the optimism and for all the love. To my brother for taking care of my mother, for being an example of maturity and responsibility and for his infinite affection. To my father for all his wisdom, for transmitting his simplicity and humility, and for teaching me to appreciate the important things in life.

Lastly, I want to especially thank Arturo. For telling me about mathematical oncology at that congress, and for conveying his passion for helping doctors with equations. For introducing me to Molab: Victor, María, Juan, ... and all the beautiful people I have met at UCLM. For all the hours we've spent together talking about math. For your generosity and empathy. For helping me to be a better person and for believing in me.

This work has been supported by Ministerio de Ciencia e Innovación, Spain (grant number PID2019-110895RB-I00), and Junta de Comunidades de Castilla-La Mancha (grant number SBPLY/17/180501/000154), the James S. Mc. Donnell Foundation (USA) 21st Century Science Initiative in Mathematical and Complex Systems

Approaches for Brain Cancer (Collaborative award 220020450) and UCLM PhD Fellowship [2018-PREDUCLM- 8167].

Contents

List of Abbreviations

ALL	Acute lymphoblastic leukemia
BBB	Blood brain barrier
BM	Brain metastases
CAR	Chimeric antigen receptor
CNS	Central nervous system
CRS	Cytokine release syndrome
GBM	Glioblastoma
HSC	Hematopoietic stem cell
MRI	Magnetic resonance imaging
MSE	Mean square error
NSCLC	Non-small cell lung cancer
RN	Radiation necrosis
SRS	Stereotactic radiosurgery
WBRT	Whole-brain radiotherapy

Chapter 1

Introduction

1.1 Cancer

Cancer ranks as a leading cause of death and an important barrier to increasing life expectancy in every country of the world (Bray et al., 2021). According to estimates from the World Health Organization (WHO) in 2019 (WHO, 2020) cancer is the first or second leading cause of death before the age of 70 years in 112 of 183 countries and ranks third or fourth in a further 23 countries. Worldwide, an estimated 19.3 million new cancer cases and almost 10.0 million cancer deaths occurred in 2020 (Sung et al., 2021). Overall, the burden of cancer incidence and mortality is rapidly growing worldwide; this reflects both aging and growth of the population as well as changes in the prevalence and distribution of the main risk factors for cancer, several of which are associated with socioeconomic development.

Cancer is a large group of diseases that can start in almost any organ or tissue of the body. It is caused by genetic alterations—that is, changes to genes that control the way our cells function, especially how they grow and divide. The genetic changes that contribute to cancer tend to affect three main types of genes—proto-oncogenes, tumor suppressor genes, and DNA repair genes. These changes are sometimes called "drivers" of cancer.

Proto-oncogenes are involved in normal cell growth and division. When these genes are altered they may become cancer-causing genes (or oncogenes), allowing cells to grow and survive when they should not (Ewald and Ewald, 2012). Tumor suppressor genes are also involved in controlling cell growth and division. Cells with certain alterations in tumor suppressor genes may divide in an uncontrolled manner. Finally, DNA repair genes are involved in fixing damaged DNA. Cells with mutations in these genes tend to develop additional mutations in other genes and changes in their chromosomes, such as duplications and deletions of chromosome parts (Chakravarthi, Nepal, and Varambally, 2016). Together, these mutations may cause the cells to become cancerous.

In addition, cancer cells are capable of infiltrating or penetrating normal tissues and invade them. A cancer that has spread from the place where it first formed to another place in the body is called metastatic cancer (Liu et al., 2017). Metastatic cancer has the same name and the same type of cancer cells as the original or primary cancer. Under a microscope, metastatic cancer cells generally look the same as cells of the original cancer. Moreover, metastatic cancer cells and cells of the original cancer usually have some molecular features in common, such as the presence of specific chromosome changes.

Hallmarks of cancer

Despite each cancer can be considered as a different disease, at the same time they share some common traits that collectively dictate their behavior. The hallmarks of cancer comprise biological capabilities acquired during the multi-step development of human tumors. They include sustaining of proliferation signaling, evading growth suppressors, avoiding immune destruction, enabling replicative immortality, tumor-promoting inflammation, activating invasion and metastasis, inducing angiogenesis, genome instability and mutations, resisting cell death and deregulating cellular energy (Hanahan and Weinberg, 2011). Figure 1.1 shows a summary of these characteristics.

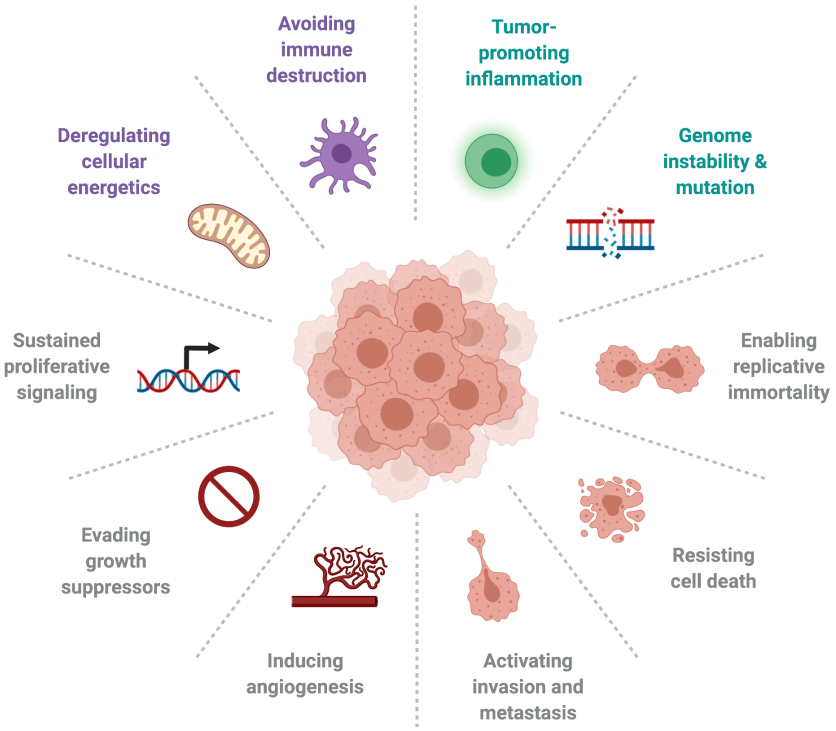

FIGURE 1.1: **The hallmarks of cancer.** Figure adapted from Hanahan and Weinberg, 2011. Created with BioRender.com.

A better understanding of these processes will lead to the development of more effective and long-lasting therapies for human cancer.

1.2 Types of Cancer

Types of cancer are usually named for the organs or tissues where the cancers form. Moreover, cancers also may be described by the type of cell that formed them. Here are some categories of cancers that begin in specific types of cells:

- **Carcinoma:** This is the most common type of cancer. They are formed by epithelial cells, which are the cells that cover the inside and outside surfaces of the body.

- **Sarcoma:** These are cancers that form in bone and soft tissues, including muscle, fat, blood vessels, lymph vessels, and fibrous tissue (such as tendons and ligaments).
- **Leukemia:** This is a cancer that arises in the bone marrow, which produces blood cells.
- **Lymphoma:** This is a cancer originated in the glands or nodes of the lymphatic system.
- **Myeloma:** This is a cancer originated in the plasma cells of bone marrow.
- **Brain and spinal cord cancers:** Cancer can start in the cells of the brain or spinal cord. The majority of tumors arise in neuroepithelial tissue, the largest category, that includes astrocytomas and ependymomas.
- **Mixed types:** Mixed cancers develop in two different types of cell from one category or multiple categories.

Due to its importance for the understanding of the studies developed in this thesis, we will deepen into two specific types: brain cancers and leukemias. Their main characteristics will be described in detail below.

1.2.1 Brain cancers

A brain tumor is an abnormal growth of tissue in the brain or central spine that can disrupt proper brain function. There are two general groups of tumors based on where the tumor cells originated:

- **Primary:** Tumors that start in cells of the brain are called primary brain tumors. Primary brain tumors may spread to other parts of the brain or to the spine, but rarely to other organs.
- **Metastatic:** Metastatic or secondary brain tumors begin in another part of the body and then spread to the brain. These tumors are more common than primary brain tumors and are named by the location in which they begin.

Benign brain tumors originate from cells within or surrounding the brain, do not contain cancer cells, grow slowly, and typically have clear borders that do not spread into other tissue. Malignant brain tumors originate from cancer cells. They are considered to be life threatening because they grow rapidly and invade surrounding brain tissue.

All types of brain tumors may produce symptoms that vary depending on the size of the tumor and the part of the brain that is involved. Where symptoms exist, they may include headaches, seizures, problems with vision, vomiting and mental changes. Other symptoms may include difficulty walking, speaking, with sensations, or unconsciousness.

Primary brain tumors

Primary brain tumors are a group of heterogeneous tumors that arise from cells within the Central Nervous System (CNS). Malignant primary brain tumors are one of the leading causes of cancer mortality in children and young adults, with few therapeutic options (Ostrom et al., 2020). In adults, glioblastomas, the most common

primary brain tumors, remain uniformly fatal, with a median survival of less than 21 months, despite surgical resection, targeted radiation therapy, high-dose chemotherapy, and novel approaches such as tumor treatment fields.

Glioblastoma (GBM) has a fast growth and a diffusive profile. Consequently, one of the characteristics of this tumor is the presence of an inner necrotic area. This is one of the most aggressive tumors, which also embodies intratumor heterogeneity and improved phenotypic adaptability (Celiku, Gilbert, and Lavi, 2019). The current standard therapy, defined by Stupp et al., 2005, includes neurosurgery and subsequent doses of radiotherapy in combination with the chemotherapeutic agent temozolomide, to kill the remaining cells. However, a cure for glioblastoma is unlikely, and the tumor usually reappears over a period of months. New therapies, such as antiangiogenic drugs, have failed to improve survival and, although there are many ongoing clinical trials testing new immune drugs, the future is yet not bright for this cancer.

Brain metastases

Brain metastases (BMs) are cancer cells that have spread to the brain from tumors in other organs in the body. A substantial number, between 10% - 35% of adult cancer patients, develop BMs (Fox et al., 2011). BMs are a major cancer-related complication and are ten times more common than malignant primary brain tumors. The incidence of BMs is rising because improved systemic therapies control systemic disease and prolong survival but cross the blood–brain barrier (the highly selective membrane barrier that separates the circulating blood from the brain) too poorly to be able to control BMs. The most common primary tumors that metastasize to the brain, in order of incidence, are non-small cell lung cancer (NSCLC), small cell lung cancer (SCLC), melanoma, breast cancer, and kidney cancer.

Figure 1.2 shows a schematic representation of the main stages of brain colonization by cancer cells in the case of metastases from lung cancer, but the characterization can be extended for any other primary tumor.

The treatment of BM patients who have well-controlled extracranial disease and three or fewer measurable lesions consists typically of high localized doses of radiation (Stereotactic Radio Surgery- SRS) on the visible lesions, and sometimes whole brain radiotherapy (WBRT) to target potentially occult BMs. This therapeutic approach allows metastatic lesions to be controlled in many, but not all BM patients. The median survival for patients with brain metastases has improved over the years, but varies by subset: lung cancer, 12 months; breast cancer, 16 months; melanoma, 10 months; gastrointestinal cancer, 8 months; and renal cancer, 12 months (Sperduto et al., 2020).

Blood Brain Barrier (BBB) structure

The blood–brain barrier (BBB) is a diffusion barrier, which impedes influx of most compounds from blood to brain. Three cellular elements of the brain microvasculature compose the BBB—endothelial cells, astrocyte end-feet, and pericytes (PCs) (Ballabh, Braun, and Nedergaard, 2004). Tight junctions (TJs), present between the cerebral endothelial cells, form a diffusion barrier, which selectively excludes most blood-borne substances from entering the brain. Figure 1.2 shows some of the elements within the composition of the BBB. The separation of the blood and brain is further enhanced by the absence of the lymphatic system from the central nervous

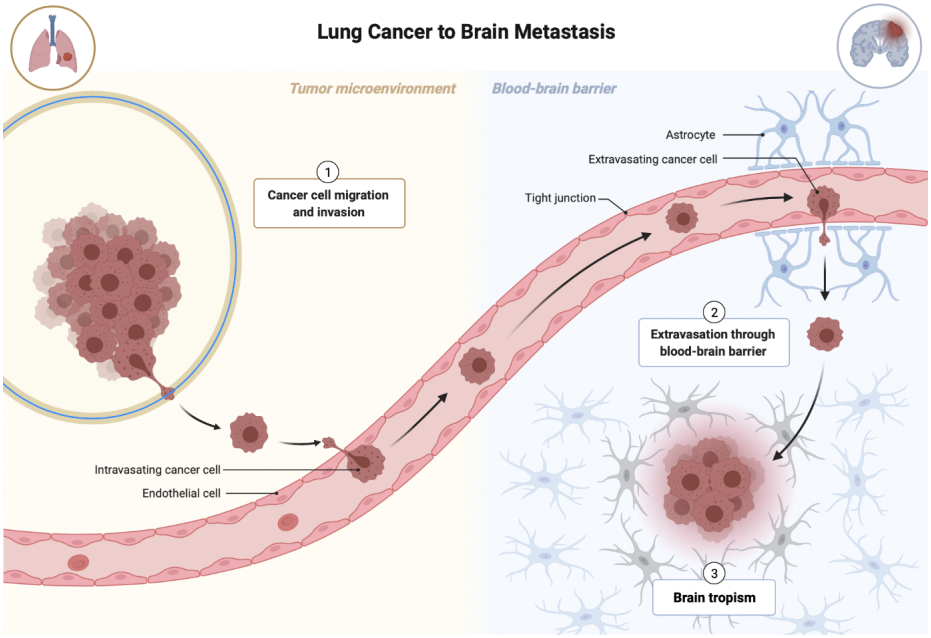

FIGURE 1.2: **A schematic representation of the main stages of metastasis to the brain** Cancer cells from primary lesions invade into surrounding tissues, intravasate into the circulatory system and survive during hematogenous transit. Metastatic cells extravasate through vascular walls into the brain parenchyma. At the metastatic niche cancer cells proliferate, form colonies, and the subsequent proliferation of cells leads to clinically detectable metastatic lesions. Created with BioRender.com.

system preventing macromolecules from entering the brain by passive transport, thereby creating an immunologically distinct space.

However, these same features also hinder the delivery of systemic therapies into brain tumors. The BBB is disrupted during tumor progression and is then referred to as the blood–tumor barrier (BTB). Although the BTB is more permeable than the BBB, its heterogeneous permeability to small and large molecules as well as heterogeneous perfusion contributes to suboptimal drug accumulation in brain tumors (Arvanitis, Ferraro, and Jain, 2019). As such, the BBB is one of the rate-limiting factors in clinically effective therapy.

The BBB/BTB harbors considerable structural and functional heterogeneity within the microenvironment of the same lesion and across different cancer subtypes. These findings highlight the need to optimize and define tumor- specific therapeutic windows to disrupt CNS barriers and increase drug efficacy in the CNS with minimal side effects.

1.2.2 Leukemias

Leukemia is a group of blood cancers caused by an increase in abnormal cells and begins in the tissues that make up blood, such as the bone marrow. The incidence of leukemia varies by pathological types and among different populations. Globally, the number of newly diagnosed leukemia cases increased from 354.5 thousand in 1990 to 518.5 thousand in 2017 and this last number has been the trend in recent years, where almost half a million new cases have been diagnosed of leukemia per

year (Dong et al., 2020). The 5-year survival is about 65%. They are the most common cancer types in children from birth to 14 years of age and account for around 3% of all cancers diagnosed in developed countries. Survival in children is higher and improving, yet blood cancer remains the leading cause of cancer death in pediatric patients.

In blood cancers, the normal development process, starting from stem cells and leading to a hierarchy of more differentiated cells, is interrupted by the uncontrolled abnormal growth of specific types of blood cell. Figure 1.3 A shows the process of differentiation of blood cells from stem cells in the case of cells derived from lymphoids. At the top of the hierarchy governing normal hematopoietic there are the hematopoietic stem cells (HSCs). Hematopoietic stem cells can give rise to lymphoid (or myeloid). Lymphoid progenitors can generate either lymphoblasts, which will become B or T lymphocytes, or natural killer cells. Similarly, myeloid progenitors can also lead to a wide variety of cells, including erythrocytes, thrombocytes, or other cells of the non-specific immune system (Wang and Dick, 2005).

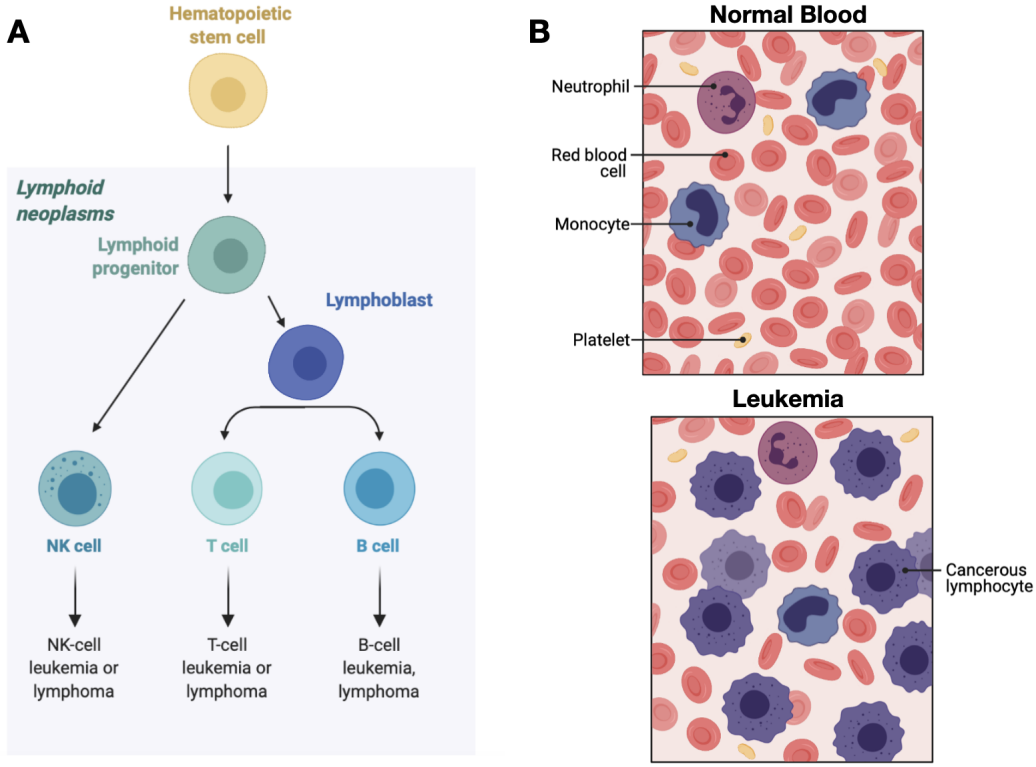

FIGURE 1.3: **A) Differentiation tree for blood cell. B) Representation of the appearance of blood in the presence or absence of leukemic cells.** Created with BioRender.com.

In this framework, the type of cell that becomes cancerous determines the specific type of blood cancer. For instance, leukemia can be either myeloid (or myelogenous), or lymphoid (or lymphoblastic, or lymphocytic). This divides leukemias into lymphoblastic or lymphocytic leukemias and myeloid or myelogenous leukemias. Furthermore, they are also divided into its acute and chronic forms. Thus, there are four different classes of leukemia: acute lymphoblastic leukemia (ALL), chronic lymphocytic leukemia (CLL), acute myelogenous leukemia (AML) and chronic myelogenous leukemia (CML).

Leukemia is generally diagnosed by repeated complete blood counts. The results of molecular or biochemical analysis and so-called flow cytometry techniques will determine the specific the type of leukemia. Figure 1.3 B shows a representation of how the blood looks in the presence or not of leukemic cells.

1.3 Medical imaging

Medical imaging refers to several different technologies that are used to view the human body in order to diagnose, monitor, or treat medical conditions. Imaging may also be used to guide biopsies and other surgical procedures. They have become a major tool since it enables rapid diagnosis with visualization and quantitative assessment. There are many different types of images, some of the most used in cancer are computed tomography (CT), magnetic resonance imaging (MRI) and positron emission tomography (PET). These techniques produce very large amounts of data. The Digital Imaging and Communication in Medicine (DICOM) Standard is used globally to store, exchange, and transmit medical images such as CT, MRI and others.

1.3.1 Computed Tomography Imaging

In a CT scan, an X-ray beam circulates around specific part of the body and a series of images captured from various angles. The computer uses this information to create a series of two-dimensional (2D) cross-sectional image of the organ and combines them to make a three-dimensional (3D) image, which provides a better view of the organs. Positron emission tomography (PET) is a variant of CT where a contrast agents is injected into the body in order to highlight abnormal regions. CT scans are recommended in many conditions such as hemorrhages, blood clots or cancer.

A CT scan can find cancer and show things like a tumor's shape and size. CT scans are most often an outpatient procedure. The scan is painless and takes about 10 to 30 minutes. CT scans show a slice, or cross-section, of the body. The image shows bones, organs, and soft tissues more clearly than standard x-rays. An example of a lung CT scan for a stage I carcinoma tumor is shown in the Figure 1.4 A.

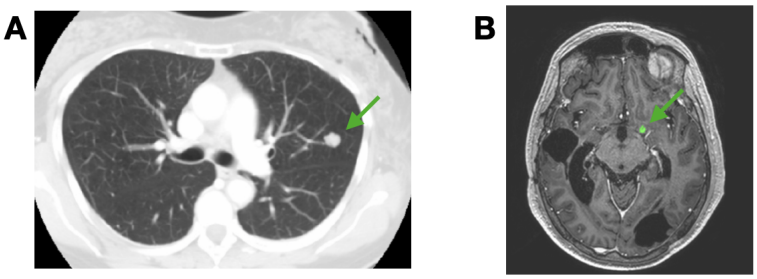

FIGURE 1.4: **Medical imaging example.** A) Lung CT scan showing a carcinoma stage I tumor. B) T1-weighted MRI scan showing a metastatic lesion.

1.3.2 Magnetic Resonance Imaging

MRI is a radiation free and therefore a safer imaging technique than CT and provides finer details of the brain, spinal cord and vascular anatomy due to its good contrast. Axial, sagittal, and coronal are the basic planes of MRI to visualize the brain's anatomy. The most commonly used MRI sequences for brain analysis are Tl-weighted, T2-weighted, and fluid attenuated inversion recovery (FLAIR). Tl-weighted scan provides gray and white matter contrast. T2-weighted is sensitive to water content and therefore well suited to diseases where the water accumulates inside brain tissues. The third sequence is fluid attenuated inversion recovery (FLAIR) which is similar to T2-weighted image except for its acquisition protocol. FLAIR is used in pathology to distinguish between cerebrospinal fluid (CSF) and brain abnormalities. FLAIR can locate an edema region from CSF by suppressing free water signals, and hence periventricular hyperintense lesions are clearly visible in the images (Ellingson et al., 2014). Figure 1.4 shows an example of Tl-weighted MRI for a brain metastasis.

1.4 Cancer treatments

The main goal of cancer treatment is to achieve a cure for cancer, although this is sometimes not possible. If a cure is not possible, treatments may be used to shrink cancer or slow its growth to allow to live without symptoms for as long as possible. There are many types of cancer treatments, using one treatment or another depends on the type of cancer and the progression of the disease. Some people with cancer get only one treatment, but in most cases they receive a combination of treatments. Some of the most common treatments are:

- **Surgery:** It is a procedure in which a surgeon removes cancer either completely or partially.
- **Chemotherapy:** It is the use of any drug to kill cancer cells.
- **Radiotherapy:** It uses high doses of radiation to kill cancer cells and shrink tumors.
- **Immunotherapy:** It is a type of cancer treatment that helps immune system fight cancer.
- **Targeted therapy:** It is a type of cancer treatment that targets the changes in cancer cells that help them grow, divide, and spread.

Other possible treatments are hormone therapy, stem cell transplant and precision medicine. The following will go into detail in the description of two specific treatments. These are stereotactic radiosurgery (SRS) treatment and chimeric antigen receptor (CAR) T cell therapy, which have been part of the object of study in this thesis.

1.4.1 Stereotactic radiosurgery

Stereotactic radiosurgery, commonly called radiosurgery, is the medical procedure of radiotherapy in which fine beams of radiation are administered, generated in megavoltage units (cyclotron, the Gamma Knife and the linear accelerator), with which

it is possible to irradiate high and precisely localized doses, in a specific anatomical area or structure, avoiding the administration of toxic doses to adjacent tissues (Shepard et al., 2008). The closer the prescription dose is matched to the treated target and the steeper the dose gradient around the target, the less normal tissue is irradiated. For the case of brain tumors, SRS was introduced as an alternative treatment option to conventional whole-brain radiotherapy (WBRT).

Similar to conventional radiotherapy, this therapy works by radiation-induced DNA damage by ions and free radicals. Figure 1.5 shows a summery of the death mechanisms caused by radiation. The vascular endothelium is the primary target with contribution from endothelial-cell apoptosis, microvascular dysfunction, and T-cell response. Histologically, a brisk inflammatory response and severe vasculopathy occur in lesions that respond well to radiation (Joiner and Kogel, 2018).

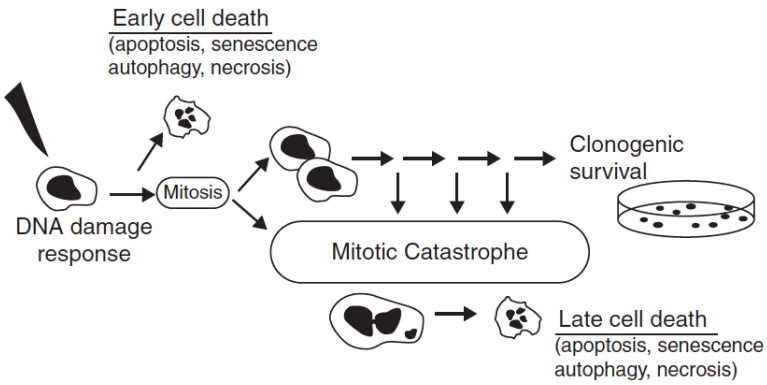

FIGURE 1.5: **Schematic of cell death following irradiation.** Figure adapted from Joiner and Kogel, 2018.

There are different devices in operation for stereotactic radiosurgery, which differ in both the type of radiation delivered and the method of focusing the beams to the target. SRS uses multiple, convergent beams of high energy x-rays, gamma rays, or protons, delivered to a discrete, radiographically-defined, treatment volume (Shepard et al., 2008). The steep radiation fall-off into surrounding tissues limits toxicity and side effects and maintains safety.

Radiation dose is measured in gray (Gy), which is the absorption of one joule of radiation energy per kilogram of matter. The SRS dose is adjusted to be biologically equivalent to five to six weeks of daily conventional radiation therapy. The dose is delivered in either a single session or two to five sessions of fractionated therapy over days.

Stereotactic radiosurgery is appropriate for patients with brain metastasis and some primary tumors, including meningiomas, vestibular schwannomas, pituitary tumors, and others, that are resistant to conventional WBRT. It is the treatment of choice for patients with a small number of cerebral metastases that are not amenable to resection (Niranjan et al., 2019).

1.4.2 CAR T cell therapy

Cancer immunotherapy approaches use components of a patient's own immune system to selectively target cancer cells. Immunotherapies are already an effective treatment option for several cancers due to their selectivity, long-lasting effects, and benefits for overall survival (Koury et al., 2018).

CAR T cell therapy represents a major step in personalized cancer treatment, and is the most successful type of immunotherapy. This therapy is predicated on the use of gene-transfer technology to instruct T lymphocytes to recognize and kill cancer cells. CARs are synthetic receptors that mediate antigen recognition, T cell activation, and co-stimulation to increase T cell functionality and persistence. For the clinical application, the patient's T cells are obtained, genetically engineered ex vivo to express the synthetic receptor, expanded and infused back into the patient (Sadelain, 2015). Figure 1.6 shows an overview of CAR T cell therapy.

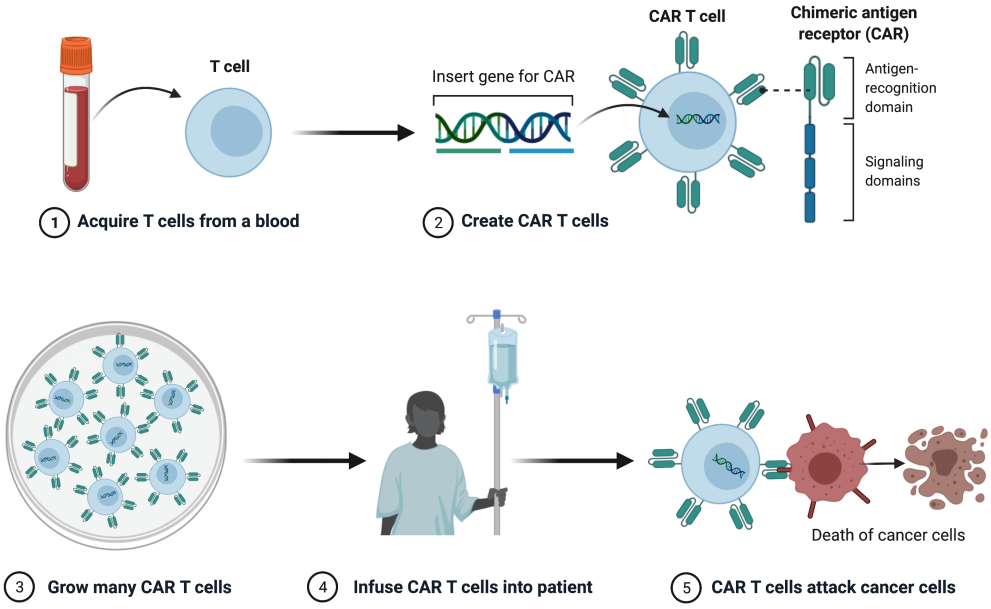

FIGURE 1.6: **CAR T cell therapy: an overview.** Created with BioRender.com.

CARs are recombinant receptors that typically target surface molecules (Feins et al., 2019). CARs are typically composed of an extracellular antigen-recognition moiety that is linked, via spacer/hinge and transmembrane domains, to an intracellular signaling domain that can include costimulatory domains and T-cell activation moieties. CARs recognize unprocessed antigens independently of their expression of major histocompatibility antigens, which is unlike the physiologic T-cell receptors (TCRs). Hence, CAR T-cells can circumvent some of the major mechanisms by which tumors avoid major histocompatibility class.

Clinical trials have shown promising results in end-stage patients with B-cell malignancies due to their expression of the CD19 protein (Sadelain, 2017). CAR T cells engineered to recognize this antigen have led to an early clinical response of up to 92% in B-ALL patients (Miliotou and Papadopoulou, 2018). Good results have been reported for large B-cell lymphomas and multiple myelomas. These successes have led to the approval of CAR T therapies for use against CD19 for treatment of B-ALL and diffuse large B-cell lymphomas (Sadelain, 2017).

CAR T-related toxicities are cytokine release syndrome (CRS), due to the release of cytokines during CAR T cell action, and immune effector-cell-associated neurotoxicity syndrome (ICANS). CRS symptoms including hypotension, pulmonary oedema, multiorgan failure, and even death, are now better controlled using IL-6 inhibitor tocilizumab (Neelapu et al., 2018).

1.5 Mathematical modeling in cancer

Mathematics plays an increasingly prominent role in cancer research, with applications ranging from theoretical studies to clinical trials designed using mathematical models. As such, mathematical oncology – defined as the use of mathematics in cancer research – has gained momentum in recent years with the rapid accumulation of clinical data and applications of mathematical methodologies.

Through mathematics, modeling and simulation, primarily through the use of patient-specific clinical data, the personalization of medicine is achieved.

Mathematical models—whose role is to describe, quantify, and predict multifaceted behaviors—have the potential to help in finding optimal administration protocols, provide a deeper understanding of the dynamics, help in the design of clinical trials and more (Altrock, Liu, and Michor, 2015; Pérez-García et al., 2016). Mathematical models (also called in silico models) have proved useful for deriving a detailed understanding of mechanisms and processes in cancer. Data sets and biological results can be perfectly complemented with analysis coming from mathematical models. When there are doubts about the processes that are behind of the obtained results, mathematical models might be useful to clarify the situation.

Another characteristic that makes mathematical models powerful, is to establish the relative importance of different processes in the final result. The relevance of each process can be estimated performing computational simulations with different parameters values and comparing the results. Performing laboratory experiments to study the relevance of the different process is normally much more difficult to do. In addition, mathematical simulations are less time-consuming and cheaper than laboratory experiments. Once a reasonable model is available, computer simulations can be quickly carried out to analyze the outcome of the system under different initial conditions.

There are countless mathematical models designed to describe biological processes related to cancer, which can be grouped according to similar characteristics. Systems that are deterministic (exactly or approximately) can be described by ordinary differential equations (ODEs), partial differential equations or logical deterministic cellular automata. The main characteristic of ODEs is that they have one independent variable. For dynamical systems, the independent variable is time. Dependent variables can be the volume of a tumor, the fraction of a genetic alteration in a population or the chance of finding a receptor in a certain state at a certain time. ODEs can describe systems of few and many dimensions, and allow chaotic and complex behavior. For dynamic systems in which the quantities of interest depend on more than one independent variable (for example, time and space), partial differential equations (PDEs) are used. This is beneficial especially when descriptions in higher dimensions are needed.

Stochastic models can describe the evolution of interacting cell populations, in which the relevant events for each individual (e.g. birth and death) occur randomly. In the limit of large cell-populations, these models are approximated by deterministic kinetic rate models, which are widely used in the modeling of cell populations. Each state of the system is considered a random variable with a certain probability distribution. From a given initial condition, many different outputs can be obtained. Non-Markovian processes, jump Markovian processes or continuous Markovian processes belongs to this group, which are mathematically modeled with a generalized master equation, a master equation and stochastic-differential equation respectively (Fedotov, Iomin, and Ryashko, 2011; Gupta et al., 2011; Durrett, 2015).

Hybrid models combine spatial reaction–diffusion (such as growth–consumption dynamics on a continuous scale) with discrete cellular dynamics (for example, on a lattice), which describe cell growth and motility. Hybrid models are among the most sophisticated approaches in mathematical cancer modeling (Rejniak and Anderson, 2011; Macklin et al., 2009).

Although important advances have been made in the quantitative description of cancer progression and treatment dynamics, several important issues remain to be resolved. For example, quantitative approaches are needed to help explain the response of treatment to immunotherapies and to help identify patients who may respond to such agents or who will experience life-threatening side effects. In addition, the best way to combine a specific immunotherapy agent with chemotherapies, targeted therapies or radiation could be explored.

Quantitative approaches to metastases are still relatively descriptive, mainly due to the lack of detailed data from multiple sites in many patients. Indeed, as the ability of a model to predict the dynamics of the system depends on its parameterization, it is essential to obtain accurate estimates of the parameters from clinical trials or in vitro and/or in vivo model systems. Due to the paucity of such data, closer collaboration between mathematical modelers and experimental and clinical researchers would be necessary.

In this thesis, we address some of the problems mentioned above, as recently important issues in basic and clinical cancer research. Each problem was approached with the most appropriate mathematical tools according to their particularities, in our opinion. Deterministic mathematical models were developed in the form of ordinary differential equations in the simplest possible way. A discrete stochastic model was also developed for a better description of cell interactions and better understanding of the spatial aspects present in solid tumors. Some of the research presented were supported by real data, both human and mouse, thus achieving the ideal nexus between mathematical modeling and cancer. In other cases this was not possible, although the results of clinical studies and biological experiments were taken into account both for the modeling itself and for the evaluation of the veracity of the results obtained.

Part I

Solid Tumor Growth and Response to Stereotactic Radiosurgery

Chapter 2

Macroscopic tumor growth

2.1 Introduction

Tumor growth is a highly dynamic process that depends on many biological processes, such as the driving molecular alterations with the associated heterogeneity, angiogenesis, the action of the immune system, the role of tumor microenvironment and surrounding healthy structures, the effect of treatments on the different tumor subpopulations, etc. The complexity of tumor growth dynamics represents an obstacle in attempts to study and model tumor response to available therapeutics, and ultimately hinders our efforts towards personalized cancer therapy.

The study of effective mathematical laws to describe the dynamics of tumor growth has been a topic of interest in mathematical oncology. Numerous mathematical models of cancerous tissue growth at different levels, from gene expression to the phenomenological description of macroscopic tumor development, have been formulated. The data that support these models come from patient-derived cell lines cultured in vitro or else from either allotransplantation of murine cells into syngeneic immunocompetent inbred mice or from xenotransplantation of patient-derived cells into immunocompromised mice (Kuang, Nagy, and S.E.Eikenberry, 2016; Benzekry et al., 2014; Jarrett et al., 2018; Gerlee, 2013; West and Newton, 2013). In these cases many data are available but these experimental models do not have all of the biological complexities of human tumors described above.

Describing cancer growth in humans is a more complex problem that presents several challenges. In first place, the growth of real cancers is an emergent phenomenon resulting of the combination of different biological mechanisms having different weights in different tumor stages. It is often not clear a prior which elements of that complexity are to be retained to account for the growth dynamics. Furthermore, modeling human tumor growth is a clinic challenging due to there is an intrinsic difficulty related to the lack of data. It may seem surprising that data availability might be a problem for such a widespread disease. Macroscopic tumor growth data are typically obtained from medical imaging, that is performed routinely for most cancer patients in order to monitor the disease dynamics.

The problem is that after detection and diagnosis therapeutic actions are promptly performed when appropriate, what affects the tumor natural history. Untreated patient data are scarce since typically this corresponds either to benign tumors having a very favorable prognosis or to terminal patients that are not followed by imaging. These facts have limited the studies of tumor growth laws in humans to using only two time points, what allows to obtain information on the rates of tumor growth but not on the functional form (Stensjøen et al., 2015; Talkington and Durrett, 2015).

In this work we wanted to study the macroscopic dynamics of tumor growth. For that, we collected data of different cancer types imaged at diagnosis before receiving any treatment directed at the tumor in question. An extensive search allowed us to

obtain several datasets of patients bearing tumors being either malignant initially of becoming malignant during the time course of the disease. For a better description of macroscopic tumor growth, more than two image points of follow-up data were used. Despite the limitations using animal models to measure and predict tumor growth dynamics, we also included data provided by two animal models because their close relationship to their human counterparts. These data sets were used to complement the results obtained in humans, providing robustness to the study.

2.2 Methods

2.2.1 Patients and image acquisition

Several patient datasets were used for our study. The first was a set of brain metastases in which one of the lesions was either below target definition or left without therapy for medical reasons. The second set included low-grade gliomas that underwent surgery and received no other treatment for long times but whose evolution was monitored by MRI until their transformation into high-grade gliomas. The third was from patients enrolled in a lung cancer screening program. After detection of lung nodules with no signs of malignancy, they were followed up by low-dose CT scans. Many of these tumors had growth that accelerated up to a point at which further therapeutic actions were taken. Finally, we included a subset of petroclival meningiomas that showed signs of atypical behavior (cases 5, 6, 9, 11 in Figure 7 and cases 14, 18 in Figure 8 of Havenbergh et al., 2003).

The main characteristics and inclusion criteria of the patients analyzed are described below.

Brain metastasis patients

Patients were participants in the METMATH (Metastasis and mathematics) study, a retrospective multicentre and non-randomized study that was approved by the IRB of the participating institutions. Five of the 200 patients analyzed were included in the data set (one man, four women, age range 38–67 years, median 52 years). These corresponded to patients diagnosed with a brain metastasis of a primary lung cancer with an untreated lesion based on three or more consecutive MRI studies before treatment. Primary cancers included four NSCLC and one breast luminal b cancer. A total of 16 imaging studies were included, with 3–4 studies per patient. The post-contrast T1-weighted sequence was a gradient echo sequence using a 3D spoiled-gradient recalled echo or a 3D fast-field echo after the intravenous administration of a single dose of gadobenate dimeglumine (0.10 mmol kg^{-1}), with a delay time of 6–8 min.

MRI studies were performed in the axial plane with a 1.5 T Siemens scanner, a 3 T Philips scanner or a 1 T Philips scanner. The imaging parameters were no gap, a slice thickness of 1–1.6 mm, 0.438–0.575 mm xy resolutions and 0.8–1.3 mm spacing between slices.

Low-grade glioma (LGG) patients

A total of 82 patients who were diagnosed with grade II gliomas (for whom astrocytoma, oligoastrocytoma or oligodendroglioma, according to the WHO 2007 classification, was confirmed with biopsy or surgery) and followed at the Bern University

Hospital between 1990 and 2013 were initially included in the study. The study was approved by Kantonale Ethikkommission Bern.

From this patient population, we selected patients receiving either no treatment or only surgery, for whom at least five post-surgery consecutive images showing tumor growth were available. Six patients who were initially diagnosed with grade II gliomas (4 astrocytomas and 2 oligodendrogliomas, age range 29–50 years, mean 37 years) were included. A total of 34 imaging studies were used, with 4–7 studies (mean 6) per patient.

Lung cancer patients

The patients included were participants in the SCALAMATH (scaling laws and mathematical models in cancer) study. Five patients (three men, two women, age range 60–72 years, median 68 years) were included. Three of these patients were diagnosed with adenocarcinoma and two with squamous cell carcinomas. All of the cancers were initially stage I tumors and progressed without treatment.

We drew scans from the database of follow-up screenings in the International Early Lung Cancer Action Program between 2008 and 2019, which were performed according to a common protocol (Henschke, 2019) using low-dose CT. Enrollment in the study was limited to those aged 50 years or older, with a smoking history of at least 10 pack-years, no previous cancer and general good health. Participants who harbored a parenchymal solid or part-solid non-calcified nodule with at least three or more follow-up CTs were identified according to criteria specified in the protocol. A total of 22 imaging studies were used, with 3–6 studies per patient.

Thoracic CT scans used a 16-acquisition-channel multidetector CT scanner (Siemens Emotion 16) with a maximum section collimation of 1 mm, 0.7 mm of spacing between slices, a slice thickness of 1 mm and a 0.584–0.783 mm range in xy resolutions. The CT scans were performed with 120 kVp and 30 mAs, with less than 1 s tube rotation time. Contiguous images were reconstructed in the trans-axial plane using a 1 mm thickness. Lung image sets were reconstructed with a high-frequency algorithm, and mediastinal image sets were reconstructed with an intermediate frequency algorithm.

The diagnosis of lung cancer was made by the histopathological examination of needle core biopsy or resection specimens, or by the cytopathological examination of bronchoscopic or needle aspiration biopsy samples. Resected tumors were classified based on the WHO classification of lung neoplasms. Adenocarcinomas were classified according to the classification of lung adenocarcinoma sponsored by the International Association for the Study of Lung Cancer, the American Thoracic Society and the European Respiratory Society. All of the lung cancer diagnoses were reviewed centrally. The tumors were staged using the International Association for the Study of Lung Cancer staging guidelines (Henschke, 2019).

Hamartoma patients

Included in our study were six patients (five men, one woman, age range 51–63 years, median 58 years) who were diagnosed with lung hamartomas with longitudinal follow-up. These patients were participants in a retrospective study approved by the Valencia Oncology Institute Foundation (IVO) specifically for the study of the scaling laws. The imaging methods were the same as those for the previous subgroup. A total of 46 imaging studies were used, with 5–12 studies (mean 8) per patient.

Atypical meningiomas

Finally, we included a subset of petroclival meningiomas that showed signs of atypical behavior (cases 5, 6, 9, 11 in Figure 7 and cases 14, 18 in Figure 8 of Havenbergh et al., 2003). Patients were treated conservatively during a minimal period of 4 years with regular clinical and radiological control examinations.

2.2.2 Image analysis

MRI image analysis

Brain metastasis T1-weighted images were collected in Digital Imaging and Communication in Medicine (DICOM) format and analyzed. An experienced radiologist revised and validated the tumor delineation.

T1-weighted images in DICOM files were imported into the scientific software package Matlab (R2018b, The MathWorks). The tumor T1-weighted images were placed manually in a 3D box and then semi-automatically delineated using a grey-level threshold that was chosen to identify the metabolic tumor volume (MTV). Segmentations were corrected manually slice by slice as in Pérez-Beteta et al., 2018.

For low-grade gliomas, T2/FLAIR MRI studies were used to define the tumor volume. Radiological glioma growth was quantified by manual measurements of tumor diameters on successive MRI studies (T2/FLAIR sequences). For older imaging data that were available only as jpeg images, we used the ellipsoidal approximation Pallud et al., 2006 to compute the tumor volume.

CT image analysis

The patients included were participants in the SCALAMATH study. CT images of lung cancer nodules were obtained in DICOM format. An experienced radiologist localized the lesion and then an image expert performed the segmentations following the same methodology as for T1-weighted images.

2.2.3 Animal studies

The animal experiments were carried out in the National Cancer Research Center (CNIO) and in the Carlos III-UFIEC Health Institute in Madrid, Spain. The experiments were not carried out by the author of this thesis. Here, we explain in detail the animal models and how the experimental data was obtained.

Animal studies with H2030-BrM3 cells

The human lung adenocarcinoma brain tropic model H2030-BrM (Nguyen et al., 2009) was injected into the heart of nude mice in order to induce the formation of brain metastasis from systemically disseminated cancer cells. Brain colonization and growth of metastases were followed using non-invasive bioluminescence imaging since BrM cells express luciferase. Upon administration of the substrate D-luciferin, bioluminescence generated by cancer cells was measured over the course of the disease. The increase in photon flux values is a well established correlate of tumor growth in vivo (Nguyen et al., 2009; Valiente et al., 2014).The experiments were performed in accordance with a protocol approved by the CNIO, Instituto de Salud Carlos III and Comunidad de Madrid Institutional Animal Care and Use Committee. Athymic nu/nu (Harlan) mice of 4-6 weeks of age were used. Brain colonization assays were performed by injecting 100 μl PBS into the left ventricle containing

100,000 cancer cells. Anesthetized mice (isofluorane) were injected retro-orbitally with d-luciferin (150 mg/kg) and imaged with an IVIS Xenogen machine (Caliper Life Sciences). Bioluminescence analysis was performed using Living Image software, version 3. The absolute unit of radiance is photons/sec/cm^2/steradian, and refers to the photons per second of light that radiate from the mouse in a unit area (1 cm^2) and unit angle (1 steradian) (Zinn et al., 2008).

Mouse glioma xenografts

Primary glioma cells expressing the luciferase reporter gene into the brain of nude mice were injected . One month after the injection, weekly monitoring animals is started using IVIS Spectrum In vivo Imaging System. The Total Flux (in photons per second) was measured to assess tumor growth. Animal care and experimental procedures were performed in accordance to the European Union and National guidelines for the use of animals in research and were reviewed and approved by the Research Ethics and Animal Welfare Committee at our institution (Instituto de Salud Carlos III, Madrid) (PROEX 244/14). Stereotactically guided intracranial injections in athymic nude Foxn1nu mice were performed by administering 1×105 L0627 cells resuspended in 2 μl of culture media. The injections were made into the striatum (coordinates: A-P, –0.5 mm; M-L, +2 mm; D-V, -3 mm; related to Bregma) using a Hamilton syringe. One month after injection, monitoring of reporter expression in tumors begins. For that, animals received and intraperitoneal injection of Luciferin (Fisher) (150mg/Kg) and the Luciferase activity was visualized in an IVIS Spectrum in vivo imaging system (Perkin Elmer).

2.3 Mathematical model

The proposed mathematical model is focused on the relationship between tumor size and metabolism. We begin by considering the metabolic rate of a tumor to be $B \propto V^{\beta}$, where V is the total volume occupied by viable cells and $\beta > 0$ is the scaling exponent. Due to energy conservation, the temporal dynamics of tumor growth is given by $B = aV + b\frac{dV}{dt}$, where the first and second right-hand terms represent cell maintenance and proliferation, respectively. This model was first proposed by Bertalanffy, 1957 and also later studied in West, Brown, and Enquist, 2001. The resulting first-order differential equation describing the time variation of $V = V(t)$ can be written as

$$\frac{dV}{dt} = -\gamma V + \alpha V^{\beta}, \tag{2.1}$$

with an initial condition for the tumor volume at time $t = t_0$, $V(t_0) = V_0$. Assuming that most of the energy is used for cell biosynthesis, we may neglect the linear term in Eq. (2.1) as far as there is net tumor growth and thus approximately write

$$\frac{dV}{dt} = \alpha V^{\beta}. \tag{2.2}$$

When the value of $\beta = 1$ we are in the presence of an exponential volumetric growth. Otherwise, the resulting ordinary differential equation can be solved in closed form as

$$V(t) = \left[V_0^{1-\beta} + \alpha(\beta - 1)(t - t_0)\right]^{1/(1-\beta)}, \tag{2.3}$$

where V_0 is the volume at time t_0. If $\beta > 1$ there is a finite time at which the tumor 'blows up', given by

$$t_{\text{crit}} = t_0 + V_0^{1-\beta} / \left[\alpha(\beta - 1)\right]. \tag{2.4}$$

Note that in this case the Eq. 2.2 describes a super exponential (or super-linear) growth, understanding this as a faster growth than the exponential (than a linear function), i.e. $\lim_{V\to\infty} \frac{\alpha V^\beta}{\alpha V} \longrightarrow \infty$ for $\beta > 1$.

Whereas if $\beta < 1$ the Eq. 2.2 describes a volumetric growth slower than the exponential one (sublinear growth). In particular, Kleiber observed the exponent $\beta = 3/4$ for the power law scale of metabolic rate and animal mass ($B \propto V^{3/4}$, assuming volume is proportional to body mass) (Niklas and Kutschera, 2015). Kleiber's law is considered one of the few quantitative laws in biology. West, Brown, and Enquist, 1997 proposed that the exponent found by Kleiber could be the result of principles of minimal energy.

2.4 Results

2.4.1 Longitudinal tumor growth dynamics in humans

We fitted the longitudinal volumetric growth data for each patient using different power-law models given by Eq. (2.2). First, we fitted the datasets with choice of exponents $\beta = 5/4$, 1 (exponential growth law) and $3/4$ (size-limited Kleiber law, West, Brown, and Enquist, 1997). Subsequently, we searched for the exponent that minimized the mean square error (MSE) for all patients within each tumor type.

In all the examined cases, the existence of an explosive growth dynamics was confirmed (see Figure 2.1 b,c,d,f). A comparison of the MSEs for the different exponents and tumor types is shown in Figure 2.1 g. We also performed a least-squares fitting to find α, β parameters for each patient and computed the mean and standard deviation for patients of each histology. The results obtained were 1.493 ± 0.0197 (BMs), 1.360 ± 0.2922 (NSCLC), 1.466 ± 0.269 (LGGs) and 1.690 ± 0.452 (AMs) respectively. Thus, exponents obtained using the two methodologies were compatible between them and above one.

We also collected longitudinal volumetric growth data from a group of patients with lung hamartomas, the most frequent benign lung tumor type, and found a best fit to Eq. (2.2) with $\beta = 0.5 \pm 0.2$ (see Figure 2.1 e). Hence, not all human tumors manifest an explosive growth. The last result corresponds to those obtained in previous studies of the growth dynamics of untreated WHO (World Health Organization) grade II gliomas (Mandonnet et al., 2003), petroclival meningiomas (Havenbergh et al., 2003), and head and neck paragangliomas (Heesterman et al., 2003), in which growth dynamics consistent with sublinear scaling were observed for slowly growing non-malignant tumors.

2.4.2 Longitudinal tumor growth dynamics in animal models

To determine whether animal models could also provide evidence of super exponential tumor growth dynamics, our biomedical collaborators performed two animal models chosen because of their close relationship to their human counterparts. First, the group of Manuel Valiente at CNIO (Madrid, Spain) injected the human lung adenocarcinoma brain tropic model H2030-BrM (Nguyen et al., 2009) into the

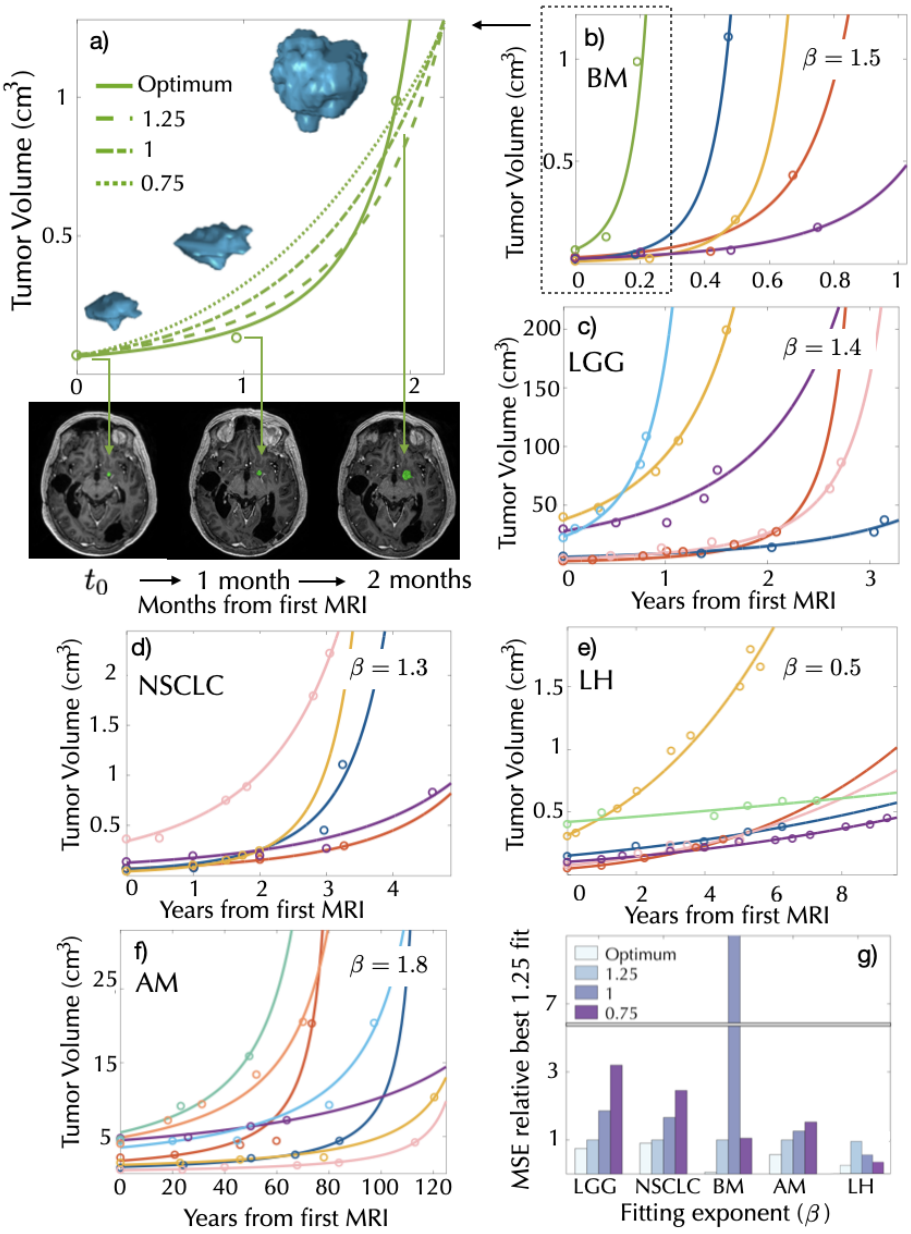

FIGURE 2.1: **Explosive longitudinal volumetric dynamics of untreated malignant human tumors.** a–f, Longitudinal volumetric data for patients with untreated brain metastases (BMs, a,b), low-grade gliomas (LGGs, c), NSCLCs (d), atypical meningiomas (AMs, f) and lung hamartomas (LHs, e). Solid curves show the fits with the optimal exponents (β values provided in each part) that give the smallest MSEs. The longitudinal three-dimensional (3D) reconstruction of a BM and representative axial slices highlighting tumor location at three time points are displayed in a, together with the fitting curves obtained for different exponents. MSE values for the five datasets and exponents 0.75, 1 and 1.25 (taken as a reference), in comparison with the optimal exponent, are shown in g. In b-f, the colors correspond to different patients.

heart of nude mice in order to induce the formation of brain metastasis from systemically disseminated cancer cells. The exponent best fitting the dynamics of the brain metastasis measured using bioluminiscence, assuming a dynamics ruled by

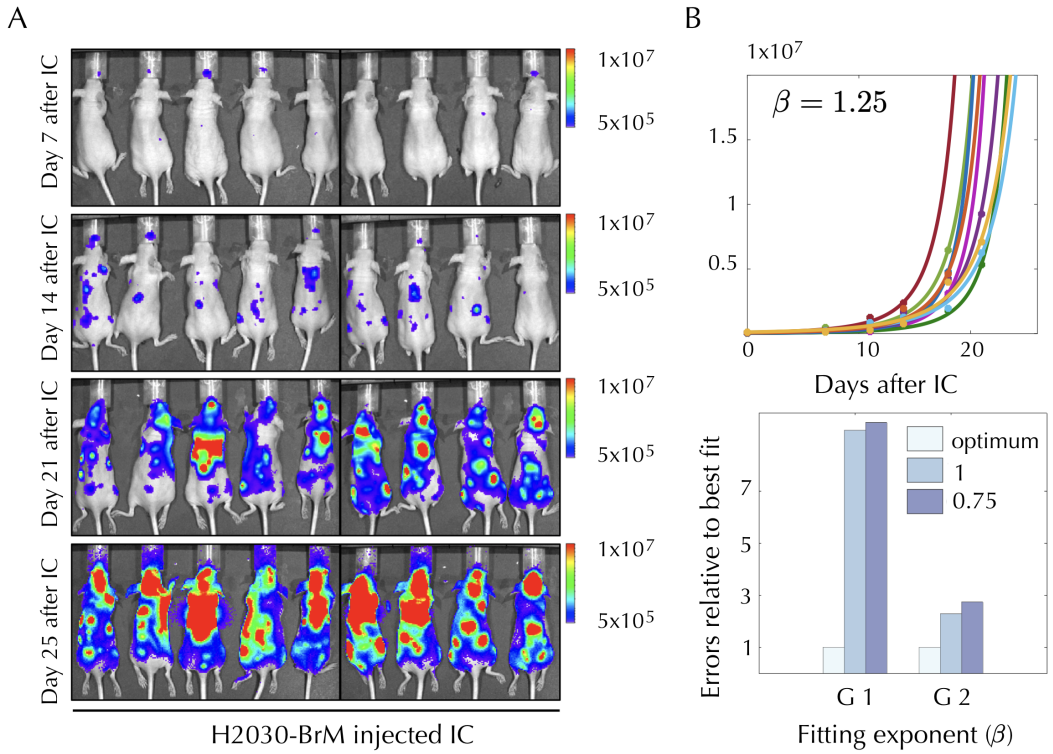

FIGURE 2.2: **Two human cancer animal models display superlinear growth dynamics.** Group 1 (G1) data correspond to untreated nude mice injected with the human lung adenocarcinoma brain tropic model H2030-BrM (see methods). Group data (G2) correspond to primary glioma cells (L0627) expressing the luciferase reporter gene injected into the brain of nude mice (see methods). Bioluminiscence images for G1 for some mice are shown in panel A. Total tumor mass growth curves for G1 showed superlinear dynamics with best fitting exponent $\beta = 1.25$ (for G2 it was $\beta = 1.3$). (B, upper panel). Errors relative to best fit were found to be substantially smaller with the optimal superlinear fits than for both the linear and sublinear fits (exponents 1 and 0.75 respectively) (B, lower panel).

Eq. (2.2), and data from all the mice was $\beta = 1.3$. In addition, the total tumor load in the animals showed similar behavior, with $\beta = 1.25$ (see Figure 2.2). In this group, some temporal instances were excluded from the fitting because tumor sizes greater than the tumor capacity compatible with the animal's life were reported (approximately 10^8 photons/sec/cm^2/steradian).

In a second set of experiments, researchers at Instituto de Salud Carlos III (Madrid) led by Pilar Sánchez Gómez injected primary glioma cells closely resembling the dynamics observed in patients (Gargini et al., 2020) and expressing the luciferase reporter gene into the brains of nude mice. One month after the injection, weekly monitoring of the animals was started, measuring the total flow to assess tumor growth. The optimal exponents obtained was $\beta = 1.25$. Furthermore, Figure 2.2 B shows that errors relative to best fit were substantially smaller with the optimal superlinear fits than for both the linear and sublinear fits (exponents 1 and 0.75 respectively).

2.5 Discussion and conclusion

In this chapter we have analyzed the dynamic behavior of tumor growth on a macroscopic scale for five different histologies of solid tumors over long periods of time. The database that supports this study was the result of a substantial collection effort and has an unmatched richness as it contains more than two data points for tumors without direct treatments during the study time. Therefore, the fact of being able to have volumetric images and more than two time points available allowed for a better understanding of the real growth dynamics and compatibility with the proposed model, thus avoiding an over-fitting.

Using a simple mathematical model, we studied the volumetric dynamics growth for our data sets. Our results show that untreated human malignant cancers display a superlinear explosive dynamics in the form of an exponent $\beta > 1$ in Eq. (2.2). This superlinear dynamics is also obtained after fitting the data from animal models, which were designed to recreate tumors with great similarity to tumors in humans. On the other hand, in the specific case of hammartomas, which are benign tumors, a slow growth dynamic was obtained, given by a value of $\beta < 1$.

This observation of the explosive behavior of malignant tumors was complemented by other results reported in Pérez-García et al., 2020 on the laws of superlinear metabolic scaling in cancer. Additionally, a data subset of those reported in Heesterman et al., 2003 showed signs of atypical behavior which are in correspondence with an accelerated volumetric growth. These results suggest that human cancers, as they progress, decrease the efficiency of their local vascular network, which would tend to increase their scaling exponents and cause them to significantly deviate from Kleiber's law ($\beta = 3/4$).

The existence of a superlinear scaling law between metabolism (or proliferation) and volume implies increasingly accelerated volumetric growth, which results in the formation of a finite-time singularity. In real cancers that type of dynamics cannot be continued up to the blow-up point since they are subject to physical and nutrient-supply constraints, and the patient would die well before reaching that limit. However, it matches very well the terminal stages in which fast cancer progression leads to cachexia and substantial damage to the patient leading to death.

The value of $\beta > 1$ indicates a continuous increase of the tumor growth rate. The mechanism behind superlinear growth could be attributed to the evolutionary dynamics of competition between cell types. Once a new cell type emerges with a higher duplication rate, it begins to dominate the tumor. The continued emergence of new cell types with greater fitness advantages leads to increased tumor growth rate.

Our results emphasize the need to obtain a better understanding of the evolutionary steps in different tumor histologies and to target these transformations to avoid growth acceleration. They also raise the question of whether working with experimental tumor models that show slower than super exponential growth could miss essential features of cancer dynamics. Finally, it would be advisable to plan the treatments in a period of time in which the evolutionary dynamics have not generated a great richness of genotypes/phenotypes and the tumor volume is not close to the blow-up point.

In summary, we have described the dynamics of tumor growth using a simple model based on the relationship between tumor size and metabolism. Longitudinal volumetric data from malignant tumors shown explosive growth beyond classical growth-limited or exponential laws. This result suggests superlinear scaling laws in human cancers. These laws differ substantially from Kleiber's law, which governs

the growth of many life forms, and point to accelerated growth due to underlying evolutionary dynamics that select more aggressive subpopulations.

Chapter 3

Stereotactic radiosurgery response: Analysis with a continuous mathematical model

3.1 Introduction

As explained in the introduction, stereotactic radiosurgery nowadays is an effective tool for the treatment of brain metastases. Brain metastasis is a condition ten times more frequent than primary brain tumors. It is thus striking that so many mathematical papers have studied primary brain tumors and their time dynamics while BMs have received scarce attention. In the following study, we focused on describing the response of BMs to this successfully treatment.

Applied mathematicians have studied different aspects of metastatic processes: the growth and distribution of untreated metastatic tumors (Iwata, Kawasaki, and N.Shigesada, 2000; Barbolosi et al., 2009; Barbolosi et al., 2017; Mollard et al., 2017; Bilous et al., 2019), the extravasation process (Brodland and Veldhuis, 2012), cancer metastasis networks (L.LChen et al., 2009; Newton et al., 2013; Scott et al., 2013; Newton et al., 2012), the interaction between the primary and metastatic tumors (Diego, Calvo, and Pérez-García, 2013) and therapeutic strategies minimizing the metastatic burden (Haeno et al., 2012), to cite a few examples.

To our knowledge, few studies have considered the mathematical modeling of BM growth and response to radiation therapy (Watanabe et al., 2016; Dehghan and Narimani, 2020). This is a situation of interest since the tumor's response to radiation therapy, either alone or in combination with other treatments, has been thoroughly studied in other brain tumors such as glioblastoma (see e.g. Leder et al., 2014; Rockne et al., 2009; Rockne et al., 2010; Yu et al., 2015; Chakwizira et al., 2018; Hawkins-Daarud et al., 2015) or low-grade glioma (e.g. Ribba et al., 2012; Badoual et al., 2014; Pérez-García et al., 2015; Galochkina, Bratus, and Pérez-García, 2015; Henares-Molina et al., 2017).

As a first step we developed a minimal mathematical model able to describe the longitudinal dynamics of BMs. This was done using BM patient imaging data to feed ordinary differential equations, in biologically-grounded tumor growth models. First, the extent to which these models could describe the dynamics of untreated BMs was analyzed. Next, the dynamics of response to radiosurgery over time was studied when death mechanisms and damaged cell compartments were included.

In the context of our simplifying assumptions, we assumed the proliferation rate of the BMs to be the same after treatment than before it. The phenomenon of growth acceleration of residual tumors of certain histologies after fractionated radiotherapy courses, the so-called accelerated repopulation, has been known for a long-time

(Joiner and Kogel, 2018). However, repopulation rate has been found to be lower in tumors with increased cell loss, as it happens in radiation surgery (Hessel et al., 2003). In fact, there are no reports of observations of accelerated repopulation after radiation surgery treatments. This is also consistent with the observation in experimental tumors that the triggering of accelerated repopulation requires minimum total treatment duration times longer than than 3–4 weeks in human tumors (Joiner and Kogel, 2018).

Other biological processes could also lead to differences in proliferation rate with time. It has been hypothesized on the basis of different sources of biomedical data and studied mathematically, that actions on the primary tumor could influence the dissemination and growth dynamics of metastasis (Diego, Calvo, and Pérez-García, 2013; Hanin and Rose, 2018; Franssen et al., 2019). However, in the case of brain metastases the BBB may provide a chemical firewall for the communication between the primary tumor and metastatic colonies and the fact is that no solid evidences of such chemical links have been provided. Moreover in the case studied here of stage IV lung cancer, surgical treatment of the primary tumor is not typically a therapeutic option. This is why we did not account for any "communication" between the primary tumor and the BMs in our modeling approach.

In our mathematical model we used a single population of proliferating metastatic cells accounting effectively for the tumor dynamics. Brain metastases, and specifically lung cancer ones, are heterogeneous and composed of genetically and phenotypically different subpopulations (Liu et al., 2020; Shih et al., 2020; Perus and Walsh, 2019). This heterogeneity leads to a differential response to radiation therapy depending on many molecular factors such as EGFR overexpression (Akimoto et al., 1999), TopBP1 and Claspin (Choi et al., 2014), MET (Stella et al., 2019), CAVEOLIN-1 (Duregon et al., 2019), and many others (Soffietti et al., 2020; Ahmed et al., 2017). Indeed, radiation resistance is associated not only to specific individual features of the cancer cells. It is being increasingly recognized that the tumor microenvironment, cell-cell communications and other factors play a role in this complex emergent property (Smart et al., 2015; Voglstaetter et al., 2019). Here we intended to develop a minimal model able to describe observed volumetric dynamics, that is the only follow-up information available through standard MRI-imaging.

3.2 Methods

3.2.1 Patients

Patients included were participants in the study METMATH (Metastasis and mathematics), a retrospective multicenter and non-randomized study approved by the institutional review boards of the three participating institutions. We reviewed the METMATH records to look for patients satisfying the following inclusion criteria: patients diagnosed with brain metastasis of a primary lung cancer that had undergone at least a T1-weighted MRI examination with contrast before SRS, and at least two T1-weighted MRIs after SRS. The time interval between the diagnostic MRI and SRS had to be at most two weeks. Patients who received whole brain radiation therapy within four months before SRS, or during the followup period, were excluded. Patients who received surgery were also excluded. 45 patients satisfied the inclusion criteria. Patients with more than one treated brain metastasis were analyzed; 32 patients had only one BM, 11 patients had 2 BMs and 2 patients had 3 BMs. Finally, 60 brain metastases were included. Median patient age was 60 years (range 43-80) and sex was 59% male, 41% female.

The dose and fractionation schedule was chosen at the discretion of the treating radiation oncologists and performed using γ rays. A total of 46 lesions were treated with a single dose (range 17–24 Gy), six lesions with three dose fractions (range 5.5–8.8 Gy) and eight lesions received between 4 and 6 dose fractions (range 4–9.5 Gy). The mean follow-up period of the patients studied was 11 months (range 3–30 months).

Contrast-enhanced T1-weighted sequence was gradient echo using 3D spoiled-gradient recalled echo or 3D fast-field echo after intravenous administration of a single dose of gadobenate dimeglumine (0.10 mmol/kg) with a (6-8)-min delay.

MRI studies were performed in the axial or coronal plane with either a 1.5 T Siemens scanner (259), a 3 T Philips scanner (45) or a 1 T Philips scanner (13). Imaging parameters were no gap, slice thickness of 0.5 - 2.0 mm (mean 1.1 mm), 0.4-1.1 mm (mean 0.6 mm) resolutions in the x and y planes, and 0.6 - 2.0 mm spacing between slices (mean 1.5 mm).

3.2.2 Tumor Segmentation

Brain metastasis T1-weighted images were collected in DICOM format and analyzed. Also, they were reviewed by the either a senior radiologist or an image expert with 5 years' expertise in tumor segmentation. The tumor volume for each brain metastasis was defined on gadolinium-enhanced magnetic resonance imaging (T1Gd-MRI) as the contrast-enhancing (CE) compartment of the tumor combined with the central non-enhancing (non-CE) compartment enclosed by the contrast (the latter usually represented necrosis).

Segmentation was performed by importing image files into the scientific software package Matlab (R2019b, The MathWorks, Inc., Natick, MA, USA). Images were manually placed in a 3D box and then semi-automatically delineated using a gray-level threshold chosen to identify the contrast-enhancing volume. Segmentation was corrected manually slice by slice as described in Pérez-Beteta et al., 2018.

3.2.3 Mathematical model of response to radiosurgery

Our mathematical model to describe growth and response to therapy of brain metastases is based on a set of ordinary differential equations for the different cellular compartments involved in a simplified description of the tumor growth dynamics. The first was the proliferating tumor cells $P(t)$. Since BMs are often small tumors that are detected at an early phase of growth, far from the brain's carrying capacity, the number of proliferating cancer cells can be described by an exponential model of the form

$$\frac{dP}{dt} = \rho P. \tag{3.1a}$$

In Eq. (3.1a), $P(t)$ represents the number of proliferating cancer cells at time t and ρ the rate of proliferation. In the previous section, we explored different tumor growth dynamics and concluded that the growth dynamics of brain metastasis could be better described by a superlinear growth law. For the sake of simplicity, in this work we kept the simpler and more classical growth law given by Eq. (3.1a).

Stereotactic radiosurgery is a highly precise form of radiation therapy that lethally damages a fraction $1 - S_f$ of the irradiated proliferating cancer cells. Lethal damage,

caused by high doses of radiation, cannot be repaired and occurs via different pathways. Here we accounted for the two most important, in the response to SRS. The first process is fast and leads to a fraction ϵ of lethally damaged cells being incorporated directly into the necrotic cell ($N(t)$) compartment. The second process leads to a population $D(t)$ of lethally damaged cells that may undergo one or more divisions before dying by mitotic catastrophe (Joiner and Kogel, 2018). The evolution of this cellular compartment was given by the equation

$$\frac{dD}{dt} = -\frac{\rho}{k}D, \tag{3.1b}$$

where k is the average of mitosis cycles completed before death. In practice k/ρ provides a, typically long, time scale for the death of this population of damaged cells. This type of model have been found to provide a good description for the response of low-grade glioma (Pérez-García et al., 2015) and prostate cancer (Lorenzo et al., 2019) to radiation therapy.

There is evidence in the literature that SRS destroys tumor vascular beds, thereby deteriorating the tumor microenvironment and leading to indirect tumor cell death (Kim et al., 2015). These phenomena can produce regions of hypoxia, tumor necrosis and massive release of tumor antigens, elevating antitumor immune response in a short period of time. Furthermore, tumor hypoxia may persist after vascular injury caused by SRS and both oxygenated and hypoxic cells are ablated by high-dose radiation (Brown, Carlson, and D.J.Brenner, 2014). This fact, together with the impossibility of accounting for the number of hypoxic cells in brain metastases through MRI, motivated the non-inclusion of this population within the mathematical model. Thus, we also accounted for a population of immune cells $I(t)$ present in the tumor, whose dynamics were governed by the equation

$$\frac{dI}{dt} = \alpha N - \lambda_I I, \tag{3.1c}$$

In Eq. (3.1c), α is a stimulation parameter that accounts for the immune system activation by the presence of necrosis and λ_I is the decay rate of the immune activation.

Finally, the dynamics of the necrotic cell (or necrosis) compartment was governed by the equations

$$\frac{dN}{dt} = \frac{\rho}{k}D - \lambda_N N I. \tag{3.1d}$$

Thus, we described necrosis dynamics by the contribution of damaged cells through mitotic death and the interaction with the immune system, which in turn is activated by the release of a variety of pro-oxidant and pro-inflammatory cytokines such as tumor necrosis factors (Rock and Kono, 2008). The first term in Eq. (3.1d) corresponds to the contribution of damaged cells, and the second describes the elimination of necrotic cells by the action of immune cells. This process is modulated by the constant λ_N.

As to the initial data, before treatment the tumor was assumed to be composed mostly of proliferating cells. SRS was performed at a given time t_0 on a tumor cell population $T(t_0)$. As stated above, a fraction of tumor cells S_f suffered either no damage or only sublethal damage and remained viable. A further fraction $(1 - S_f)T_0$ received lethal damage of which a fraction ϵ died on a short time scale (i.e. days) and the remainder moved into the compartment of lethally damaged cells. This means

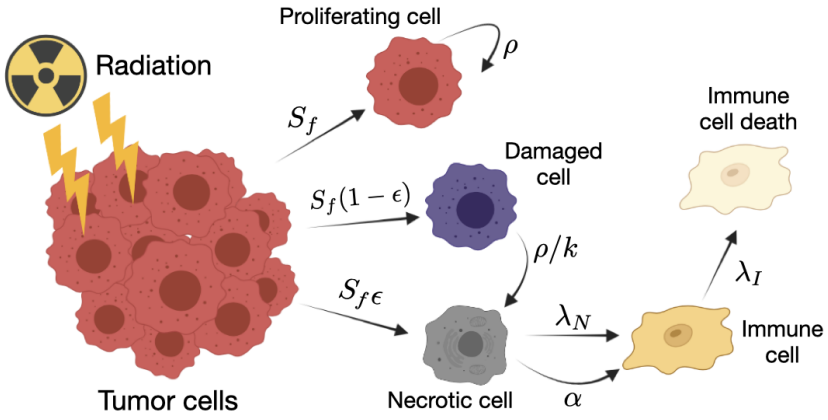

FIGURE 3.1: **Schematic description of the compartments included in Eq. (3.1) and the effect of radiosurgery.** Different cellular compartments appear after SRS on metastatic cells. Proliferating cells $P(t)$ continue to grow at a rate ρ. Damaged cells $D(t)$ become necrotic $N(t)$ at a rate of ρ/k because of the mitotic catastrophe. Necrosis stimulates the immune cell $I(t)$ activation with a stimulation parameter α, and is removed by its interaction with them. Immune cells are inactivated with a decay rate λ_I. Created with BioRender.com.

that,

$$P(t_0) = S_f T(t_0), \tag{3.2a}$$
$$D(t_0) = (1-S_f)(1-\epsilon)T(t_0), \tag{3.2b}$$
$$N(t_0) = (1-S_f)\epsilon T(t_0), \tag{3.2c}$$
$$I(t_0) = 0, \tag{3.2d}$$

where S_f and $\epsilon \in (0,1)$. Figure 3.1 summarizes the different compartments included in the model and the effect of radiosurgery. In this study we assumed the pretreatment number of immune cells to be very small. Intratumoral areas in lung cancer brain metastases have been reported to contain low numbers of inflammatory cells (Berghoff et al., 2008), high levels of immunosupressive molecules (Jiang et al., 2020) and a suppressed immune microenvironment (Kudo et al., 2019).

In addition to damaging cancer cells, SRS damages healthy tissue cells located in the field of the ionizing radiation. In spite of the increasing spatial precision of current radiosurgery techniques, radiation necrosis (RN) of normal cells is a frequent complication. Since brain tissue renewal occurs on very long time scales of many months, this damage appears typically more than a year after SRS (Vellayappan et al., 2018). This effect has nothing to do with tumor recurrence but can be confused with it on imaging because of the increase in the inflammatory compartment. To account for that, we included an explicit additional source term in the necrotic compartment $h(t)$ in Eq. (3.1d)

$$\frac{dN}{dt} = \frac{\rho}{k}D - \lambda_N N I + h(t). \tag{3.3}$$

Note that $T(t) = P(t) + D(t) + N(t) + I(t)$ is a measure of the number of cellular elements in the tumor and its environment. We assumed it to be related to the observed tumor volume, that appears in MRIs as a combination of active areas $(P + D + I)$ plus a necrotic component (N).

The model was solved and fitted to the available longitudinal volumetric data using `ode45` and `fmincom` functions included in the scientific software package Matlab (R2019b, The MathWorks, Inc., Natick, MA, USA). All parameters were fitted for each metastasis individually, even in the case of lesions belonging to the same patient.

3.3 Results

3.3.1 Model equations (3.1) describe the response to radiosurgery

Figure 3.2 shows examples of the time evolution of the volume of brain metastases treated with SRS in three patients. The cases chosen provide instances of three different typical behaviors. In the first case (Figure 3.2 a), the patient had a sustained response lasting for at least 17 months. In a second patient (Figure 3.2 b), the tumor reduced its volume for approximately 184 days and relapsed after the initial response. Finally, in Figure 3.2 c) the tumor continued to grow after radiosurgery treatment. Henceforth, we denoted the lesion behaviors described in the cases shown as monotonically decreasing lesions (MDL), lesions that at first are decreasing and later increasing (DIL), and monotonically increasing lesions (MIL), respectively.

Our mathematical model was able to describe the different scenarios shown in Figure 3.2. Figure 3.3 shows additional examples for 9 of the 60 metastases. The model was able to describe different dynamics of response to treatment in all cases. It also provided good fits for the longitudinal volumetric data of 36 metastases, which showed evolution framed within one of the three behaviors mentioned above: six metastases showed a MDL behavior, 19 showed a DIL behavior and 11 showed a MIL behavior.

This study included only 13 patients with more than one metastasis treated and thus a statistical analysis to assess similarities in the behavior of the lesions could not be performed . Four of the 11 patients were observed to have the same post-treatment dynamics in all of their metastases but the other seven patients had lesions with different longitudinal dynamics after treatment therapy.

3.3.2 The mathematical model describes the early inflammatory dynamics observed in the post-SRS response

Following SRS, six brain metastases in our dataset contained MRI imaging in the following three months. These BMs increased their size initially, suggesting treatment failure. However, they decreased their size after a few weeks, which was shown by the second examination post-SRS. This is due to an early inflammatory response to the treatment that is assumed to occur in most cases. In fact, this is the reason why the first control post-treatment MRI is typically performed three months after SRS once the effect of early inflammation has vanished. Figure 3.4 a,b show the longitudinal volumetric dynamics of BMs and the best fits using the mathematical model for two of those patients.

It is interesting that when breaking the total tumor volume into the different components (color lines in Figure 3.4), it was obvious that the initial volumetric growth was actually associated with an increase in immune activation. In both cases, radiation generated a large initial number of necrotic cells which stimulated immune cells. The sum of all the cellular compartments resulted in an increase in the total volume, but in fact, the number of proliferating cells was smaller after SRS treatment.

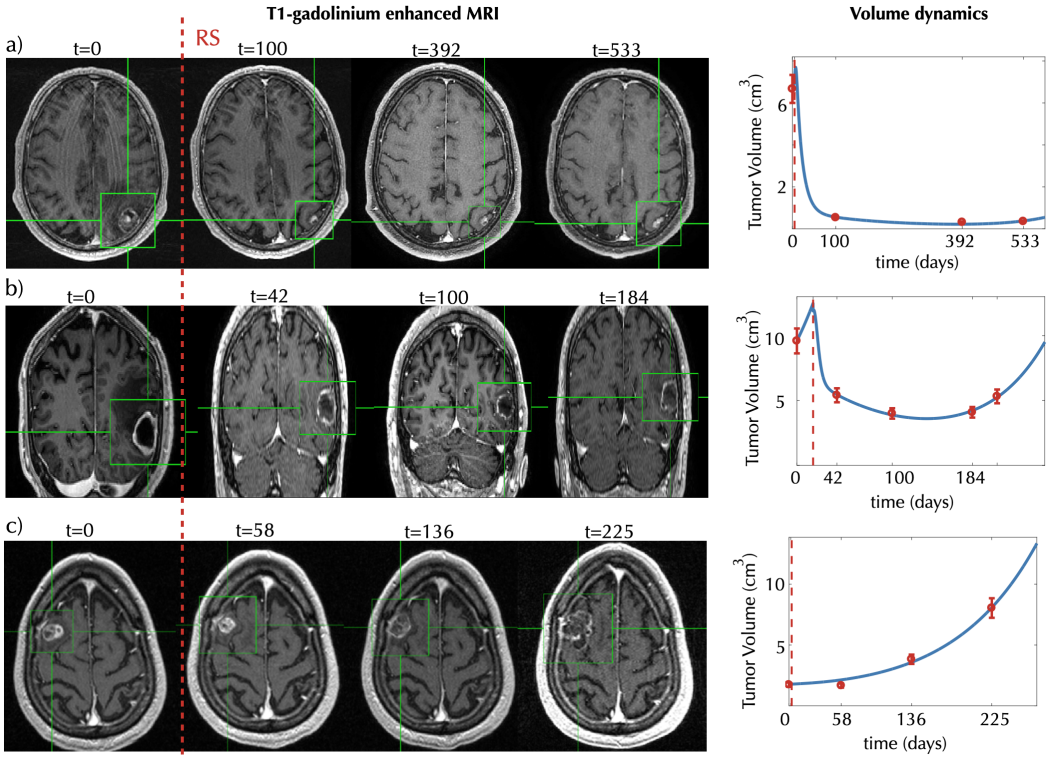

FIGURE 3.2: **Evolution of tumor response for three BM patients.** Left subplots show characteristic two-dimensional slices of the contrast-enhanced T1-weighted MRI scans showing the metastasis response to SRS for different times (in days) starting from a baseline pretreatment scan (taken to be $t = 0$ days). Subplots in (a), (c) show axial slices and (b) coronal slices. Green boxes containing the tumors are shown to help locate them. Panels in the rightmost column show the volumetric longitudinal data obtained from the 3D segmentations (red dots) and the best fits (blue lines) obtained using the mathematical model of Eqs. (3.1). The model parameters obtained for the best fits are (a) $S_f = 0.02 \times 10^{-2}$, $\epsilon = 0.90$, $\rho = 0.01$, $\lambda_N = 0.06$, $\lambda_I = 0.07$, $\alpha = 0.10$, (b) $S_f = 0.12 \times 10^{-1}$, $\epsilon = 0.60$, $\rho = 0.02$, $\lambda_N = 0.20$, $\lambda_I = 0.01$, $\alpha = 0.04$ and (c) $S_f = 0.40$, $\epsilon = 0.10$, $\rho = 0.01$, $\lambda_N = 0.01$, $\lambda_I = 0.10$, $\alpha = 0.01$.

We calculated $T(I_{max})$, representing the time when the immune cell population reaches its peak for the model fits. Figure 3.4 c shows the histogram of the calculated times for the 42 metastases classified within the above response groups.

The computed times were adjusted to a Gamma distribution with shape parameter $a = 1.4$ and scale parameter $b = 36$, and had a mean value equal to 51 days and a variance equal to 43 days. This means that the peak of inflammation occurs more frequently between months one and two post-SRS. Thus our model confirms that when MRI scans are performed before three months post-treatment, the results may be affected by early inflammation events and do not provide a reliable measure of the proliferating tumor component.

It is important to emphasize that all four classes of response dynamics studied so far (monotonically decreasing lesions, lesions that are first decreasing and later increasing, monotonically increasing lesions, and early inflammation) were accurately described by the mathematical model given by Eqs. (3.1). Figure 3.5 shows the mean

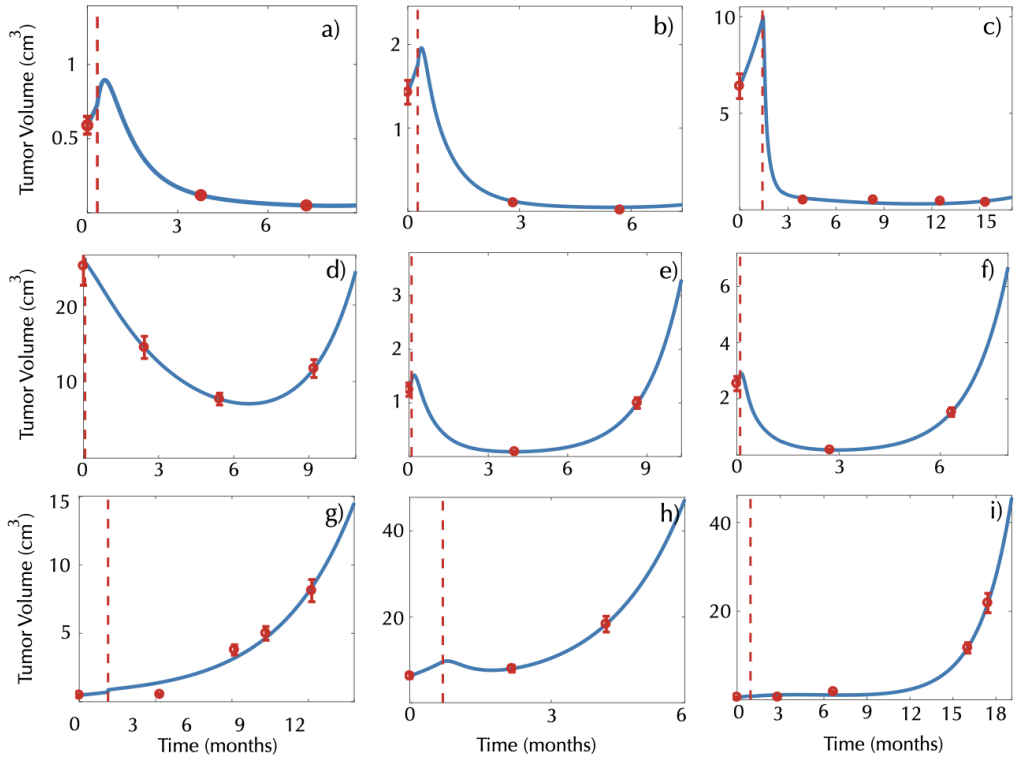

FIGURE 3.3: Examples of longitudinal volumetric tumor data (red circles) and best fits obtained with the model (3.1) (blue lines) for patients showing (a-c) MDL, (d-f) DIL and (g-i) MIL . The vertical dashed red lines mark the radiosurgery date. All times are measured in months from the baseline pretreatment scan.

square errors (MSE) of the best fits obtained using the mathematical model for this subset of brain metastases.

3.3.3 Damage to healthy tissue could lead to late inflammatory response and radiation necrosis

Late radiation necrosis is a frequent event after SRS treatment (Kohutek et al., 2015; Donovan, Parpia, and Greenspoon, 2019). This is typically observed in MRIs as volumetric growth of the lesion, typically between one and two years post-SRS, followed by spontaneous (partial or complete) remission. Radiation necrosis (also denoted to as "pseudoprogression") poses a challenge to radiologists since it is very difficult to differentiate from true tumor progression. In the former case, there is no need for anti-tumoral treatment, while the latter requires a different therapy.

In our dataset, seven BMs were diagnosed with radiation necrosis and an additional 11 BMs presented late episodes of volume increase followed by volume decrease compatible with that condition. Figure 3.6 shows two examples of the dynamics and the best fits obtained, using different mathematical models. First, we tried to fit the dynamics using Eqs. (3.1). However the model did not accurately describe the dynamics (see dashed blue lines in Figure 3.6 a,b with large MSEs (Figure 3.6 e).

To explain the inflammatory response in this group of patients, we included the late damage to the surrounding healthy tissue as described by Eq. (3.3). To do so, the parameters in Eqs. (3.1a), (3.1b), (3.1c) and (3.3) were fitted for each metastasis

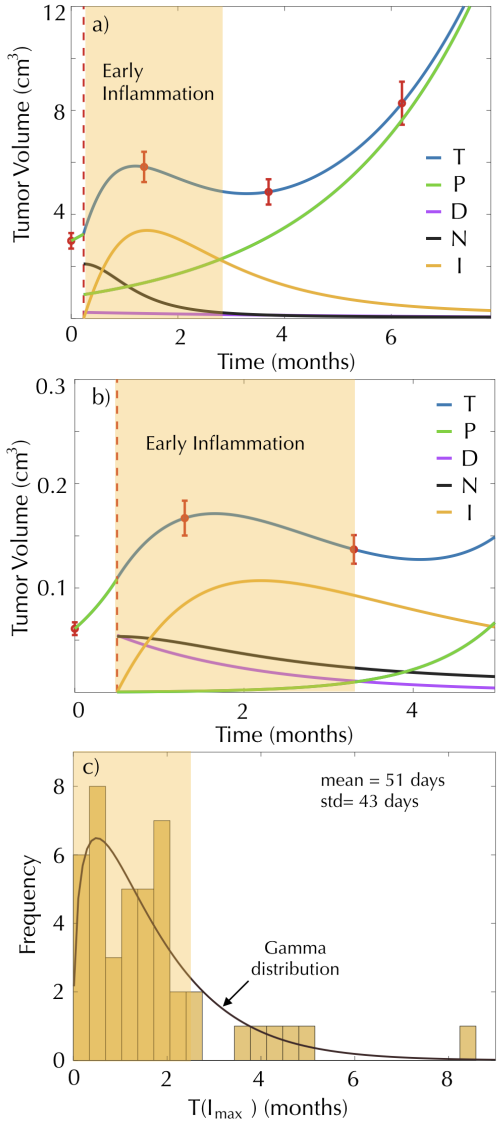

FIGURE 3.4: **Early inflammation occurs in the early response post-surgery.** The subplots (a) and (b) show the dynamics of the proliferating cells (green line), damaged cells (magenta line), necrotic cells (black line), immune cells (yellow line) and total tumor cells (blue line) governed by Eq. (3.1) of two patients. Red circles represent the tumor volume measurement, and dashed red lines mark the radiosurgery date. (c) Histogram and distribution function of $T(I_{max})$ for the model fits of 42 BMs.

using a Gaussian form for the damage function $h(t) = kNormal(\mu, \sigma)$. A substantial reduction of the MSE was obtained (Figure 3.6 f) in line with the model dynamics, closely resembling the data (see solid blue lines in Figure 3.6 a,b).

3.3.4 Time to tumor progression can be obtained from the mathematical model

Finally, our mathematical model allowed for a theoretical estimation of the time of tumor progression from the initial response data.

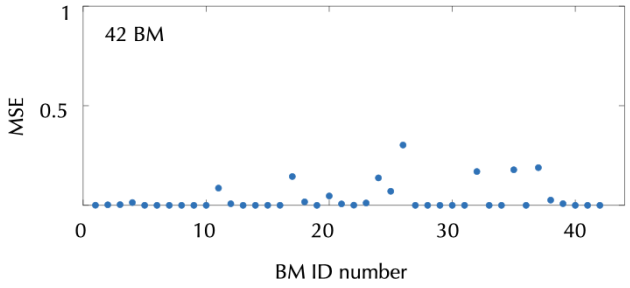

FIGURE 3.5: Mean square errors of the best fits of the model (3.1) to the metastasis volumetric data for the 42 metastases showing a monotonous decrease (MDL), decrease first and later increase (DIL), monotonous increase (MIL), and early inflammation in response to SRS. The formula used is given by the expression MSE$= \frac{1}{n}\sum_{i=1}^{n}(\widehat{V}_i - V_i)^2$, where n is the total number of follow-up MRIs performed for each metastases, V_i the segmented volume of scan i and $\widehat{V}_i$ the volume estimated with the model at the time of scan i.

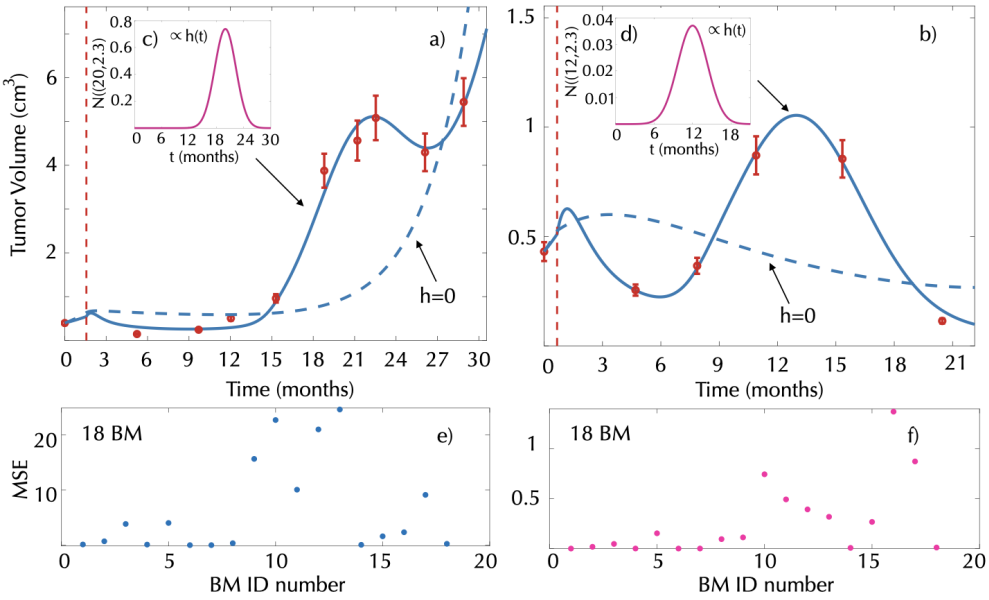

FIGURE 3.6: **Late inflammatory response and result of model fit.** (a), (b) Tumor volumetric longitudinal dynamics (solid red circles) for two patients receiving radiosurgery and best fits obtained using either Eqs (3.1) (dashed blue lines) or Eq. (3.1a), (3.1b), (3.1c) and (3.3) (solid blue line). Vertical dashed red lines represent the SRS date. Best fits for the healthy tissue damage were obtained in the first case by (c) $h(t) = 130 \times N(20, 2.3)$ and (d) $h(t) = 6.5 \times N(12, 2.3)$, respectively. MSE obtained when fitting the model to the group of 18 BMs using (e) Eq. (3.1) and (f) Eqs. (3.1a), (3.1b), (3.1c) and (3.3).

After therapy, proliferating cells have exponential growth given by the explicit solution $P(t) = P_0 e^{\rho t}$. Similarly, damaged cells have exponential decay given by $D(t) = D_0 e^{-\rho t/k}$. When $dT/dt > 0$ tumor volume grow back. In ideal conditions, the immune system is able to efficiently counteract necrotic cells and both

populations would eventually disappear. Under this assumption, tumor progression is determined by the populations of proliferating and damaged cells, i. e. $P_0 e^{\rho t} - \frac{1}{k} D_0 e^{-\rho t/k} > 0$. Taking the most reasonable value, $k = 2$, i.e. damaged cells dying after two cell cycles on average, and substituting the values of P_0 and D_0 using Eq. (3.2), the previous inequality is satisfied if

$$t_p > \frac{2}{3}\frac{1}{\rho} \ln \frac{(1 - S_f)(1 - \epsilon)}{2S_f}, \tag{3.4}$$

where $(1 - S_f)(1 - \epsilon) > 2S_f > 0$, when $D_0 > 2P_0$. If $D_0 < 2P_0$, the inequality is satisfied for all values of $t > t_0$. Eq. (3.4) can provide an estimate of the time to progression under the assumptions that there is no damage to the healthy tissue ($h = 0$), and that the survival fraction is positive ($S_f > 0$). The value provided by this equation can be compared with the progression time observed for each patient.

Figure 3.7 shows three examples of the longitudinal dynamics of BMs after treatment using the mathematical model. Panels on the left display the dynamics for the three patients. The rightmost panels show the dynamics of the different populations according to the mathematical model (3.1).

In the first example (see Figure 3.7 a,d), in a tumor without inflammation, the progression time clearly indicates the moment in which the proliferating cells outgrow half of the damaged cell compartment, thus dominating tumor growth. For this patient, there is an increase in tumor volume right after the progression time t_p computed from our mathematical model (Eq. (3.4)).

The second and third examples correspond to patients diagnosed with radiation necrosis. The progression time could be used in these cases to distinguish between an increase in the tumor volume caused only by the radiation necrosis (false progression) and an increase caused by real growth. Specifically, the second example (Figure 3.7 b,e) corresponds to a patient with radiation necrosis without progression. In this case, the tumor volume increase can be associated with the radiation necrosis, as it occurs 10 months before progression was expected. In the third example, radiation necrosis occurs after the progression time. In the graph it is possible to see how even if the tumor volume increases due to the radiation necrosis, it continues growing after the inflammation decreases, suggesting the co-existence of radiation necrosis and tumor progression.

3.4 Discussion and Conclusions

In this study, we put forward a mathematical model that describes the effect of SRS on brain metastases. The mathematical model included only four cellular compartments (proliferating, necrotic, damaged and immune) to account for the different dynamics observed after SRS. Interestingly, the simple model was able to describe the volumetric evolution of the lesions observed in the clinic and the different scenarios related to inflammation.

It is interesting that the model was able to describe qualitatively the observed dynamics without accounting for other relevant biological details of response to radiation therapy such as the differential response of well-oxygenated and hypoxic cells to radiation therapy (Joiner and Kogel, 2018) that has been included in other, more detailed models of radiation therapy of brain tumors by different authors (see e.g. (Toma-Dasu and Dasu, 2013; Rockne et al., 2015; Lewin et al., 2018; Kuznetsov and Kolobov, 2020)). Another effect not accounted for in this study was the fact that

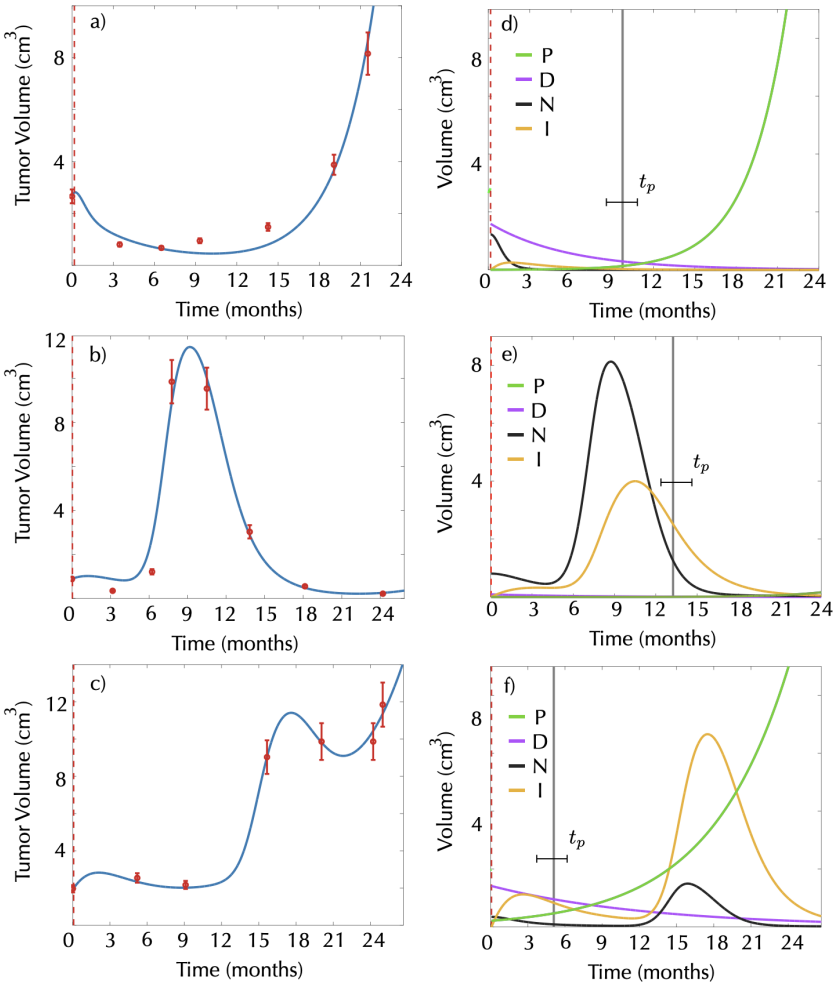

FIGURE 3.7: **Real longitudinal dynamics of three BMs and of the different compartments after SRS according to the model (3.1).** Red dots in panels (a–c) represent the longitudinal tumor volumetric data for the three BMs chosen. Solid blue lines show the best fits obtained using the model equations (3.1). The second column (d–f) shows radiosurgery response for proliferating cells (green line), damaged cells (magenta line), necrotic cells (black line) and immune cells (yellow line) obtained from the model. Dashes red lines mark the date of SRS and vertical black lines mark the time of tumor progression as calculated by Eq. (3.4).

irradiated cells may undergo cell cycle arrest or become quiescent for long times after sublethal radiation doses (Ribba et al., 2012). As imaging techniques progress and provide biological data on metastasis status able to feed more complex mathematical models, it may be relevant to develop models including all those biological processes.

Early post-treatment inflammation was very easily accounted for in the model by incorporating early cell death (necrosis) and associated inflammatory response. Radiation necrosis events, assumed to be the result of damage to healthy tissue, were incorporated in a simple and rather ad-hoc way by the function $h(t)$. The effect of radiation on healthy tissue as additional source of necrosis could be analyzed under different forms of this function, but we have chosen the Gaussian form as a first approximation. Incorporating more details of the SRS-induced damage to healthy

tissue could allow us to write mechanistic equations for the normal tissue behavior in response to treatment. As a first approach, we wanted to keep the model simple and with a minimal number of parameters but more complex mathematical models could account for this effect in a more elegant way.

In this work we chose S_f to be an adjustable parameter instead of a fixed predetermined value. In the context of elementary "static" mathematical approaches to radiation therapy such as the linear-quadratic equation, it is customary to assume a given S_f value to solve problems in therapy replanning, etc. That given S_f value would be characteristic of the tumor histology. However, that approach is of limited use in the context of radiation surgery of brain metastasis since there is a broad variety of potential outcomes to SRS treatment ranging from no response to complete response even for the same primary types. This is probably due to the intra and inter-patient heterogeneity as well as the role of many other elements in the response such as the tumor or immune environments, as discussed previously.

According to the results of the model fits, it seems that this simple model has some limitations in describing the tumor dynamics in some patients undergoing radiation necrosis. The model fitting in these cases showed mean square errors larger than those obtained in the more common scenarios of early response to SRS. This suggests that radiation necrosis is a more complex phenomenon where different biological factors may play a role.

One of the current problems in clinical practice is to differentiate between tumor progression and radiation necrosis, as both display a similar course as observed in the MRI, requiring advanced diagnostic techniques for identification (Essig et al., 2012; Barajas et al., 2009). In this study, we obtained an analytical estimate for the progression time due to the growth of remnant proliferating cells after SRS. This estimated time may be the basis for biomarkers helping clinicians to distinguish between progression and radiation necrosis. If the tumor increases in size at a time close to the predicted tumor recurrence, this could be an indication of tumor progression. On the other hand, tumor outgrowths at times much earlier than the estimated by the model could be an indication of the presence of an inflammatory process.

The key point in moving from Eq. (3.4) to a clinically relevant biomarker would be to define the requirements for a reliable estimate of the outgrowth time, since this must be done from MRI data. In principle, only a small number of data points are necessary to obtain the value of this parameter (ρ, ϵ, S_f). If there are two MR imaging exams before SRS, they would allow the tumor proliferation rate ρ to be estimated. Interestingly, performing a second MRI immediately before SRS also has advantages from the clinical point of view, since it would allow for a more precise definition of the target volume. It has been reported recently that (Salkeld et al., 2018; Garcia et al., 2018) measurable changes occur in brain metastasis over a short period of time, on the order of a week, so a final planning right before SRS would help in achieving greater therapeutic efficacy and provide a second MRI to obtain a baseline growth rate estimate.

The parameters ϵ and S_f can be obtained using the first few (2-3) MRIs of the standard follow-up after radiosurgery. So patients with two pretreatment MRIs and one year follow-up after SRS could have precise progression time estimates that could be used for comparison with the observed dynamics after the first year. Unfortunately, our database did not have patients fulfilling these requirements, i.e. all patients who presented radiation necrosis or progression had only one pretreatment MRI so that we could not explore the idea in more detail. As future work, we will address this by planning either a retrospective search for such patients, or a prospective study.

In conclusion, we have developed a mathematical model based on a set of ordinary differential equations which describe the observed longitudinal dynamics of brain metastases after SRS. The model allowed the varying early longitudinal dynamics observed in patients to be accurately described, and with very few parameters. Radiation necrosis events were described in a simplified way, and in most cases they were also fitted accurately using the model. We obtained an equation for the expected tumor progression time based on a few parameters that could be the basis for biomarkers to help in discriminating between radiation necrosis and true progressions, which currently represents a major challenge in the clinical setting.

Chapter 4

Tumor growth after stereotactic radiosurgery response: Analysis with a stochastic model

4.1 Introduction

Motivated by the results obtained with the previous continuous model, in this chapter we wanted to delve into the study of tumor growth dynamics after treatment with SRS. To do this, we developed a multiscale hybrid stochastic model based on the discrete model recently described in Jiménez-Sánchez et al., 2021. The goal of this study was to shed light on a clinical problem: the differentiation of tumor relapses from radiation necrosis. Radiation necrosis is the most common side effect of SRS and has characteristics similar to tumor progressions on standard anatomic MRI. As mentioned in Section 3, the latter constitutes a relevant problem since it is difficult to differentiate radiation necrosis from tumor progression using conventional MRI, making it a major diagnostic dilemma for radiologists (Furuse et al., 2019; Chuang et al., 2016; Vellayappan et al., 2018; Lee et al., 2020).

The mathematical model takes into account the main biological processes at the cellular level: mitosis, migration and cell death. In this model, cell populations are followed instead of individual cells. Brain metastases growth was described on a mesoscopic scale in the simplest possible way, taking into account only one clonal population. Although it is known that these tumors present cellular heterogeneity in their composition, it is not fully characterized as in the case of glioblastomas. For this reason, our results are not focused on describing the best growth dynamics of BMs, as in Section 2, where real data were available. On the other hand, it has been known that tumor treatments induce a reduction of the clonal complexity in the point of maximal response due to the action of selective pressures of the drugs (Dagogo-Jack and Shaw, 2018), which supports our simplification of a single clonal population to describe the response to SRS.

The spatial domain was set as a 3D grid discretized in cubic compartments (voxels) of side length $\triangle x$, fixed at 1 mm. Each voxel has a specific dynamic that depends on its occupation and surroundings, and can contain several cells belonging to each cells population with an upper limit indicated as local carrying capacity K. The different populations of cells will attempt to perform all available basic processes at each time step. Theses processes can be described by a binomial distribution with a probability associated with the process. That is, the number of cells successfully

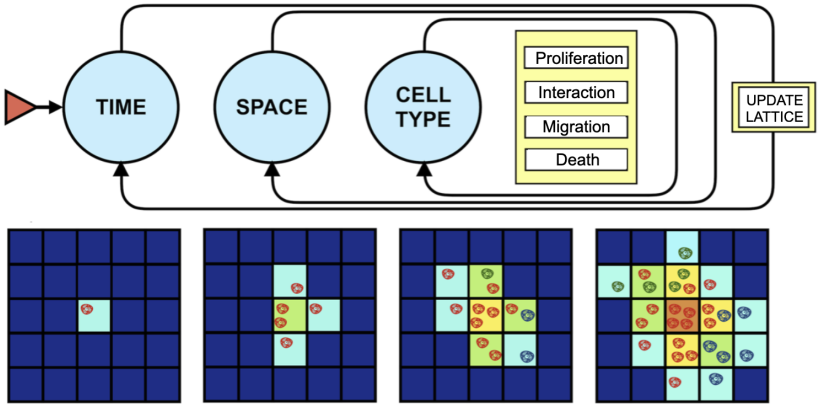

FIGURE 4.1: Basic algorithm for implementation purposes. Figure adapted from Jiménez-Sánchez et al., 2021.

undergoing division, death, migration or transition to another population are calculated voxel-wise and state-wise at each time step, randomly sampling the corresponding binomial distribution, whose N will be the number of cells in the population corresponding given within a voxel, and whose probability will be the rate of the process modulated by the time step length $\triangle x$. All processes, their probabilities and associated binomial distributions are thoroughly described below. A summary of basic idea of the algorithm is shows in Figure 4.1.

The simulator was implemented in Julia (version 1.5.3). Simulation file processing and graphics were done in MATLAB (R2020b, MathWorks). Simulations were performed on 2.7 GHz, Intel Core i7, 16 GB memory MacBook Pro machine.

4.2 Stochastic model

4.2.1 Stochastic mesoscopic model of tumor growth

To simulate tumor growth three cellular population were accounted: healthy cells, tumor cells and necrotic cells. Biological processes, namely cell division, death and migration were implemented similarly to model in Jiménez-Sánchez et al., 2021, although a small modification was incorporated in the tumor death process to reproduce specific characteristics observed in brain metastases.

The probabilistic events for this process reads as follows

$$P_{\text{Trep}} = \frac{\triangle x}{\tau_{\text{Trep}}}\left(1 - \frac{n_t + n_n + n_h}{K}\right), \tag{4.1}$$

$$P_{\text{Tmig}} = \frac{\triangle x}{\tau_{\text{Tmig}}}\left(\frac{n_t + n_n + n_h}{K}\right), \tag{4.2}$$

$$P_{\text{Tdeath}} = \frac{\triangle x}{\tau_{\text{Tdeath}}}\left(\tanh\left(\frac{10(n_t + n_n + n_h - K_{\text{act}})}{K}\right)\right), \tag{4.3}$$

$$P_{\text{Hmig}} = \frac{\triangle x}{\tau_{\text{Hmig}}}\left(\tanh\left(\frac{10(n_t + n_n + n_h - 0.45K)}{K}\right)\right), \tag{4.4}$$

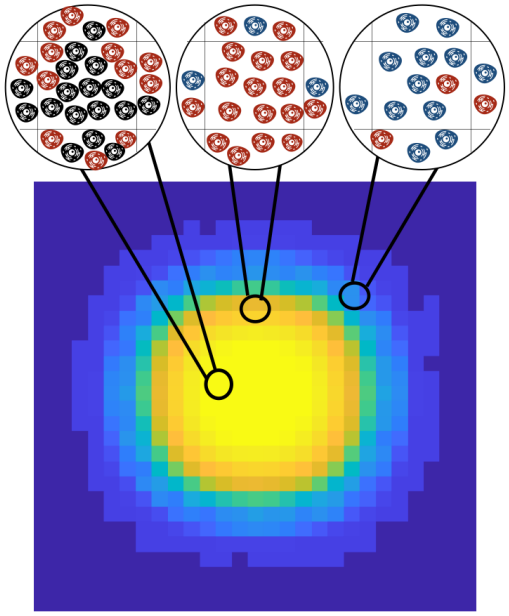

FIGURE 4.2: Bottom image is a slice of an actual simulation of tumor without treatment, with colors indicating occupation. Cells color indicates the different cell populations, with blue representing healthy cells, red representing tumor cells and black representing necrotic cells.

where n_t, n_n and n_h denotes the number of total tumor cells, necrotic cells and healthy cells inside a given voxel, respectively. Parameters τ represent the characteristic times of each process and K_{act} is the local threshold of voxel capacity from which tumor cells begin to die due to lack of resources.

Then, the total numbers of proliferating and dying cells from tumor population are drawn from binomial distributions $B(n_t, P_{\text{Trep}})$ and $B(n_t, P_{\text{Tdeath}})$, respectively. Due to the acquired capacity of tumor cells to evade apoptosis (Hanahan and Weinberg, 2000), we assumed that apoptosis signaling is activated once 75% of the voxel limit carrying capacity (K_{act}) is exceeded, simulating a significant lack of resources for the tumor cells. This is incorporated in the probability of death P_{Tdeath} by the term of the hyperbolic tangent as a function of the voxel capacity. The number of migrating cells was drawn from the respective binomial distribution $B(n_t, P_{\text{Tmig}})$ and then they are distributed around a neighborhood of 26 voxels (Moore neighborhood) according to a multinomial distribution (Jiménez-Sánchez et al., 2021). For simplicity we have assumed all tumor cells comes from the same clonal population without including mutation events.

For healthy cells we assumed that the levels of cell division and death remain in balance due to the ability of these cells to self-regulate, and that the biological process of migration is the only one that is affected by the evolution of tumor cells. Therefore, the numbers of migrating healthy cells were drawn from the binomial distribution $B(n_h, P_{\text{Hmig}})$ being displaced by the pressure performed by the tumor cells colonization when the total number of cells in the voxel exceeds 45% of its maximum capacity. Figure 4.2 shows a slice of an actual simulation, where the colors indicate the voxel occupation. Note that each voxel can contain a different number of cells.

4.2.2 Stochastic mesoscopic model of response to SRS

When tumors are treated with radiosurgery, tumor cells are lethally damaged or killed due to high doses of radiation. In addition, a fraction of the surrounding healthy tissue can also be damaged. As a consequence, the immune system is activated and immune cells move to the irradiated region to repair the damage caused. To describe the response to this treatment we have included three new cell populations: damaged tumor cells, activated immune cells and damaged healthy cells.

The dynamics of these populations is given by the following probabilistic events:

$$P_{Ddie} = \frac{\triangle x}{k \cdot \tau_{\text{Trep}}}, \tag{4.5}$$

$$P_{\text{Iact}} = \frac{\triangle x}{\tau_{\text{act}}} \cdot \frac{n_n}{n_i} \left(1 - \frac{n_t + n_n + n_h + n_d + n_{hd} + q \cdot n_i}{K}\right), \tag{4.6}$$

$$P_{\text{Ikill}} = \frac{\triangle x}{\tau_{\text{kill}}} \cdot \frac{n_i}{n_n} \left(1 - \frac{n_t + n_n + n_h + n_d + n_{hd}}{K}\right), \tag{4.7}$$

$$P_{\text{Ideath}} = \frac{\triangle x}{\tau_{\text{Ideath}}}, \tag{4.8}$$

$$P_{\text{Imig}} = \frac{\triangle x}{\tau_{\text{Imig}}} \left(\frac{n_t + n_n + n_h + n_d + n_{hd} + q \cdot n_i}{K}\right), \tag{4.9}$$

$$P_{\text{Hdie}} = \tanh\left(\frac{t - 2\tau_{Hrep}}{\sigma_{Hrep}}\right)/2 + 1/2, \tag{4.10}$$

where n_d, n_i and n_{hd} denote the number of total damaged tumor cells, activated immune cells and damaged healthy cells inside a given voxel, respectively. Similarly, parameters τ represent the characteristic times of each process and new cell populations are incorporated into the saturation process. Note that q is a scalar that normalizes the size of immune cells with respect to the size of healthy and tumor cells, assuming that the latter have similar sizes.

The number of necrotic cells, that comes from damaged tumor cells, are drawn from the binomial distribution $B(n_d, P_{Ddie})$. The damaged tumor cells population dies after the k cycle of mitosis while trying to repair the damage caused and passes into the necrotic cell compartment. The number of necrotic cells, that comes from damaged healthy cells, are drawn from the binomial distribution $B(n_{hd}, P_{Ddie})$. The basal time of cell division of healthy cells is slower than that of tumor cells. Because of this, we have simulated the probability of death by mitotic catastrophe of healthy cells damaged by radiation using a translation of a hyperbolic tangent function, where $2\tau_{Hrep}$ represents the basal reproduction time after the second cycle of cell division and σ_{Hrep} is a correction of the measure. Note that P_{Hdie} depends on t, which is the discretized time after radiosurgery. Therefore, there is a small probability that healthy damaged cells die, which will increase with sigmoid kinetics until approaching maximum ($P_{\text{Hdie}} = 1$, where all cells die). The transition occurs when cells fail trying to repair the damage, which is described by the term $\frac{t-2\tau_{Hrep}}{\sigma_{Hrep}}$.

The number of necrotic cells that are eliminated by interaction with immune cells and the number of immune cells activated are drawn form the binomial distribution $B(n_n, P_{\text{Ikill}})$ and $B(n_i, P_{\text{Iact}})$, respectively. Further, the activated immune cells are removed naturally and this process is simulated form the binomial distribution $B(n_i, P_{\text{Ideath}})$. Analogous to tumor cells migration, the number of migrating immune cells is drawn from the binomial distribution $B(n_i, P_{\text{Imig}})$ using the same algorithm.

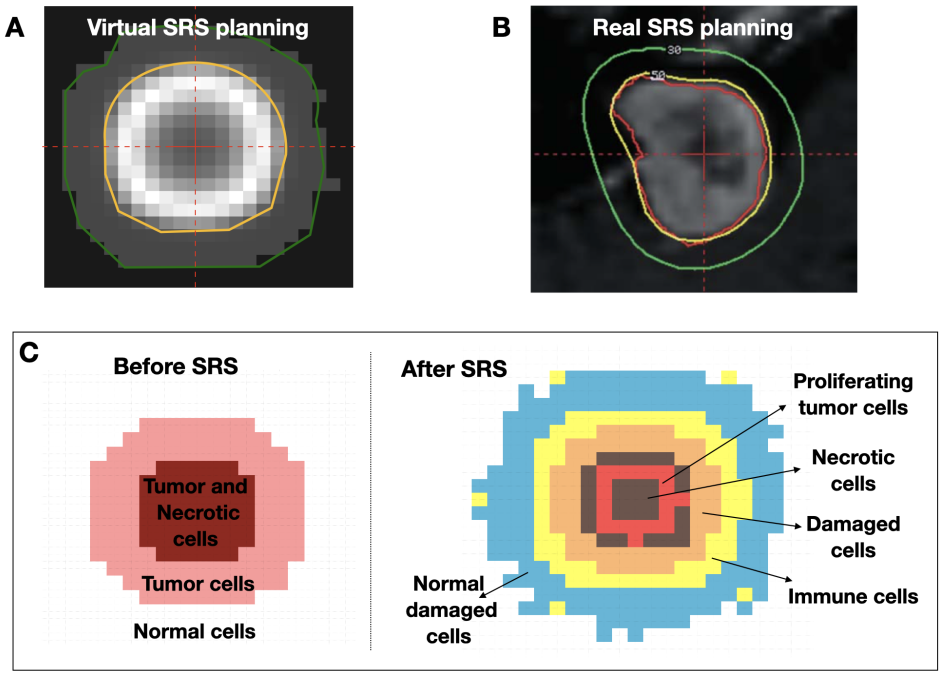

FIGURE 4.3: A) A single-shot treatment plan for a virtual simulation of SRS treatment.The target is outlined in yellow, and it is the area most affected by SRS. The green line encloses another area affected with less intensity. B) A real example of Gamma Knife isodose plot with the target outlined in red, the 50% isodose line in yellow, and the 30% isodose line in green. Figure adapted from Shepard et al., 2008. C) Spatial distribution of cell populations before and after SRS. The voxels can be occupied by more than one cell population but the colors per voxel of the representative samples of each population are shown.

Therapy was implemented to resemble the actual radiosurgery in the experimental part of this study. To simulate the spatial distribution of radiation, we relied on the typical isodose plot for a Gamma Knife patient, as shown in Figure 6.3 A,B. In this example, the isodose surface that encloses the target (which is often taken as the prescription dose) is typically 50% of the maximum dose in the target. In addition, radiation doses (30% of the maximum dose) are also administered in a larger volume around the lesion, with an additional 1 to 2 mm diameter. This percentage may vary depending on the technique and machines used (Shepard et al., 2008).

A single dose of SRS was simulated in silico as follows: *i)* a fraction of tumor cells S_f will suffer either no damage and will remain viable, an additional fraction $(1 - S_f)$ will receive lethal damage of which a fraction ϵ will die on a short time scale (i.e. days), and the remainder will move into the compartment of lethally damaged cells; *ii)* a fraction of immune cells I_f will be activated and *iii*) a fraction of healthy cells surrounding the tumor $1 - S_n$ will suffer lethal damage and a fraction S_n will suffer either no damage and will remain viable. Figure 6.3 C shows an example of the spacial distribution of cell population before and after SRS as described above.

4.2.3 Estimation of parameters

To fix the initial data we used the sizes typically found in the clinical setting for the tumor sizes pre-SRS treatment, which are around 0.5-2 cm^3 and the tumor maximum

sizes until 10 cm^3. Hence, we selected L = 60 voxels per spatial length to make these sizes attainable. The time step was fixed to 4 hours. From typical cell sizes (Milo et al., 2009) we estimated the carrying capacity of a single voxel N_{max} to be 2×10^5 cells and we have assumed same size for all type of cells. The choice of division, death, and migration basal rates used the doubling times estimations (Kobets et al., 2020) and imaging data from real BMs in the previous Section 3.

Several studies indicated increased microglial activation, proliferation, and phagocytosis may contribute to onset of neuroinflammation-induced brain injury. To estimate the parameters related with the immune system we have based on this cell population (He et al., 2020; Wagner et al., 2020). Microglia are the resident macrophages of the brain, comprising 0.5%—16.6% of the total number of cells in the human brain (Askew et al., 2017). For this reason, we set the initial number of immune cells as 10% of the healthy cells surrounding the tumor ($I_f = 0.1$). Microglial activation is characterized by morphological changes, including an increase in size. There is great heterogeneity in the cell morphology of the microglia. Based on previous morphological studies (Davis et al., 2017) we assume that in the normal state microglia cells have the same size and in the activation state they present an increase of 50% in their size, hence the parameter $q = 3/2$ in the saturation process. Recent studies have reported the microglial landscape changes radically within a few weeks, with cells dying and other taking their place (Askew et al., 2017). Thus, we take the mean lifetime of immune cells in a voxel to be around 2 months and activation to be in the range of 12-20 hours.

All the proposed parameters are associated with cellular processes, which combined result in whole-tumor rates. Cellular traits were randomly sampled from the range of allowed basal rates for each simulation. This provided variability between individual simulations and allowed us to assess the robustness of the model's behavior.

TABLE 4.1: Relevant parameter values for model.

Parameter	Meaning (average times per voxel)	Value
τ_{Trep}	Tumor cells reproduction	$450 - 550$h
τ_{Tmig}	Tumor cells death	$7000 - 1500$h
τ_{Tdeath}	Tumor cells migration	$1000 - 2000$h
τ_{Imig}	Immune cells migration	$150 - 250$h
τ_{Imig}	Immune cells death	$1440 - 1560$h
τ_{act}	Immune cells activation	$12 - 20$h
τ_{kill}	Necrotic cells elimination	$72 - 96$h
τ_{Hrep}	Healthy cells reproduction	4680h (6.5 mos.)
σ_{Hrep}	Standard deviation of the reproduction time of healthy cells	480h

4.2.4 Dynamics of longitudinal tumor growth post-treatment

Motivated by the analysis of the longitudinal volumetric growth dynamics for solid tumors shown in Section 2, we tried to study post-treatment volumetric growth for the simulated tumors. Therefore, the equation to fit is

$$\frac{dV}{dt} = \alpha V^{\beta},$$

which corresponds to the Von Bertalanffy model (Eq. (2.2)) described in Section 2.3.

Solving Eq. (2.2), leads to

$$\frac{V(t)^{-\beta+1}}{-\beta+1} - \frac{V_0^{-\beta+1}}{-\beta+1} = \alpha(t - t_0). \tag{4.11}$$

Since we have information of the dynamics at three time points (t_0, V_0), (t_1, V_1) and (t_2, V_2), the two parameters α and β can be completely determined by evaluating (4.11) at the times t_1, t_2, leading to

$$\frac{1 - (V_1/V_0)^{-\beta+1}}{1 - (V_2/V_0)^{-\beta+1}} = \frac{t_1 - t_0}{t_2 - t_0}. \tag{4.12}$$

Eq. (4.12) is an algebraic equation for β that was solved by using the MATLAB function fzero (which returns the root of a nonlinear function) for each set of known values V_0, V_1, V_2, t_0, t_1, t_2.

4.2.5 Virtual BMs simulations

To simulate the tumor growth dynamics after SRS, we ran a set of 400 simulations of BMs starting from 10^3 tumor cells, allowing them to grow until reaching diagnostic volumes in the range of $0.5 - 2$ cm^3. Then, the radiosurgery event was simulated and post-treatment tumor evolution continued as described in Section 4.2.2. Each simulation had a different set of basal rates, sampled randomly from the ranges specified in Table 4.1. Because the large number of parameters in the model is sufficient to guarantee variability between the different tumor responses to treatment, the ranges of tumor proliferation and migration rates were reduced to 500h ($\pm$10) and 1000h ($\pm$10) respectively.

Furthermore, we assumed that radiosurgery achieves an initial reduction in the volume of the lesion. To do this, we used the following voxel survival fraction

$$S_f \;=\; S_{\hat{f}} \cdot \tanh\left(\frac{10(n_n - 0.45K)}{K}\right), \tag{4.13}$$

where $S_{\hat{f}}$ is the maximum survival fraction. This expression is supported by the fact that well oxygenated cells are less resistant to radiation (more radio sensitive). Thus, the cells that are farthest away and that do not get enough oxygen and nutrients to survive are those that are found in the voxels with the highest number of necrotic cells. For the simulations, $S_{\hat{f}}$ values in the range of $(0, 1)$ and ϵ values in the range $(0.1, 0.7)$ were used.

The simulations were divided into two groups. First, a control group of 200 BM simulations was performed under the condition of not damage to the healthy tissue surrounding the tumor ($S_n = 1$). A second group of 200 BM simulations accounted for the damage induced by SRS to healthy tissue next to the lession ($0.1 \leq S_n \leq 0.7$). The latter would be the situation that was expected to occur in the clinics.

Tumor volume measurement

Let ν be the set of voxels that have reached more than 45% of their carrying capacity, considering all cell types including necrotic cells. Let us define the number of elements in ν by $N_\nu = |\nu|$. Then, if individual voxel volume is V_{vox} we define the tumor volume as $V = N_\nu V_{vox}$. This quantity can be obtained from in silico simulations

of our mathematical model. Our simulations was performed in voxels of 1 mm^3. Therefore, the tumor volume is equal to the number of occupied voxels counted N_v in mm^3.

Calculation of β exponent for a virtual BM

In this study, we focused our attention on the dynamic behavior of tumors after the second follow-up (six months after radiosurgery). Taking into account that the average time between follow-ups in the clinic is 3 months, for each case we calculated the following three volume measurements from six months post-SRS, that is, t = 6, 9 and 12 months.After that, we fitted the volumes to the growth law as explained in Section 4.2.4 and solved Eq. (4.12) to calculate the value of the exponent β.

To avoid possible conditioning of the estimate in the choice of time points, the three time instances were taken within the following ranges: $t_0 \in (180, 180 + 15)$ days, $t_1 \in (t_0 + 80, t_0 + 100)$ days and $t_2 \in (t_1 + 80, t_1 + 100)$ days. Then, we estimated β for each combination of t_0, t_1 and t_2, repeating this procedure 20 times. Finally, we obtained the estimated $\hat{\beta}$ value for the corresponding simulated tumor as the median value of all the previously calculated values.

4.3 Results

4.3.1 Volumetric dynamics of BM after SRS

With the virtual BMs generated, we studied their volumetric growth dynamics after therapy. Figure 4.4 shows three examples of these in silico simulations. First column (A, C, E) shows the dynamics of the different cell populations present: proliferating tumor cells, damaged cells, necrotic cells, immune cells and total tumor cells for the three cases. The second column (B, D, F) shows the longitudinal volumetric dynamics of the simulation displayed in the first column. In each case, 20 β growth exponents were calculated as explained in Section 4.2.5. Additionally, $\hat{\beta}$ median was obtained for each simulation. In two of the cases, sublinear growths ($\hat{\beta} < 1$) were obtained for relapses. These simulations were generated with small or no damage to healthy tissue, i.e, $S_n = 1$ (Figure 4.4 A,B) and $S_n = 0.7$ (Figure 4.4 E,F). On the other hand, when there was a substantial damage to healthy tissue $S_n = 0.1$, the volumetric evolution displayed a superlinear growth ($\hat{\beta} > 1$), as shown in Figure 4.4 C,D.

Thus, in order to characterize the volumetric growth post-SRS of the BMs using the scaling exponent, the values of β were calculated for the set of 400 virtual BMs. The results obtained for the first group ($S_n = 1$) are shown in Figure 4.5 A. The values of β were grouped according to the value of $S_{\hat{f}}$ used in the simulation. Medians and the quartiles of the box plots were mostly below 1, although for small values of $S_{\hat{f}}$ there were a set of outliers with high estimates of β. These exponents described the dynamics of relapsing lesions.

For the second group, which included damage to healthy tissue, there were two behaviors observed in silico. Figure 4.5 C shows the scatter plot of the $\hat{\beta}$ median calculated for the virtual BMs according to the different values of ($S_{\hat{f}}$, S_n) simulated. Values of $\hat{\beta} > 1$ were obtained for cases where SRS eliminates most of the tumor cells (values of $S_{\hat{f}} \leq 0.1$). Here, the volume re-growth was due to the inflammatory component. Otherwise, for larger tumor remnants re-growth simulations (values of $0.1 < S_{\hat{f}} < 1$) the calculated $\hat{\beta}$ exponents were less than 1. This behavior corresponds

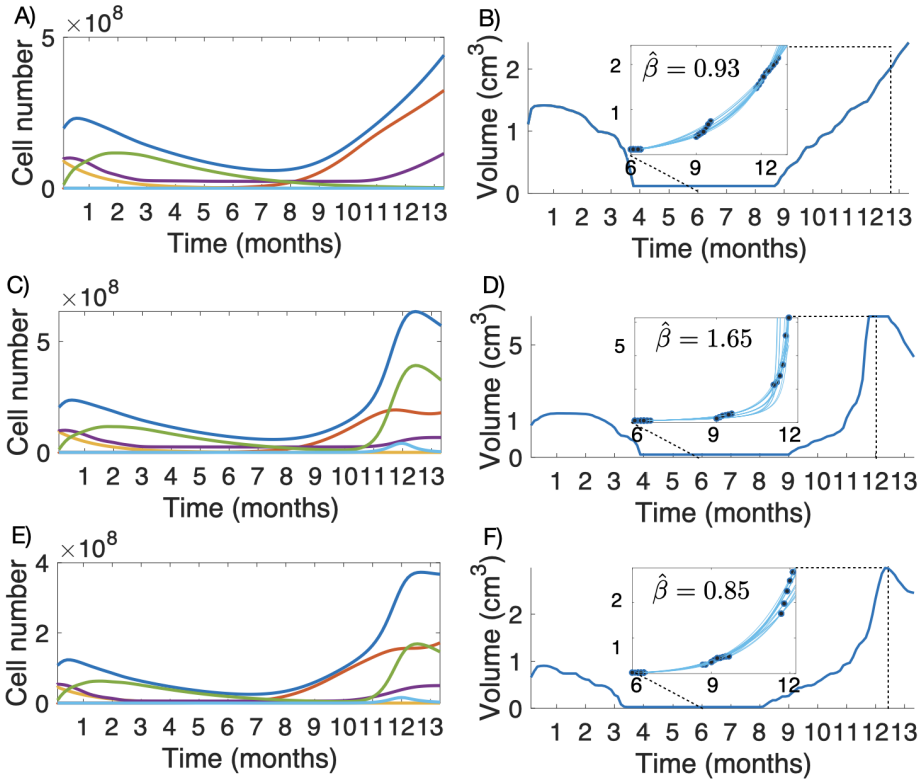

FIGURE 4.4: **Longitudinal tumor growth dynamics after SRS**. The first column shows the dynamics of the proliferating cells (red line), damaged cells (orange line), necrotic cells (violet line), immune cells (green line) and total tumor cells (blue line). The second column shows the longitudinal tumor volumetric dynamics. Subplots (A-B) correspond with a tumor simulation with no damage to healthy tissue ($S_n = 1$), subplots (E-F) correspond with small damage to healthy tissue ($S_n = 0.7$) and subplots (C-D) correspond with high damage to healthy tissue $S_n = 0.1$.

to a tumor relapse. In addition, we can see in Figure 4.5 B the β values calculated for the cases simulated with $0.1 \leq S_n \leq 0.7$ and $S_{\hat{f}} \leq 0.1$. Despite the presented variability, β values obtained were typically greater than 1.

In the next section, to have a single measure of β per simulation, we will work with $\hat{\beta}_i$ that corresponds to the median of the values obtained in simulation i.

4.3.2 Inflammatory events displayed the fastest growth dynamics allowing to discriminate them from relapses

One of the main challenges in clinical practice is the identification of radiation necrosis, due to its similarity in MRI with tumor progression. Inflammatory events after SRS do not usually require therapeutic actions because inflammation may decrease spontaneously, while tumor relapses commonly need treatments to control them. The computational results suggest that β value could be used to distinguish inflammatory response from tumor progression.

We studied the differences between the fitting exponents of the groups of inflammatory response and relapses BMs. Inflammatory group is made up of in silico

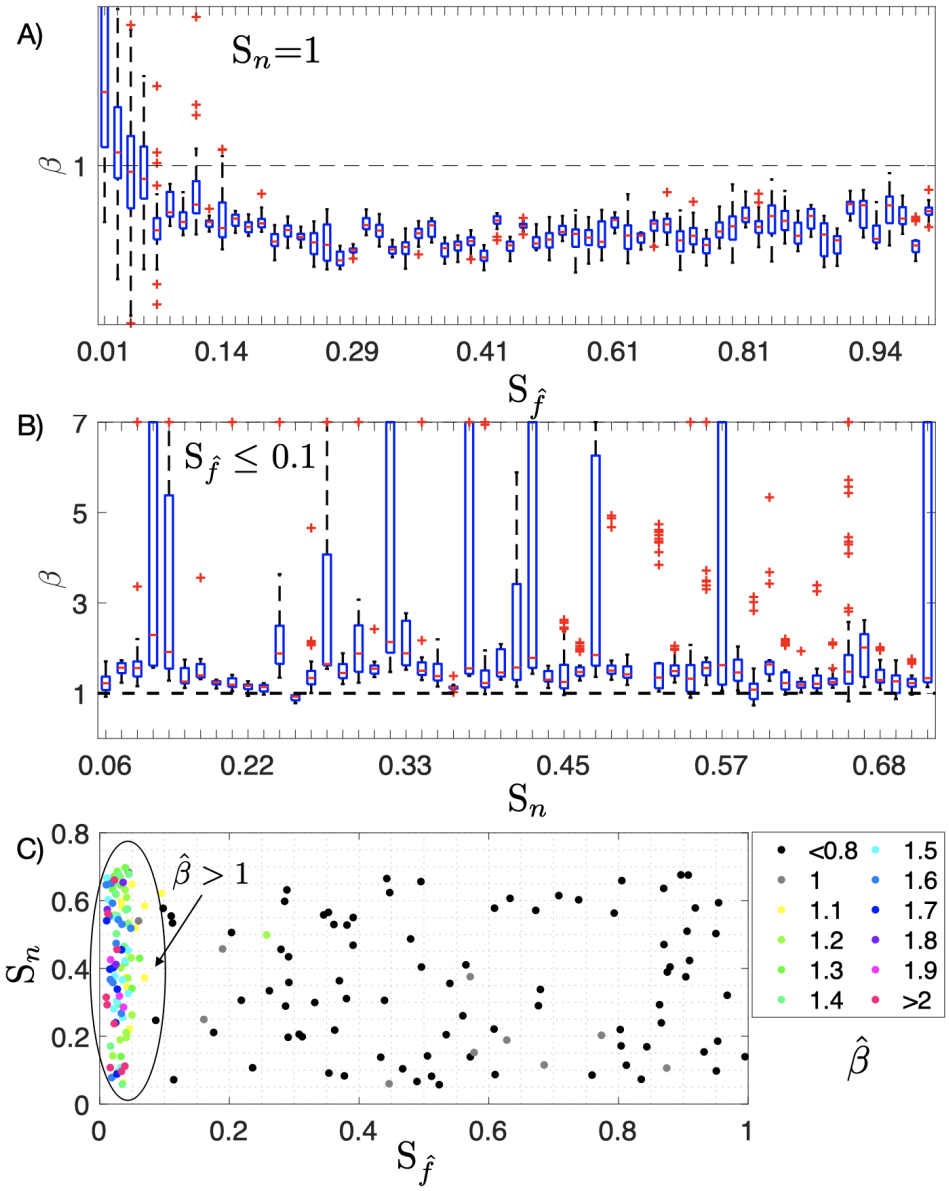

FIGURE 4.5: (A-B) Comparison of box plots for the growth exponents β calculated for virtual BMs. A) Cases was simulated with $S_n = 1$ and $0 < S_{\hat{f}} < 1$. B) Cases was simulated with $0.1 \leq S_n \leq 0.7$ and $0 < S_{\hat{f}} < 0.1$. C) Scatter plot that shows the β median calculated for the virtual BMs which were simulated with different values of ($S_{\hat{f}}$, S_n). Parameters for this simulation are as in Table 4.1.

simulations where SRS eliminates most of the tumor cells but damages the considerable part of the healthy tissue surrounding the lesion, i.e, values of $0.1 < S_n < 0.7$ and $S_{\hat{f}} < 0.1$. While the relapse groups are made up of the simulations performed for a higher number of remaining tumor cells, i.e, values of $S_{\hat{f}} > 0.1$. The ANOVA test for the comparison with the BMs virtual lead to significant differences between inflammatory response group and relapses groups ($p=1.85 \times 10^{-12}$). Box plots for the different subgroups are shown in Figure 4.6 A.

The area under the ROC curve (AUC) in Figure 4.6 B illustrates the ability of the exponent $\hat{\beta}$ to discriminate between responses groups. We obtained AUC=0.97

and the optimal threshold calculated to maximize the sensitivity and specificity values was $\beta_{threshold} = 1.05$. This means that inflammatory events show faster growth dynamics than relapses.

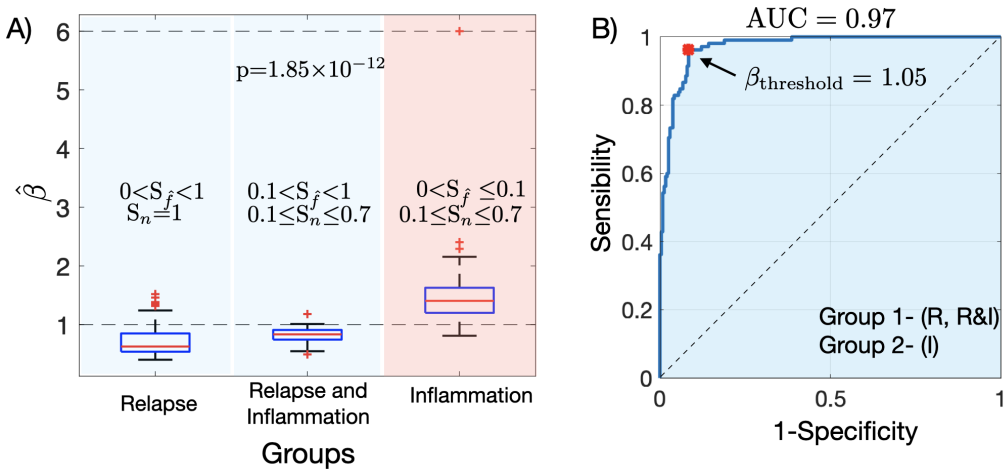

FIGURE 4.6: A) Box plots showing the comparison of the growth exponents $\hat{\beta}$ between the different simulated BMs: relapse group (R), whose response is characterized by tumor progression ($0 < S_{\hat{f}} < 1$, $S_n = 1$), relapse and inflammation group (R & I), whose response is characterized by tumor progression and inflammation ($0.1 < S_{\hat{f}} < 1$, $0.1 \leq S_n \leq 0.7$) and inflammation group (I), whose response is characterized by inflammation ($0 < S_{\hat{f}} \leq 0.1$, $0.1 \leq S_n \leq 0.7$). B) ROC curve for the discrimination between tumor progression (R and R&I groups) and inflammatory response (I group) according to the growth exponent $\hat{\beta}$.

4.4 Discussion and conclusions

In this work, a mesoscale stochastic simulator has been presented that describes the dynamic growth of the tumor and its response to SRS. The model included the main cell populations and the biologically meaningful assumptions necessary to address the problem of late inflammation vs progression.

Continuous models can potentially neglect spatial correlations between the locations of individuals, specially when different species or subpopulations are take into account. On the contrary, the model developed took into account these relationships by combining discrete, spatial and stochastic dynamics. This made it possible to analyze the dynamic behavior of the tumor in terms of volume in a more complete and precise approach. With a better description of the biological aspects present after radiation, the model was used to simulate the different possible scenarios according to the damage caused to the healthy tissue surrounding the tumor and the survival fraction of the tumor cells after therapy.

The incorporation of the healthy cell population allowed a better description of the damage caused to the healthy tissue surrounding the tumor caused by therapy. Healthy cells that were damaged by radiation, after the DNA repair attempt, turned on the mechanisms of cell death (apoptosis, mitotic catastrophe or necrosis). The triggering of cell death activated and stimulated the immune cell population. As a consequence, there was an increase in cell density in the irradiated area, causing an

apparent increase in tumor volume that could be confused with tumor recurrence. This situation constitutes one of the common clinical responses in patients treated with SRS.

In the study of the behavior of the tumor volumetric dynamics of relapses, a slower growth dynamics was obtained than that found in Section 2 for untreated BMs. The in silico result of $\beta < 1$ for relapses was in line with recently obtained results for the post-SRS longitudinal dynamics of real patient BMs (Ocaña-Tienda et al., 2021). Ocaña-Tienda et al., 2021 also addressed the hypothesis that a "first strike" with radiosurgery could reduce the heterogeneity of the population, where the substantial reduction of the growth exponent may imply a direct effect on the complexity of the tumor. We have based on this starting hypothesis for the assumption to include a single tumor cell clonal population in the discrete model for dynamic post-SRS analysis. However, the volumetric behavior caused by the post-SRS inflammatory response displayed a faster growth dynamic than that of BM relapses. The growth exponent β values for inflammatory events were typically greater than 1.

Radiation necrosis or inflammation must be distinguished from recurrent tumor to determine appropriate medical action. Initial treatment of RN often involves management of edema using corticosteroids, antiangiogenic therapies, and hyperbaric oxygen therapy. Sometimes even it resolve spontaneously and require no further actions. However, relapses tumor usually requires therapeutical actions like surgery when the primary tumor and possibly other metastases are under control. Discriminating RNs from relapses radiologically is often a difficult task (Furuse et al., 2019; Chuang et al., 2016; Lee et al., 2020). Since the diagnosis of radiation necrosis can be complex, new techniques are necessary for the detection and discrimination between both conditions.

Our results suggest that the value of β exponent could be have a direct clinical application. The model supports that when three MRI studies are available satisfying our inclusion criteria, computing β for a particular patient could allow to diagnose the growth as inflammation or tumor progression. Additionally, this result is consistent with the study carried out in Ocaña-Tienda et al., 2021 on a group of real patients with and without radiation necrosis, where the evolutionary dynamics was observed at a macroscopic level in the form of an exponent $\beta > 1$ in patients with a diagnosis of RN.

Part II

CAR T Cell Immunotherapy

Chapter 5

CAR T cell therapy in B-cell acute lymphoblastic leukemia

5.1 Introduction

Chimeric antigen receptor (CAR)-T cells are modified autologous or allogeneic T cells. Their extracellular domain is engineered to recognize a tumor-associated antigen, and the intracellular domain contains a T-cell activation signal. Upon CAR engagement with the associated antigen, primary T-cell activation occurs and leads to cytokine release, cytolytic degranulation, resulting in target cell death, and T-cell proliferation (Feins et al., 2019).

Cancer immunotherapy with CAR T cells is a promising therapeutic option already available for B cell hematological cancers. Despite the success of CAR T cell therapy, a variable fraction, between 30% and 60%, of patients relapse after treatment. There are two different types of post-CAR relapse. In the first type, post-CAR leukemic cells show expression of the $CD19^{+}$ antigen and other immunophenotypic characteristics that are the same as those of the original clone. This is consistent with the recurrence of the initial leukemic clone. In this case, pre-CAR and post-CAR blasts typically show the same CD19 expression levels.

This type of recurrence shows a down-regulation of the CD19 antigen (Xu et al., 2019). In this situation, CAR T cells cannot recognize their targets and the tumor regrows. In contrast to $CD19^{+}$ recurrence, $CD19^{-}$ recurrence occurs despite functional persistence of CAR T cells and ongoing B-cell aplasia (Xu et al., 2019; Ghorashian et al., 2019).

There are many previous studies devoted to the mathematical modeling of tumor-immune cell interactions, see for instance (Eftimie, Bramson, and Earn, 2011; Starkov and Krishchenko, 2014; Eftimie, Gillard, and Cantrell, 2016; López, Seoane, and Sanjuán, 2017; Konstorum et al., 2017; Mahlbachera, Reihmera, and Frieboes, 2019) and references therein. CAR T cell treatments have attracted the interest of mathematicians in the context of gliomas (Sahoo et al., 2020), melanomas (Baar et al., 2016) and B-cell malignancies (Kimmel, Locke, and Altrock, 2019; Rodrigues, Barros, and Almeida, 2019; Carvalho-Barros, Rodrigues, and Almeida, 2020; Mostolizadeh, Afsharnezhad, and Marciniak-Czochra, 2018; Stein et al., 2019).

In this study, we described mathematically the longitudinal dynamics of B cells, leukemic clones and CAR T cells. The mathematical models were shown to provide both a mechanistic explanation for the results of different clinical trials and formulas quantifying some of the observed phenomena. We discussed some implications for $CD19^{+}$ relapses and how it might be possible to control them by re-challenging the cancer early with CAR T cells.

5.2 Mathematical models and parameter estimation

5.2.1 Basic mathematical model

Our mathematical model accounts for the evolution over time of several interacting cellular populations distributed into five compartments. Let $C(t)$, $L(t)$, $B(t)$, $P(t)$, and $I(t)$ denote the non-negative time-varying functions representing the number of CAR T cells, leukemic cells, mature healthy B cells, CD19$^-$ hematopoietic stem cells (HSCs), and CD19$^+$ B cell progenitors (i.e. Pre-B, Pro-B and immature bone marrow B cells), respectively. Our initial autonomous system of differential equations is as follows:

$$\frac{dC}{dt} = \rho_C (L+B) C + \rho_\beta IC - \frac{1}{\tau_C} C, \tag{5.1a}$$

$$\frac{dL}{dt} = \rho_L L - \alpha LC, \tag{5.1b}$$

$$\frac{dB}{dt} = \frac{1}{\tau_I} I - \alpha BC - \frac{1}{\tau_B} B, \tag{5.1c}$$

$$\frac{dP}{dt} = \rho_P (2a_P s(t) - 1) P - \frac{1}{\tau_P} P, \tag{5.1d}$$

$$\frac{dI}{dt} = \rho_I (2a_I s(t) - 1) I - \frac{1}{\tau_I} I + \frac{1}{\tau_P} P - \alpha\beta IC. \tag{5.1e}$$

Equation (5.1a) involves two proliferation terms of CAR T cells due to stimulation by encounters with their target cells: either $L(t)$, $B(t)$ or $I(t)$. The parameter $\rho_C > 0$ measures the stimulation to mitosis after encounters with CD19$^+$ cells disseminated throughout the whole body (mostly in the circulatory system). The parameter $\rho_\beta = \beta\rho_C$, where $0 < \beta < 1$, accounts for the fact that immature B cells are located mostly in the bone marrow and encounters with CAR T cells are less frequent. The last term describes the decay of CAR T cells with a mean lifetime τ_C.

In contrast to previous modeling approaches (Kimmel, Locke, and Altrock, 2019; Rodrigues, Barros, and Almeida, 2019; Mostolizadeh, Afsharnezhad, and Marciniak-Czochra, 2018), we excluded a death term in the CAR T cell compartment due to interaction with target cells. This is because the CAR T cells do not undergo apoptosis after killing the target cell (Davenport et al., 2015; Davenport et al., 2018). Also, unlike in those models, there is no *standard* proliferation term proportional to the population of CAR T cells, since these cells do not divide spontaneously (Tough and Sprent, 2018), instead their clonal expansion is directly dependent on stimulation with the CD19 antigen.

Leukemic cells (see Eq. (5.1b)) have a net proliferation rate $\rho_L > 0$ and die due to encounters with CAR T cells. The parameter α measures the probability (per unit time and cell) of an encounter between CAR T and CD19$^+$ cells. α and ρ_C are, in general, different due to possible asymmetric cell interactions. Namely, if $\alpha > \rho_C$, this implies that CAR T cells kill CD19$^+$ target cells relatively faster than their own proliferation rate per target cell encountered. In contrast, if $\alpha < \rho_C$ then, on average, the killing process is slower than the proliferation rate per target cell encountered by CAR T cells. For completeness, we considered both cases via the dimensionless parameter $k = \rho_C/\alpha$. Other processes, encompassed by the term $-\alpha LC$, include target cell recognition, killing and detachment, which are relatively much faster than the complete *rendezvous* kinetics (Benmebarek et al., 2019). Our model implicitly assumed that all T lymphocytes in the CAR product have a similar cell killing capacity. This could be the case if both CD4$^+$ T helper cells and CD8$^+$

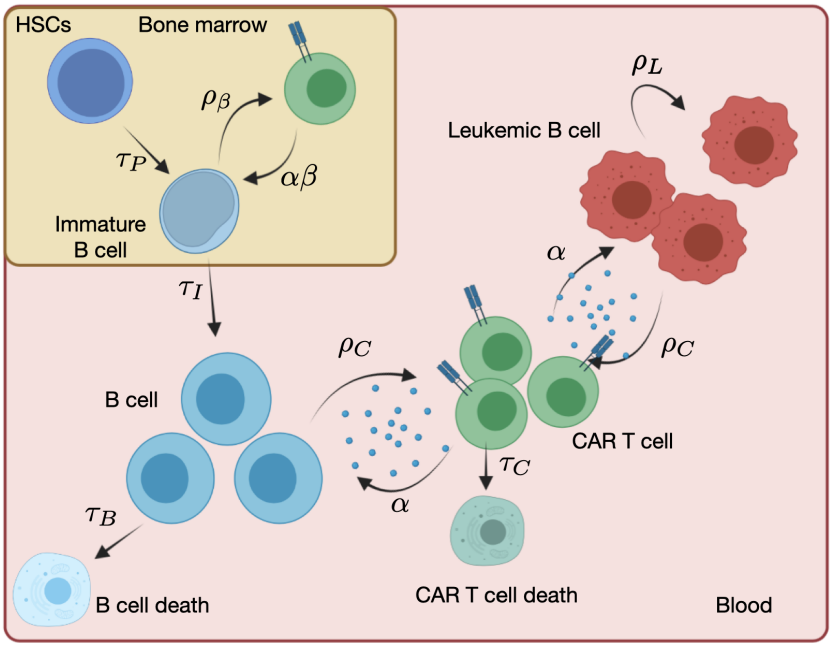

FIGURE 5.1: **Processes included in the mathematical model (5.1).** Mature B lymphocytes are generated from the CD19$^-$ hematopoietic stem cells (HSCs) and through differentiation of immature CD19$^+$ progenitors with characteristic lifetimes τ_P and τ_I, respectively. CAR T cells are stimulated when meeting CD19$^+$ B cells (normal, leukemic or immature) with stimulation parameters ρ_C and ρ_β, and undergo apoptosis with a lifetime τ_C. leukemic cells proliferate with a rate ρ_L. Both mature B and leukemic cells are destroyed via encounters with the CAR T cells with a killing efficiency α. Created with BioRender.com.

T cells had a similar cell killing capacity, or if most of the CAR product contains CD8$^+$ cells. A more complex mathematical framework should incorporate potential differences in killing capacity of these two T lymphocytes (Benmebarek et al., 2019; Liadi et al., 2015).

Equations (5.1c)-(5.1e), which involve B cells, consist of a compartment for CD19$^-$ HSCs (i.e. $P(t)$) with an asymmetric division rate a_P and a differentiation rate $1/\tau_P$ into a new compartment accounting for all of the other CD19$^+$ differentiated states of bone marrow progenitor B cells (Pro-B, Pre-B, and immature cells) (embodied in $I(t)$). These cells are the source of mature B cells. Since all cells in the $I(t)$ compartment already express the CD19$^+$ antigen, they are targets for the fraction of CAR T cells in the bone marrow, namely $\beta C(t)$. Finally, mature B cells $B(t)$, which cannot subsequently proliferate, are the terminal differentiation stage of these cells. They have a mean lifetime τ_B, which is present in the last term of Eq. (5.1c). The structure of the two hematopoietic compartments is similar to that proposed in previous studies with hematopoiesis models (Marciniak-Czochra et al., 2009). In line with those models, the signaling function $s(t)$ can be assumed to be of the saturable form $s(t) = 1/\left[1 + k_s\left(P + I\right)\right]$, with $k_s > 0$.

To describe CRS, let us define a variable $Y(t)$ for the cytokines released upon stimulation of CAR T cells by the antigens with rate ρ_Y and cleared with rate $1/\tau_Y$. ICANS is related to the number of CAR T cells infiltrating the central nervous system, and is expected to be proportional to the total number of CAR T cells, with a

proportionality coefficient ρ_N, and removed at a rate $1/\tau_N$. Thus, toxicity can be described by the following equations:

$$\frac{dY}{dt} = \rho_Y C\,(L+B) - \frac{1}{\tau_Y}Y, \tag{5.1f}$$

$$\frac{dN}{dt} = \rho_N C - \frac{1}{\tau_N}N. \tag{5.1g}$$

Notice that Eqs. (5.1a)-(5.1e) are uncoupled from Eqs. (5.1f)-(5.1g). A schematic summary of the biological processes encompassed by our basic mathematical model (5.1a-5.1g) is shown in Figure 5.1.

Section 5.3.1 shows some mathematical results on the existence, uniqueness and positiveness of the solutions of system (5.1a)-(5.1e).

5.2.2 Reduced mathematical models

Equations (5.1a)-(5.1e) exclude different biological facts such as heterogeneity in the CAR T-lymphocyte subpopulations, the differential expression of the CD19 antigen over leukemic and healthy B cells subclones, the role of regulatory T-cells, etc. However, there are still many parameters to be determined. The contribution of the bone marrow Eqs. (5.1d)-(5.1e) is to account for the generation of new B-cells. Hence, to capture their role while simplifying the full system, we can compute the equilibrium for Eqs. (5.1d)-(5.1e)

$$I = \frac{\frac{1}{\tau_P k_S}\left(\frac{2a_P\tau_P\rho_P}{1+\tau_P\rho_P}-1\right)}{\frac{1}{\tau_I}+\frac{1}{\tau_P}+\rho_I\left[1-\frac{a_I}{a_P}\left(1+\frac{1}{\tau_P\rho_P}\right)\right]+\alpha\beta C} \equiv \frac{I_0}{1+C/C_{50}}, \tag{5.2}$$

and assume (7.12) to hold for all time. This provides a suitable representation of the contribution of immature B cells in the bone marrow to global disease dynamics. Then, Eqs. (5.1a)-(5.1e) reduce to the set

$$\frac{dC}{dt} = \rho_C\,(L+B)\,C + \frac{\rho_C\beta I_0}{1+C/C_{50}}C - \frac{1}{\tau_C}C, \tag{5.3a}$$

$$\frac{dL}{dt} = \rho_L L - \alpha L C, \tag{5.3b}$$

$$\frac{dB}{dt} = \frac{I_0/\tau_I}{1+C/C_{50}} - \alpha B C - \frac{1}{\tau_B}B. \tag{5.3c}$$

In the first weeks after CAR T injection, the main contribution to the dynamics is the expansion of these cells and their effect on the healthy B and leukemic cells. Thus, we may neglect the contribution of the hematopoietic compartments in Eqs. (5.3a) and (5.3c) to get

$$\frac{dC}{dt} = \rho_C\,(L+B)\,C - \frac{1}{\tau_C}C, \tag{5.4a}$$

$$\frac{dL}{dt} = \rho_L L - \alpha L C, \tag{5.4b}$$

$$\frac{dB}{dt} = -\alpha B C - \frac{1}{\tau_B}B. \tag{5.4c}$$

The study of existence and uniqueness of solutions, together with the stability of the critical points for both systems, are presented in 5.3.2.

5.2.3 Parameter estimation

B-cell lymphocyte lifetime τ_B is known to be about 5-6 weeks (Fulcher and Basten, 1997). These cells account for a variable fraction between 5% and 20% (Stollar, 1998) of the total lymphocyte number (Alberts et al., 2015) leading to $> 10^{11}$ B-lymphocytes in humans. Since CAR T cells are injected after lymphodepleting treatment, in most simulations we set the initial number of B-lymphocytes to be 2.5 $\times 10^{10}$ to account for the effect of this treatment.

ALLs are fast-growing cancers with proliferation rates ρ_L of the order of several weeks (Marciniak-Czochra et al., 2009; Skipper and Perr, 1970). Naïve $CD8^+$ T cells are quiescent, their mean lifetime ranges from months to years, and they enter the cell cycle following interaction with their antigen (Nayar, Dasgupta, and Galustian, 2015; Kasakovski, Xu, and Li, 2018). These activated $CD8^+$ T cells induce cytolysis of the target cells and secrete cytokines such as TNF-α and IFNγ. Following activation, most effector cells undergo apoptosis after two weeks, with a small proportion of cells surviving to become $CD8^+$ memory T cells capable of longer survival (Nayar, Dasgupta, and Galustian, 2015). Recent studies have reported longer survival values of about one month (Ghorashian et al., 2019). Thus, we take the mean lifetime τ_C of CAR T cells to be in the range of 2-4 weeks.

To estimate the interaction parameter α we use the fact that when measured by flow cytometry or qPCR, CAR T cells in children treated for ALL reached a maximum in vivo expansion at around 14 days (Lee et al., 2015), which is a typical value observed in other clinical studies. Finally, the mitotic rate ρ_C, related to the stimulating effect of each encounter between T cells and the $CD19^+$ cells, is taken to be proportional to α ($\rho_C = k\alpha$), with $k \in (0.05, 2)$. The exact value would depend on the properties of the CAR T product, but taking $B + L$ initially to be around 10^{11} and using Eqs. (5.4a) we obtain an initial exponential growth rate for CAR T cells of around k day^{-1} , in line with values reported in other models (e.g in Stein et al., 2019, the authors obtained 0.89 day^{-1} from data).

The parameter values used in this paper are summarized in Table 5.1.

Parameter	Meaning	Value	Units	Source
τ_B	B-lymphocyte lifetime	$30 - 60$	day	Fulcher and Basten, 1997
ρ_L	Leukemic growth rate	$1/60 - 1/30$	day^{-1}	
τ_C	Activated CAR T cell lifetime	$14 - 30$	day	Nayar, Dasgupta, and Galustian, 2015 Ghorashian et al., 2019
ρ_C	Mitotic stimulation of CAR T cells by $CD19^+$ cells	$(0.05 - 2)$ $\times\alpha$	day^{-1} $\times$ cell^{-1}	
α	Killing efficiency of CAR T cells	$\sim 10^{-11}$	day^{-1} $\times$ cell^{-1}	Estimated from Lee et al., 2015
k	ρ_C and α ratio	$0.05 - 2$	–	Estimated and compatible with Stein et al., 2019
τ_I	Immature B cell lifetime	$2 - 6$	day	Rolink, Andersson, and Melchers, 1998 Shahaf et al., 2016
β	Fraction of CAR T cells in the bone marrow	$0.01 - 0.5$	–	Yasuyuki et al., 2018

TABLE 5.1: Relevant parameter values for model Eqs. (5.4)

5.3 Basic properties of mathematical models

In this section we show some basic properties of the previous mathematical models. First, we studied the existence and uniqueness of the positive solutions and then we analyzed the equilibrium points and the local stability of the reduced models.

5.3.1 Existence and uniqueness of positive solutions

Proposition 1. *For any non-negative initial data* $(C(0), L(0), B(0), P(0), I(0))$ *and all parameters of the initial value problem given by Eqs. (5.1a)-(5.1e) being positive, the solutions for* $C(t), L(t), B(t), P(t)$, *and* $I(t)$ *exist for all* $t > 0$, *are unique and non-negative.*

Proof. We first prove the non-negativity of the solutions. Let $\mathbf{F} = \mathbf{F}(\mathbf{x})$ denote the vector field representing the right-hand-side of Eqs. (5.1a)-(5.1e), with function $\mathbf{x} \equiv (C, L, B, P, I)$. Also, let $\mathbf{n}_j$ denote the outward normal unit vector to plane $x_j = 0$, with $j = 1, 2, \ldots, 5$. That is, $\mathbf{n}_1 = (-1, 0, 0, 0, 0)$ and analogously for other $\mathbf{n}_j$. Consider the scalar products of the ODE system $\frac{d\mathbf{x}}{dt} = \mathbf{F}(\mathbf{x})$ with each $\mathbf{n}_j$ and assume that the initial data $(C(0), L(0), B(0), P(0), I(0))$ are positive. Then, $\frac{d\mathbf{x}}{dt}\cdot\mathbf{n}_1 = \mathbf{F}\cdot\mathbf{n}_1 = 0$, $\frac{d\mathbf{x}}{dt}\cdot\mathbf{n}_2 = \mathbf{F}\cdot\mathbf{n}_2 = 0$ and $\frac{d\mathbf{x}}{dt}\cdot\mathbf{n}_4 = \mathbf{F}\cdot\mathbf{n}_4 = 0$ at hyper-surfaces $C = 0$, $L = 0$ and $P = 0$, respectively. Then, the hyper-surfaces $C = 0$, $L = 0$ and $P = 0$ are invariant.

Next, $\frac{d\mathbf{x}}{dt}\cdot\mathbf{n}_5 = \mathbf{F}\cdot\mathbf{n}_5 = -\frac{1}{\tau_P}P \leq 0$ at plane $I = 0$. Finally, $\frac{d\mathbf{x}}{dt}\cdot\mathbf{n}_3 = \mathbf{F}\cdot\mathbf{n}_3 = -\frac{1}{\tau_I}I \leq 0$ at plane $B = 0$. Hence, pieces of hyper-surfaces $\{I = 0\} \cap \mathbf{R}^5_{+,0}$ and $\{B = 0\} \cap \mathbf{R}^5_{+,0}$ are semipermeable inward $\mathbf{R}^5_{+,0}$.

As a result, $\mathbf{R}^5_{+,0}$ is a positively invariant domain for Eqs. (5.1a)-(5.1e). Therefore, non-negativity of solutions (C, L, B, P, I) follows.

Since all parameters in Eqs. (5.1a)-(5.1e) are finite and the right-hand-side of the system is a continuous function in (C, L, B, P, I) in the domain $\mathbf{R}^5_{+,0}$, existence of solutions of Eqs. (5.1a)-(5.1e) follows from the Cauchy-Peano theorem. Moreover, as the partial derivatives of the right-hand side of the system are also continuous and bounded in $\mathbf{R}^5_{+,0}$, uniqueness follows from the Picard-Lindelöf theorem. This completes the proof. □

Analogous, we have the following propositions for system (5.3) and (5.4), which are similar to the previous proposition for system (5.1) and therefore details of the proof are omitted:

Proposition 2. *For any non-negative initial data* $(C(0), L(0), B(0))$ *and all parameters of the initial value problem given by Eqs. (5.3a)-(5.3c) being positive, the solutions for* $C(t), L(t)$ *and* $B(t)$ *exist for all* $t > 0$, *are unique and non-negative.*

Proposition 3. *For any non-negative initial data* (C_0, L_0, B_0) *and all the parameters of the model being positive, the solutions to Eqs.* (5.4) *exist for* $t > 0$, *are non-negative and unique.*

5.3.2 Equilibrium points and local stability analysis

Reduced mathematical model: system (5.4)

Before delving into the analysis of system (5.3), it is convenient to first understand the dynamics of a simplified version of (5.3) given by Eqs. (5.4). We begin by calculating the fixed points and determining their stability. These are the points $P_1 = (0, 0, 0)$ and $P_2 = (\frac{\rho_L}{\alpha}, \frac{1}{\rho_C\tau_C}, 0)$.

To analyze the stability of these points, we calculate the Jacobian matrix of Eqs. (5.4):

$$J(C,L,B) = \begin{pmatrix} \rho_C(L+B) - \frac{1}{\tau_C} & \rho_C C & \rho_C C \\ -\alpha L & \rho_L - \alpha C & 0 \\ -\alpha B & 0 & -\alpha C - \frac{1}{\tau_B} \end{pmatrix}.$$

- Equilibrium point $P_1 = (0,0,0)$. The Jacobian matrix is

$$J(P_1) = \begin{pmatrix} -\frac{1}{\tau_C} & 0 & 0 \\ 0 & \rho_L & 0 \\ 0 & 0 & -\frac{1}{\tau_B} \end{pmatrix},$$

  and the eigenvalues are $\lambda_1 = 1/\tau_C, \lambda_2 = \rho_L$ and $\lambda_3 = -1/\tau_B$. Thus, P_1 is a saddle point and therefore, an unstable equilibrium point.

- Equilibrium point $P_2 = (\frac{\rho_L}{\alpha}, \frac{1}{\rho_C \tau_C}, 0)$.

  If we make the following linear change of coordinates $x = C - \rho_L/\alpha$, $y = L - 1/\rho_C\tau_C$ and $z = B$ we move the point P_2 to the origin and the system (5.4) becomes

$$\frac{dx}{dt} = \frac{\rho_C \rho_L}{\alpha}(y+z) + \rho_C(y+z)x, \tag{5.5}$$

$$\frac{dy}{dt} = -\frac{\alpha}{\rho_C \tau_C}x - \alpha xy, \tag{5.6}$$

$$\frac{dz}{dt} = -(\rho_t + \frac{1}{\tau_B})z - \alpha xz. \tag{5.7}$$

  The Jacobian matrix for this point is:

$$J(P_2) = \begin{pmatrix} 0 & \frac{\rho_C \rho_L}{\alpha} & \frac{\rho_C \rho_L}{\alpha} \\ -\frac{\alpha}{\rho_C \tau_C} & 0 & 0 \\ 0 & 0 & -\rho_L - \frac{1}{\tau_B} \end{pmatrix}.$$

  The eigenvalues of the matrix are $\lambda_{1,2} = \pm\sqrt{\frac{\rho_L}{\tau_C}}i$ and $\lambda_3 = -\rho_L - \frac{1}{\tau_B}$.

  Since $\lambda_{1,2}$ are imaginary eigenvalues, this point is a non-hyperbolic point. This means that for the linearized system, P_2 is a center, but it is not possible to conclude its stability for the nonlinear system.

  On the other hand, since $\lambda_3 < 0$, P_2 possesses a local stable manifold corresponding to that eigenvalue. Thus, P_2 has a local center manifold (corresponding to the eigenvalues $\lambda_{1,2}$) of dimension 2 and a local stable manifold (corresponding to the eigenvalue λ_3).

  Since λ_3 is negative, all the orbits starting near the equilibrium point approach the center manifold. It is straightforward (although somewhat tedious) to verify that the center manifold is given by $z = h(x,y) = 0$. So, the qualitative

behavior of the local flow can then be determined from the flow of the following system on the center manifold $z = 0$:

$$\frac{dx}{dt} = \frac{\rho_C \rho_L}{\alpha} y + \rho_C xy, \tag{5.8}$$

$$\frac{dy}{dt} = -\frac{\alpha}{\rho_C \tau_C} x - \alpha xy. \tag{5.9}$$

Making the following change of variables

$$t \to \frac{\alpha}{\rho_C \tau_C} \sqrt{a} t, \quad y \to \sqrt{a} y,$$

where $a = \rho_C^2 \rho_L \tau_C / \alpha^2$, $b = \rho_C^2 \tau_C / \alpha$ and $m = \rho_C \tau_C$, we obtain

$$\begin{aligned} \frac{dx}{dt} &= y + \frac{b}{a} xy, \\ \frac{dy}{dt} &= -x - \frac{m}{\sqrt{a}} xy. \end{aligned} \tag{5.10}$$

If we introduce polar coordinates, defined by

$$x = r \cos\theta, \quad y = -r \sin\theta,$$

system (5.10) becomes

$$\begin{aligned} \dot{r} &= \mathcal{R}(r, \theta), \\ \dot{\theta} &= 1 + \Theta(r, \theta), \end{aligned} \tag{5.11}$$

where

$$\begin{aligned} \mathcal{R}(r, \theta) &= -\frac{b}{a} r^2 \cos^2\theta \sin\theta - \frac{m}{\sqrt{a}} r^2 \sin^2\theta \cos\theta, \\ \Theta(r, \theta) &= \frac{b}{a} r \cos\theta \sin^2\theta - \frac{m}{\sqrt{a}} r \sin\theta \cos^2\theta. \end{aligned} \tag{5.12}$$

Thus, we can derive an equation for r as a function of θ through the differential equation

$$\frac{dr}{d\theta} = -\frac{\frac{b}{a} r^2 \cos^2\theta \sin\theta + \frac{m}{\sqrt{a}} r^2 \sin^2\theta \cos\theta}{1 + \frac{b}{a} r \cos\theta \sin^2\theta - \frac{m}{\sqrt{a}} r \sin\theta \cos^2\theta}. \tag{5.13}$$

In a neighborhood of $r = 0$,

$$\left(1 + \frac{b}{a} r \cos\theta \sin^2\theta - \frac{m}{\sqrt{a}} r \sin\theta \cos^2\theta\right)^{-1} = 1 + \frac{m}{\sqrt{a}} r \sin\theta \cos^2\theta - \frac{b}{a} r \cos\theta \sin^2\theta + O(r^2).$$

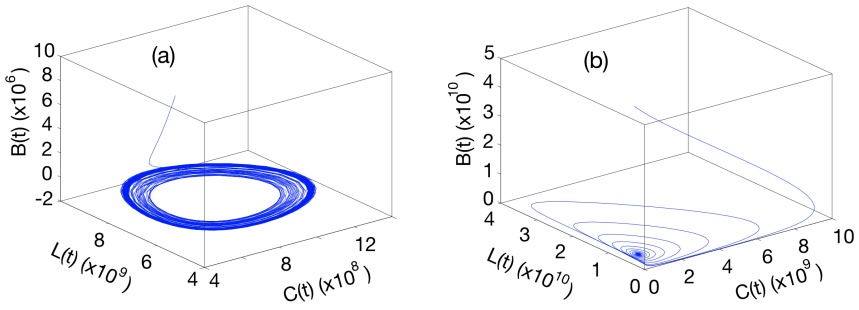

FIGURE 5.2: (a) An orbit of the phase portrait of system (5.4). (b) An orbit of the phase portrait of system (5.3). The parameters used to calculate such orbits are given in Table 5.1.

As a result, for small r we obtain the following expression as the Taylor series of Eq. (5.13):

$$\begin{aligned}\frac{dr}{d\theta} &= -\left[\frac{b}{a}\cos^2\sin\theta + \frac{m}{\sqrt{a}}\sin^2\theta\cos\theta\right]r^2 \\ &+ \left[\frac{b^2}{a^2}\cos^3\theta\sin^3\theta - \frac{m^2}{a}\sin^3\theta\cos^3\theta + \frac{bm}{a\sqrt{a}}\sin^4\theta\cos^2\theta\right]r^3 \\ &- \left[\frac{bm}{a\sqrt{a}}\cos^4\theta\sin^2\theta\right]r^3 + O(r^4).\end{aligned}$$

Now, we use the method of averaging to carry out a change of variable with the effect of reducing the non-autonomous differential equation to an autonomous one. Let the transformation be

$$r = \rho + g_1(\theta)\rho^2 + g_2(\theta)\rho^3, \tag{5.14}$$

with

$$\begin{aligned}g_1'(\theta) &= -\frac{b}{a}\cos^2\theta - \frac{m}{\sqrt{a}}\sin^2\theta\cos\theta, \\ g_2'(\theta) &= \left(\frac{b^2}{a^2} - \frac{m^2}{a}\right)\cos^3\theta\sin^3\theta + \frac{bm}{a\sqrt{a}}\sin^4\theta\cos^2\theta - \frac{bm}{a\sqrt{a}}\cos^4\theta\sin^2\theta,\end{aligned}$$

and formally arrive at the equation

$$\frac{d\rho}{d\theta} = 0. \tag{5.15}$$

At this point, we are in a position to apply the Center Theorem of Lyapunov (see for instance Hale and Kocak, 1991) which ensures that when $dr/d\theta$ can formally be transformed to zero, the equilibrium point is a center. Thus, the origin is a center and so the equilibrium point P_2 is also a center.

It is also possible to find a Lyapunov function of the system (5.10) as

$$V(x,y) = \frac{a}{b}x + \frac{\sqrt{a}}{m}y - \frac{a^2}{b^2}\log\left(1+\frac{b}{a}x\right) - \frac{a}{m^2}\log\left(1+\frac{m}{\sqrt{a}y}\right), \tag{5.16}$$

and $\dot{V} = 0, \forall (x, y) \in \mathbb{R}^2$. As $\mathbb{R}^2_+$ is a positively invariant manifold, all the orbits go periodically around P_2. An orbit of the phase portrait for a solution of system (5.4) is shown in Figure 5.2 a.

Finally, let $(C(t), L(t))$ be an arbitrary solution of (5.4) for $B = 0$, and denote its period by $\mathcal{L} > 0$. It is possible to calculate the time average of variables C and L (that is, the number of CAR T and leukemic cells, respectively). Dividing the first equation of (5.4) by C, the second by L and integrating from 0 to $\mathcal{L}$ and using the fact that the solutions are periodic, we get

$$0 = \log C(t)\big|_0^{\mathcal{L}} = \rho_C \int_0^{\mathcal{L}} L(t)dt - \frac{1}{\tau_c}\mathcal{L}, \tag{5.17}$$

and

$$0 = \log L(t)\big|_0^{\mathcal{L}} = \rho_L P - \alpha \int_0^{\mathcal{L}} C(t)dt. \tag{5.18}$$

Hence

$$\frac{1}{\mathcal{L}}\int_0^{\mathcal{L}} C(t)dt = \frac{\rho_L}{\alpha}, \tag{5.19}$$

$$\frac{1}{\mathcal{L}}\int_0^{\mathcal{L}} L(t)dt = \frac{1}{\rho_C \tau_C}, \tag{5.20}$$

whose values are equal to the equilibrium point P_2 for the two first coordinates.

Reduced mathematical model: system (5.3)

On the other hand, the non-negative equilibrium points of system (5.3) are:

- Equilibrium point $P_1 = (C_1^*, L_1^*, B_1^*) = \left(0, 0, \frac{\tau_B}{\tau_I} I_0\right)$.
- Equilibrium point P_2 is given by

$$\begin{aligned} P_2 &= (C_2^*, L_2^*, B_2^*) \\ &= \left(\frac{\rho_L}{\alpha}, \frac{1}{\rho_C \tau_C} - \frac{I_0(\tau_B + \beta\,(1+\rho_L\tau_B)\tau_I)}{(1+\rho_L\tau_B)\left(1+\frac{\rho_L}{\alpha C_{50}}\right)\tau_I}, \frac{I_0\tau_B}{(1+\rho_L\tau_B)\left(1+\frac{\rho_L}{\alpha C_{50}}\right)\tau_I}\right) \end{aligned}$$

  where we assume that

$$\frac{1}{\rho_C\tau_C} > \frac{I_0(\tau_B + \beta\,(1+\rho_L\tau_B)\tau_I)}{(1+\rho_L\tau_B)\left(1+\frac{\rho_L}{\alpha C_{50}}\right)\tau_I}. \tag{5.21}$$

- $P_3 = (C_3^*, L_3^*, B_3^*) = \left(C_3^*, 0, \frac{1}{\rho_C\tau_C} - \frac{\beta I_0}{1+C_3^*/C_{50}}\right)$ where C_3^* is given by

$$\begin{aligned} C_3^* &= -\frac{C_{50}}{2}\left(1 + \frac{1}{\alpha\tau_B C_{50}} - \rho_C\beta I_0\tau_C\right) \\ &+ \frac{C_{50}}{2}\sqrt{\left(1 + \frac{1}{\alpha\tau_B C_{50}} - \rho_C\beta I_0\tau_C\right)^2 + \frac{4\rho_C I_0\tau_C}{\alpha C_{50}}\left(\frac{\beta}{\tau_B} + \frac{1}{\tau_I} - \frac{1}{\rho_C I_0\tau_C\tau_B}\right)} \end{aligned}$$

with the following conditions holding

$$\frac{\beta}{\tau_B}+\frac{1}{\tau_I}>\frac{1}{\rho_C I_0 \tau_C \tau_B},\quad \frac{1}{\rho_C\tau_C}>\frac{\beta I_0}{1+C_3^*/C_{50}}. \tag{5.22}$$

- $P_4=(C_4^*,L_4^*,B_4^*)=\left(C_4^*,0,\frac{1}{\rho_C\tau_C}-\frac{\beta I_0}{1+C_4^*/C_{50}}\right)$ where C_4^* is given by

$$\begin{aligned} C_4^* &= -\frac{C_{50}}{2}\left(1+\frac{1}{\alpha\tau_B C_{50}}-\rho_C\beta I_0\tau_C\right)\\ &- \frac{C_{50}}{2}\sqrt{\left(1+\frac{1}{\alpha\tau_B C_{50}}-\rho_C\beta I_0\tau_C\right)^2+\frac{4\rho_C I_0\tau_C}{\alpha C_{50}}\left(\frac{\beta}{\tau_B}+\frac{1}{\tau_I}-\frac{1}{\rho_C I_0\tau_C\tau_B}\right)} \end{aligned}$$

with the following conditions being satisfied

$$1+\frac{1}{\alpha\tau_B C_{50}}<\rho_C\beta I_0\tau_C,\ \frac{\beta}{\tau_B}+\frac{1}{\tau_I}<\frac{1}{\rho_C I_0\tau_C\tau_B},\ \frac{1}{\rho_C\tau_C}>\frac{\beta I_0}{1+C_4^*/C_{50}}. \tag{5.23}$$

Regarding the study of the stability of the equilibrium points, we obtain the following conclusions:

- The eigenvalues of P_1 are

$$\lambda_1=\rho_L,\quad \lambda_2=-\frac{1}{\tau_B},\quad \lambda_3=\frac{I_0\rho_C\tau_B\tau_C-\tau_I+I_0\beta\rho_C\tau_C\tau_I}{\tau_C\tau_I}$$

  and therefore P_1 is an unstable point (saddle point).

- Using the Routh-Hurwitz criterion, it follows that P_2 is asymptotically stable for any positive I_0 value, assuming that condition (5.21) is satisfied. Since for $I_0=0$ we obtain the system (5.4), it means that a small perturbation of $I_0=0$, i.e. $I_0=\varepsilon$, with ε sufficiently small, transform the centers obtained in the system (5.4) into asymptotically stable foci. Therefore, $I_0=0$ is a bifurcation point since for this value the type of stability changes, and we obtain a Hopf bifurcation. An orbit of the phase portrait for a solution of system (5.3), for this case, is shown in Figure 5.2 b.

- Carrying out a stability study, in a general way, for both P_3 and P_4 is very complex, so we have performed a study within the confines of the parameter range collected in Table 5.1, which are biologically relevant.

  We have observed that for all parameters in Table 5.1, P_4 has at least one negative component, and thus we do not consider such biologically unfeasible scenarios.

There exist parameters for P_3 for which the components C_3^*, L_3^*, and B_3^* are all positive and correspond to a point that is an asymptotically stable focus. Figure 5.3 shows the region where the real eigenvalue, say λ_1, is negative or positive, as a function of I_0 and k and for different values of α. Figure 5.4 depicts all the eigenvalues of P_3 for different values of I_0, k and α. As can be seen, the real part of the complex eigenvalues λ_2 and λ_3, is always negative. On the other hand, the real eigenvalue λ_1 changes its sign for different values of I_0, k and α. Then, the stability and instability of P_3 is given by the sign of λ_1.

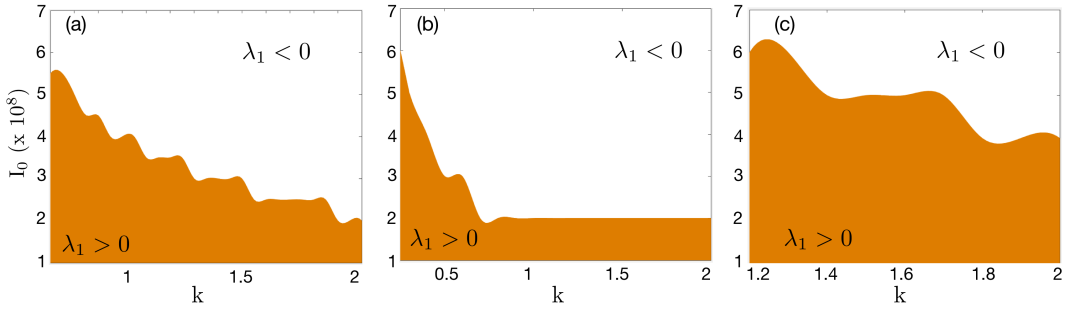

FIGURE 5.3: Values of the sign of eigenvalue λ_1 for different values of I_0 and k for (a) $\alpha = 4.5 \cdot 10^{-11}$ (b) $\alpha = 10^{-10}$ (c) $\alpha = 3 \cdot 10^{-11}$. The orange shaded region corresponds to eigenvalue λ_1 positive.

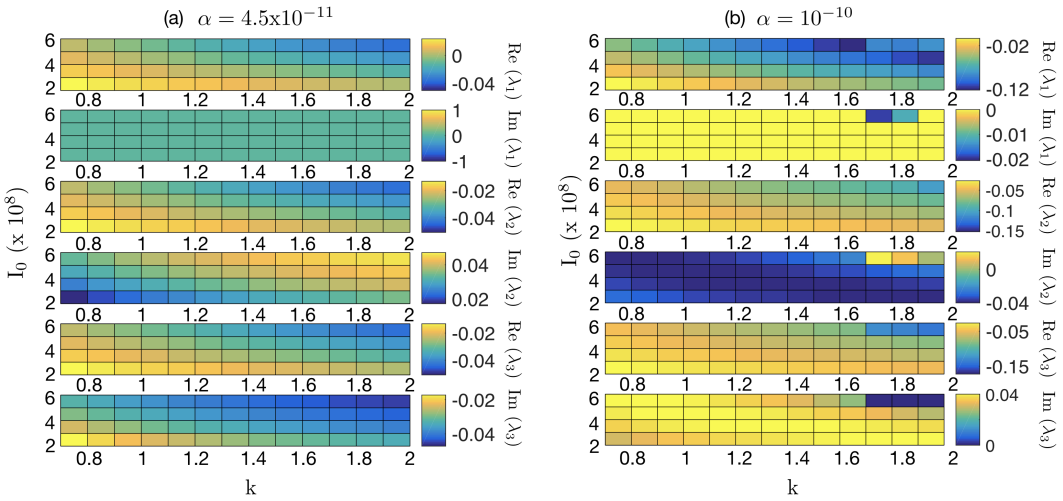

FIGURE 5.4: Pseudocolour plots of the real and imaginary parts of P_3 for different values of I_0 and k for (a) $\alpha = 4.5 \cdot 10^{-11}$ and (b) $\alpha = 10^{-10}$

5.3.3 Analytical formulation of maximum expansion of CAR T cells for system (5.4)

The positive solutions to Eqs. (5.4b) and (5.4c) are given, respectively, by

$$L(t) = L_0 \exp\left(\rho_L t - \alpha \int_0^t C(s)ds\right), \tag{5.24a}$$

$$B(t) = B_0 \exp\left(-\frac{t}{\tau_B} - \alpha \int_0^t C(s)ds\right). \tag{5.24b}$$

Then, calculating its quotient, it is easy to obtain the following expression for all $t > 0$.

$$\frac{L(t)}{B(t)} = \frac{L_0}{B_0} \exp\left[\left(\rho_L + \frac{1}{\tau_B}\right)t\right]. \tag{5.25}$$

Proposition 4. *Let t_{max} denote the time at which a local positive maximum of the CAR T cell solution $C = C(t)$ to Eq. (5.4a) occurs. Then, the positive solutions to Eqs. (5.4b) and*

(5.4c) at $t = t_{max}$ satisfy

$$L(t_{max}) = \frac{L_0\, e^{\left(\rho_L + \frac{1}{\tau_B}\right)t_{max}}}{\rho_C \tau_C \left(B_0 + L_0\, e^{\left(\rho_L + \frac{1}{\tau_B}\right)t_{max}}\right)}, \tag{5.26a}$$

$$B(t_{max}) = \frac{B_0}{\rho_C \tau_C \left(B_0 + L_0\, e^{\left(\rho_L + \frac{1}{\tau_B}\right)t_{max}}\right)}, \tag{5.26b}$$

where L_0 and B_0 are the initial conditions for the leukemic and B cells, assumed to be positive numbers.

Proof. If $C = C(t)$ has a local positive maximum at $t = t_{\max}$, then $\frac{dC}{dt} = 0$ at $t = t_{\max}$. Using Eq. (5.4a), we get $\rho_C \left(L(t_{\max}) + B(t_{\max})\right) - \frac{1}{\tau_C} = 0$. Thus, $L(t_{\max}) + B(t_{\max}) = \frac{1}{\rho_C \tau_C}$. Combining this expression with the above formula (5.25) evaluated at $t = t_{\max}$, Eqs. (5.26) follow. □

Proposition 5. *Let t_{max} denote the time at which a local positive maximum of the CAR T cell solution $C = C(t)$ to Eq. (5.4a) occurs. Then t_{max} can be calculated from the implicit relation*

$$\log\left[\rho_C \tau_C \left(L_0\, e^{\rho_L t_{max}} + B_0\, e^{-\frac{t_{max}}{\tau_B}}\right)\right] - \alpha \int_0^{t_{max}} C(t)dt = 0 \tag{5.27}$$

Proof. Combining (5.24a) and (5.24b), and setting $t = t_{\max}$, we get

$$L(t_{\max}) + B(t_{\max}) = \left(L_0\, e^{\rho_L t_{\max}} + B_0\, e^{-\frac{t_{\max}}{\tau_B}}\right) e^{-\alpha \int_0^{t_{\max}} C(s)ds}. \tag{5.28}$$

Using the fact that $L(t_{\max}) + B(t_{\max}) = \frac{1}{\rho_C \tau_C}$, Eq. (5.28) can be finally written as (5.27). □

Proposition 6. *Let C_{max} be the value of the local positive maximum of the CAR T cell solution $C = C(t)$ to Eq. (5.4a), occurring at time t_{max}. Then,*

$$\begin{aligned} C_{max} &= C_0 + \frac{\rho_C}{\alpha}\left(L_0 + B_0 - \frac{1}{\rho_C \tau_C}\right) - \frac{1}{\tau_C}\int_0^{t_{max}} C(s)ds \\ &+ \frac{\rho_L \rho_C}{\alpha}\int_0^{t_{max}} L(s)ds - \frac{\rho_C}{\alpha \tau_B}\int_0^{t_{max}} B(s)ds\,. \end{aligned} \tag{5.29}$$

Proof. We first combine Eqs. (5.4) in the form

$$\frac{1}{\rho_C}\frac{dC}{dt} + \frac{1}{\alpha}\left(\frac{dL}{dt} + \frac{dB}{dt}\right) = -\frac{1}{\rho_C \tau_C}C + \frac{\rho_L}{\alpha}L - \frac{1}{\alpha \tau_B}B. \tag{5.30}$$

Upon integration, we get

$$\begin{aligned} C(t) &= C_0 - \frac{\rho_C}{\alpha}(L(t) + B(t) - L_0 - B_0) \\ &- \frac{1}{\tau_C}\int_0^t C(s)ds + \frac{\rho_L \rho_C}{\alpha}\int_0^t L(s)ds - \frac{\rho_C}{\alpha \tau_B}\int_0^t B(s)ds\,. \end{aligned} \tag{5.31}$$

Setting $t = t_{\max}$ and using $L(t_{\max}) + B(t_{\max}) = \frac{1}{\rho_C \tau_C}$ in (5.31), the result follows. □

Numerical evaluation of the three integrals on the right-hand side of (5.31) reveals that, for the parameters shown in Table 5.1, each is smaller (by at least one order of magnitude) than the second term (note that there is also partial cancellation among the three integrals). Hence, we may approximate (5.31) by

$$C_{\max} \simeq C_0 + \frac{\rho_C}{\alpha}\left(L_0 + B_0 - \frac{1}{\rho_C \tau_C}\right), \tag{5.32}$$

Thus, the maximum number of CAR T cells that can be reached during the first expansion phase is related to the initial populations L_0 and B_0 multiplied by the amplification factor $\frac{\rho_C}{\alpha}$. Note also that, in practice, the contribution of C_0 is much smaller than the second term in Eq. (5.32) and can be ignored, suggesting that the initial number of injected CAR T cells does not affect the peak, although it does contribute in (5.27) when computing $t_{\max}$.

5.4 Results

In this section, we present the results obtained from systems (5.3) and (5.4). Since model (5.4) is a particular case of the model (5.3), we first show the results for the model (5.4). This allows us to go from a simpler analysis to a more general one.

5.4.1 Mathematical model (5.4) describes post CAR T cell injection dynamics

We first studied the dynamics of the system post-CAR T cell injection numerically, as described by Eqs. (5.4). Figure 5.5 shows a typical example. During the first two months of the simulation, CAR T cells expanded, showing a peak at about two weeks post-injection, before their numbers stabilized and began to decrease. Both the leukemic and B-cell compartments experienced a continuous decrease towards undetectable values representing the dynamics of a patient without residual disease. The expansion of the CAR T population was exponential, increasing by several orders of magnitude (see Figure 5.5 b), in line with reported clinical experience and patient datasets (Ghorashian et al., 2019).

5.4.2 The number of injected CAR T cells does not affect treatment outcome, but the stimulation rate does

We next studied the dynamics of Eqs. (5.4) under different numbers of injected CAR T cells. A typical example is displayed in Figure 5.6 a. The change of one order of magnitude in the initial CAR T cell load resulted in minor changes in the maximum expansion achieved (of around 6%). A reduction in the time to peak expansion in silico of about 3 days was observed. However, the persistence of CAR T cells was not affected by their initial load.

It has already been observed that when the number of CAR T cells seeded is small, the therapy can fail (Hartmann et al., 2017). We simulated in silico, and saw that the effect of a reduction in the growth efficiency of the cells (the stimulation rate ρ_C) and the dynamics were substantially affected (see Figure 5.6). A reduction in the efficiency of stimulation in the CAR T cells led to a slower growth of this population in silico, resulting in leukemic cells reaching higher numbers for almost two months without any clinical response.

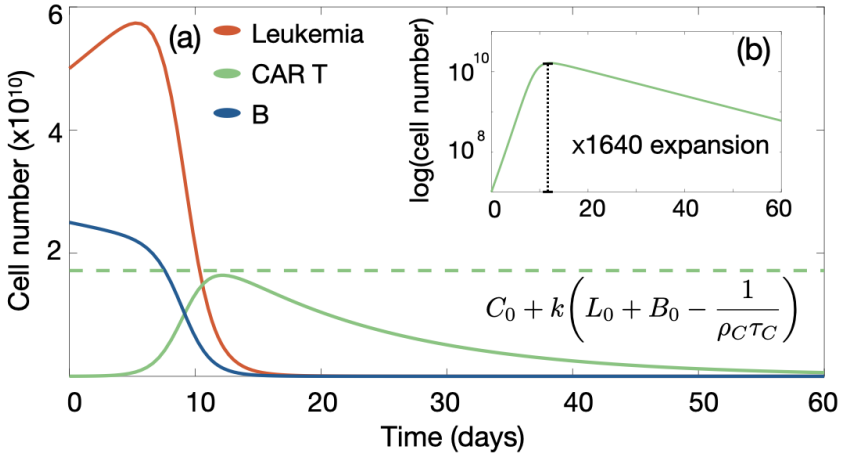

FIGURE 5.5: **Typical dynamics of leukemic cell (red curve), B-cell (blue curve) and CAR T cell (green curve) compartments according to Eqs. (5.4).** (a) Simulations for parameters $\alpha = 4.5\times 10^{-11}$ day^{-1}cell^{-1}, $\tau_C = 14$ days, $\rho_L = 1/30$ day^{-1}, $\rho_C = 0.25\alpha$, $\tau_B = 60$ days and injected cells $C_0 = 10^7$ corresponding, to 5×10^5 cells per kg for a 20 kg child. Also, $L_0 = 5 \times 10^{10}$ and $B_0 = 2.5 \times 10^{10}$, which correspond to typical values after lymphodepleting chemotherapy. (b) Logarithmic plot of the CAR T cell population.

5.4.3 Maximum expansion of CAR T cells in vivo and CRS

System (5.4) is amenable to finding useful analytical and semi-analytical expressions, which are all derived in Section 5.3.3. At time $t_{\max}$, which typically occurs within 2-4 weeks after injection of the CAR T cells, a first maximum in their number, denoted by $C_{\max} \equiv C(t_{\max})$, is achieved during the expansion phase. The value of $t_{\max}$ can be calculated from the implicit relation given by Eq. (5.27). Furthermore, it is possible to estimate the maximum number of CAR T cells $C_{\max}$, which is approximately given by Eq. (5.32). Also, explicit formulas for computing the leukemic and B cell loads in patients at time $t_{\max}$ are given by Eqs. (5.26).

Since toxicity, accounted for by Eqs. (5.1f) and (5.1g), depends on the maximum CAR T cell number, one would expect a smaller ratio $\frac{\rho_C}{\alpha}$ to lead to lower toxicities. Figure 5.7 shows the linear dependence of the maximum number of CAR T cells on ρ_C as obtained from simulations of Eqs. (5.4), which is well approximated by Eq. (5.32). The above result points to a proportional relation between the total leukemic load and the severity of the CRS syndrome. In fact, a strong correlation between the severity of CRS and disease load at the time of CAR T cell infusion has been noted in multiple clinical trials of CAR T cell therapy of hematological malignancies (Lee et al., 2015; Maude et al., 2014; Davila et al., 2014; Turtle et al., 2017).

5.4.4 CAR T cell persistence depends on the T cell mean lifetime

The recent clinical study Ghorashian et al., 2019 showed much longer persistence of the CAR T cells when their mean lifetime was increased to $\tau_C = 30$ days, larger than the more common value $\tau_C = 14$ days. We simulated the dynamics of Eqs. (5.4) for both values of τ_C. An example is shown in Figure 5.8. While the B-cells and leukemic cells exhibited similar behavior, CAR T cells showed a much longer persistence in line with the clinical observations.

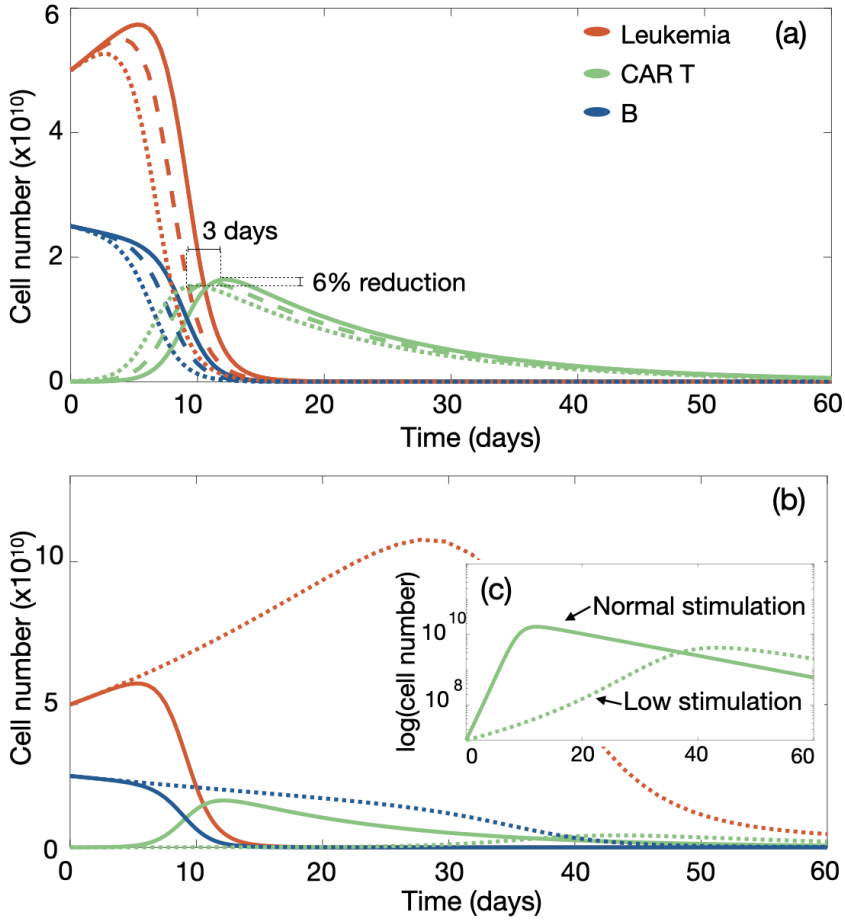

FIGURE 5.6: **The number of injected CAR T cells does not affect treatment outcome, but the stimulation rate does.** (a) Dynamics of leukemic cells (red line), B-cells (blue line) and CAR T cells (green line) according to Eqs. (5.4) for the virtual patient of Figure 5.5 subject to injections of 5×10^5 cells/kg (solid lines), 15×10^5 cells/kg (dashed lines) and 45×10^5 cells/kg (dotted lines). (b,c) Dynamics for stimulation rates $\rho_C = 0.25\alpha$ (solid line) and $\rho_C = 0.05\alpha$ (dotted lines). (c) CAR T cell expansion in log scale.

5.4.5 CD19$^+$ relapses could be a dynamical phenomenon

We performed simulations of Eq. (5.4) for longer timescales (with parameters as in Figure 5.5) and observed a long-time relapse (see Figure 5.9) at about one year after infusion, in what would be a CD19$^+$ relapse. Leukemic growth continued for several months but finally there was an outgrowth of CAR T cells after the relapse that was able to control the disease. This is an important nonlinear dynamical phenomenon that could help explain some CD19$^+$ relapses.

When $B \sim 0$, as after CAR T cell expansion, Eqs. (5.4) become the well-known Lotka-Volterra predator-prey mathematical model. That model gives rise to periodic oscillations corresponding to ecological cycles that have been observed both in ecosystems (Brauer and Castillo-Chavez, 2000) and in experimental models (Blasius et al., 2020). In our present case, the period of the cycles would be related to the cancer relapse time. This period has been previously described as showing a complex dependence on a conserved quantity, $\mathcal{K}$ (Shih, 1997) (having in our case units of s^{-1}), and given by

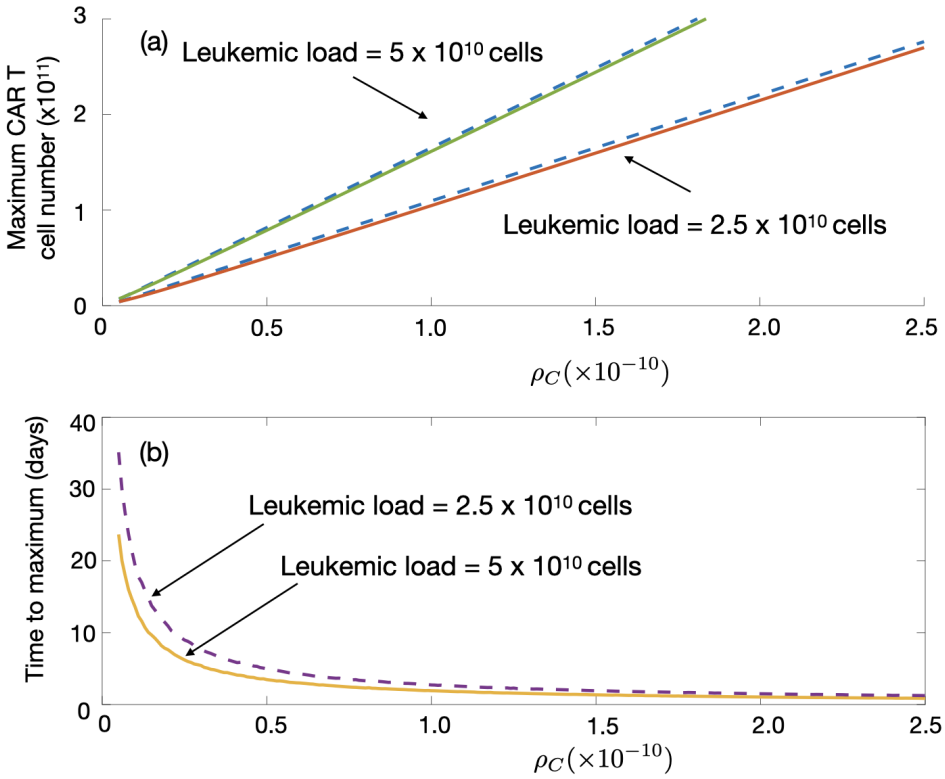

FIGURE 5.7: **Dependence on ρ_C of the maximum number of CAR T cells and the time t_{max} taken to achieve the maximum.** Common parameters for all plots are as in Figure 5.5: $\alpha = 4.5\times 10^{-11}$ cell^{-1} day^{-1}, $\tau_C = 14$ days, $\rho_L = 1/30$ day^{-1}, $\tau_B = 60$ days and initial cell numbers $C_0 = 10^7$ cells, $B_0 = 2.5 \times 10^{10}$ cells. (a) Maximum value number of CAR T cells obtained for initial leukemic loads of 5×10^{10} cells (red) and 2.5×10^{10} cells as a function of ρ_C. Solid line indicates the results obtained from Eqs. 5.4 and the dashed line the upper bound given by Eq. (5.32). (b) Time to maximum value of CAR T cells for different initial leukemic loads computed from Eq. (5.27).

$$\mathcal{K} = \alpha C - \rho_L \log\left(\frac{\alpha C}{\rho_L}\right) + \rho_C L - \frac{1}{\tau_C}\log\left(\rho_C \tau_C L\right) \sim \rho_C\left(L_0 + B_0\right). \quad (5.33)$$

The conserved quantity $\mathcal{K} \gg 1$, can be approximated by the asymptotic formula (Oshime, 2003), which in our case yields the period $\mathcal{L}$ of oscillations

$$\begin{aligned}\mathcal{L}(\mathcal{K}) &= \frac{\rho_C\tau_C(L_0+B_0)}{\rho_L} + \frac{1}{\rho_L}\log\left[\rho_C\tau_C\left(L_0+B_0\right)\right] \\ &+ \tau_C \log\left[\frac{\rho_C\left(L_0+B_0\right)}{\rho_L}\right] + O\left(\frac{\log E}{E}\right) \sim \frac{\rho_C\tau_C\left(L_0+B_0\right)}{\rho_L}. \end{aligned} \quad (5.34)$$

Because of the approximations involved, Eq. (5.34) should only be taken as an order-of-magnitude estimate for the cancer relapse time. However, it is interesting that longer lifetimes of the CAR T cells resulted in longer relapse times according to Eq. (5.34). This could be the reason why so few CD19$^+$ relapses were observed in the recent trial (Ghorashian et al., 2019), with $\tau_C = 30$ days, much longer than the more

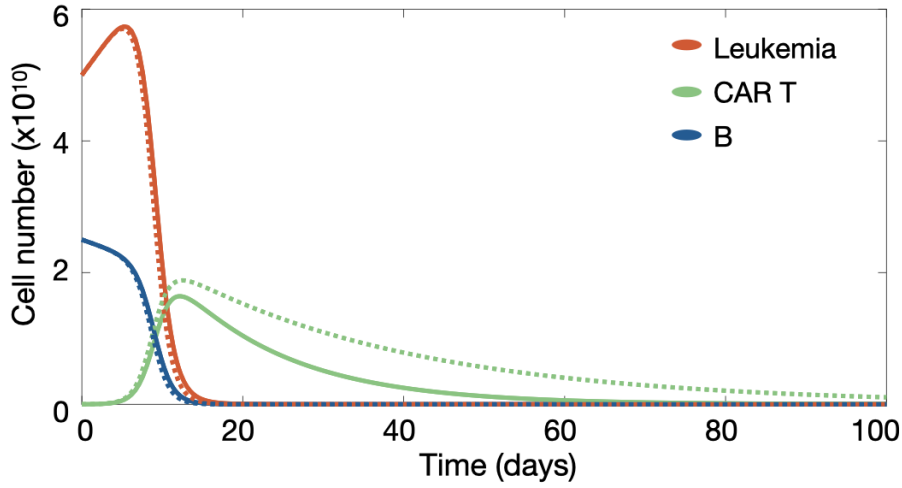

FIGURE 5.8: **CAR T cell persistence when varying its lifetime τ_C.** Dynamics of the leukemic cell (red), B-cell (blue) and CAR T cell (green) according to model Eqs.(5.4). Solid and dashed curves correspond to $\tau_C = 14$ days and $\tau_C = 30$ days, respectively, with the rest of parameters and initial data as in Figure 5.5.

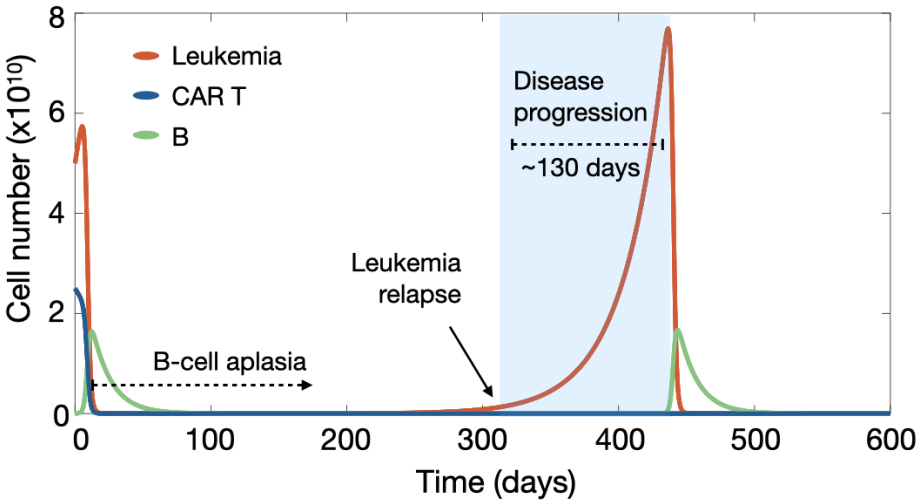

FIGURE 5.9: **CD19$^+$ relapses could be a dynamical phenomenon.** Long-time dynamics of Eqs. (5.4) for leukemic (red), B (blue) and CAR T (green) cells in the time interval [0,600] days, displaying a CD19$^+$ relapse as the result of predator-prey type dynamics in silico. Parameters are as in Figure 5.5. The shaded area indicates the time interval in which the disease would be progressing without further interventions. Notice the subsequent emergence of CAR T cells after the CD19$^+$ cell relapse.

common value $\tau_C \sim 14$ days.

A very intriguing question is whether those relapses could resolve spontaneously due to the predator-prey type competition between the CAR T and leukemic cells. Owing to the long progression time, this could pass unnoticed, since after progression, other therapeutic actions would be taken, such as hematopoietic transplants, before allowing the CAR T to appear again.

Although our simulations point to a potentially interesting scenario, the model

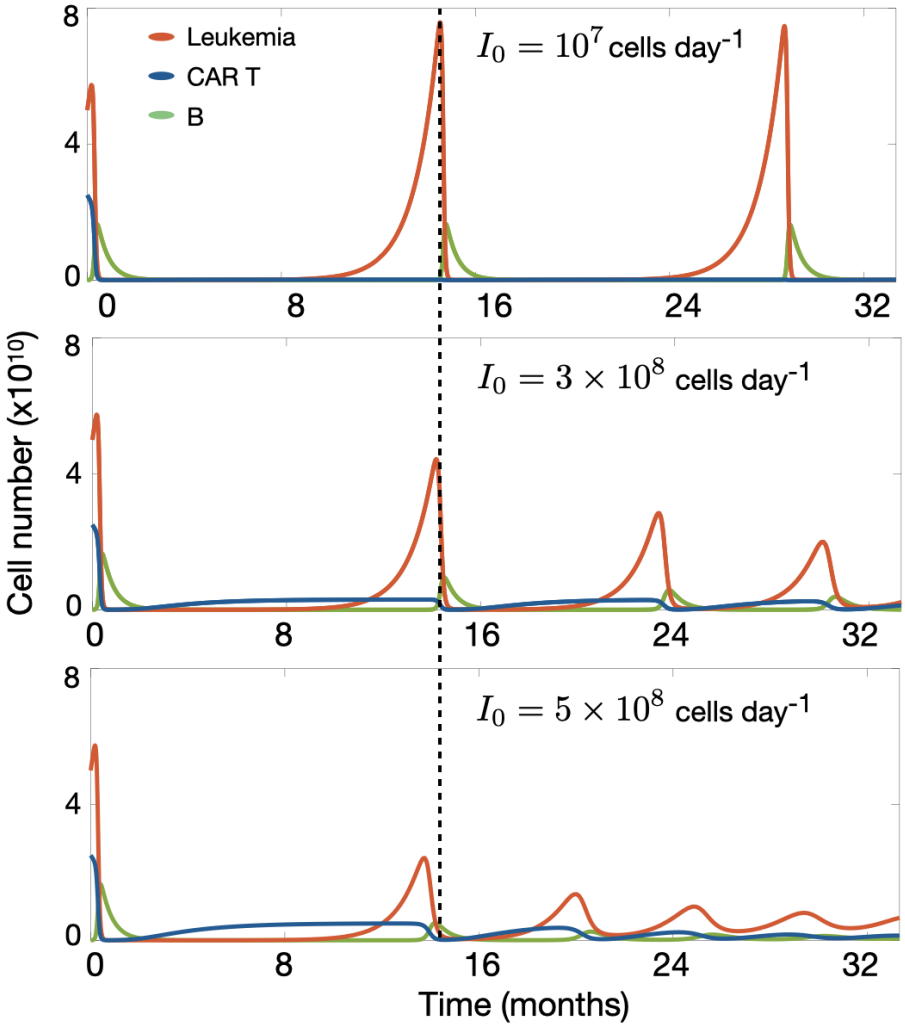

FIGURE 5.10: **Long-time dynamics of virtual patients predicted by Eqs. (5.3).** Parameters are $\alpha = 4.5 \times 10^{-11}$ cell^{-1} day^{-1}, $\beta = 0.1$, $\tau_C = 14$ days, $\tau_B = 60$ days, $\rho_L = 1/30$ day^{-1}, $\rho_C = 0.25\alpha$, $C_{50} = 10^9$ cells, $\tau_I = 6$ days. The subplots show the dynamics of the leukemic cell (red), B-cell (blue) and CAR T cell (green) compartments. (a) Case $I_0 = 10^7$ cell day^{-1}. (b) Case $I_0 = 3 \times 10^8$ cell day^{-1}, (c) Case $I_0 = 5 \times 10^8$ cell day^{-1}.

given by Eqs. (5.4) is not good for studying long-term phenomena. One of the missing biological processes in Eqs. (5.4) is the potential contribution of B-cell production in the bone marrow from CD19$^-$ hematopoietic stem cells to the maintenance of a pool of CAR T cells. Thus, to get a more realistic insight into the dynamics, we simulated Eqs. (5.3) for the same virtual patients and biologically reasonable parameters $\beta = 0.1$, $\tau_I = 6$ days (see Table 5.1) and different values for the production of B cells in the bone marrow embodied by I_0.

One set of examples is shown in Figure 5.10. The more realistic model given by Eqs. (5.3) still presents first relapse at a time independent of the choice of the flux I_0. However this parameter influenced the post-relapse dynamics. For values of I_0 smaller than approximately 10^7 cells/day, which is the typical number of injected CAR T cells (Hartmann et al., 2017), there were no substantial changes in the dynamics with subsequent relapses following a periodic pattern. Larger values of I_0 led to relapses of B cells before the relapse of leukemic cells and later of CAR T cells. Also,

the relapse dynamics were in line with damped oscillations, with both leukemic and CAR T cell relapses having smaller amplitudes. Interestingly, our model Eqs. (5.3) predict that a significant increase of B cells could be used as a potential clinical biomarker indicative of subsequent cancer relapse.

5.4.6 CAR T cell reinjection may allow the severity of relapse to be controlled

In the framework of our modeling approach leukemia relapses would be transient. However, the long potential duration of such relapses would require further intervention to prevent patients from suffering undesirable harm during such periods. An interesting question is whether it would be possible to control these recurrences by acting on the leukemia by reinjecting CAR T cells , and what the appropriate timings and doses for that intervention would be.

Using the mathematical model (5.3), we simulated the reinjection of $C = 10^7$ CAR T cells at different times: before relapse ($t = 300$ days), at relapse ($t = 360$ days), and after relapse ($t = 415$ days) and compared the outcome with the case without reinjection. An example is shown in Figure 5.11 a,b.

Significant reductions of both the peak leukemic cell number and relapse duration were obtained, the best results being when reinjection was performed on relapse. Thus, our in silico results suggest that the early reinjection of CAR T cells in a $CD19^+$ B-leukemia relapse could reduce disease load and help in early control of the disease. This has interesting implications since, after relapse is detected, CAR T preparation requires blood extraction, apheresis, T cell modification and expansion {*ex vivo*, and finally patient infusion. In clinical practice this process takes from three to six weeks. From the practical point of view, a possibility for increasing the speed of action after leukemic cell identification would be to freeze and keep some of the CAR T cells initially obtained so that they could be reinjected and aid in early control of the disease.

We also studied the effect of the number of CAR T cells injected at the optimal time. An example is shown in Figure 5.11 c,d. The effects of a very small infusion of $C = 10^5$ cells are compared with those of a more standard dose of $C = 10^7$ cells. The number of T cells injected affected the outcome. This was different from our previous observation that the number of CAR T cells injected initially did not affect the treatment outcome. The reason is that, initially, there are many targets, both leukemic and B cells, allowing for a huge expansion of the CAR T population. However, on relapse, the target population is smaller and a larger initial number of CAR T cells helps in making the expansion process faster.

5.4.7 Model (5.3) predicts a scenario leading to zero leukemic cells

The analysis of the non-negative equilibrium points of system (5.3), set out in 5.3.2, shows the possibility of reaching $L = 0$ after starting with a non-zero leukemic cell population. Using the parameters given in Table 5.1, we observe that there exist ranges for the ratio k and the bone marrow B cell production I_0 where one of the equilibrium points, P_3 (a focus), is asymptotically stable for different values of α. Hence, one of its associated eigenvalues will be real (see Figure 5.3 in 5.3.2) while the other two eigenvalues will be complex conjugate (see Figure 5.4 in 5.3.2). Figure 5.12 illustrates an example with different initial conditions and the same set of parameters for them. It should be pointed out that in all cases shown in Figure 5.12, both

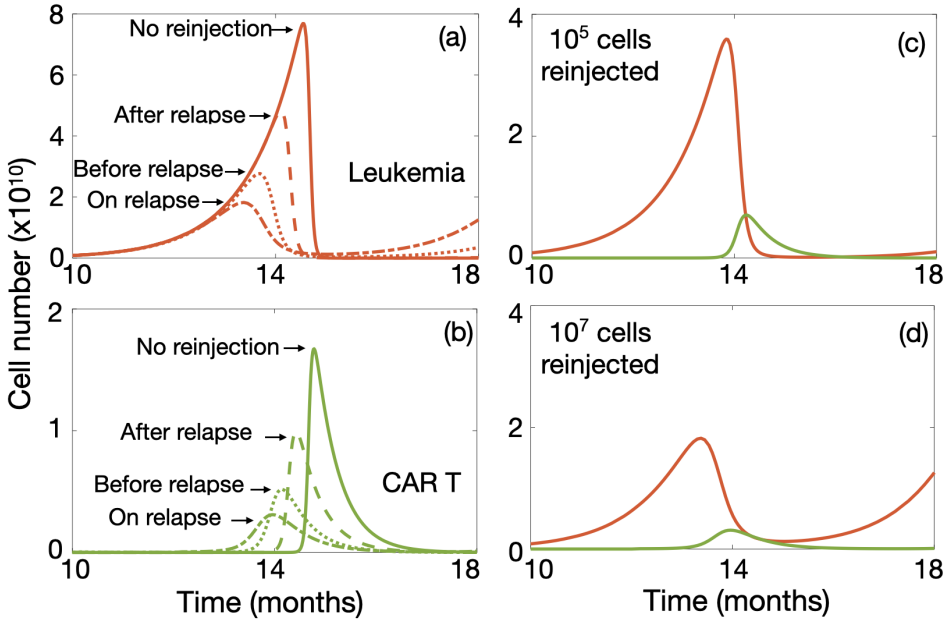

FIGURE 5.11: **CAR T cell reinjection may allow severity of relapse to be controlled**. Simulations of Eqs.(5.4) for parameter values $\alpha = 4.5 \times 10^{-11}$ cell^{-1} day^{-1}, $\beta = 0.1$, $\tau_C = 14$ days, $\tau_B = 60$ day, $\rho_L = 1/30$ day^{-1}, $\rho_C = 0.25\alpha$, $C_{50} = 10^9$ cells, $\tau_I = 6$ days, and $I_0 = 2 \times 10^5$ cell day^{-1}. All subplots show the dynamics of leukemic (red) and CAR T (green) cells upon reinjection of CAR T cells. Cases (a) and (b) display the dynamics of (a) leukemic and (b) CAR T cells, respectively, for doses of $C = 10^7$ cells administered at times: $t = 300$ days (dash-dot line), $t = 360$ days (dotted line) and $t = 415$ days (dashed line) in comparison with the dynamics without reinjection (solid line). Subplots (c) and (d) illustrate the combined dynamics of leukemic and CAR T cells after reinjection of: (c) $C = 10^5$ cells and (d) $C = 10^7$ cells at $t = 360$ days.

the CAR T and the B cells remain at non-zero levels (of the order of 5×10^8 and 10^9, respectively) when the leukemic cell population effectively becomes extinct ($L < 1$.)

These results are interesting as they suggest that there is a range of biologically relevant parameters where the cancer may eventually disappear. Our simulations indicate that the larger I_0, k and α, the more likely it is that $L = 0$ can be reached. In particular, if I_0 is increased, this would imply higher production of both B and CAR T cells, due to the contribution of immature B cells from the bone marrow, resulting in a greater chance of eradicating the leukemic cells. This scenario provides another proof of the concept that the mathematical model put forward here can be useful in the clinical setting and may trigger new exploratory pathways.

5.4.8 Sensitivity analysis

A sensitivity analysis was carried out to identify the model parameters with the greatest influence on the equilibrium for CAR T, leukemic and B cells are I_0, α and k. To do so, we calculated the first-order sensitivity coefficient using Sobol's method (Saltelli et al., 2010) to measure the fractional contribution of a single parameter to the output variance. Using a priori information on the parameters, we defined the distribution functions in the table shown in Figure 5.13. We generated a

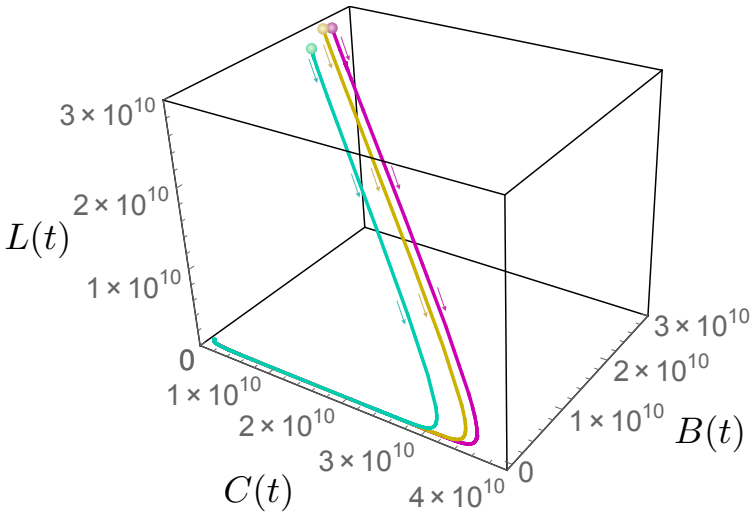

FIGURE 5.12: **Routes to leukemic cell extinction.** Phase portrait of system (5.3) showing three orbits with different initial conditions (coloured dots) that lead to leukemic extinction. Parameters for all orbits are $\alpha = 5 \times 10^{-11}$ cell^{-1} day^{-1}, $\beta = 0.1$, $\tau_C = 20$ days, $\tau_B = 40$ day, $\rho_L = 1/45$ day^{-1}, $\rho_C = 0.7\alpha$, $C_{50} = 10^9$ cells, $\tau_I = 2.4$ days, and $I_0 = 2 \times 10^8$ cell day^{-1}.

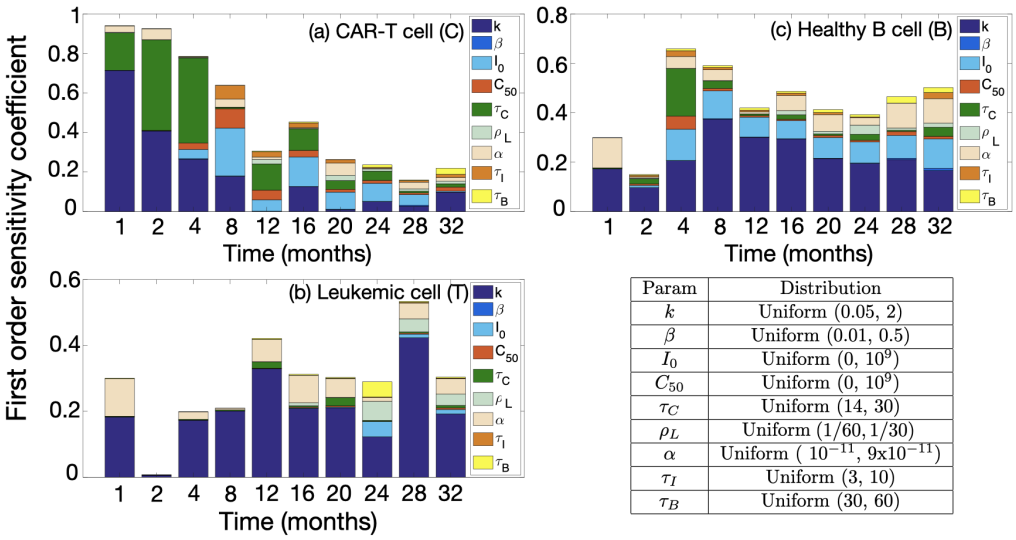

Param	Distribution
k	Uniform (0.05, 2)
β	Uniform (0.01, 0.5)
I_0	Uniform (0, 10^9)
C_{50}	Uniform (0, 10^9)
τ_C	Uniform (14, 30)
ρ_L	Uniform (1/60, 1/30)
α	Uniform (10^{-11}, 9x10^{-11})
τ_I	Uniform (3, 10)
τ_B	Uniform (30, 60)

FIGURE 5.13: Sensitivity analysis of system (5.3) to identify the influence of the model parameters on the solutions for (a) CAR T, (b) leukemic and (c) B cells. The parameter ranges studied and distributions used are displayed in the lower-right table.

set of parameters of size 1000 to calculate the sensitivity indices. The results of the sensitivity analysis of Eqs. (5.3) are shown in Figure 5.13.

The results show that the parameters with the greatest influence on the solutions for CAR T, leukemic and B cells are k, α, τ_C and I_0. However, their impact varies depending on the specific cell compartment and time. For CAR T cells, k and τ_C are the most significant during the first four months after injection. For longer times, I_0 becomes the most important. For leukemic cells, k and α are the most influential parameters, both during the first weeks of the CAR T cell treatment and later during relapse. For healthy B cells, k and α are the most relevant parameters during the first weeks, but later on, on relapse, I_0 also becomes important. Such parameter

dependencies are also suggestive in order to target specific mechanisms that would allow partial control over them.

5.5 Discussion and conclusion

In this chapter, we put forward a mathematical model incorporating the main cell populations involved in the growth of ALL. The model included not only leukemic clones and CAR T cells, but also the hematopoietic compartment that would be responsible for the persistence of CAR T cells by the continuous generation of $CD19^+$ progenitors from $CD19^-$ stem cells.

One simplified version of the full model already allowed us to describe the clinical evolution of B-ALL in the first months after CAR T injection yielding explicit formulas of clinical added value such as the maximum number of CAR T cells that can be reached. Also, it provided a rational support to several clinical observations. Interestingly, the model predicted the possibility of $CD19^+$ relapses being dynamical phenomena resembling predator-prey oscillations. The more complex mathematical models were used to confirm this dynamic and to further give support for therapeutically rechallenging the leukemia with CAR T cells in $CD19^+$ relapses.

It is interesting to point out that in homeostasis there is a population of T cells, the T regulators (Tregs), that control the total number of T cells and have a role in limiting autoimmune processes. We did not incorporate Tregs in our mathematical description. This could be a good approximation for the first weeks of the CAR T cell expansion because the initial lymphodepletion also affects Tregs. However, after the first 3-4 weeks, this population will be able to expand again and has an effect on a faster reduction of the total CAR T cell load. There is not much data available on the dynamics of Treg cells and their reconstitution after the CAR T cell peak. We plan on accounting for this population in future works.

The results obtained using the reduced mathematical model show that the number of CAR T cells initially injected does not affect the subsequent dynamics. Since at the outset CAR T cells do have a huge in vivo target pool, including leukemic and healthy B cells allowing them to expand, even small doses of properly functioning immune cells would lead to a response. Thus, according to our modeling approach, it may be better to store (freeze) part of the cells generated so that they could be ready for later leukemia rechallenging in case of a $CD19^+$ relapse. There, the combination of a fast action after the detection of the disease and the injection of a substantial number of CAR T cells would be clinically relevant according to our mathematical model-based predictions. The reason is that a prompt action would allow both for a reduced growth of the disease and for a smaller toxicity of the disease, thus reducing risks for the patient such as CRS and ICANS. The rationale behind the injection of larger CAR T loads on relapse is that the target population would be smaller in general than at the start of the treatment. Moreover, our model implies that a periodic treatment with CAR T cells to avoid relapse would be quite ineffective, since they would not be expected to expand well unless there is a substantial target population.

Our mathematical model allowed us to obtain an estimate for the very relevant parameter of the relapse time, that would be the optimal time to perform the reinjection of CAR T cells. The estimation obtained by Eq. (5.34) shows that the relapse time depends on the parameters related to CAR T cells (ρ_C and τ_C), the growth rate ρ_L of leukemic cells and their density at the beginning of treatment. In the framework of our continuous model all leukemia experience a relapse, however longer

relapse times may correspond in some simulation runs to leukemia having intermediate densities that are unrealistically low for very long times. Thus, we may expect that leukemia with quite long relapse times, according to our modeling approach, would never relapse. We may act therapeutically on ρ_C and τ_C by designing CAR T cells with higher stimulation ratios and longer persistence.

One of the most interesting findings in this research was the very relevant role of the flux of generation of $CD19^+$ progenitors from $CD19^-$ hematopoietic stem cells, I_0. Although these stem cells are known to be a very small population (typically around 1% of all cells in the bone marrow), what matters most is the flow into the compartment of B-cells.

Our mathematical model also allows us to pose another interesting hypothesis. B-ALL is a field where substantial progress has been made by designing initial intensive treatment regimes combining different types of cytotoxic chemotherapies. On the basis of our mathematical model, and leaving aside the important economic costs, one would expect that substantially less aggressive chemotherapy regimes could be quite effective after CAR T cell injection to eliminate the residual disease (mainly by greatly reducing the ρ_C parameter). This strategy would also be beneficial to control $CD19^-$ relapses. In this case one should balance the side effects of current protocols versus a combination of CAR T cells with a reduced chemo infusion. The main limitation of this approach would be the sustained B-lymphodepletion provoked by the immunotherapy treatment, but one can envision autologous B stem cell transplants after in vitro treatment with CAR T cells to select for $CD19^-$ HSCs.

In conclusion we have put forward a mathematical model describing the response of acute lymphoblastic leukaemias to the injection of CAR T cells. Our theoretical framework provided a mechanistic explanation of the observations reported in different clinical trials. Moreover, it also predicted that $CD19^+$ leukaemia relapses could be the result of the competition between leukemic and CAR T cells in an analogous fashion to predator-prey dynamics. As a result, the severity of relapses could be controlled by early rechallenging of the leukaemia with previously stored CAR T cells.

Chapter 6

CAR T cell therapy in T-cell acute lymphoblastic leukemia

6.1 Introduction

Through the impressive outcomes seen in CD19 antigen bearing B-cell malignancies, CAR T cell therapy is being explored to address new targets. Specifically, there has been a lot of interest on the possibility of using CAR T cells for the treatment of T-cell malignancies (Alcantara et al., 2019; Breman et al., 2018; Fleischer, Spencer, and Raikar, 2019; Sánchez-Martínez et al., 2019).

However, the extension of this therapy to T-cell malignancies presents several challenges because of the shared expression of target antigens between CARTs, T-lineage cancer cells and normal T cells. The first one is fratricide, that refers to the mutual killing of CAR T cells. This phenomenon may prevent the generation, expansion and persistence of CAR T cells. The second one is the prolonged and profound T-cell aplasia induced by the destruction of normal T cells, that exposes patients to severe opportunistic infections. The third one is the potential contamination of CAR T cell products with malignant T cells. In the specific case of T-ALL, circulating leukemic T cells are often found in the peripheral blood of patients, this being less frequent in other types of T-cell malignancies. Furthermore, leukemic T cells may have similar properties as normal T cells, being possible to collect, transduce, expand and infuse them together with T cells as concomitant in the production of CAR T. Thus, developing CAR T cells for T-cell malignancies requires avoiding contamination of the CAR T cell product with malignant transduced T cells (Alcantara et al., 2019). A summary of the challenges associated with CART therapies for T-ALL is shown in Figure 6.1.

Recent preclinical studies showed that T cells transduced with either CD7, CD3, CD5, or T-cell receptor CARs (the most expressed T-cell antigens) efficiently eliminate T-ALL blasts in vitro and are able to control the disease in vivo, although innovative techniques are necessary for the disruption of the target antigen in T cells prior to CAR transduction to avoid extensive autoantigen-driven fratricide (Sánchez-Martínez et al., 2019).

To the best of our knowledge, no mathematical model has considered yet CAR T cell treatments of T-cell malignancies. In this chapter we presented a first minimal mathematical model describing the dynamics of cancer cells in T-cell leukemia and normal T cells plus a population of injected CAR T cells. Our intention was to describe mathematically the effect of the fratricide and to obtain conclusions of practical interest. This interesting phenomenon, that involves a nonlinear self-interaction within the CAR T cell compartment was shown to pose a limit for the production of these cells in vitro. Using the mathematical model, we also studied some questions similar to those addressed in the previous Chapter 5, such as those related to

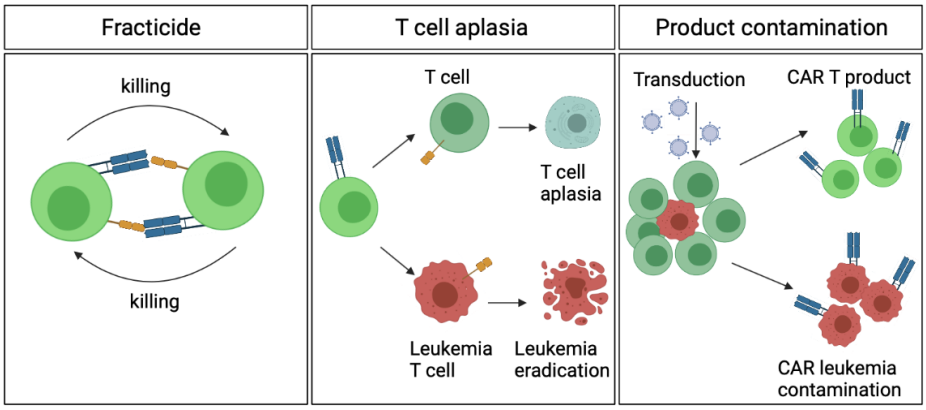

FIGURE 6.1: **Challenges associated with the development of CAR T-cell therapy for the treatment of T ALL.** Created with BioRender.com.

the administered dose, the possibility of CAR T re-injection, and the dynamics of relapses.

Theoretical and simulation results support that CAR T cells could be able to control cancer in vivo to a certain extent. We have shown that it may not be possible to get rid of all cancer cells, but that the treatment could be useful either as a bridge treatment or as a way to make the disease chronic. In this study we focus on carrying out a preliminary exploration of the biological problem and obtain conclusions of practical applicability, using as a test bed numerical simulations of the mathematical model.

6.2 Mathematical model

Our mathematical model accounts for the dynamics of several cellular populations: CAR T cells $C(t)$, leukemic T cells $L(t)$, and normal T cells. The equations describing the dynamics of these populations are

$$\frac{dC}{dt} = \rho_C (T + L + C) C - \frac{1}{\tau_C} C - \alpha C^2 + \rho_I C, \tag{6.1a}$$

$$\frac{dL}{dt} = \rho_L L - \alpha L C, \tag{6.1b}$$

$$\frac{dT}{dt} = g(T, L, C) - \alpha T C. \tag{6.1c}$$

CAR T cells, described by Eq. (6.1a), have a finite lifespan τ_C and proliferate due to stimulation by target cells (either $L(t)$ or $T(t)$ or the CAR T cell themselves $C(t)$). The parameter ρ_C measures the mitosis stimulation after encounters with target cells. The parameter α in Eq. (6.1a) is a cell kill term accounting for the fratricide. It measures the probability that CAR T cell encounters lead to the death of one of the cells. Once the CAR T cell identifies the target cell, killing and detachment are very fast processes (Benmebarek et al., 2019). We consider here only serial killing excluding multiplexed killing that would be a less relevant process and have a different kinetics.

In line with models for CAR T cell dynamics in B-cell leukemia described in Section 5.2, we did not include a CAR T cell death term due to encounters with target

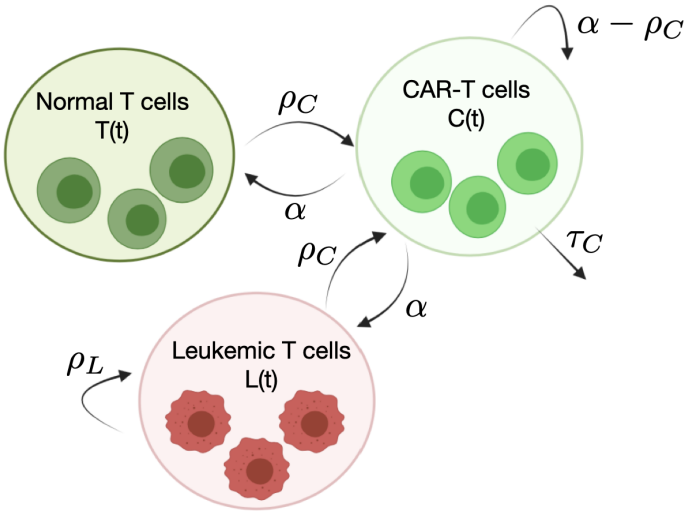

FIGURE 6.2: **Cellular populations and biological processes included in the mathematical model (6.1).** Normal $T(t)$ and leukemic $L(t)$ T cells are killed by CAR T cells $C(t)$ at a rate α and stimulate CAR T cell proliferation at a rate ρ_C, both per cell. Leukemic T cells proliferate at a rate ρ_L. As a result of fratricide and self-stimulation, CAR T cells are eliminated at a rate $\alpha - \rho_C$ per CAR T cell. CAR T cell finite lifetime τ_C also results in cell loss. Created with BioRender.com.

cells. The reason is that CAR T cells do not die after killing target cells (Davenport et al., 2015; Davenport et al., 2018). Also, T cells do not divide in vivo spontaneously (Tough and Sprent, 2018), their clonal expansion being dependent on the stimulation with the target antigen, thus in vivo $\rho_I = 0$. When CAR T cells are expanded in vitro cytokines are added externally forcing the cells to divide thus in that context we will assume $\rho_I \neq 0$.

Leukemic cells (Eq. (6.1b)) proliferate with a rate ρ_L and die to the encounters with the CAR T cells with the rate α.

For the normal T-cell compartment we have only considered a simplified effective description accounting for the different lineages expressing the same target antigen in an aggregate form. It was assumed that these cells are killed a rate α per cell assumed to be similar to that of the other subpopulations and are produced at a rate $g(T, L, C)$. This function is expected to depend on the total number of T cells via cytokines signaling, on the effect of CAR T cell on T-cell progenitors, etc. In this work we assume $g(T, L, C)$ to be very small and contribute only to a minimal residual level of normal T cells that would not be relevant for the system nonlinear dynamics. In what follows we have taken $g(T, L, C) = 0$.

Figure 6.2 summarizes the relationships between the different cell subpopulations and the assumptions behind our model.

6.2.1 In vitro equilibrium

The expansion in vitro during the CAR T cell production can be described by setting $L = T = 0$ in Eqs. (6.1), and taking $\rho_I \neq 0$, thus

$$\frac{dC}{dt} = \hat{\rho}C - \hat{\alpha}C^2. \tag{6.2}$$

The parameter $\hat{\rho} = \rho_I - 1/\tau_C > 0$ always in vitro and the effective cell kill rate $\hat{\alpha} = \alpha - \rho_C \geq 0$, since the killing rate is expected to be larger than the stimulation rate due to the different speeds of the killing and replication processes.

Eq. (6.2) is a logistic equation, that for positive initial values satisfies that

$$C_{[t\to\infty]} \longrightarrow C_* = \hat{\rho}/\hat{\alpha}. \tag{6.3}$$

This result is in line with the observation that CAR T cells targeting T-cell antigens cannot be expanded beyond a certain value (Breman et al., 2018). Here we show that this value will depend on the cytokines stimulation provided and the fratricide cell killing rate.

6.2.2 Parameter estimation

Some parameters in model Eq. (6.1) were estimated in the Section 5.2.3, such as the typical lifetime of activated CAR T cells τ_c. Furthermore, T-cell leukemia, like B-cell leukemia, are typically rather aggressive cancers with small doubling times that can be estimated to be around $\rho_L \in (1/60, 1/30)$. Finally, α and ρ_C can also be expected to be in the range of B-cell leukemia, where they have been found to be around 10^{-11} day^{-1}cell^{-1}. One would expect ρ_C to be of the order or smaller than α since it corresponds to the number of new cells generated by each encounter of CAR T cells with target cells.

As to the initial data, the total number of T-lymphocytes in the human body is around 10^{11} and typical disease load in T-ALL can be in a similar range (Bains et al., 2009). As explained in the introduction, most CAR T administration regimes are preceded by a lymphodepleting treatment that creates a favorable cytokines profile, favoring the growth of injected cells. Thus, the previous numbers are substantially reduced when the treatment is started. We take our initial data to be around $\sim 10^{10}$ for leukemic and normal T cells.

Finally, the number of CAR T cells injected would depend on the maximal expansion obtained in vitro what could range from as low as 10^4 when fratricide is present to larger numbers around 10^7 depending on the strategies used to overcome it.

6.3 Basic properties of the model

6.3.1 Large initial data display unbounded dynamics

Proposition 7. *For any non negative initial data (C_0, L_0, T_0) and all the parameters of the model being positive, the solutions to Eqs. (6.1) exist for $t > 0$, are non negative and unique.*

Proof. The ODE system (6.1) has bounded coefficients and the right hand side of the system is a continuous function of (C, L, T), thus the local existence of solutions follows from classical ODE theory. Since the partial derivatives of the velocity field are continuous and bounded, uniqueness follows from the Picard-Lindelof theorem.

Let us rewrite Eqs. (6.1) when $g = 0$ as

$$\dot{C} = [\rho_C (T + L + C) - 1/\tau_C - \alpha C] C, \tag{6.4a}$$
$$\dot{L} = (\rho_L - \alpha C) L, \tag{6.4b}$$
$$\dot{T} = -(\alpha C) T, \tag{6.4c}$$

then we may write

$$C(t) = C_0 \exp\left(\int_{t_0}^{t}\left[\rho_C T(t') + \rho_C L(t') + (\rho_C - \alpha)C(t') - \frac{1}{\tau_C}\right]dt'\right), \quad (6.5a)$$

$$L(t) = L(t_0)\exp\left(\int_{t_0}^{t}\left(\rho_L - \alpha C(t')\right)dt'\right), \quad (6.5b)$$

$$T(t) = T(t_0)\exp\left(-\int_{t_0}^{t}\alpha C(t')dt'\right), \quad (6.5c)$$

what leads to the positivity of solutions. □

Definition. The sum of all cellular populations studied will be denoted to as $S(t)$, i.e.

$$S(t) = C(t) + T(t) + L(t).$$

Proposition 8. *Let $C(t), L(t), T(t)$ be solutions of Eqs. (6.1) with initial data $C(t_0) = C_0 > 0, L(t_0) = L_0 > 0, T(t_0) = T_0 > 0, S(t_0) = S_0 > 0$. If*

H1 $\rho_C > \alpha$

H2 $(\rho_C - \alpha)\tau_C S_0 > 1$,

then $S(t)$ increases monotonically with time and $\lim_{t\to\infty} S(t) = \infty$.

Proof. Let us first sum the three equations Eq. (6.1) to obtain

$$\frac{dS}{dt} = (\rho_C - \alpha)\, SC - \frac{1}{\tau}C + \rho_L L.$$

Then, the positivity of $L(t)$ implies that, $\underline{S}$ defined as the solution of

$$\frac{d\underline{S}}{dt} = (\rho_C - \alpha)\,\underline{S}C - \frac{1}{\tau}C, \quad (6.6)$$

satisfying $\underline{S}(t_0) = S_0$ is a subsolution of $S(t)$, i.e. satisfying $\underline{S}(t) < S(t), \forall t > t_0$. Obviously, under our hypothesis

$$\left.\frac{d\underline{S}}{dt}\right|_{t=t_0} = \left[(\rho_C - \alpha)\,\underline{S}_0 - \frac{1}{\tau}\right]C_0 > 0,$$

but then, using Eqs. (6.6), this leads to $d\underline{S}/dt > 0$ for all $t > t_0$. Moreover, from Eq. (6.1a) and using that $S(t) > C(t)$, for all $t > t_0$ we get

$$\frac{dC}{dt} = \rho_C SC - \frac{1}{\tau_C}C - \alpha C^2 > \left[(\rho_C - \alpha)\, S - \frac{1}{\tau_C}\right]C, \quad (6.7)$$

where we have used that $\rho_C SC - \frac{1}{\tau_C}C - \alpha C^2 > \rho_C SC - \frac{1}{\tau_C}C - \alpha C\,(C + L + T)$.

This means that $C(t) > C_0$ for any nonzero initial data, then

$$\frac{d\underline{S}}{dt} > (\rho_C - \alpha)\,\underline{S}_0 - \frac{1}{\tau}C_0 \equiv Q_0 > 0, \quad (6.8)$$

then $S(t) > \underline{S}(t) > Q_0 t + S_0$, what proves the unboundedness of the total population $S(t)$, i.e. the fact that $\lim_{t\to\infty} S(t) = \infty$. □

Proposition 9. *(Global existence) Let us consider Eq. (6.4) under the following hypotheses*

H1 *Positive initial data,* $(C_0, L_0, T_0) > 0$.

H2 *All the parameters are positive.*

H3 $(\rho_C - \alpha) < 0$

Then, under these hypotheses the solutions to Eq. (6.4) are global in time (i.e. exist for every $t > 0$*).*

Proof. Hypotheses H1, H2 and Theorem 7 imply that the solutions of Eq. (6.4) are non-negative. Since $(\rho_C - \alpha) < 0$, from Eqs. (6.4) we get

$$\begin{array}{rcll} \dot{C} & = & \left[\rho_C\left(T+L+C\right) - 1/\tau_C - \alpha C\right] C & \leq \rho_C\left(T+L\right) C \\ \dot{L} & = & \left(\rho_L - \alpha C\right) L & \leq \rho_L L \\ \dot{T} & = & -\left(\alpha C\right) T & \leq 0 \end{array}$$

Hence, for every fixed $\bar{t} > 0$ we have $T(t) \leq T_0 := \bar{T}$ and $L(t) \leq L_0 e^{\rho_L \bar{t}} := \bar{L}$. Therefore, $\dot{C} \leq \rho_C(\bar{T} + \bar{L})C$ and this implies $C(t) \leq C_0 e^{\rho_C(\bar{T}+\bar{L})\bar{t}} := \bar{C}$. This means that both the variables $C(t), T(t), L(t)$ and their derivatives are bounded for every fixed $t > 0$. This automatically guarantees that the solutions can be extended forward this point and thus the existence of solutions for every $t > 0$. □

6.3.2 Equilibrium of the model Eqs. (6.1) and local stability analysis

The equilibrium of Eqs. (6.1) in the case of interest $g = 0$, are given by the equations

$$0 = \rho_C\left(T+L+C\right) C - \frac{1}{\tau_C} C - \alpha C^2, \tag{6.10a}$$

$$0 = \rho_L L - \alpha L C, \tag{6.10b}$$

$$0 = -\alpha T C. \tag{6.10c}$$

Eq. (6.10c) leads to either $T = 0$ or $C = 0$. The later leads to $L = 0$ using Eq. (7.9b) and the former to either $L = 0$ or $C = \rho_L/\alpha$. Then using Eq. (7.9a) allows us to obtain the expressions for the three equilibrium points of Eqs. (6.1)

$$E_1 = (0, 0, T_*), \tag{6.11a}$$

$$E_2 = \left(\frac{\rho_L}{\alpha}, \frac{1}{\rho_C \tau_C} + \frac{\rho_L}{\rho_C} - \frac{\rho_L}{\alpha}, 0\right). \tag{6.11b}$$

$$E_3 = \left(\frac{1}{\tau_c\left(\rho_C - \alpha\right)}, 0, 0\right). \tag{6.11c}$$

for any T_*. The Jacobian of the differential equations (6.1) is

$$J = \begin{pmatrix} 2\left(\rho_C - \alpha\right) C - 1/\tau_C + \rho_C\left(T+L\right) & \rho_C C & \rho_C C \\ -\alpha L & \rho_L - \alpha C & 0 \\ -\alpha T & 0 & -\alpha C \end{pmatrix}. \tag{6.12}$$

Let us now use Eq. (7.13) to study the local stability of the different equilibrium given by Eqs. (7.12). First, for E_1 we get

$$J\left(E_1\right) = \begin{pmatrix} \rho_C T_* - 1/\tau_C & 0 & 0 \\ 0 & \rho_L & 0 \\ -\alpha T & 0 & 0 \end{pmatrix}. \tag{6.13}$$

The eigenvalues of $J(E_1)$ are

$$\lambda_1 = 0, \lambda_2 = \rho_L, \lambda_3 = \rho_C T_* - 1/\tau_C, \tag{6.14}$$

thus the equilibrium point E_1 is unstable. For the second equilibrium point we get

$$J(E_2) = \begin{pmatrix} \rho_L\left(\frac{\rho_C}{\alpha} - 1\right) & \rho_C\rho_L/\alpha & \rho_C\rho_L/\alpha \\ -\alpha\left(\rho_L + 1/\tau_C\right)/\rho_C + \rho_L & 0 & 0 \\ 0 & 0 & -\rho_L \end{pmatrix}. \tag{6.15}$$

Thus $\lambda_3 = -\rho_L < 0$ and $\lambda_{1,2}$ satisfy the equation

$$\lambda^2 + \lambda\left(1 - \frac{\rho_C}{\alpha}\right)\rho_L + \rho_L^2\left(1 - \frac{\rho_C}{\alpha}\right) + \frac{\rho_L}{\tau} = 0, \tag{6.16}$$

what leads to the eigenvalues

$$\lambda_\pm = \frac{1}{2}\rho_L\left(\frac{\rho_C}{\alpha} - 1\right) \pm \frac{1}{2}D^{1/2}, \tag{6.17}$$

with the discriminant D being given by

$$\frac{D}{\rho_L^2} = \left(1 - \frac{\rho_C}{\alpha}\right)^2 - 4\left(1 - \frac{\rho_C}{\alpha}\right) - \frac{4}{\rho_L\tau_C}. \tag{6.18}$$

Let us study the case $\rho_C/\alpha < 1$ since the system will be unstable otherwise (Section 6.3.1). Then,

$$0 < 1 - \frac{\rho_C}{\alpha} < 1.$$

Since $(1 - \frac{\rho_C}{\alpha})^2 < 1 - \frac{\rho_C}{\alpha}$, we get

$$\frac{D}{\rho_L^2} < -3\left(1 - \frac{\rho_C}{\alpha}\right) - \frac{4}{\rho_L\tau_C} < 0.$$

Thus, the equilibrium is a stable node-focus.

Finally, for E_3 we get

$$J(E_3) = \frac{1}{\tau_C}\begin{pmatrix} 1 & \frac{\rho_C}{\rho_C - \alpha} & \frac{\rho_C}{\rho_C - \alpha} \\ 0 & \rho_L\tau_c + \frac{\alpha}{\alpha - \rho_C} & 0 \\ 0 & 0 & \frac{\alpha}{\alpha - \rho_C} \end{pmatrix}. \tag{6.19}$$

The eigenvalues of $J(E_3)$ are

$$\lambda_1 = 1/\tau_C > 0, \tag{6.20}$$
$$\lambda_2 = \rho_L\tau_c + \alpha/(\alpha - \rho_C) > 0, \tag{6.21}$$
$$\lambda_3 = \alpha/(\alpha - \rho_C) > 0, \tag{6.22}$$

thus E_3 is an unstable node.

In conclusion, there is only one stable equilibrium point E_2 given by Eqs. (7.12) of node-focus type, which can be an attractor for the dynamics of the system (6.1).

6.4 Results

6.4.1 CAR T cells allow for control of T-cell leukemia in the presence of fratricide

To obtain further insight into the global dynamics of solutions of Eq. (6.1) we simulated different initial data in a set of biologically feasible parameter and initial data regions. In all cases studied, we found an oscillatory behavior of the solutions towards the stable node-focus point E_2 after a fast reduction of the initial normal T cell number.

Figure 6.3 provides a typical example of the dynamics. There we see how the number of cancer cells increase for a short time, typically 10-15 days, while CAR T cells expand. The CAR T cell expansion persists for more than four orders of magnitude in cell number (Figure 6.3 c), with a peak at about 15 days after injection (Figure 6.3 b). This leads to a substantial decrease in leukemic cell load and T-cell aplasia (Figure 6.3 a,b). For this parameter set, cancer was not controlled for long times and relapse was noticeable a few months after the injection date of CAR T cells. After relapse oscillations of leukemic and CAR T cells are observed in their course towards the equilibrium, in this case corresponding to 3×10^8 CAR T cells and 2.7×10^9 leukemic cells. Interestingly, the number of leukemic cells in this case is one order of magnitude smaller than the initial leukemic load (2×10^{10} cells), what supports the possibility of CAR T cells effectively controlling cancer to clinically acceptable levels.

The numerical results used to construct Figure 6.3 c, show that in less than two months after injection, treatment was able to reduce leukemic load from the initial level of 2×10^{10} cells down to a minimum level of 2.59×10^8 cells, i.e. a decrease of about two orders of magnitude.

6.4.2 Higher mitotic stimulation rates improve control of the disease

The asymptotic equilibrium values of leukemic cells and CAR T cells are given by E_2, i.e.

$$L_2 = \frac{1}{\rho_C}\left(\rho_L + \frac{1}{\tau_C}\right) - \frac{\rho_L \rho_C}{\alpha}, \tag{6.23a}$$

$$C_2 = \frac{\rho_L}{\alpha}. \tag{6.23b}$$

Interestingly, the equilibrium level of CAR T cells does not depend on the mitotic stimulation rate ρ_C, but only on the growth and death rates of leukemic cells. However, what matter the most due to their clinical implications are the leukemia equilibrium levels L_2, and the maximum leukemic load $\max_t L(t)$. Maxima would typically be attained in time during the CAR T cell expansion stage.

Let us note that

$$\frac{dL_2(\rho_C)}{d\rho_C} = -\frac{1}{\rho_C^2}\left(\rho_L + \frac{1}{\tau_C}\right) - \frac{\rho_L}{\alpha} < 0, \tag{6.24}$$

this means that $L_2(\rho_C)$ is a monotonically decreasing function. Since $\rho_C \alpha > 0$, the minimum of $L_2(\rho_C)$ over the range $\rho_C \in [0, \alpha]$ would be obtained when $\rho_C = \alpha$. Figure 6.4 confirms that the asymptotic values of L_2 decrease with the mitotic stimulation rate ρ_C and thus larger values of the mitotic stimulation rate lead to better

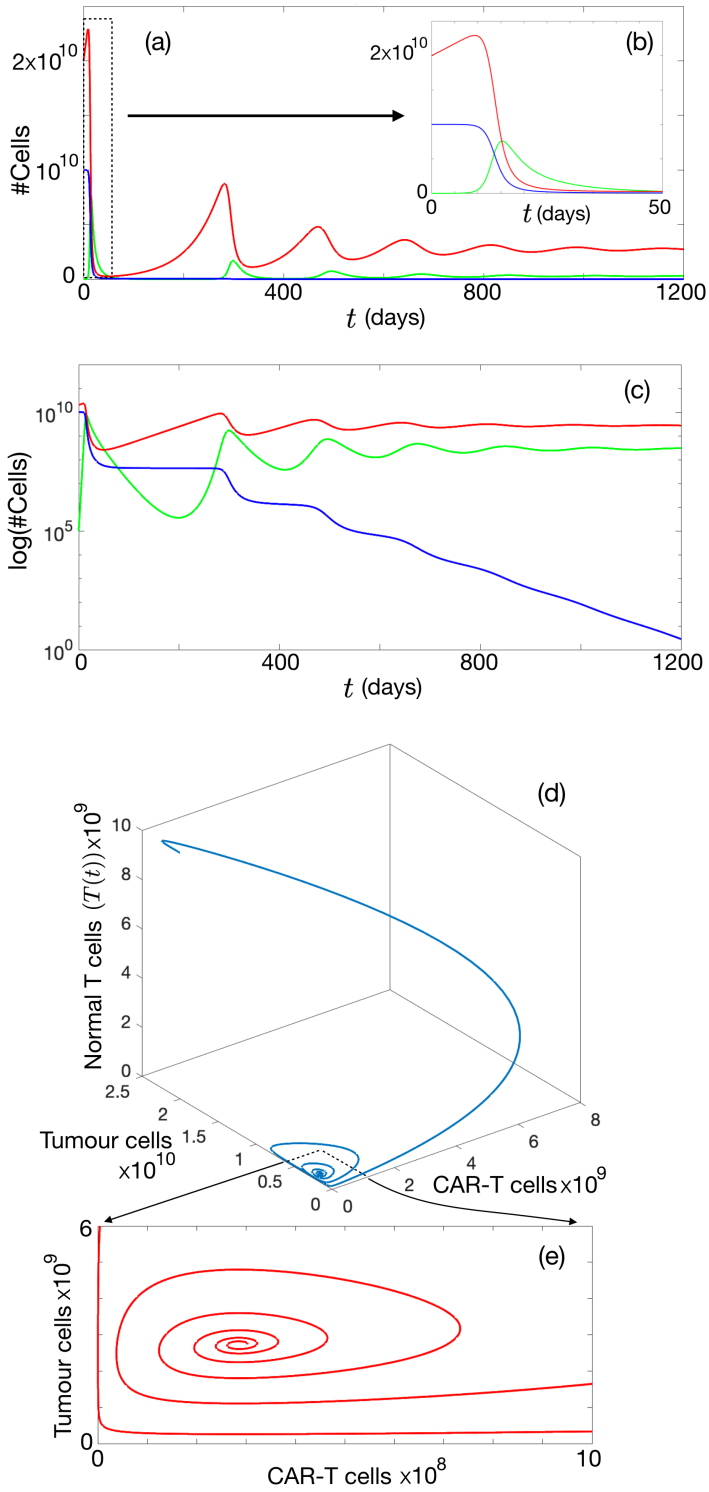

FIGURE 6.3: **Typical dynamics of cell populations ruled by Eq. (6.1).** Results of a simulation are shown for parameter values $\tau_C = 14$ days, $\rho_L = 1/60$ day^{-1}, $\alpha = 5.84 \times 10^{-11}$ day^{-1} cell^{-1}, $\rho_C = \alpha/2$, and initial data $T_0 = 10^9, L_0 = 2 \times 10^9, C_0 = 10^5$ cells. (a-c) Dynamics of the populations of CAR T (green), leukemic (red) and normal T cells (blue). Dynamics are depicted on the intervals of times $t \in [0, 1200]$ (a,c) and $t \in [0, 50]$ (b) , and in linear (a,b) and logarithmic (c) scales. (d) Trajectory of the solution in the phase space. (e) Projection of the selected part of the trajectory on the $(T(t), C(t))$ plane.

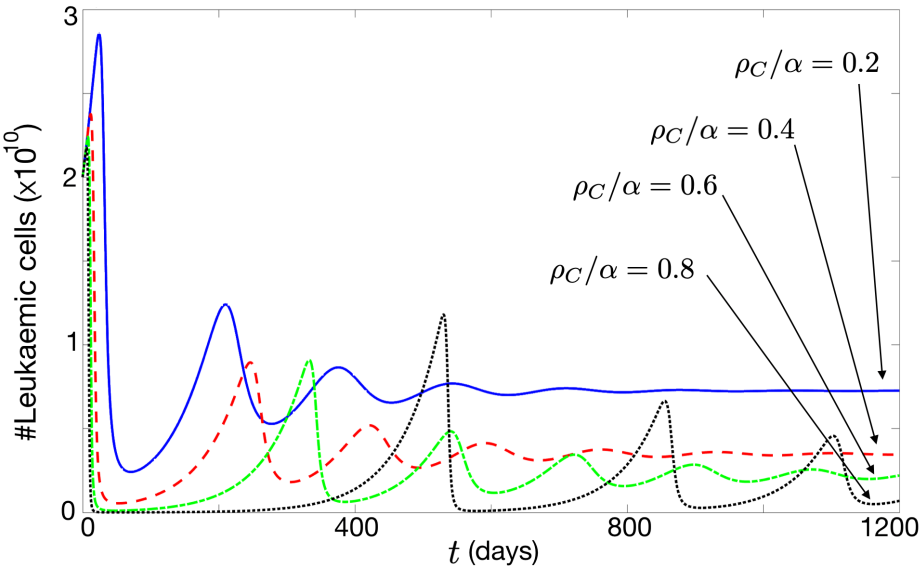

FIGURE 6.4: **Dynamics of leukemic cells considering variations in mitotic rate.** Simulations are ruled by Eq. (6.1) and are shown for initial data $T_0 = 10^9, L_0 = 2 \times 10^9, C_0 = 10^5$ cells, and parameter values $\tau_C = 14$ days, $\rho_L = 1/60$ day^{-1}, $\alpha = 5.84 \times 10^{-11}$ day^{-1} cell^{-1}. The different curves correspond to stimulation rates $\rho_C = 0.2\alpha$ (blue solid line), $\rho_C = 0.4\alpha$ (green red dashed line), $\rho = 0.6\alpha$ (green, dash-dotted line), $\rho = 0.8\alpha$ (black, dotted line).

disease control. However, going beyond $\rho_C = \alpha$ destabilizes the system, as discussed in Section 6.3.1. Thus it may be necessary to control in detail the CAR T manufacturing process to get both high mitotic stimulation rates while at the same time not getting too close to the instability regime.

6.4.3 Initial number of CAR T cells injected does not affect the therapy outcome

Next, we studied the effect of the number of CAR T cells initially injected on the system's dynamics. To do so, we performed an extensive number of simulations over the biologically feasible range and found a very weak dependence of the dynamics on the number of injected CAR T cells. An example is shown in Figure 6.5 for a broad range of cells initially injected ranging from 10^4 to 10^6. Although there was a difference of two orders of magnitude in C_0, it lead to a small variation in the time to peak expansion of a few days, a negligible increase of the maximum CAR T and leukemic cell number and a minor differences in the times to T leukemia relapse.

6.4.4 Contribution of the leukemic growth rate on leukemic cells dynamic

A study of model dynamics under modifications of the leukemic growth rate in whole the feasible range for fast-growing leukemia $\rho_C \in [1/60, 1/20]$ has been performed. The result of typical simulations are shown in Figure 6.6.

The short term dynamics in response to the CAR T injection was found to be qualitatively similar independently of leukemic growth rate, with a peak of leukemic cell number obtained around day 10 post-injection (Figure 6.6 b). Small differences were observed in the peak number of leukemic cells obtained, essentially due to the

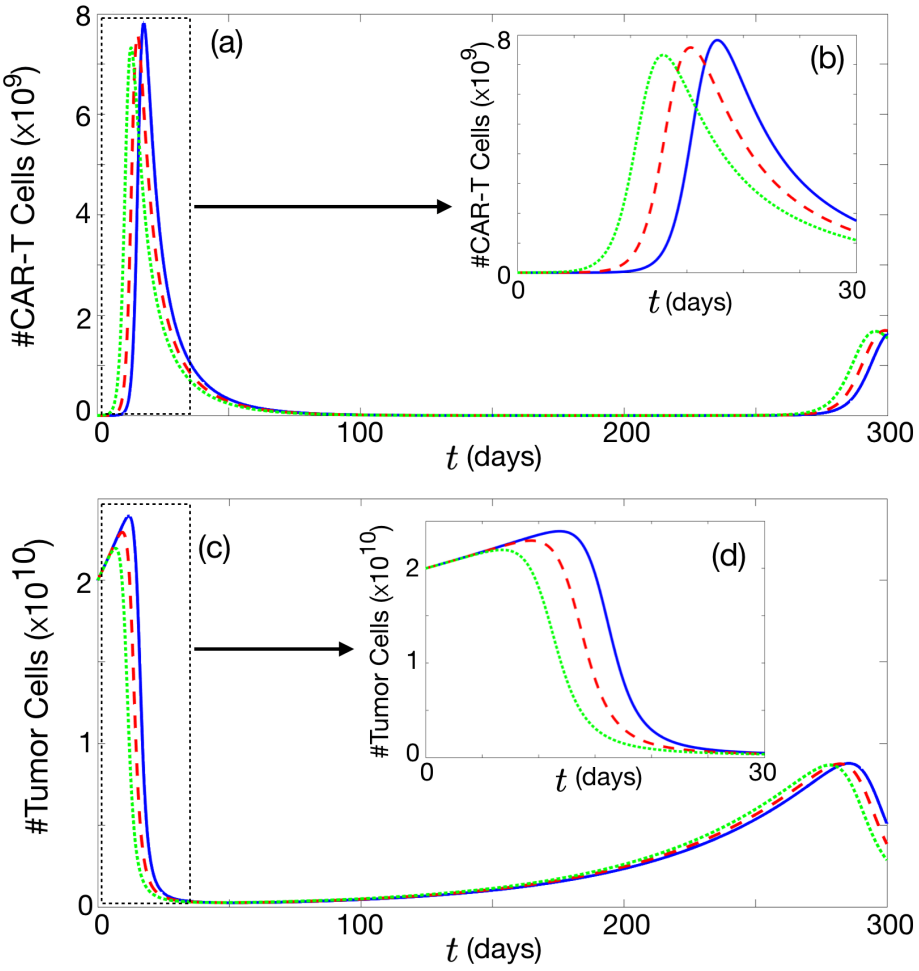

FIGURE 6.5: **Therapy outcome for different initial doses of CAR T cells injected.** Dynamics of the number of CAR T cells (a,b) and leukemic cells (c,d) ruled by Eq. (6.1) over the time range [0,300] days (a,c). We show also the details of the initial response of the treatment over the time interval [0,30] (b,d). Initial data used in the simulations were $T_0 = 10^9, L_0 = 2 \times 10^9$ cells, and parameter values $\tau_C = 14$ days, $\rho_L = 1/60$ day^{-1}, $\alpha = 5.84 \times 10^{-11}$ day^{-1} cell^{-1}. The curves correspond to different values of $C_0 = 10^4$ (blue solid line), $C_0 = 10^5$ (red dashed line), $C_0 = 10^6$ (green dash-dotted line).

fact that faster growing leukemic cells could grow further during the initial CAR T expansion phase. After CAR T cell expansion, there was a response phase for the different leukemic growth speeds and then a relapse was observed (Figure 6.6 a). The relapse time was found to depend on the proliferation rate. This is in line with what one would expect for the amplitude and frequency of oscillations towards the equilibrium point E_2 that are both proportional to ρ_L according to Eq. (6.17).

As expected from the expression for E_2, and the values of the parameters, there was a weak dependence of the number of leukemic cells in the equilibrium on ρ_L in the range of relevance (Figure 6.6 c), given analytically by $L_2 = 1.5289 \times 10^9 + 4.2808 \times 10^9 \rho_L$, with $\rho_L \in [1/60, 1/20]$. Thus the major contribution to the asymptotic leukemic cell count was $L_2 \sim 1/(\rho_C \tau_C)$.

Although the therapy had a substantial effect, logarithmic scale plots (Figure 6.6 d) show the persistence of measurable disease for all times.

Let us define the maximum leukemic cell load reduction achieved by the treatment as

$$R = \max_t (T(t)) \,/\, \min_t (T(t)) \,. \tag{6.25}$$

In the simulations shown in Figure 6.6, this quantity was found to be $R(\rho_L = 1/20) = 65$, $R(\rho_L = 1/30) = 72$, $R(\rho_L = 1/40) = 78$, $R(\rho_L = 1/50) = 82$, $R(\rho_L = 1/60) = 88$, thus always smaller than 100 (two orders of magnitude). It is easy to see that CAR T cells decreased in number with time as it did the leukemic load but they were always above the numbers of cells initially injected. In fact, for most leukemic growth rates the number of CAR T cells was more than one order of magnitude above the level injected.

6.4.5 CAR T cell reinjection does not improve the therapy outcome.

Analogous to B-ALL, an interesting question is whether relapses could be controlled by acting on leukemic cells by reinjection of CAR T cells. We simulated the reinjection of $C = 10^5$ CAR T cells at different times and quantify the variations of maximum leukemic load respect to the case without reinjection after the first relapse. Figure 6.7 shows the results in percentages for different leukemic growth rates in the range $\rho_C \in [1/60, 1/20]$. We have scanned the reinjection time, starting 10 days after the first injection until 300 days later. Small improvements were obtained for slow-growing leukemia, resulted in a negligible reduction (of around 2%). It is even observed that early reinjections may increase the maximum leukemic load at the first relapse (negative percentages).

6.5 Discussion and conclusion

As stated in the introduction, one of the challenges faced by these treatments is the fratricide, i.e. the fact that CAR T cells, belonging to the T cell lineage and expressing common antigens with the leukemic cells would become targets themselves of the therapy. This poses the very interesting question of what would be the outcome of such a therapy, provided that it poses challenges even for CAR T cell production in vitro.

In this study, we have developed a simple mathematical model that captures the difficulties for CAR T cell expansion in vitro, with a limit in cell production given by Eq. (6.3). Thus, the maximum number of CAR T cells that can be produced in vitro depends on the stimulation provided by the cytokines and the excess CAR T killing efficiency over the mitotic stimulation.

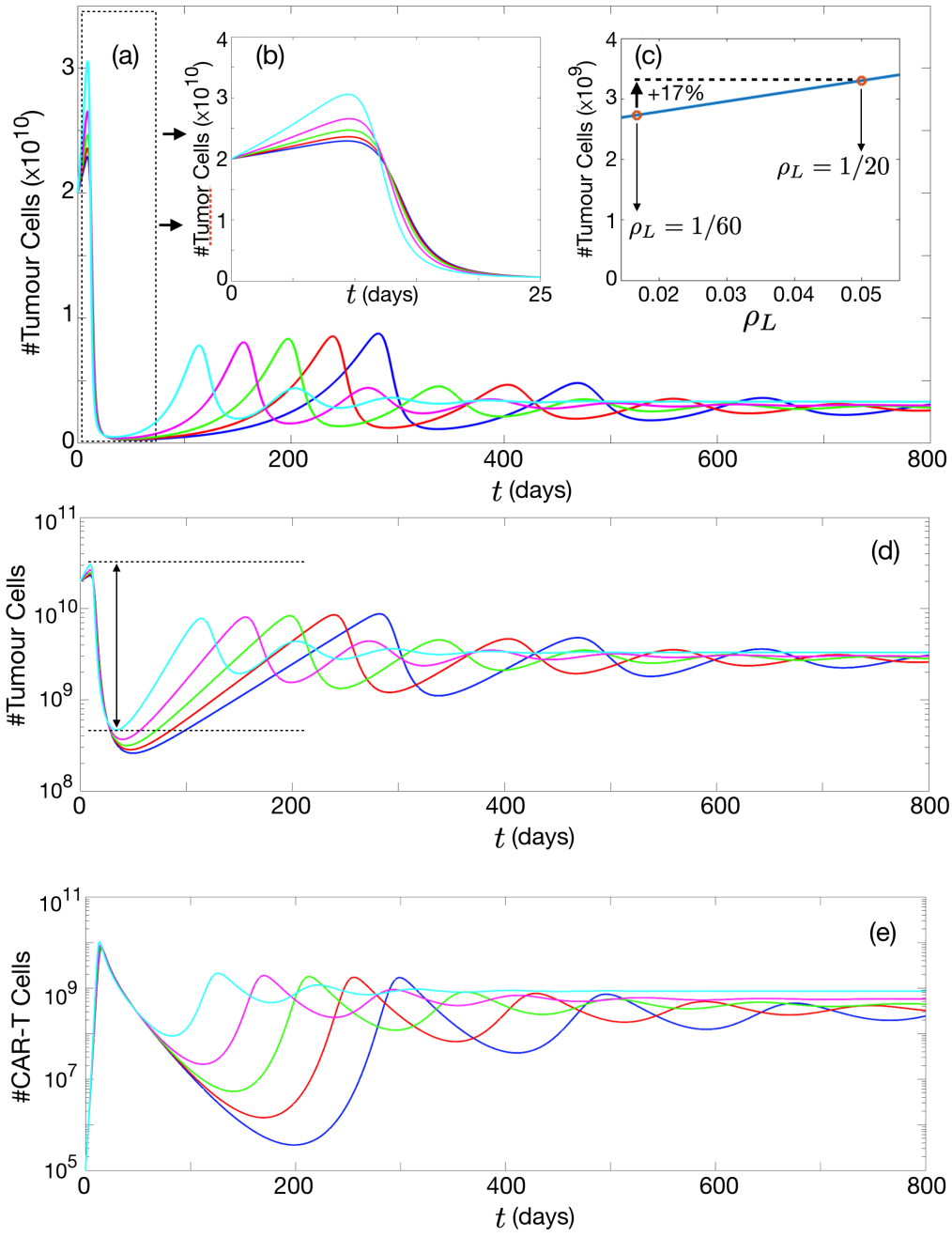

FIGURE 6.6: **Leukemic growth rate effects on initial response, asymptotic values, and time to relapse.** Dynamics of the leukemic population ruled by Eq. (6.1) for initial data $T_0 = 10^9, L_0 = 2 \times 10^9, C_0 = 10^5$ cells, and parameter values $\tau_C = 14$ days, $\alpha = 5.84 \times 10^{-11}$ day^{-1} cell^{-1}, $\rho_C = 0.5\alpha$, for different values of ρ_L. The different curves correspond to different values of $\rho_L = 1/60$ (blue line), $\rho_L = 1/50$ (red line), $\rho_L = 1/40$ (green line), $\rho_L = 1/30$ (magenta line), $\rho_L = 1/20$ (cyan line) (a) Dynamics over the time range [0,800] days. (b) Details of the dynamics for the time interval [0,25]. (c) Dependence of the asymptotic leukemic values obtained from Eq. (6.23a). (d) Leukemic cell number evolution in logarithmic scale. The rate between the maximum and minimum leukemic load is indicated with an arrow for the case $\rho_L = 1/20$. (e) Evolution of the number of CAR T cells.

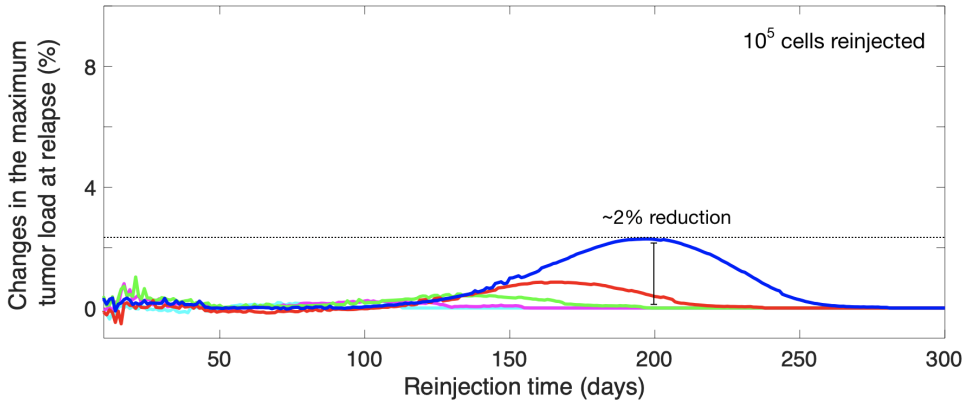

FIGURE 6.7: **CAR T cell reinjection.** The variations of the maximum leukemic load in the first relapse when reinjecting $C = 10^5$ for different reinjection times using initial data $T_0 = 10^9, L_0 = 2 \times 10^9, C_0 = 10^5$ cells, and parameter values $\tau_C = 14$ days, $\alpha = 5.84 \times 10^{-11}$ day^{-1} cell^{-1}, $\rho_C = 0.5\alpha$, for different values of ρ_L. The different curves correspond to different values of $\rho_L = 1/60$ (blue line), $\rho_L = 1/50$ (red line), $\rho_L = 1/40$ (green line), $\rho_L = 1/30$ (magenta line), $\rho_L = 1/20$ (cyan line).

Numerical simulations of the model showed that when they are injected, even in the small numbers that can be obtained in vitro, the CAR T cells find many targets initially on the healthy and leukemic T cells. During this initial stage, the CAR T population is amplified even in the presence of fratricide. We also found in silico that the outcome of the therapy did not depend on the number of CAR T cells injected.

A relapse was always observed in the framework of our model simulations and the number of leukemic T cells was initially reduced by a factor smaller than 100, with the persistence of measurable disease for all times, so that the treatment did not eradicate the disease in our numerical simulations. However, CAR T cells were able to control leukemic growth after two weeks and then, even in spite of the oscillations, the high initial leukemic loads were never found to appear again. Relapse time after the CAR T cell treatment was found to depend strongly on the proliferation rate.

Regarding the question related to CAR T cells re-injection could be beneficial at a given time point, our computational results answer that additional injections do not have any substantial effect on the leukemic cells dynamics. The reason is that CAR T cells decreased in number transiently in time after reaching the peak expansion but their levels were always above the numbers of cells initially injected, typically by more than one order of magnitude. This means that injecting small numbers of CAR T cells in relation to those already present would not contribute to reducing the number of leukemic cells.

The fact that the equilibrium $L_2 \sim 1/(\rho_C \tau_C)$ implies that there are two ways to improve the long-term efficacy of CAR T cell therapy for T-cell leukemia. The first one would be to improve the persistence of the CAR T cells, something that has been done for B-cell leukemia by a using CD19 CAR with lower affinity than FMC63, the high-affinity binder used in many clinical studies (Ghorashian et al., 2019). The second one would be to improve the mitotic stimulation rate, but keeping in mind the restriction $\alpha > \rho_C$.

In conclusion, we have developed a mathematical model of the dynamics of leukemic cells, healthy T cells and CAR T cells, after the therapeutic injection of

the later population. The mathematical model showed the potential of the treatment to control, but nor eradicate, the disease. This would result in a chronification of the disease what could last for long times or buy some time to try alternative therapeutic strategies. Our work is a first simple mathematical attempt to provide light on the potential outcomes of these treatments. There are different types of T-cell malignancies and specifically T-cell leukemia and the particular features of each type could be incorporated in more detailed models incorporating additional biological details.

Chapter 7

Dual-Target CAR Ts in Solid Cancers

7.1 Introduction

Advances in CAR T cell engineering have increased scientific, clinical and commercial interest in adapting this exciting technology for the treatment of solid cancers (Martínez and Moon, 2019). These successes have led to ongoing clinical trials for a variety of cancers, including glioblastomas, gastrointestinal cancers, genitourinary cancers, breast cancers, lung cancers, and others (Bagley and O'Rourke, 2020). However, CAR T cell treatments of solid tumors face significant challenges. The first is the identification of suitable tumor antigens expressed only in cancerous, rather than in healthy cells, i.e., limiting the on-target off-tumor activity of the product (Castellarin et al., 2018). It is also necessary that the antigens selected for the therapy be humanized, to avoid the generation of antibodies that block the CAR T (Hege et al., 2017). Other major issues include T-cell persistence and expansion, T-cell trafficking into tumors, and immune resistance mechanisms that may define the ultimate fate of CAR T cells (Ma et al., 2017).

For these reasons, it is essential to develop strategies to improve the effectiveness of therapy (Hong, Clubb, and Chen, 2020). Combined CAR targeting has been explored as a way to improve antigen recognition and limit the possibility of tumor escape (Han et al., 2019; Rafiq, Hackett, and Brentjens, 2020). Several preclinical studies have evaluated the simultaneous targeting of two tumor-restricted antigens (Hegde et al., 2013; Roybal et al., 2016) and sequential treatments such as CAR T cocktails (Feng et al., 2017). One of the main multi-antigen-targeted CAR T cell therapies under study here is that of dual CAR T cells, where individual T cells are engineered to co-express two separate CARs specific to cognate antigens.

In this chapter we study, in silico, using a mathematical model, the response of a solid tumor to a dual CAR T product targeting both CD19 and a tumor-associated antigen. Our idea, to be explored computationally, is to use B cells expressing the CD19 antigen to amplify the CAR T population in a patient, which may allow for substantially higher levels of CAR T cells to attack the tumor, thus helping to overcome the tumor's immunosuppressive capabilities.

In order to undertake this research, we describe and study two minimal mathematical models describing the response of a solid tumor (GBM) to two different CAR T cell-based treatment strategies. The first describes the effect of a CAR T targeting a tumor antigen in the presence of immune suppression. The second describes the response to dual CAR T cells with one of the CAR groups targeting the tumor antigens and the other targeting CD19, in order to achieve an off-tumor amplification of the product within the patient.

In this work, we take glioblastoma (GBM) as a specific example, but the concept explored here could be applied to different cancer types without substantial modification. Different tumor antigens that have been targeted in CAR T clinical trials in GBM include IL13Rα2, EGFRvIII, and Her2 (Brown, Ebert, and Gargett, 2019). The main obstacles for CAR T therapies in GBM are antigen escape due to tumor immune suppression, heterogeneous expression of identified tumor antigens, and toxicity problems (Bagley et al., 2019; Mostolizadeh, Afsharnezhad, and Marciniak-Czochra, 2018).

The results of trial studies with IL13Rα2 on GBM are encouraging with regard to safety and penetration of CAR T cells (Brown et al., 2015; Brown et al., 2016). Persistence of CAR T cells was observed in that study, as was the fast increase in endogenous immune cells and inflammatory cytokines after each infusion. Also, a study with CAR T cells targeting EGFRvIII showed transient expansion of CAR T cells, and trafficking to the brain and regions of active GBM (O'Rourke et al., 2017). All these results have been used as support to ensure a realistic view in the results.

7.2 Mathematical models

7.2.1 Model of solid tumor response to a CAR T cell treatment in the presence of immune suppression

The first mathematical model to be used in this study describes the competition between a tumor population $T(t)$ and CAR T cells $C(t)$, neglecting spatial aspects and other components of the immune system. In this model we assume that CAR T cells would be amplified only at the tumor site, provided the tumor antigen is specific enough, and thus $C(t)$ would describe the CAR T cell population in the tumor areas. The equations of our model read

$$\frac{dC}{dt} = \frac{\rho_C C T}{g_T + T} - \frac{\alpha_1 C T}{g_C + C} - \frac{1}{\tau_C} C, \tag{7.1}$$

$$\frac{dT}{dt} = \rho_T T - \alpha_2 C T. \tag{7.2}$$

The first term in Equation (7.1) accounts for the stimulation of CAR T cell proliferation after encounters with tumor cells with a rate constant ρ_C and a typical saturation population on the order of g_T (Mahlbacher, Reihmer, and Frieboes, 2019). The second term describes the inactivation of CAR T cells by tumor cells, with a maximal inactivation rate α_1 per tumor cell, and a typical cellular saturation level around g_C CAR T cells. The last term in Equation (7.1) describes the natural death (or inactivation) of activated CAR T cells. Equation (7.2) describes the dynamics of tumor cells, with the first term accounting for the net growth rate (with coefficient ρ_T) and the second accounting for tumor cell killing by the CAR T cells with a rate α_2. In this approach ρ_T measures the difference between the tumor proliferation rate and any natural tumor cell death.

The parameter α_1 describes the strength of CAR T cell inactivation by the tumors. There are many mechanisms leading to T-cell dysfunction in solid tumors. Altered signaling pathways in tumor cells help produce a suppressive tumor microenvironment enriched by inhibitory cells. Metabolic constraints to cell function and survival shape tumor progression and immune cell function. In the face of persistent antigen, chronic T-cell receptor signaling drives T lymphocytes to a functionally exhausted

state (Anderson, Stromnes, and Greenberg, 2018). However, in spite of these difficulties, immune checkpoint blockade (e.g., anti-PD-1, anti-PD-L1, or anti-CTLA-4), designed to amplify endogenous anti-tumor T-cell responses, has revolutionized cancer treatment (Sharma and Allison, 2015; Robert, 2020). In 2011, ipilimumab, the first antibody blocking an immune checkpoint (CTLA-4) was authorized. This was rapidly followed by the development of monoclonal antibodies targeting PD-1 (pembrolizumab and nivolumab) and PDL1 (atezolizumab and durvalumab). The success of this approach was notable in melanoma and non-small-cell lung cancers that often contain numerous genetic mutations (Lawrence et al., 2013). Today, anti-PD-1/PD-L1 antibodies are among the most widely prescribed anticancer therapies and are used as single agents or in combination with chemotherapies as first or second lines of treatment for about 50 cancer types. In line with their mechanisms of action in this paper we assume that immune checkpoint blockade therapies will have a direct effect on α_1 by reducing its value, although the exact reduction is very difficult to quantify. These drugs are not expected to have a major effect on survival as monotherapies in glioblastoma (Reardon et al., 2020); however they could have synergistic effects with the CAR T cells as will be discussed later.

In Equation (7.2) we choose an exponential model to describe glioblastoma growth. This is a standard model, found to be valid for describing this type of tumor growth kinetics (Stensjøen et al., 2015) and has the advantage of having only one adjustable parameter. In addition, it can properly describe tumor relapse from an infiltrative disseminated tumor. More complex growth models can also describe the limited experimental data available (Stensjøen et al., 2015), and the proposed in Section 2. However, for the analysis described in this paper, we keep the simplest form given by Equation (7.2).

Figure 7.1 shows a schematic summary of the biological processes encompassed by our basic mathematical model (7.1-7.2) for the specific case of glioblastoma.

7.2.2 Modeling CAR T cells targeting on-tumor and off-tumor antigens

The second model presented accounts for CAR T cells with dual CAR groups targeting two different antigens. As an example, for the case of GBM the tumor-associated antigen could be IL13Rα2, which is associated with poor prognosis and is overexpressed in >60% of those tumors, but not on normal brain tissue (Stein et al., 2018). This antigen is assumed to be present homogeneously in the population of tumor cells. The second antigen will be expressed by a normal tissue, whose elimination would be assumed to be compatible with life. In this work we think of this second antigen as being CD19, expressed by B cells. However, the same ideas should be applicable to other antigens from a normal cell population whose eradication does not compromise patient survival.

When the therapy is delivered intravenously, CAR T cells are initially amplified upon their encounters with $CD19^+$ cells in peripheral blood and in the bone marrow, and will also trafficking to the tumor sites.

Let $\bar{C}(t)$, $C(t)$, $B(t)$ and $T(t)$ be non-negative time-varying functions considering the number of CAR T cells away from the tumor site, CAR T cells at the tumor site, normal cells expressing the second antigen (in our case, B cells) and tumor cells,

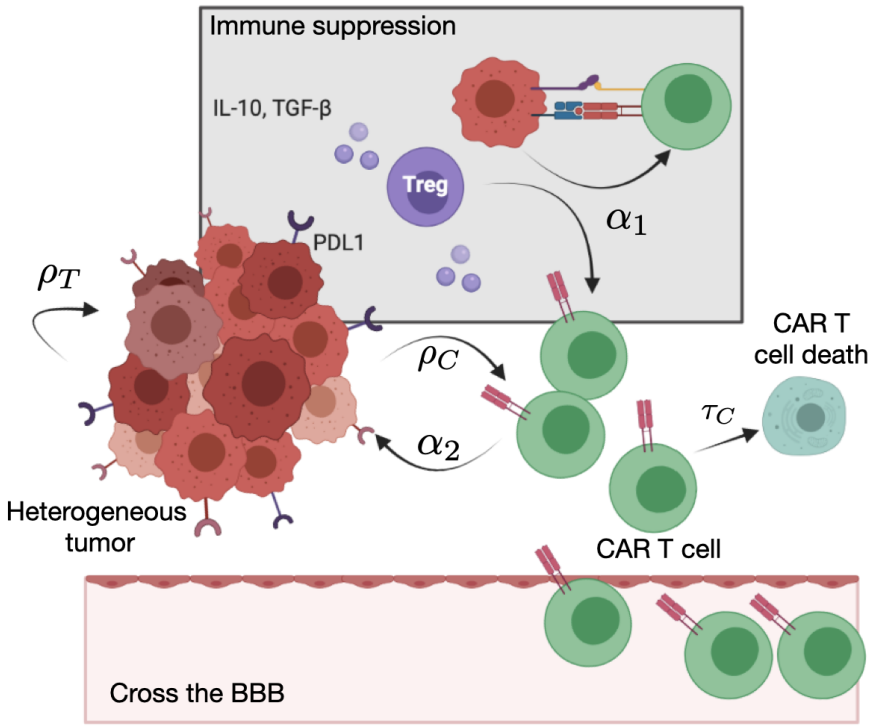

FIGURE 7.1: **Biological processes included in the mathematical model (6.1) for the specific case of glioblastoma**. CAR T cells are stimulated when meeting tumor cells with stimulation parameter ρ_C and undergo apoptosis with a lifetime τ_C. As a result of tumor microenvironment, CAR T cells are inactivated at rate α_2. Tumor cells proliferate with a rate ρ_T and are destroyed via encounters with the CAR T cells with a killing efficiency α_2. Created with BioRender.com.

respectively. A simplified set of equations describing the dynamics of these populations is

$$\frac{d\bar{C}}{dt} = \frac{\rho_{\bar{C}}\bar{C}B}{g_B + B} - \frac{1}{\tau_C}\bar{C} - k\bar{C}, \tag{7.3}$$

$$\frac{dB}{dt} = -\alpha_B B\bar{C} - \frac{1}{\tau_B}B, \tag{7.4}$$

$$\frac{dC}{dt} = k\bar{C} + \frac{\rho_C CT}{g_T + T} - \frac{\alpha_1 CT}{g_C + C} - \frac{1}{\tau_C}C, \tag{7.5}$$

$$\frac{dT}{dt} = \rho_T T - \alpha_2 CT. \tag{7.6}$$

Equations (7.3) and (7.4) describe the off-tumor interaction between CAR T and B cells as in Section 5.2.2. The first term in Equation (7.3) represents B cell induced CAR T proliferation. The second term represents natural cell death, where τ_C is the activated CAR T lifespan. Finally, the term $-k\bar{C}$ represents the trafficking of CAR T cells to brain areas having active GBM cells, where $0 < k < 1$ is the average fraction of CAR T cells crossing the blood-brain barrier (BBB) and infiltrating the tumor site.

The CAR T effect on B-cell growth is included in this model through the term $-\alpha_B B\bar{C}$ in Equation (7.4), which represents the rate of CAR T cell induced B cell death. The mean lifetime of B cells is described by τ_B in the last term of Equation (7.4). In the framework of our simplified approach and in line with other modeling

studies we did not include a source term for newborn B cells in the bone marrow. This is a very good approximation when dealing with the short term dynamics after the injection of the CAR T cells, since new cell production would be orders of magnitude smaller than B cell death. It has been hypothesized in Section 5, that the continuous production of B-cells from $CD19^-$ progenitors could lead to the maintenance of a reservoir of CAR T cells in the bone marrow. This could have an additional positive effect in preventing relapse in B-cell malignancies, but would have no substantial effect in the context studied, since it is highly unlikely that these small populations could migrate to the brain and have any effect on relapse in malignancy.

Equation (7.5) and (7.6) are inspired in the Kuznetsov model (Kuznetsov et al., 1994) and describe the response of effector cells to the growth of tumor cells. The CAR T cells that reach the tumor region, described by Equation (7.5), are stimulated by target cells $T(t)$. The stimulation rate $\rho_C CT/(g_T + T)$ takes into account the increase in CAR T proliferation due to encounters with tumor cells, and has a maximum value of ρ_C as T gets large. CAR T cells are killed or inactivated by tumor cells $T(t)$ with a rate α_1 and are assumed to have a finite lifespan τ_C. Tumor cells (Equation (7.6)) proliferate with a rate ρ_T and die from encounters with CAR T cells with a rate α_2.

Thus, the biological effects governing the dynamics of CAR T cells in this mathematical model are: migration to the tumor site, stimulation by the antigens, natural cell death, and inactivation by the tumor cells. The sum of $\bar{C}(t)$ and $C(t)$ represents the total number of CAR T cells at time t.

7.2.3 Parameter Estimation

The models described have several parameters to be estimated. The maximum mitotic rate ρ_C and $\rho_{\bar{C}}$, related to the stimulation effect of the T cells by the interaction with the targets (CD19 or tumor antigen), will depend on the properties of the CAR T product. These parameters are taken in the range 0.2–0.9 day^{-1} according to the values reported in other models (Stein et al., 2019) and in agreement with the fact that stimulated CAR T cells can undergo a few mitotic divisions per day. For current CAR T products the mean lifetime τ_C of activated CAR T cells is in the range of 1–4 weeks (Ghorashian et al., 2019). To estimate the tumor inactivation rate, we relied on the inhibitory role of PD-1 in immune responses (Carter et al., 2002). A biologically broad range of values has been explored for the maximum tumor inactivation rate α_1 in the range 0.01–0.99 day^{-1}. This number has been estimated from tumor growth data in previous studies. For instance, the c parameter in Radunskaya, Kim, and Woods, 2018 gives roughly $c = 10^{-11}$ day^{-1} $\text{cell}^{-1} \sim \alpha_1/g_C$, which leads to a maximum value of $\alpha_1 \sim 0.05$, taking, for g_C, the typical levels of T cells in blood. The value of α_1 would be substantially smaller, by a factor between 10 and 10^3, under the action of anti-PD-1 treatments (Halkola et al., 2020; Benchaib et al., 2019). The biochemical process of T-cell inactivation by tumor cells could be much faster. Larger values could also be possible biologically, however, we assume that for tumors with very high immunosuppressive capabilities, PD-1 inhibitors could be used as adjuvant treatment to take α_1 into the range of values studied (Khasraw et al., 2020).

Glioblastomas are fast-growing malignant primary brain tumors with proliferation rate ρ_T on the order of several weeks, but have considerable variation in growth rates between individual patients (Stensjøen et al., 2015). Thus, we are take ρ_T to be in the range 0.001–0.2 day^{-1}.

We assume that CAR T cells have similar killing efficiency against both the tumor (α_2) and $CD19^+$ cells (α_B), with values around 10^{-11} day^{-1} (Lee et al., 2015). B-cell

TABLE 7.1: Parameter values for the Equations (7.1)-(7.6).

Parameter	Meaning	Value	Units	Source
ρ_C	Mitotic stimulation of CAR T cells by tumor cells	0.2–0.9	day^{-1}	Stein et al., 2019
g_T	T cell concentration for half-maximal CAR T cell proliferation	10^{10}	cell	Estimated from Stein et al., 2019
α_1	Tumor inactivation rate	0.01–0.99	day^{-1}	Radunskaya, Kim, and Woods, 2018
g_C	CAR T concentration for half-maximal tumor inactivation	5×10^8 -5×10^9	cell	Estimated from Radunskaya, Kim, and Woods, 2018
τ_C	Activated CAR T cell lifetime	7–30	day	Ghorashian et al., 2019
ρ_T	Tumor growth rate	(0.001–0.2)	day^{-1}	Stensjøen et al., 2015
α_2	Killing efficiency of CAR T cells against tumor	$\sim 10^{-11}$	$day^{-1} \times cell^{-1}$	Estimated from Chapter 5
$\rho_{\bar{C}}$	Mitotic stimulation of CAR T cells by CD19	(0.2–0.9)	day^{-1}	Stein et al., 2019
g_B	B-cell concentration for half-maximal CAR T cell proliferation	10^{10}	cell	Estimated from Stein et al., 2019
τ_B	B-lymphocyte lifetime	30–60	day	Fulcher and Basten, 1997
α_B	Killing efficiency of CAR T cells against $CD19^+$ cells	$\sim 10^{-11}$	$day^{-1} \times cell^{-1}$	Estimated from Lee et al., 2015

lymphocyte lifetime τ_B is known to be about 5–6 weeks (Fulcher and Basten, 1997). We assume that in dual therapy, CAR T cells are injected after lymphoid depletion treatment to promote expansion of CAR T by stimulation with B cells, as usual. We set the initial number of B lymphocytes to be 2.5 $\times 10^{10}$ to account for the effect of this treatment as in Sections 5.2.3 and 6.2.2.

Finally, the values of g_T and g_B indicate the inflection points from which the rate of stimulation of CAR T cells increases, and are related to the antigen levels. These values have been estimated in previous studies by adjusting the data in experiments with mice (Kuznetsov et al., 1994). In our case, because of the lack of experimental results on the dual CAR Ts proposed here, they were estimated using the Equations (7.1) and (7.2) and the results obtained in Stein et al., 2019 (stimulation rate, the maximum of transgenic copies of tisagenlecleucel, and the time of peak expansion of CAR T cells). To do so, we neglected the immune suppression term, which is not present in leukemia, and the parameters related to the type of cancer were chosen as in Chapter 5. Values of g_T and g_B around 1–2 $\times 10^{10}$ cell were obtained.

A summary of the model parameters and their numerical values is given in Table 7.1.

7.3 Basic properties of the mathematical models

7.3.1 Mathematical model Eqs. (7.1–7.2)

Existence and uniqueness of positive solutions

Theorem 1. For any non-negative initial data (C_0, T_0) and with all the parameters of the model being positive, the solutions to Eqs. (7.1–7.2) exist for $t > 0$, are non-negative and unique.

Proof. The ODE system (7.1–7.2) has bounded coefficients and the right hand side of the system is a continuous function of (C, T) in the domain $\mathrm{R}^2_{+,0}$, thus the local existence of solutions follows from classical ODE theory. Since the partial derivatives of the velocity field are continuous and bounded, uniqueness follows from the Picard-Lindelof theorem.

Rewrite Eqs. (7.1–7.2) as

$$\dot{C} = \left[\frac{\rho_C T}{g_T + T} - \frac{\alpha_1 T}{g_C + C} - 1/\tau_C\right] C, \tag{7.7a}$$

$$\dot{T} = (\rho_T - \alpha_2 C)\, T, \tag{7.7b}$$

then we may write

$$C(t) = C_0 \exp\left(\int_{t_0}^{t} \left[\frac{\rho_C T(t')}{g_T + T(t')} - \frac{\alpha_1 T(t')}{g_C + C(t')} - \frac{1}{\tau_C}\right] dt'\right), \tag{7.8a}$$

$$T(t) = T_0 \exp\left(\int_{t_0}^{t} (\rho_T - \alpha_2 C(t'))\, dt'\right), \tag{7.8b}$$

which leads to the positivity of solutions. □

Equilibria and local stability analysis

The equilibria of Eqs. (7.1–7.2) are given by the equations

$$0 = \left[\frac{\rho_C T}{g_T + T} - \frac{\alpha_1 T}{g_C + C} - 1/\tau_C\right] C, \tag{7.9a}$$

$$0 = [\rho_T - \alpha_2 C]\, T, \tag{7.9b}$$

Eq. (7.9b) leads to either $T = 0$ or $C = \rho_T/\alpha_2$. Using $T = 0$ and Eq. (7.9a) we obtain $C = 0$. Then using $C = \rho_T/\alpha_2$ and Eq. (7.9a) allows the quadratic expressions for T to be obtained,

$$\alpha T^2 + T(\alpha g_T - \rho_C + 1/\tau_C) + g_T/\tau_C = 0, \tag{7.10}$$

where $\alpha = \frac{\alpha_1}{g_C + \rho_T/\alpha_2}$. The solutions of Eq. (7.10) are

$$T^*_{1,2} = \frac{-(\alpha g_T - \rho_C + 1/\tau_C) \pm \sqrt{(\alpha g_T - \rho_C + 1/\tau_C)^2 - 4\alpha g_T/\tau_C}}{2\alpha}, \tag{7.11}$$

where the discriminant is non-negative and the solutions are real and positive in the case: *i)* $\rho_C \geq (\sqrt{\alpha g_T} + \sqrt{1/\tau_C})^2$.

The equilibrium points of the system under these conditions are

$$E_1 = (0,0), \tag{7.12a}$$
$$E_{2,3} = (\frac{\rho_T}{\alpha_2}, T^*_{1,2}). \tag{7.12b}$$

In the particular case $\rho_C = (\sqrt{\alpha g_T} + \sqrt{1/\tau_C})^2$, there are only two equilibria since $E_2 = E_3 = (\frac{\rho_T}{\alpha_2}, \frac{1}{\sqrt{\alpha g_T \tau_C}})$.

The Jacobian of the differential equations (7.1–7.2) is

$$J = \begin{pmatrix} \frac{\rho_C T}{g_T+T} - 1/\tau_C - \frac{\alpha_1 TC}{(g_C+C)^2} & \frac{\rho_C g_T C}{(g_T+T)^2} - \frac{\alpha_1 C}{g_C+C} \\ -\alpha_2 T & \rho_T - \alpha_2 C \end{pmatrix}. \tag{7.13}$$

Let us now use Eq. (7.13) to study the local stability of the different equilibria given by Eqs. (7.12). First, for E_1 we get

$$J(E_1) = \begin{pmatrix} -1/\tau_C & 0 \\ 0 & \rho_T \end{pmatrix}. \tag{7.14}$$

The eigenvalues of $J(E_1)$ are

$$\lambda_1 = -1/\tau_C, \lambda_2 = \rho_T. \tag{7.15}$$

thus the equilibrium point E_1 is unstable. For the other equilibrium points the Jacobian matrices are cumbersome and do not allow simple information on the stability of the equilibria to be obtained. This is why we studied the phase space of the system in the two-dimensional phase space of cancer cells and CAR T cells. Figure 7.2 shows the trajectories for different initial conditions and a typical parameter choice.

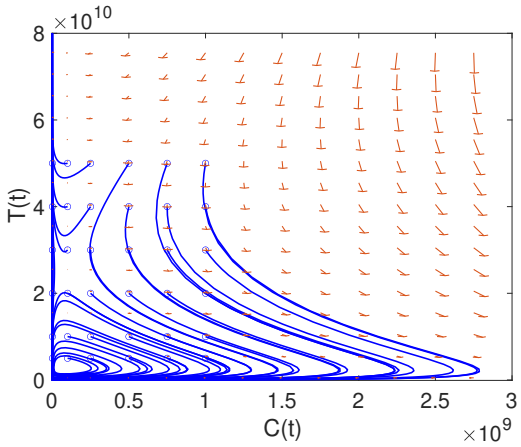

FIGURE 7.2: **Phase space of model equations (7.1–7.2).** Some dynamics are represented as trajectories in the two-dimensional space (C(t),T(t)) (CAR T cells, tumor cells) for default parameter values $\tau_C = 7$ days, $\rho_C = 0.9$ day^{-1}, $\rho_T = 1/50$ day^{-1}, $\alpha_1 = 0.04$ day^{-1} cell^{-1}, $\alpha_2 = 2.5 \times 10^{-10}$ day^{-1} cell^{-1}, $g_T = 10^{10}$ and $g_C = 2 \times 10^9$.

In the particular case depicted in Figure 7.2, we computed numerically the eigenvalues of the Jacobian matrix on the three fixed points and found that $E_1 = (0,0)$ was unstable (as expected). We obtained that $E_2 = (\rho_T/\alpha_2, T^*_1)$ had real eigenvalues, one of them positive, and thus was also an unstable point and $E_3 = (\rho_T/\alpha_2, T^*_2)$ was

found to be an unstable spiral with two complex eigenvalues with a positive real part.

7.3.2 Mathematical model Eqs. (7.3–7.6)

Existence and uniqueness of positive solutions

Theorem 2. For any non-negative initial data $(\bar{C}_0, B_0, C_0, T_0)$ and with all the parameters of the model being positive, the solutions to Eqs. (7.3–7.6) exist for $t > 0$, are non-negative and unique.

Proof. We analyze the behavior of the vector field to prove the non-negativity of the solutions. Let $F = F(x) = \frac{dx}{dt}$ be the vector field of the system (7.3–7.6) with solutions $x = (\bar{C}(t), B(t), C(t), T(t))$. Starting from the positive initial condition $(\bar{C}_0, B_0, C_0, T_0)$, we study the direction of the vector field F at hyper-surfaces $\bar{C} = 0$, $B = 0$, $C = 0$ and $T = 0$. Let n_i be the normal unit vector in the negative direction to plane $x_i = 0$, for $i = 1, 2, 3, 4$ (i.e, $n_1 = (-1, 0, 0, 0)$, $n_2 = (0, -1, 0, 0)$, ..., $n_4 = (0, 0, 0, -1)$) and consider the scalar products $F \cdot n_i$. Then, $F \cdot n_1 = 0$, $F \cdot n_2 = 0$ and $F \cdot n_4 = 0$ at hyper-surfaces $\bar{C} = 0$, $B = 0$ and $T = 0$, respectively. Then, the hyper-surfaces $\bar{C} = 0$, $B = 0$ and $T = 0$ are invariant. In the case of hyper-surface $C = 0$ it is found that $F \cdot n_3 = -k\bar{C} < 0$. Hence, $\mathrm{R}^4_{+,0}$ is a positive invariant domain for Eqs. (7.3–7.6). Therefore, we have proved the non-negativity of solutions $(\bar{C}(t), B(t), C(t), T(t))$.

Since the ODE system (7.3–7.6) has non-negative solutions and the right-hand side of the system is a continuous function of $(\bar{C}, B, C, T)$ in the domain $\mathrm{R}^4_{+,0}$, the existence of solutions follows form the Cauchy-Peano theorem. Moreover, the partial derivatives of the velocity field are also continuous and bounded in $\mathrm{R}^4_{+,0}$. Then, using the Picard-Lindelof theorem we have proved the uniqueness of solutions. □

Equilibrium and local stability analysis

We begin by calculating the fixed points and determining their stability. These are the points $E_1 = (0, 0, 0, 0)$ and $E_2 = (0, 0, \frac{\rho_T}{\alpha_2}, T^*_{1,2})$, where $T^*_{1,2}$ corresponds to the point previously calculated in Eq. 7.11. To analyze the stability of these points, we calculate the Jacobian matrix of Eqs.(7.3–7.6)

$$J = \begin{pmatrix} \frac{\rho_C B}{g_B + B} - 1/\tau_C - k & \frac{\rho_C \bar{C} g_B}{(g_B+B)^2} & 0 & 0 \\ -\alpha_B B & -\alpha_B \bar{C} - 1/\tau_B & 0 & 0 \\ k & 0 & \frac{\rho_C T}{g_T+T} - 1/\tau_C - \frac{\alpha_1 TC}{(g_C+C)^2} & \frac{\rho_C g_T C}{(g_T+T)^2} - \frac{\alpha_1 C}{g_C+C} \\ 0 & 0 & -\alpha_2 T & \rho_T - \alpha_2 C \end{pmatrix}.$$

For the equilibrium point $E_1 = (0, 0, 0, 0)$, the Jacobian matrix is

$$J = \begin{pmatrix} -1/\tau_C - k & 0 & 0 & 0 \\ 0 & -1/\tau_B & 0 & 0 \\ k & 0 & -1/\tau_C & 0 \\ 0 & 0 & 0 & \rho_T \end{pmatrix}.$$

and the eigenvalues are $\lambda_1 = -(k + 1/\tau_C)$, $\lambda_2 = -1/\tau_B$, $\lambda_3 = -1/\tau_C$ and $\lambda_4 = \rho_T$. Thus, E_1 is an unstable equilibrium point. The study of the stability of E_2 is similar to its analogue in the case of Eqs.(7.1–7.1), where a simple analytical expression for the eigenvalues cannot be obtained.

7.4 Results (I): Therapy outcomes under immune suppression using CAR T cells with a single CAR group targeting a tumor antigen.

7.4.1 A high level of immune suppression prevents in-patient expansion of CAR T cells

Firstly, we studied the effect of the immunosuppressive strength of tumor cells as measured by α_1, on the dynamics of model Equations (7.1) and (7.2). Note that in Equation (7.1), the term proportional to α_1 represents CAR T cell growth inhibition. When immune suppression is neglected, i.e., $\alpha_1 = 0$, an initial condition C_0 can always be found such that the treatment leads to an initial reduction of the total number of tumor cells, i.e., $T(t)$ would initially decrease, allowing for tumor control over long times. Using Equation (7.2) and the condition $dT/dt < 0$ it is easy to find that the condition for the therapy to be initially effective is $C(t) > \rho_T/\alpha_2$.

Figure 7.3 a,c provides an example of an effective therapy in the absence of tumor-mediated immune suppression. An initial dose of $C_0 = 8 \times 10^7$ CAR T cells sufficed to reduce the tumor load below observable limits in a few weeks.

Next, we studied the tumor response to CAR T cell infusion in the presence of tumor immune suppression, i.e., for values of $\alpha_1 > 0$. Tumor control was also obtained for small α_1 values (see Figure 7.3 a,c), where the CAR T population overcame the immune suppression and grew, promoting the death of a large number of tumor cells. The expansion of the CAR T cell population was slower than for $\alpha_1 = 0$ and the reduction of the tumor load also occurred on longer time scales, but tumor control was also achieved in this situation, with low α_1 values corresponding to tumors with low immunosuppressive capability.

We can also see in Figure 7.3 b,d that when the value of the immune suppression parameter was increased beyond the threshold $\alpha_1 > 0.03$, the tumor and CAR T cell dynamics changed substantially. In that situation, CAR T cells could not expand in vivo and no longer controlled the disease, and the tumor continued growing after treatment infusion.

The threshold of α_1, below which the tumor dynamics were controlled by the treatment, was also found to be dependent on the value of the saturation parameter g_C, as shown in Figure 7.4.

Our choice of seven days to study the response was motivated by the observations of Brown et al., 2016 where CAR T cells were detected in the CSF after each intraventricular administration for a maximum of seven days. Similar thresholds are obtained in our analysis for values between four and seven days.

7.4.2 Initial number of CAR T cells injected affects the outcome of the therapy

Next, we studied the effect of the number of CAR T cells initially injected on the system's dynamics for the case of CAR T cells targeting only the on-tumor antigen. To do so, we performed an extensive number of simulations of Equations (7.1) and (7.2) over the biologically feasible range of parameters. We found a dependence of the dynamics on the number of injected CAR T cells. Results shown in Figure 7.5 present some examples for numbers of cells initially injected ranging from 5×10^7 to 7×10^8 cells.

There were two different types of dynamics in the tumor response depending on the initial choice of C_0. For the parameters listed in Figure 7.5, there was a qualitative

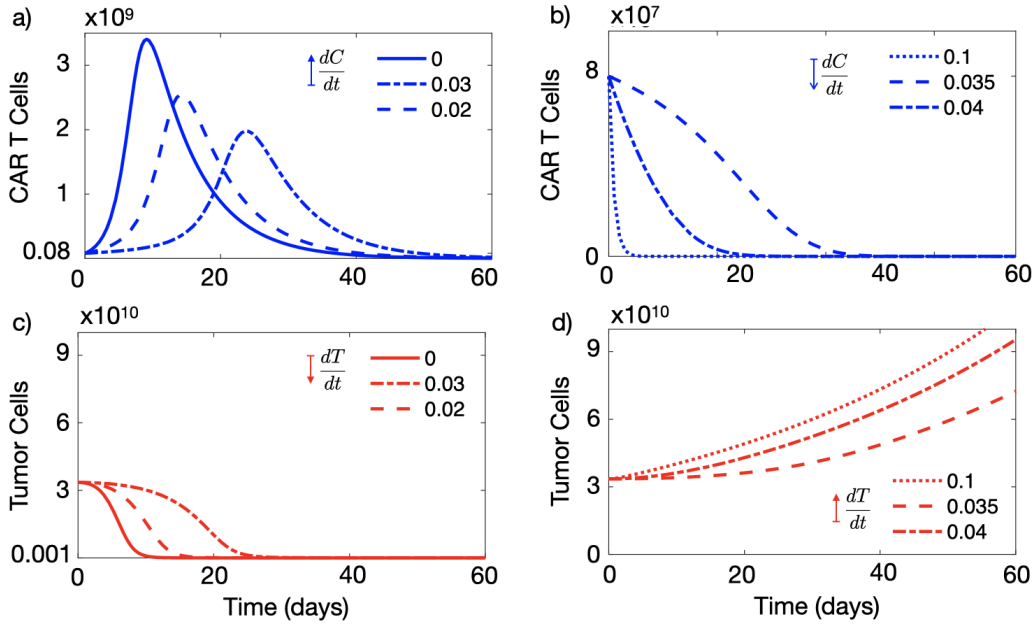

FIGURE 7.3: **Tumor immune suppression governs the expansion of CAR T cells in silico.** Dynamics of the number of CAR T (blue curves) and tumor cells (red curves) governed by Equations (7.1) and (7.2) in different immune suppression scenarios. Subplots (a) and (c) show the results for $\alpha_1 = 0$ (solid lines), $\alpha_1 = 0.02$ day^{-1} (dashed lines) and $\alpha_1 = 0.03$ day^{-1} (dash-dotted lines) and subplots (b) and (d) for $\alpha_1 = 0.035$ day^{-1} (dashed lines), $\alpha_1 = 0.04$ day^{-1} (dash-dotted lines) and $\alpha_1 = 0.1$ day^{-1} (dotted lines). Initial data used in the simulations $C_0 = 8 \times 10^7$ cells, $T_0 = 3.35 \times 10^{10}$ cells and parameter values $\tau_C = 7$ days, $\rho_C = 0.9$ day^{-1}, $\rho_T = 1/50$ day^{-1}, $\alpha_2 = 2.5 \times 10^{-10}$ day^{-1} cell^{-1}, $g_T = 10^{10}$ and $g_C = 2 \times 10^9$.

change in the dynamics around $C_0 = 2 \times 10^8$ cells. Thus, small doses of CAR T cells led only to a small reduction in the tumor load (Figure 7.5 a), while for doses larger than this threshold, the therapy was able to control tumor growth in silico (see Figure 7.5 b). The threshold was found to be related to the particular choice of parameter values and would change under different conditions.

This dynamic differs from what happens in leukemia in which the outcome does not depend on the number of cells injected. This is mainly due to the immune suppression capabilities of solid tumors included in our model equations.

7.4.3 Injection of a large number of CAR T cells could allow for cure or prolonged tumor control in the presence of immune suppression

Next, we used the mathematical model as a tool to tackle the problem of tumor immune suppression against CAR T and explored different CAR T cell treatment strategies in silico. As a first test, we increased the dose of the CAR T product with respect to that used in Figure 7.5 to 4×10^8 cells injected. Figure 7.6 a shows that in that situation and with a tumor immune suppression rate of $\alpha_1 = 0.04$ day^{-1} it was possible to obtain a significant reduction in the number of tumor cells, of more than four orders of magnitude, lasting for six months, which could either be compatible with cure or could provide a window of opportunity for the application of other therapies.

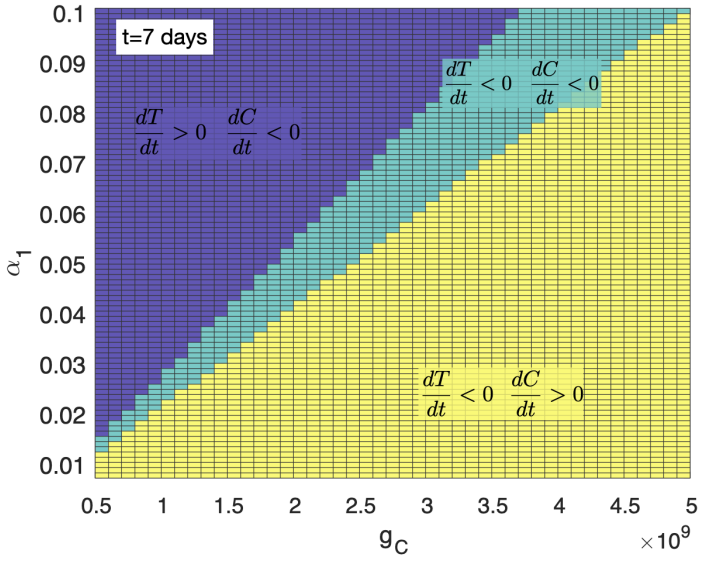

FIGURE 7.4: **Parameter regions of control of the tumor growth dynamics seven days after infusion as a function of α_1 and g_C.** Yellow areas show the parameter areas in which $dT/dt < 0, dC/dt > 0$, i.e., tumor was reducing its size and CAR T cell population increasing after seven days. Green areas are those in which $dT/dt < 0, dC/dt < 0$ after seven days, thus the tumor mass was reducing its size but the CAR T cell was being destroyed by the cancer cells' immune suppression corresponding to transient effect of the therapy. Purple regions are those in which $dT/dt > 0, dC/dt < 0$. Thus, the tumor was increasing its size and the CAR T cell population decreasing after seven days, leading to therapy failure. Initial data used in the simulations were $C_0 = 8 \times 10^7$, $T_0 = 3.35 \times 10^{10}$ and parameter values $\tau_C = 7$ days, $\rho_C = 0.9$ day^{-1}, $\rho_T = 1/50$ day^{-1}, $\alpha_2 = 2.5 \times 10^{-10}$ day^{-1} cell^{-1}, $g_T = 10^{10}$.

However, the same figure shows that higher levels of immune suppression ($\alpha_1 = 0.07$ day^{-1} and $\alpha_1 = 0.1$ day^{-1}) led to the failure of the therapy and a continuous increase in the population of cancerous cells. Higher doses of CAR T would have to be injected at these rates of immune suppression to achieve control of the disease. Figure 7.8 c shows that for $\alpha_1 = 0.1$ day^{-1} increasing the dose above 1.5×10^9 cells, led again to disease control.

This means that, even with immune suppression active, achieving very high levels of CAR T cells could allow the tumor defenses to be overcome, and the tumor to be defeated. However, achieving such an initial high doses is practically unfeasible. Section 7.4.5 will discuss how to achieve those large CAR T cell doses without having to infuse them externally.

7.4.4 A high initial tumor load favors CAR T cell expansion

Surgical resection is performed regularly as an up-front therapy in different cancer types. For glioblastoma, it is part of the standard treatment as it helps to rapidly reduce mass effect and neurological symptoms. The initial tumor load plays a dual role. On the one hand, a high tumor load would favor the initial expansion of the CAR T cells, but on the other, it may enhance tumor immune suppression. Thus the

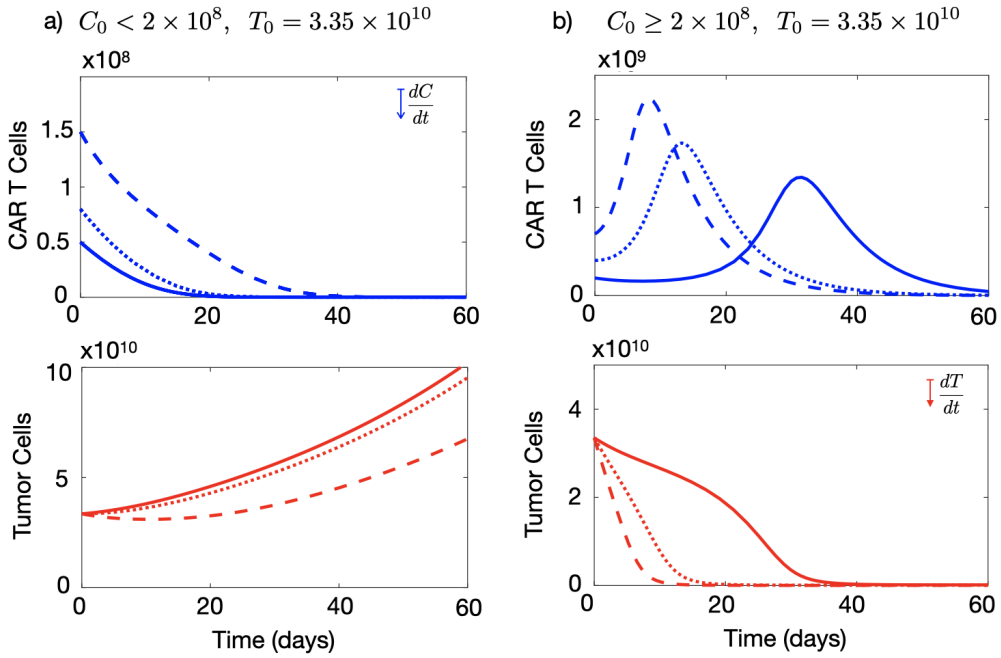

FIGURE 7.5: **Injection of large numbers of CAR T cells allows immune suppression effects of solid tumors to be overcome in silico.** Longitudinal dynamics of the total number of CAR T (blue) and tumor cells (red) ruled by Equations (7.1) and (7.2). The curves correspond to different values of CAR T cells injected into a patient bearing a number of $T_0 = 3.35 \times 10^{10}$ tumor cells. (a) CAR T cell dynamics for $C_0 = 5 \times 10^7$ (solid line), $C_0 = 8 \times 10^7$ (dotted line), $C_0 = 1.5 \times 10^8$ (dashed line). (b) Longitudinal dynamics of the CAR T cells for $C_0 = 2 \times 10^8$ (solid line), $C_0 = 4 \times 10^8$ (dotted line) and $C_0 = 7 \times 10^8$ (dashed line). The parameter values used in the simulations were $\tau_C = 7$ days, $\rho_C = 0.9$ day^{-1}, $\rho_T = 1/50$ day^{-1}, $\alpha_1 = 0.04$ day^{-1} cell^{-1}, $\alpha_2 = 2.5 \times 10^{-10}$ day^{-1} cell^{-1}, $g_T = 10^{10}$ and $g_C = 2 \times 10^9$.

question arises of what would be the optimal approach to use CAR T cell treatments in combination with surgical resections.

To shed some light on the question, we computationally explored the idea of using CAR T cells after performing a partial surgical resection of the tumor, a frequent situation in the context of brain tumors. In that scenario one would start treatment with a hypothetical first-line therapy with CAR T cells, with a substantially smaller initial number of cancer cells. Assuming that the tumor load has been reduced to 20% of the initial one shown in Figure 7.6 a, Figure 7.6 b shows the dynamics of CAR T and tumor cells for $T_0 = 6.7 \times 10^9$ maintaining a low dose of CAR T, $C_0 = 8 \times 10^7$. The decrease in the initial tumor load led to lower stimulation of the CAR T cells and therapy failure even for tumors with low immune suppression capabilities ($\alpha_1 = 0.04$ day^{-1}). However, tumor relapse could be controlled by the CAR T cells in those tumors. Some additional tumor decrease was possible in the cases of greater immune suppression ($\alpha_1 = 0.07$ day^{-1} and $\alpha_1 = 0.1$ day^{-1}) by increasing the initial CAR T cell dose, as Figure 7.6 c shows. In that case, transient tumor stabilization was achieved lasting for several weeks, although the final outcome was the same as in Figure 7.6 a.

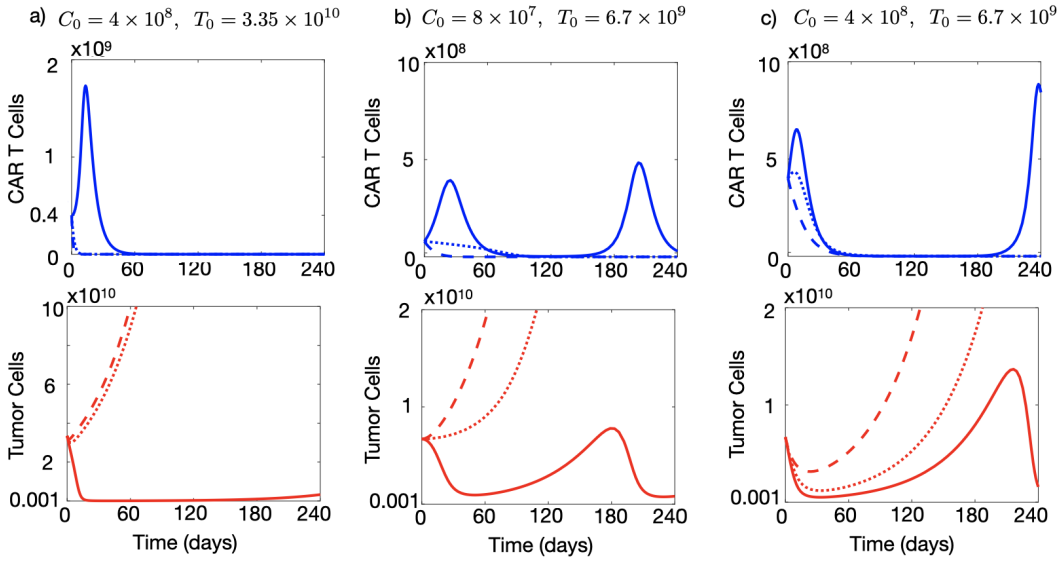

FIGURE 7.6: **Simulated tumor and CAR T dynamics under different initial conditions for the number of injected cells and initial tumor load.** Dynamics of the number of CAR T cells (blue curves) and tumor cells (red curves) governed by Equations (7.1) and (7.2) in three different scenarios of immune suppression: $\alpha_1 = 0.04$ day^{-1} (solid lines), $\alpha_1 = 0.07$ day^{-1} (dotted lines) and $\alpha_1 = 0.1$ day^{-1} (dashed lines). Parameter values used in the simulations $\tau_C = 7$ days, $\rho_C = 0.9$ day^{-1}, $\rho_T = 1/50$ day^{-1}, $\alpha_2 = 2.5 \times 10^{-10}$ day^{-1} cell^{-1}, $g_T = 10^{10}$ and $g_C = 2 \times 10^9$.

7.4.5 Results (II): Therapy outcomes under tumor immune suppression using CAR T cells with dual CAR groups with on- and off-tumor activity

7.4.6 CAR T cells with two targets provided long-time tumor control advantages in silico

We performed long-term simulations of Equations (7.1) and (7.2) with parameters as in Figure 7.6 a and $\alpha_1 = 0.04$ day^{-1}, corresponding to weak immune suppression. In this case, we observed the relapse of the disease in silico (see Figure 7.7 a) around eight months after infusion. Tumor growth continued for several months leading to disease progression, while CAR T cells were exhausted approximately 4 months before relapse.

However, when repeating the same simulation using model Equations (7.3)–(7.6), i.e., when using the CAR T cells with two targets, substantially improved disease control was observed in silico. Results are summarized in Figure 7.7 b. The interaction between the CAR T cells in peripheral blood and the B cells stimulated the proliferation of the CAR T cells and lead to an increased flow of these cells towards the tumor. In this case, we observe an improved expansion of the initial CAR T cells delivered and persistence of the CAR T product in the tumor tissue for longer times. Thus, by overcoming the tumor immunosuppressive environment, the proposed use of dual CAR Ts could lead to improved tumor control. Figure 7.7 b also shows the results when applying dual CAR T therapy in more immunosuppressive tumors, where single-target therapy would have failed. Thus, the use of dual target CAR T with on- and off-tumor activity showed substantially improved anti-tumor activity in comparison with the single-target CARs.

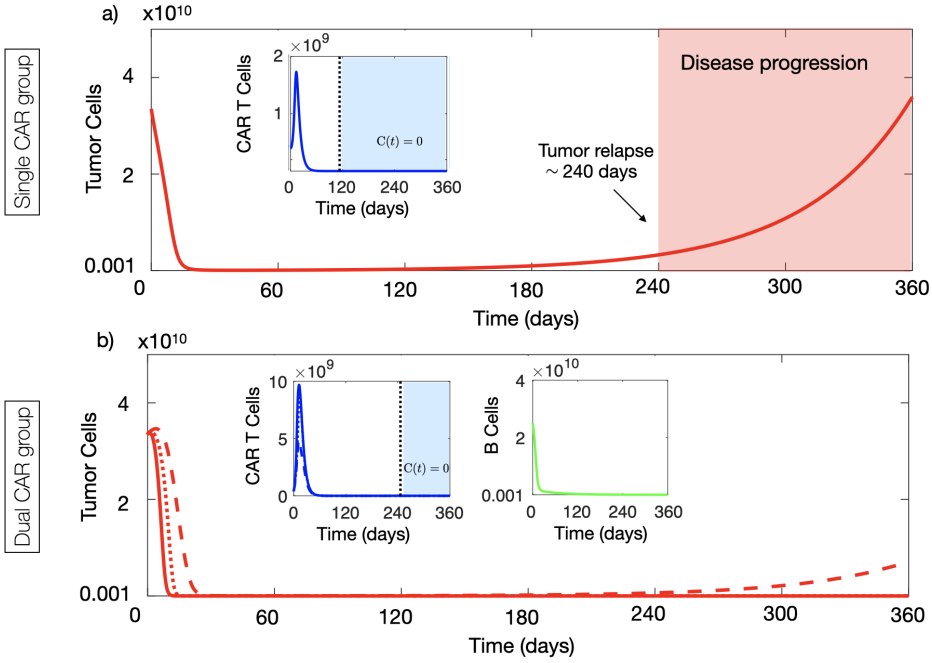

FIGURE 7.7: **Long-term dynamics of virtual patients.** (a) Dynamics of the number of CAR T (blue curve) and tumor cells (red curve) governed by Equations (7.1) and (7.2). Initial conditions and tumor inactivation rate used in the simulation were $C_0 = 4 \times 10^8$, $T_0 = 3.35 \times 10^{10}$ and $\alpha_1 = 0.01$ day^{-1}. (b) Dynamics of the number of CAR T cells (blue curves), B cells (green curve) and tumor cells (red curve) ruled by Equations (7.3)–(7.6) in three different scenarios of immune suppression: $\alpha_1 = 0.04$ day^{-1} (solid lines), $\alpha_1 = 0.07$ day^{-1} (dotted lines) and $\alpha_1 = 0.2$ day^{-1} (dashed lines). Initial conditions used in the simulation were $\bar{C}_0 = 2 \times 10^8$, $C_0 = 0$, $B_0 = 2.5 \times 10^{10}$ and $T_0 = 3.35 \times 10^{10}$ cells. Parameter values used in the simulations were $\tau_C = 7$ days, $\rho_{\bar{C}} = \rho_C = 0.9$ day^{-1} , $\rho_T = 1/50$ day^{-1}, $\alpha_2 = 2.5 \times 10^{-10}$ day^{-1} cell^{-1}, $g_T = 10^{10}$ cells, $g_C = 2 \times 10^9$ cells, $g_B = 10^{10}$ cells, $k = 0.2$, $\alpha_B = 4.5 \times 10^{-11}$ day^{-1} cell^{-1} and $\tau_B = 60$ day^{-1}.

7.4.7 Dual CAR T improves the possibility of therapy success

Finally, we performed a systematic study of the possibility of controlling tumor growth using single and double CAR T therapies. Figure 7.8 shows the results for different values of the tumor immune suppression strength as a function of the initial number of CAR T and tumor cells. Tumor was considered to be controlled if, after six months, the number of tumor cells was below 10% of its peak value. A threshold effect was clearly observed, with tumor control at six months being a function of α_1, C_0, and T_0. The best results were obtained for double CAR T cell therapy, which was capable of controlling a substantially larger number of tumors according to their size and immunosuppressive capacity, with lower doses of the CAR T product (see Figure 7.8 d–f). For the same value of α_1 (compare Figure 7.8 c,d), dual-CAR was substantially more effective in achieving tumor control. Moreover, in situations with small initial tumor cell loads, the dual-CAR treatment was effective even for large values of the tumor immune suppression parameter, which points to a potential success of the therapy when using the treatment soon after surgery.

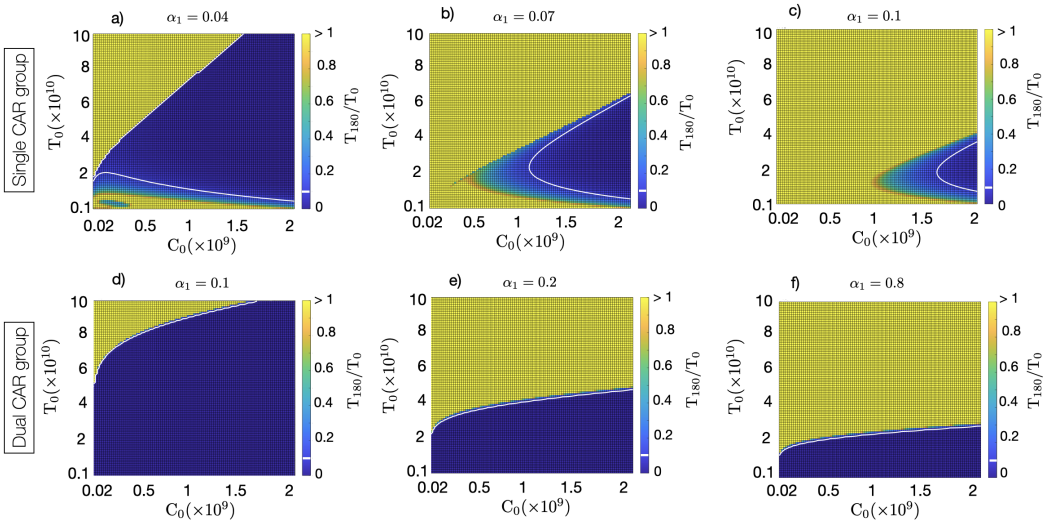

FIGURE 7.8: Colormap plots of the percentage of change in tumor load at six months compared to the initial load measured by the fraction $T(180)/T_0$, as a function of the initial number of CAR T and tumor cells, over three immune suppression scenarios: (a) $\alpha_1 = 0.04$ day^{-1} , (b) $\alpha_1 = 0.07$ day^{-1}, (c,d) $\alpha_1 = 0.1$ day^{-1}, (e) $\alpha_1 = 0.2$ day^{-1} and (f) $\alpha_1 = 0.8$ day^{-1}. Dark blue areas, delimited by the white lines, show the initial configurations of injected CAR T cells (C_0) and tumor loads (T_0) leading to tumor control after six months. Subplots (a–c) show the results obtained using a single CAR as governed by Equations (7.1) and (7.2). Subplots (d–f) shows results of computer simulations with the dual CARs obtained using Equations (7.3)–(7.6). Parameter values used in the simulations were $\tau_C = 7$ days, $\rho_{\bar{C}} = \rho_C = 0.9$ day^{-1} , $\rho_T = 1/50$ day^{-1}, $\alpha_2 = 2.5 \times 10^{-10}$ day^{-1} cell^{-1}, $g_T = 10^{10}$, $g_C = 2 \times 10^9$, $g_B = 10^{10}$, $k = 0.2$, $\alpha_B = 4.5 \times 10^{-11}$ day^{-1} cell^{-1} and $\tau_B = 60$ day^{-1}.

7.5 Discussion and conclusion

In this chapter we constructed a mathematical model based on ordinary differential equations for the total numbers of CAR T cells and tumor cells. This is probably the strongest assumption of our study, since tumors are complex entities having spatial structure with heterogeneous accessibility for the immune system, different types of niches and probably varying levels of immune suppression. Thus, a direct extension of this work would be to consider tumor spatial structure. The scenario of complete tumor macroscopic resection would be the one in which the mathematical model could most closely reflect the real in-patient dynamics, since spatial effects would be expected to be less relevant.

The simulations of our mathematical model suggest that the injection of a massive number of CAR T cells could overcome the immune suppression capabilities of the tumor. The idea is simple: throw in many more T cells than the tumor can deactivate. However, this is not currently possible technically with current CAR T products, since the number of T cells that can be obtained is orders of magnitude below the threshold for such an attack on the tumor to succeed. Moreover, only a fraction of the cells injected in the blood stream will travel to the tumor site. Although this can be partially overcome by the direct delivery of the CAR T cells to the tumor sites these ideas have not lead to sustained therapeutical success when treating glioblastomas.

Thus, one alternative option is to generate an army of CAR T cells within the body. For that purpose, any target allowing for the expansion of the T cells without a significant toxicity could be used. This lead us to the idea that dual-target CAR T cells, one with on-tumor activity and other with off-tumor activity on a large population of non-essential healthy cells whose elimination does not threaten patient survival. One example of such target could be CD19 because of the large number of B cells present in the organism, the fact that CD19 is not expressed in other tissues, and that the toxicity of current CAR T products targeting CD19 is now well controlled.

Interestingly, our mathematical model captured the difficulties for CAR T cell expansion when tumor immune suppression was accounted for. As in different clinical studies, the model showed that CAR T cells targeting solid tumors have poor persistence properties, even with high doses of CAR T. Simulations reaffirmed the relevance of the dose injected for the early outcome of the therapy. The exact threshold value that could be effective for tumor control would depend on its characteristics, and would be patient- and tumor- dependent. Immunosuppressive tumors such as glioblastoma may require higher doses of injected CAR T cells to achieve a significant reduction in the tumor load. However, even in poorly immunosuppressive environments, the escape of the tumor due to the limiting effect of immune suppression was found to be enough to allow for relapse in the medium term.

We also explored in silico the idea of treating resected tumors with the single-CAR T cells, i.e., in scenarios of a reduction of the initial tumor load. In that case, a modest expansion of CAR T cells was observed due to the lower levels of tumor targets. In principle, the reduction in tumor size could help in limiting the effect of tumor immune suppression. We found in silico that both processes overlapped, leading to an initial reduction in tumor size, but eventually the tumor grew back. Better results were obtained in silico for long-term tumor control when a high dose of CAR T cells was administered to a large initial tumor. The problem is that, taking into account the reduction of cells from those injected to those traveling to the tumor region, the amount of CAR T cells required would be too high, and thus technically unfeasible.

CAR T with dual CAR groups targeting CD19 and the tumor antigen, would promote further stimulation of CAR T cells through their interaction with B cells, providing a powerful source of tumor-targeting CAR T cells. In fact, interaction with B cells is likely to occur early as they are found in blood and lymphoid organs (**Chen**). Normal B cells would then provide a non-tumor dependent, self-renewing antigen source to support CAR T. This double targeting, on and off the tumor, would provide a simple and pragmatic solution to improving the problem of trafficking and CAR T cell deactivation due to immune suppression by tumor cells.

Our simple simulation model of this scenario provided substantial tumor control advantages in silico over the case of single-CAR. Substantial improvements in effectiveness were observed in cases in which CAR T cells with a single on-tumor target had difficulty in controlling the tumor. The first situation was with highly immunosuppressive tumors, where therapy success was significantly improved by the initial boost in anti-tumor cells generated by the substantially larger initial expansion. The second situation was the one of small initial tumor loads, in which single-target CAR T expansion would be less likely to be substantial, e.g., in cases in which an initial surgery had left only a remnant of infiltrative tumor cells. In that case, the major contribution to CAR T cell expansion came from the CD19-bearing cells and led to the success of dual CAR therapy in silico.

The proposed strategy has the only limitation of the toxicity of the treatment on $CD19^+$ cells. Acute toxicity is mostly related to cytokine release syndrome and neurotoxicity. These side effects of the treatment can be life-threatening in a subset of patients. However, tocilizumab and corticosteroids have been used to manage these toxicities, enabling CD19 CAR T cells to be administered without obvious compromise in efficacy (Hirayama and Turtle, 2019; Siegler and Kenderian, 2020).

Thus, our study suggests an optimal protocol for the use of these dual-target CAR Ts with on- and off-tumor activity. Patient blood and bone marrow samples should be taken before surgery in order to start with the preparation and in vitro expansion of the CAR T product, and the patient should meanwhile receive surgery, and a recovery time be allowed for. Subsequently, the dual CAR Ts should be infused, possibly in combination with anti-PD-1 treatment, and finally cytotoxic therapies (radiation therapy and chemotherapy) could be applied to kill potentially resistant cells not bearing the CAR T tumor target. Finally, B-cell aplasia would be expected, as happens in the treatment of hematological malignancies with CD19 antigens. However, since the bone marrow is very unlikely to contain tumor cells, the sample taken initially could be used to provide an autologous bone marrow transplant after the CAR T cells are exhausted.

In summary, we have constructed a mathematical model of a solid tumor response to CAR T cells with dual targets: one of them recognizing a tumor antigen and the other recognizing an off-tumor antigen present in normal cells such as $CD19^+$ B cells. When only the tumor antigen was present, the therapy could overcome tumor immune suppression only when unrealistically large numbers of CAR T cells were injected. The use of dual CARs allowed the expansion of the CAR T population to happen even in the presence of immune suppression by tumor cells on the T cells and allowing appropriate therapeutic levels of the T-cell population to be attained. In our simulations, this resulted in long-term tumor control, which would provide an additional tool in the fight against aggressive cancers with few therapeutic options, such as glioblastoma. We also found in silico that an optimal use of the dual-CAR T cell therapy for glioblastoma would be to inject them immediately after extensive surgical resection and before the use of cytotoxic treatments.

In this study we intend only to provide a theoretical proof of concept of the phenomenon. There is much work to do to explore mathematically the dynamical interplay of the different biological processes, and to find the parameter ranges best describing these phenomena. We hope that this work will stimulate the development of experimental studies, testing the potential effectiveness of the concepts described here. If successful, CAR T with dual targets could become a novel ingredient in combination therapies against aggressive solid tumors such as glioblastoma.

Chapter 8

Conclusions

This chapter presents the conclusions of the research described in the thesis.

Conclusions of mathematical models of solid tumor growth and response to stereotactic radiosurgery

Longitudinal follow-up of untreated malignant tumors showed explosive growth dynamics.

- Among several growth laws analyzed (classical exponential, size-limited Keiber and super-linear growth), the model that best described the longitudinal volumetric data from malignant tumors was super-linear growth law.
- In contrast, the longitudinal volumetric data corresponding to the benign tumor analyzed showed slower growth (similar to Kleiber's law of limited size).

A mathematical approach reproduces the response of brain metastases to stereotactic radiosurgery.

- A mathematical model based on ordinary differential equations that includes four cell compartments was able to describe the volumetric dynamics of brain metastases after stereotactic radiosurgery.
- Good model fits were obtained to the volumetric data of the treated lesions, describing the different dynamics observed in clinical practice including early and late post-treatment inflammation.
- We obtained an analytical estimate for the progression time due to the growth of remnant proliferating cells after SRS, which could be used to help distinguish between progression and radiation necrosis.

In silico inflammatory events after SRS displayed the fastest growth dynamics allowing to discriminate them from relapses.

- A mesoscale stochastic model that addresses new biological and spatial aspects describes volumetric dynamics of BMs to SRS.
- The volumetric behavior of the post-SRS inflammatory response showed faster growth dynamics than that of BM relapses in computational simulations. The growth exponent β values for inflammatory events were typically greater than 1 and less than 1 for tumor recurrences.
- The value of the exponent β could have a direct clinical application to distinguish volumetric regrowth after SRS as inflammation or tumor progression.

Conclusions of mathematical models of response of CAR T cell therapy

$CD19^+$ relapses in B-ALL could be the result of competition between leukemic and CAR T cells, analogous to predator-prey dynamics.

- A mathematical model incorporating the major cell populations involved in the growth of B-ALL described the short- and long-term dynamic response of leukemia to injection of CAR T cells. The model showed that the number of CAR T cells injected does not critically affect the treatment outcome.
- The model predicted that $CD19^+$ cancer relapses could be the result of competition between leukemic and CAR T cells, analogous to predator-prey dynamics. Time relapse depended on the growth rate of the leukemic cells, the stimulation rate and the lifespans of the CAR T cells.
- The possibility of controlling relapses by early re-challenging of the leukemia cells with stored CAR T cells was studied. The best results were obtained when reinjection was performed on relapse.

CAR T cells therapy could control cancer growth but not eradicate the T-ALL.

- The simple mathematical model developed captured the difficulties for CAR T cell expansion in vitro, with a limit in cell production. Maximum number of CAR T cells that can be produced in vitro depends on the stimulation provided by the cytokines and the excess CAR T killing efficiency over the mitotic stimulation.
- Numerical simulations of the model showed that CAR T population is amplified even in the presence of fratricide during initial stage after the administration of therapy. CAR T cells were able to control leukemic growth after two weeks, with peak leukemic loads lower than the initial ones.
- Relapse time after the CAR T treatment was found to depend strongly on the proliferation rate of the leukemia cells.

Dual-target CAR Ts with on- and off-tumor activity may override immune suppression in solid cancers.

- The proposed mathematical model described the competence of CAR T and tumor cells, taking into account their immunosuppressive capacity. In silico simulations showed that the use of large numbers of CAR T cells targeting solid tumor antigens is necessary to overcome the immunosuppressive potential of cancer and reduce tumor burden during the first few weeks.
- Manufacture and injection of CAR T cells targeting two antigens: CD19 and a tumor-associated antigen was proposed to achieve higher levels of CAR T cells.
- Dual-target CAR T cell therapy was able to control a substantially larger number of tumors according to their size and immunosuppressive capacity.

Chapter 9

Conclusiones Generales

Este capítulo presenta las conclusiones de la investigación descrita en la tesis.

Conclusiones de los modelos matemáticos de crecimiento de tumores sólidos y respuesta a la radiocirugía estereotáctica

El seguimiento longitudinal de tumores malignos no tratados mostró una dinámica de crecimiento explosiva.

- Entre varias leyes de crecimiento analizadas (exponencial, Keiber de tamaño limitado y crecimiento súper lineal), el modelo que mejor describió los datos volumétricos longitudinales de los tumores malignos fue la ley de crecimiento súper lineal.
- Por el contrario, los datos volumétricos longitudinales correspondientes al tumor benigno analizado mostraron un crecimiento más lento (similar a la ley de Kleiber de tamaño limitado).

Un enfoque matemático reproduce la respuesta de las metástasis cerebrales tratadas con radiocirugía estereotáctica.

- Un modelo matemático basado en ecuaciones diferenciales ordinarias que incluye cuatro compartimentos celulares fue capaz de describir la dinámica volumétrica de las metástasis cerebrales después de la radiocirugía estereotáctica (SRS por su siglas en inglés).
- Se obtuvieron buenos ajustes del modelo a los datos volumétricos de las lesiones tratadas, describiendo las diferentes dinámicas observadas en la práctica clínica incluida la inflamación postratamiento temprana y tardía.
- Obtuvimos una estimación analítica del tiempo de progresión causado por el crecimiento de células proliferativas remanentes después de la SRS, el cual podría usarse para ayudar a distinguir entre progresión y radionecrosis.

Los eventos inflamatorios in silico posteriores al SRS mostraron una dinámica de crecimiento más rápida, lo que permitió discriminarlos de las recaídas.

- Un modelo estocástico de mesoescala que aborda nuevos aspectos biológicos y espaciales describe la dinámica volumétrica de metástasis cerebrales tratadas con SRS.

- El comportamiento volumétrico de la respuesta inflamatoria post-SRS mostró una dinámica de crecimiento más rápida que el de las recaídas de las metástasis cerebrales en simulaciones computacionales. Los valores del exponente de crecimiento β para los eventos inflamatorios fueron típicamente mayores que 1 y menores que 1 para las recurrencias tumorales.
- El valor del exponente β podría tener una aplicación clínica directa para distinguir el recrecimiento volumétrico después del SRS como inflamación o progresión tumoral.

9.1 Conclusiones de los modelos matemáticos de respuesta de la terapia con células CAR T

Las recaídas de CD19 $^+$ en leucemia linfoblástica aguda de células B podrían ser el resultado de la competencia entre las células leucémicas y las células CAR T, análoga a la dinámica de depredador-presa.

- Un modelo matemático, que incorpora las principales poblaciones de células implicadas en el crecimiento de la leucemia linfoblástica aguda de células B, describió la respuesta dinámica a corto y largo plazo de la enfermedad frente la inyección de células CAR T. El modelo mostró que la cantidad de células CAR T inyectadas no afecta sustancialmente al resultado del tratamiento.
- El modelo predijo que las recaídas del cáncer CD19 $^+$ podrían ser el resultado de la competencia entre las células leucémicas y las células CAR T, similar a la dinámica de depredador-presa. El tiempo de recaída dependió de la tasa de crecimiento de las células leucémicas, la tasa de estimulación y la esperanza de vida de las células CAR T.
- Se estudió la posibilidad de controlar las recaídas mediante la reinyección temprana de las células leucémicas con células CAR T almacenadas. Los mejores resultados se obtuvieron cuando se realizó la reinyección en el momento de la recaída.

La terapia con células CAR T podría controlar el crecimiento del cáncer pero no erradicar la linfoblástica aguda de células T.

- El modelo matemático simple desarrollado capturó las dificultades para la expansión de células CAR T in vitro, con un límite en la producción celular. El número máximo de células CAR T que se pueden producir in vitro depende de la estimulación proporcionada por las citoquinas y del exceso de eficiencia de destrucción de CAR T sobre la estimulación mitótica.
- Las simulaciones numéricas del modelo mostraron que la población CAR T se amplifica incluso en presencia de fratricidio durante la etapa inicial después de la administración de la terapia. Las células CAR T pudieron controlar el crecimiento leucémico después de dos semanas, con cargas leucémicas máximas más bajas que las iniciales.
- Se obtuvo que el tiempo de recaída después del tratamiento con CAR T depende en gran medida de la tasa de proliferación de las células leucémicas.

Los CAR Ts de doble objetivo con actividad dentro y fuera del tumor pueden anular la inmunosupresión en cánceres sólidos

- El modelo matemático propuesto describió la competencia de las células CAR T y las células tumorales, teniendo en cuenta la capacidad inmunosupresora del tumor. Las simulaciones in silico mostraron que es necesario el uso de un gran número de células CAR T dirigidas a antígenos tumorales sólidos para superar el potencial inmunosupresor del cáncer y reducir la carga tumoral durante las primeras semanas.
- Para lograr niveles más altos de células CAR T se propuso la fabricación y administración de células CAR T dirigidas a dos antígenos: CD19 y un antígeno asociado a tumores.
- La terapia con células CAR T de doble diana fue capaz de controlar un número sustancialmente mayor de tumores según su tamaño y capacidad inmunosupresora.

Chapter 10

Future work

The research that has been undertaken for this thesis has highlighted a number of topics on which further research would be beneficial. Below are some of the natural extensions to this work that would help expand the results.

10.1 The growth laws of solid tumors validation

Understanding the evolutionary dynamics of cancer is one of the most important goals for the development of future treatment approaches and the extinction of the disease. It is a remarkable fact that the growth laws of untreated human malignant cancers display a signature of the evolutionary processes taking place behind the scenes in the form of an exponent $\beta > 1$ in Pérez-García et al., 2020. It would be interesting to expand the database to include new tumor histologies as well as a greater number of cases. This would allow to validate the obtained result and to develop further in the clinical implications.

The next step would be to explore the role that growth laws play in human cancers under different therapies and the eventual development of tumor cell resistance. In this line, the study developed by Ocaña-Tienda et al., 2021 addresses this question for patients with brain metastases who were treated with chemotherapy, radiotherapy and both. However, when comparing the growth dynamics in the form of the exponent β between the different groups treated and untreated, no statistically significant differences were found. Despite this, the results emerged that the treated BMs presented slower growth dynamics. Along these lines, it would be interesting to have a larger number of data, which would allow to increase the sample size and to possible obtain statistically significant results.

Finally, in relation to the results obtained in Section 4, the use of the exponent β could be validated as a tool to distinguish radiation necrosis or inflammatory events from tumor progression.

10.2 Extensions and enhancements to CAR-T cell therapy modeling

The mathematical models presented to model CAR T cell treatments have provided an understanding of the response to therapies and studied in silico the dynamics of the interaction between the tumor, CAR T cells and other relevant biological elements. The approach developed in this thesis has been of cellular kinetic-pharmacodynamic type, considering cancers as made of spatially uniform compartments. Although this could be a good initial assumption in the description of leukemias, solid tumors or lymphomas share spatial and heterogeneous aspects that make it necessary to incorporate these characteristics in the modeling. Once deterministic

mathematical models describing the patient's response to the CAR T product are available, they can be used as test beds for alternative ideas.

CAR T cell therapies are considered one of the most promising therapeutic advances in the fight against cancer. The successes of this therapy have motivated the study of the possible applicability against solid tumors, and have led to numerous ongoing clinical trials for a wide variety of cancers. In this area we propose two specific extensions for future work, although in reality there would be many interesting aspects that could be addressed with mathematical modeling.

10.2.1 A discrete simulator of single-target and dual-target CAR T therapy for brain tumors

Brain tumors have showed discrete responses to different immunotherapies that have been successful in other cancers. However, there is a potential for CAR T cell therapy to be used to treat brain tumors. In this thesis, a strategy was proposed to fight back one of the main problems faced by these therapies in solid tumors: tumor immunosuppression. It would be necessary to complement the results obtained in this line, developing a discrete model allowing to study the response of brain tumors to CART therapy with single and dual target. In addition to incorporating the spatial aspects, the discrete model allowed a better description of the tumor microenvironment, incorporating new cell populations such as immune cells. Tumor heterogeneity could also be taken into account by incorporating mutations and distinguishing between cells that express the target and those that do not.

The use of dual CARs could be more realistically tested for low initial tumor loads such as patients with macroscopically complete resection. The PD-1/PD-L1 interaction of T cells and tumor cells leads to the inhibition of the effector function of T cells, so blocking this interaction has the potential to significantly enhance the antitumor activity of the cells. T and reduce T- cellular depletion. Combining CAR-T with PD-1 blocking is a promising strategy to improve the efficacy of CAR-T cell therapies (McGowan et al., 2019). These questions are open lines that could be addressed by conducting in silico clinical trials to determine the best combined treatment strategies with CAR T and other therapies..

10.2.2 A discrete simulator to predict qualitatively the spatio-temporal dynamics of the response of B cell r/r lymphomas to CAR-T cell therapy

Lymphoma is a hematologic cancer with some similarities to solid tumors. CAR T treatment is indicated for adults with relapsed or refractory (r/r) large B-cell lymphoma who have received two or more lines of systemic therapy including diffuse large B-cell lymphoma (LDCBG), cell lymphoma High-grade B and LDCBG derived from follicular lymphoma. The overall response rate achieved with CAR T products is 52%, including 40% complete responses (Schuster et al., 2019).

A very relevant problem in this context is the identification of non-responders to CAR T cell therapy in patients with aggressive r/r B cell lymphomas. This question has been approached from classical statistical methods based on clinical, biochemical or standard imaging variables, but success has been limited by the small number of data.

The retrospective, observational and non-interventional clinical study has recently been approved. This study aims to include more than 100 patients diagnosed with r/r DLBCL from eight different institutions and treated with CAR T, including

tisagenlecleucel (CAR T product marketed by NOVARTIS currently in use in Spain for diffuse r/r large cell B lymphomas in adults). Data collection will be carried out through a GETH-MATCART-2021 project funded by NOVARTIS Global.

A large amount of data on disease and treatment will be collected (treatment start and end date, response type and relapse dates, doses administered, etc). Additionally, lymphoma evaluations will be collected at different time points when available, including clinical and biochemical variables and all follow-up images.

In this context it is proposed to develop and validate a discrete simulator to predict qualitatively the spatio-temporal dynamics of the response of B cell r/r lymphomas to CAR T therapy from data available at the time of decision to treat. We will draw on the experience acquired in the development of the discrete model of BMs treated with SRS and the continuous models of response to CAR T therapy. This conjunction will be the starting point for the in silico study of optimal therapeutic programs. of tisagenlecleucel in r/r DLBCL, personalizing therapies that might be tested later in proof-of-concept experiments.

Basic cell events considered in the model will be based on key features associated to CAR T treatment and r/r DLBCL characteristics. An adequate voxel size will be selected in order to allow comparison of simulation results with clinical imaging data. In silico twins will be built for all patients whenever possible, by reconstructing the 3D tumor structure from pre-infusion PET images, and also by accurately parameterizing the model with tumor data and PET images after treatment. Different therapy schemes will be tested over in silico twins in order to find optimal schedules.

Chapter 11

Publications and conference contributions

11.1 Full Publication List

Publications in ISI-indexed journals

1. Ocaña-Tienda B. , Pérez-Beteta J., Molina-García D., Jiménez-Sánchez J., **León-Triana O.**, Ortiz de Mendivil A., Asenjo B., Albillo D., Pérez-Romasanta L., González-Del Portillo E., Llorente M., Carballo N., Arana E., Pérez-García V.M. The growth laws of brain metastases. *PNAS* (Submitted).

   Journal impact factor (2020): 11.205, rank 8/72 in Multidisciplinary Sciences (Source: Web of Science).

2. **León-Triana O.**, Pérez-Beteta J., Albillo D., Ortiz de Mendivil A., Pérez-Romasanta L., González-Del Portillo E., Llorente M., Carballo N., Arana E., Pérez-García V.M. (2021) Brain metastasis response to stereotactic radio surgery: A mathematical approach. *Mathematics*, 9(7), 2227–7390. doi: 10.3390/math9070716

   Journal impact factor (2020): 2.258, rank 24/330 in Mathematics (Source: Web of Science).

3. **León-Triana O.**, Sabir S., Fernández-Calvo F., Belmonte-Beitia J., Chulián S., Martínez-Rubio A., Rosa M., Pérez-Martínez A., Ramirez-Orellana M., Pérez-García, V.M. (2021) CAR T cell therapy in B-cell acute lymphoblastic leukaemia: Insights from mathematical models. *Communications in Nonlinear Science and Numerical Simulation*, 94, 105570. doi: 10.1016/j.cnsns.2020.105570

   Journal impact factor (2020): 4.260, rank 5/265 in Applied Mathematics (Source: Web of Science).

4. Pérez-García V.M, **León-Triana O.**, Rosa M., Pérez-Martínez A. (2021) CAR T cells for T-cell leukemias: Insights from mathematical models. *Communications in Nonlinear Science and Numerical Simulation*, 96, 105684. doi: 10.1016/j.cnsns.2020.105684

   Journal impact factor (2020): 4.260, rank 5/265 in Applied Mathematics (Source: Web of Science).

5. **León-Triana O.**, Pérez-Martínez A., Ramírez-Orellana M., Pérez-García V.M. (2021) Dual-Target CAR-Ts with On- and Off-Tumour Activity May Override Immune Suppression in Solid Cancers: A Mathematical Proof of Concept. *Cancers*, 13(4), 703, doi: 10.3390/cancers13040703

   Journal impact factor (2020): 6.639, rank 51/242 in Oncology (Source: Web of Science).

6. Pérez-García V.M., Calvo G.F., Bosque J.J., **León-Triana O.**, Jiménez J., Perez-Beteta J., Belmonte-Beitia J., Valiente M., Zhu L., García-Gómez P., Sánchez-Gómez P., Hernández-San Miguel E., Hortigüela R., Azimzade Y., Molina-García D., Martinez Á., Rojas Á.A., de Mendivil A.O., Vallette F., Schucht P., Murek M., Pérez-Cano M., Albillo D., Honguero Martínez A.F., Jiménez Londoño G.A., Arana E., García Vicente A.M. (2020) Universal scaling laws rule explosive growth in human cancers. *Nature Physics*, 16(12), 1232–1237. doi: 10.1038/s41567-020-0978-6

   Journal impact factor (2020): 20.034, rank 4/86 in Multidisciplinary Physics (Source: Web of Science).

11.2 Congress contributions

Oral presentations

1. Title: Mathematical model of CAR T cell therapies for B-acute lymphoblastic leukemia
   Congress: XXVI Congreso de Ecuaciones Diferenciales y Aplicaciones XVI Congreso de Matemática Aplicada
   Location: Gijón, Spain
   Year: 2021

2. Title: Mathematical Model of Brain Metastasis Growth Based on MR
   Congress: Therapy Optimization in Glioblastoma (3rd anual meeting) Location: Ciudad Real, Spain
   Year: 2018

Posters contributions

1. Title: Radiation necrosis vs progression in Brain Metastases treated with stereotactic radiosurgery: How to distinguish them using mechanistic mathematical models
   Congress: Adaptation of the tumour and its ecosystem to radiotherapies
   Location: Le Bono, France
   Year: 2021
   (presented by Beatriz Ocaña-Tienda)

2. Title: Evidence of superlinear scaling laws in human cancers
   Congress: Heterogeneity and Evolution in Cancer
   Location: Madrid, Spain
   Year: 2019
   (presented by Juan Jiménez)

3. Title: Mathematical model of brain metastases growth based on MRI
   Congress: Statistical Physics Approaches to Systems Biology
   Location: Havana, Cuba
   Year: 2019

4. Title: Brain metastases: growth laws and stereotactic Radiosurgery response using simple mathematical models
   Congress: Mathematical persepectives in the biology and therapeutics of cancer in CIRM

Location: Marseille, France
Year: 2018

Bibliography

Ahmed, K.A. et al. (2017). "The radiosensitivity of brain metastases based upon primary histology utilizing a multigene index of tumor radiosensitivity". In: *Neuro Oncol* 19.8, pp. 1145–1146. DOI: 10.1093/neuonc/nox043.

Akimoto, T. et al. (1999). "Inverse relationship between epidermal growth factor receptor expression and radiocurability of murine carcinomas". In: *Clin Cancer Res* 5.10, pp. 2884–90.

Alberts, B. et al. (2015). *Molecular biology of the cell. 6th edition.* New York: Garland Science.

Alcantara, M. et al. (2019). "CAR T-cells for T-cell malignancies: challenges in distinguishing between therapeutic, normal, and neoplastic T-cells". In: *Leukemia* 11, pp. 2307–2315. DOI: 10.1038/s41375-018-0285-8.

Altrock, P.M., L.L. Liu, and F. Michor (2015). "The mathematics of cancer: integrating quantitative models". In: *Nat Rev Cancer* 15.12, pp. 730–45. DOI: 10.1038/nrc4029.

Anderson, K.G., I.M. Stromnes, and P.D. Greenberg (2018). "Obstacles Posed by the Tumor Microenvironment to T cell Activity: A Case for Synergistic Therapies." In: *Cancer Cell.* 31.3, pp. 311–325. DOI: 10.1016/j.ccell.2017.02.008.

Arvanitis, C.D., G.B. Ferraro, and R.K. Jain (2019). "The blood-brain barrier and blood-tumour barrier in brain tumours and metastases". In: *Nat Rev Cancer* 20.1, pp. 26–41. DOI: 10.1038/s41568-019-0205-x.

Askew, K. et al. (2017). "Coupled Proliferation and Apoptosis Maintain the Rapid Turnover of Microglia in the Adult Brain". In: *Cell Rep* 18.2, pp. 391–405. DOI: 10.1016/j.celrep.2016.12.041.

Baar, M. et al. (2016). "A stochastic model for immunotherapy of cancer". In: *Sci Rep* 6, p. 24169. DOI: 10.1038/srep24169.

Badoual, M. et al. (2014). "Oedema-based model for diffuse low-grade gliomas: application to clinical cases under radiotherapy". In: *Cell Prolif* 47, pp. 369–380. DOI: 10.1111/cpr.12114.

Bagley, S.J. and D.M. O'Rourke (2020). "Clinical investigation of CAR T cells for solid tumors: Lessons learned and future directions". In: *Pharmacology & Therapeutics* 205, p. 107419. DOI: 10.1016/j.pharmthera.2019.107419.

Bagley, S.J. et al. (2019). "CAR T-cell therapy for glioblastoma: recent clinical advances and future challenges." In: *Neuro Oncology* 20.11, pp. 429–1438. DOI: 10.1093/neuonc/noy032.

Bains, I. et al. (2009). "Quantifying the development of the peripheral naive CD4+ T-cell pool in humans". In: *Blood* 113.22, pp. 5480–5487. DOI: 10.1182/blood-2008-10-184184.

Ballabh, P., A. Braun, and M. Nedergaard (2004). "The blood-brain barrier: an overview: structure, regulation, and clinical implications". In: *Neurobiol Dis* 16.1, pp. 1–13. DOI: 10.1016/j.nbd.2003.12.016.

Barajas, R.F. et al. (2009). "Distinguishing recurrent intra-axial metastatic tumor from radiation necrosis following gamma knife radiosurgery using dynamic susceptibility-weighted contrast-enhanced perfusion MR imaging". In: *AJNR Am J Neuroradiol* 30, pp. 367–372. DOI: 10.3174/ajnr.A1362.

Barbolosi, D. et al. (2009). "Mathematical and numerical analysis for a model of growing metastatic tumors". In: *Mathematical Biosciences* 218.1, pp. 1–14. DOI: 10.1016/j.mbs.2008.11.00.

Barbolosi, D. et al. (2017). "Modeling therapeutic response to radioiodine in metastatic thyroid cancer: a proof-of-concept study for individualized medicine." In: *Oncotarget* 8.24, pp. 39167–39176. DOI: 10.1016/j.mbs.2008.11.00.

Benchaib, M.A. et al. (2019). "Mathematical Modeling Reveals That the Administration of EGF Can Promote the Elimination of Lymph Node Metastases by PD-1/PD-L1 Blockade." In: *Front Bioeng Biotechnol.* 7, p. 104. DOI: 10.3389/fbioe.2019.00104..

Benmebarek, M. et al. (2019). "Killing Mechanisms of Chimeric Antigen Receptor (CAR) T Cells". In: *International Journal of Molecular Sciences* 20.6, p. 1283. DOI: 10.3390/ijms20061283.

Benzekry, S. et al. (2014). "Classical mathematical models for description and prediction of experimental tumor growth". In: *PLoS Comput Biol* 10.8, e1003800. DOI: 10.1371/journal.pcbi.100380.

Berghoff, A.S. et al. (2008). "Characterization of the inflammatory response to solid cancer metastases in the human brain". In: *Clin Exp Metastasis* 30.1, pp. 69–81. DOI: 10.1007/s10585-012-9510-4.

Bertalanffy, L. Von (1957). "Quantitative laws in metabolism and growth". In: *Q Rev Biol* 32.3, pp. 217–231. DOI: 10.1086/401873.

Bilous, M. et al. (2019). "Quantitative mathematical modeling of clinical brain metastasis dynamics in non-small cell lung cancer". In: *Scientific reports* 9.1, p. 13018. DOI: 10.1038/s41598-019-49407-3.

Blasius, B. et al. (2020). "Long-term cyclic persistence in an experimental predator-prey system". In: *Nature* 577, pp. 226–30. DOI: 10.1038/s41586-019-1857-0.

Brauer, F. and C. Castillo-Chavez (2000). *Mathematical Models in Population Biology and Epidemiology*. Springer-Verlag.

Bray, F. et al. (2021). "The ever-increasing importance of cancer as a leading cause of premature death worldwide". In: *Cancer* 127.16, pp. 3029–3030. DOI: 10.1002/cncr.33587.

Breman, E. et al. (2018). "Overcoming Target Driven Fratricide for T Cell Therapy". In: *Frontiers in Immunology* 9, p. 2940. DOI: 10.3389/fimmu.2018.02940.

Brodland, G.W. and J.H. Veldhuis (2012). "The mechanics of metastasis: insights from a computational model". In: *PLoS ONE* 7.9, e44281. DOI: 10.1371/journal.pone.0044281.

Brown, C.E. et al. (2015). "Bioactivity and safety of IL13Rα2- redirected chimeric antigen receptor CD8+ T cells in patients with recurrent glioblastoma." In: *Clin Cancer Res.* 21.18, pp. 4062–4072. DOI: 10.1158/1078-0432.CCR-15-0428.

Brown, C.E. et al. (2016). "Regression of glioblastoma after chimeric antigen receptor T-cell therapy." In: *N Engl J Med.* 375.26, pp. 2561–2569. DOI: 10.1056/NEJMoa1610497.

Brown, J.M., D.J. Carlson, and D.J.Brenner (2014). "The tumor radiobiology of SRS and SBRT: are more than the 5 Rs involved?" In: *Int J Radiat Oncol Biol Phys* 88.2, pp. 254–62. DOI: 10.1016/j.ijrobp.

Brown, M. P., L. M. Ebert, and T. Gargett (2019). "Clinical chimeric antigen receptor-T cell therapy: a new and promising treatment modality for glioblastoma." In: *Clinical & Translational Immunology* 8.5, e1050. DOI: 10.1002/cti2.1050.

Carter, L.L. et al. (2002). "PD-1:PD-L inhibitory pathway affects both CD4+ and CD8+ T cells and is overcome by IL-2." In: *Eur. J. Immunol.* 32.2, pp. 634–643. DOI: 10.4049/jimmunol.1401572.

Carvalho-Barros, L.R., B.J. Rodrigues, and R.C. Almeida (2020). "CAR-T cell goes on a mathematical model". In: *Journal of Cellular Immunology* 2.1, pp. 31–37. DOI: 10.33696/immunology.2.016.

Castellarin, M. et al. (2018). "Driving CARs to the clinic for solid tumors". In: *Gene Therapy* 25.3, pp. 165–175. DOI: 10.1038/s41434-018-0007-x.

Celiku, O., M.R. Gilbert, and O. Lavi (2019). "Computational modeling demonstrates that glioblastoma cells can survive spatial environmental challenges through exploratory adaptation". In: *Nat Commun* 10.1, p. 5704. DOI: 10.1038/s41467-019-13726-w.

Chakravarthi, B.V., S. Nepal, and S. Varambally (2016). "Genomic and Epigenomic Alterations in Cancer". In: *Am J Pathol* 186.7, pp. 1724–1735. DOI: 10.1016/j.ajpath.2016.02.023.

Chakwizira, A. et al. (2018). "Mathematical modelling of the synergistic combination of radiotherapy and indoleamine-2,3-dioxygenase (IDO) inhibitory immunotherapy against glioblastoma". In: *British Journal of Radiology* 91, p. 1087. DOI: 10.1259/bjr.20170857.

Choi, S.H. et al. (2014). "TopBP1 and Claspin contribute to the radioresistance of lung cancer brain metastases". In: *Mol Cancer* 5.10, pp. 2884–90. DOI: 10.1186/1476-4598-13-211.

Chuang, M.T. et al. (2016). "Differentiating Radiation-Induced Necrosis from Recurrent Brain Tumor Using MR Perfusion and Spectroscopy: A Meta-Analysis." In: *PLoS One* 11.1, e0141438. DOI: 10.1371/journal.pone.0141438.

Dagogo-Jack, I. and A. Shaw (2018). "Tumour heterogeneity and resistance to cancer therapies". In: *Nat Rev Clin Oncol* 15, 81–94. DOI: 10.1038/nrclinonc.2017.166.

Davenport, A.J. et al. (2015). "CAR-T cells are serial killers". In: *Oncoimmunology* 4.12, e1053684. DOI: 10.1080/2162402X.2015.1053684.

Davenport, A.J. et al. (2018). "Chimeric antigen receptor T cells form nonclassical and potent immune synapses driving rapid cytotoxicity." In: *Proceedings of the National Academy of Sciences U S A* 115.9, E2068–E2076. DOI: 10.1073/pnas.1716266115.

Davila, M.L. et al. (2014). "Efficacy and toxicity management of 19-28z CAR T cell therapy in B cell acute lymphoblastic leukemia". In: *Sci Transl Med* 6, 224ra225. DOI: 10.1126/scitranslmed.3008226.

Davis, B.M. et al. (2017). "Characterizing microglia activation: a spatial statistics approach to maximize information extraction". In: *Sci Rep* 7, p. 1576. DOI: 10.1038/s41598-017-01747-8.

Dehghan, M. and N. Narimani (2020). "Radial basis function-generated finite difference scheme for simulating the brain cancer growth model under radiotherapy in various types of computational domains". In: *Computer Methods and Programs in Biomedicine* 195.6, p. 105641. DOI: 10.1016/j.cmpb.2020.105641.

Diego, D., G.F. Calvo, and V.M. Pérez-García (2013). "Modeling the connection between primary and metastatic tumors". In: *Journal of Mathematical Biology* 67, pp. 657–69. DOI: 10.1007/x00285-012-0565-2.

Dong, Y. et al. (2020). "Leukemia incidence trends at the global, regional, and national level between 1990 and 2017". In: *Exp Hematol Oncol* 9.14. DOI: 10.1186/s40164-020-00170-6.

Donovan, E.K., S. Parpia, and J.N. Greenspoon (2019). "Incidence of radionecrosis in single-fraction radiosurgery compared with fractionated radiotherapy in the

treatment of brain metastasis". In: *Current Oncology* 26.3, e328–e333. DOI: 10.3747/co.26.4749.

Duregon, E. et al. (2019). "CAVEOLIN-1 expression in brain metastasis from lung cancer predicts worse outcome and radioresistance, irrespective of tumor histotype". In: *Oncotarget* 6.30, pp. 29626–36. DOI: 10.18632/oncotarget.4988.

Durrett, R. (2015). *Branching Process Models of Cancer*. Springer. DOI: 10.1007/978-3-319-16065-8_1.

Eftimie, R., J.L. Bramson, and D.J.D. Earn (2011). "Interactions between the immune system and cancer: a brief review of non-spatial mathematical models". In: *Bull Math Biol* 73.1, pp. 2–32. DOI: 10.1007/s11538-010-9526-3.

Eftimie, R, J.J. Gillard, and D.A. Cantrell (2016). "Mathematical models for immunology: current state of the art and future research directions". In: *Bull Math Biol* 78, pp. 2091–2134. DOI: 10.1007/s11538-016-0214-9.

Ellingson, B.M. et al. (2014). "Emerging techniques and technologies in brain tumor imaging". In: *Neuro Oncol* 16.7, pp. vii12–23. DOI: 10.1093/neuonc/nou221.

Essig, M. et al. (2012). "Assessment of brain metastases with dynamic susceptibility-weighted contrast-enhanced MR imaging: initial results". In: *Radiology* 228, pp. 193–199. DOI: 10.1148/radiol.2281020298.

Ewald, P.W. and H.A. Swain Ewald (2012). "Toward a general evolutionary theory of oncogenesis". In: *Evolutionary Applications* 6.1, pp. 70–81. DOI: 10.1111/eva.12023.

Fedotov, S., A. Iomin, and L. Ryashko (2011). "Non-Markovian models for migration-proliferation dichotomy of cancer cells: anomalous switching and spreading rate". In: *Nonlin Soft Matter Phys* 84.6, p. 061131. DOI: 10.1103/PhysRevE.84.061131.

Feins, S. et al. (2019). "An introduction to chimeric antigen receptor (CAR) T-cell immunotherapy for human cancer". In: *Am J Hematol* 94.S1, S3–S9. DOI: 10.1002/ajh.25418.

Feng, K.C. et al. (2017). "Cocktail treatment with EGFR-specific and CD133-specific chimeric antigen receptor-modified T cells in a patient with advanced cholangiocarcinoma". In: *Journal of Hematology & Oncology* 10.1. DOI: 10.1186/s13045-016-0378-7.

Fleischer, L.C., H.T. Spencer, and S.S. Raikar (2019). "Targeting T cell malignancies using CAR- based immunotherapy: challenges and potential solutions". In: *J Hematol Oncol* 12.1, p. 141. DOI: 10.1186/s13045-019-0801-y.

Fox, B.D. et al. (2011). "Epidemiology of metastatic brain tumors". In: *Neurosurg Clin N Am* 22.1, pp. 1–6. DOI: 10.1016/j.nec.2010.08.007.

Franssen, L.C. et al. (2019). "A mathematical framework for modelling the metastatic spread of cancer". In: *Bulletin of Mathematical Biology* 81, pp. 1965–2010. DOI: 10.1007/s11538-019-00597-x.

Fulcher, D.A. and A. Basten (1997). "B cell life span: a review." In: *Immunol. Cell. Biol.* 75.5, pp. 446–555. DOI: 10.1038/icb.1997.69.

Furuse, M. et al. (2019). "Radiological diagnosis of brain radiation necrosis after cranial irradiation for brain tumor: a systematic review". In: *Radiat Oncol* 14.28. DOI: 10.1186/s13014-019-1228-x.

Galochkina, T., A. Bratus, and V.M. Pérez-García (2015). "Optimal radiotherapy protocol for low-grade gliomas: Insights from a mathematical model". In: *Mathematical Biosciences* 267, pp. 1–9. DOI: 10.1016/j.mbs.2015.05.006.

Garcia, M.A. et al. (2018). "Brain metastasis growth on preradiosurgical magnetic resonance imaging". In: *Pract Radiat Oncols* 8.6, e369–e376. DOI: 10.1016/j.prro.2018.06.004.

Gargini, R. et al. (2020). "The IDH-TAU-EGFR triad defines the neovascular landscape of diffuse gliomas". In: *Sci Transl Med* 12.527, eaax1501. DOI: 10.1126/scitranslmed.aax1501.

Gerlee, P. (2013). "The model muddle: in search of tumor growth laws". In: *Cancer Res* 73.8, pp. 2407–11. DOI: 10.1158/0008-5472.CAN-12-4355.

Ghorashian, S. et al. (2019). "Enhanced CAR T cell expansion and prolonged persistence in pediatric patients with ALL treated with a low-affinity CD19 CAR". In: *Nature Medicine* 25.9, pp. 1408–1414. DOI: 10.1038/s41591-019-0549-5.

Gupta, Pi.B. et al. (2011). "Stochastic State Transitions Give Rise to Phenotypic Equilibrium in Populations of Cancer Cells". In: *Cell* 146.4, pp. 633–644. DOI: 0.1016/j.cell.2011.07.026.

Haeno, H. et al. (2012). "Computational modeling of pancreatic cancer reveals kinetics of metastasis suggesting optimum treatment strategies". In: *Cell* 148.1-2, pp. 362–375. DOI: 10.1016/j.cell.2011.11.060.

Hale, J. and H. Kocak (1991). *Dynamics and bifurcation*. Springer-Verlags.

Halkola, A.S. et al. (2020). "Modelling of killer T-cell and cancer cell subpopulation dynamics under immuno- and chemotherapies". In: *Journal of Theoretical Biology* 488, p. 110136. DOI: 10.1016/j.jtbi.2019.110136..

Han, X. et al. (2019). "Multi-antigen-targeted chimeric antigen receptor T cells for cancer therapy". In: *Journal of Hematology & Oncology* 12.1, p. 128. DOI: 10.1186/s13045-019-0813-7.

Hanahan, D. and RA. Weinberg (2000). "The Hallmarks of Cancer". In: *Cell* 100.1, pp. 57–70. DOI: 10.1016/s0092-8674(00)81683-9.

Hanahan, D. and R.A. Weinberg (2011). "Hallmarks of Cancer: The Next Generation". In: *Cell* 144.5, pp. 646–674. DOI: 10.1016/j.cell.2011.02.013.

Hanin, L. and J. Rose (2018). "Suppression of metastasis by primary tumor and acceleration of metastasis following primary tumor resection: A natural law?" In: *Bulletin of Mathematical Biology* 80.3, pp. 519–539. DOI: 10.1007/s11538-017-0388-9.

Hartmann, J. et al. (2017). "Clinical development of CAR T cells-challenges and opportunities in translating innovative treatment concepts". In: *EMBO Mol Medl* 9, pp. 1183–1197. DOI: 10.15252/emmm.201607485.

Havenbergh, T. Van et al. (2003). "Natural history of petroclival meningiomas". In: *Neurosurgery* 52.1, pp. 55–64. DOI: 10.1097/00006123-200301000-00006.

Hawkins-Daarud, A. et al. (2015). "In silico analysis suggests differential response to bevacizumab and radiation combination therapy in newly diagnosed glioblastoma". In: *J. R. Soc. Interface* 12, p. 20150388. DOI: 10.1098/rsif.2015.0388.

He, B. et al. (2020). "Gamma ray-induced glial activation and neuronal loss occur before the delayed onset of brain necrosis". In: *FASEB J* 34.10, pp. 13361–13375. DOI: 10.1096/fj.202000365RR.

Heesterman, B.L. et al. (2003). "Mathematical Models for Tumor Growth and the Reduction of Overtreatment". In: *J Neurol Surg B Skull Base* 80.1, pp. 72–78. DOI: 10.1055/s-0038-1667148.

Hegde, M. et al. (2013). "Combinational Targeting Offsets Antigen Escape and Enhances Effector Functions of Adoptively Transferred T Cells in Glioblastoma". In: *Molecular Therapy* 21.11, pp. 2087–2101. DOI: 10.1038/mt.2013.185.

Hege, K.M. et al. (2017). "Safety, tumor trafficking and immunogenicity of chimeric antigen receptor (CAR)-T cells specific for TAG-72 in colorectal cancer". In: *J Immunother Cancer* 5, p. 22. DOI: 10.1186/s40425-017-0222-9.

Henares-Molina, A. et al. (2017). "Non-standard radiotherapy fractionations delay the time to malignant transformation of low-grade gliomas". In: *PLoS One* 12.6, e0178552. DOI: 10.1371/journal.pone.0178552.

Henschke, C.I. (2019). "International Early Lung Cancer Action Program: Enrollment and Screening Protocol". In: *International Early Lung and Cardiac Action Program*. URL: http://www.ielcap.org/sites/default/files/I-ELCAP-protocol.pdf.

Hessel, F. et al. (2003). "Impact of increased cell loss on the repopulation rate during fractionated irradiation in human FaDu squamous cell carcinoma growing in nude mice." In: *Int J Radiat Biol* 79.6, pp. 479–486. DOI: 10.1371/journal.pone.0178552.

Hirayama, A.V. and C.J. Turtle (2019). "Toxicities of CD19 CAR-T cell immunotherapy." In: *Am. J. Hematol.* 94.S1, S42–S49. DOI: 10.1002/ajh.25445..

Hong, M., J.D. Clubb, and Y.Y. Chen (2020). "Engineering CAR-T Cells for Next-Generation Cancer Therapy". In: *Cancer Cell.* 38.4, pp. 473–488. DOI: 10.1016/j.ccell.2020.07.005.

Iwata, K., K. Kawasaki, and N.Shigesada (2000). "A dynamical model for the growth and size distribution of multiple metastatic tumors". In: *J Theor Biol* 203.1, pp. 177–186. DOI: 10.1006/jtbi.2000.1075.

Jarrett, A.M. et al. (2018). "Classical mathematical models for description and prediction of experimental tumor growth". In: *Expert Rev Anticancer Ther* 18.12, pp. 1271–1286. DOI: 10.1080/14737140.2018.1527689.

Jiang, J. et al. (2020). "Characterization of the immune microenvironment in brain metastases from different solid tumors". In: *Cancer Med* 9.7, pp. 2299–2308. DOI: 10.1002/cam4.2905.

Jiménez-Sánchez, J. et al. (2021). "A mesoscopic simulator to uncover heterogeneity and evolutionary dynamics in tumors". In: *PLoS Comput Biol* 17.2, e1008266. DOI: 0.1371/journal.pcbi.1008266.

Joiner, M.C. and A.J.C Van der Kogel (2018). *Basic Clinical Radiobiology*. CRC Press.

Kasakovski, D., L. Xu, and Y. Li (2018). "T cell senescence and CAR-T cell exhaustion in hematological malignancies". In: *J Hematol Oncol* 11.1, p. 91. DOI: 10.1186/s13045-018-0629-x.

Khasraw, M. et al. (2020). "PD-1 Inhibitors: Do they have a Future in the Treatment of Glioblastoma?" In: *Clin Cancer Res* 26.20, pp. 5287–5296. DOI: 10.1158/1078-0432.CCR-20-1135..

Kim, M.S. et al. (2015). "Radiobiological mechanisms of stereotactic body radiation therapy and stereotactic radiation surgery". In: *Radiation Oncology Journal* 33.4, pp. 265–275. DOI: 10.3857/roj.2015.33.4.265.

Kimmel, G.J., F.L. Locke, and P.M. Altrock (2019). "Evolutionary Dynamics of CAR T Cell Therapy". In: *bioRxiv 717074*. DOI: 10.1101/717074.

Kobets, A.J. et al. (2020). "Evaluating the natural growth rate of metastatic cancer to the brain". In: *Surg Neurol Int* 11, p. 254. DOI: 10.25259/SNI_291_2020.

Kohutek, Z.A. et al. (2015). "Long-term risk of radionecrosis and imaging changes after stereotactic radiosurgery for brain metastases". In: *J Neurooncol* 125.1, pp. 149–156. DOI: 10.1007/s11060-015-1881-3.

Konstorum, A. et al. (2017). "Addressing current challenges in cancer immunotherapy with mathematical and computational modelling". In: *J R Soc Interface* 14, p. 20170150. DOI: 10.1098/rsif.2017.0150.

Koury, J. et al. (2018). "Immunotherapies: Exploiting the Immune System for Cancer Treatment". In: *J Immunol Res* 2018, p. 9585614. DOI: 10.1155/2018/9585614.

Kuang, Y., J.D. Nagy, and S.E.Eikenberry (2016). *Introduction to Mathematical Oncology*. Chapman and Hall/CRC. DOI: 10.1201/9781315365404.

Kudo, Y. et al. (2019). "Suppressed immune microenvironment and repertoire in brain metastases from patients with resected non-small-cell lung cancer". In: *Ann Oncol* 30.9, pp. 1521–1530. DOI: 10.1093/annonc/mdz207.

Kuznetsov, M. and A. Kolobov (2020). "Optimization of Dose Fractionation for Radiotherapy of a Solid Tumor with Account of Oxygen Effect and Proliferative Heterogeneity". In: *Mathematic* 8.8, p. 1204. DOI: 10.3390/math8081204.

Kuznetsov, V.A. et al. (1994). "Nonlinear dynamics of immunogenic tumors: Parameter estimation and global bifurcation analysis." In: *Bulletin of Mathematical Biology* 56.2, pp. 295–321. DOI: 10.1007/BF02460644..

Lawrence, M.S. et al. (2013). "Mutational heterogeneity in cancer and the search for new cancer-associated genes." In: *Nature* 499.7457, pp. 214–218. DOI: 10.1038/nature12213.

Leder, K. et al. (2014). "Mathematical modeling of PDGF-driven glioblastoma reveals optimized radiation dosing schedules". In: *Cell* 156, pp. 603–616. DOI: 10.1016/j.cell.2013.12.029.

Lee, D. et al. (2020). "Brain Metastasis Recurrence Versus Radiation Necrosis: Evaluation and Treatment". In: *Neurosurg Clin N Am* 31.4, pp. 575–587. DOI: 10.1016/j.nec.2020.06.007.

Lee, D.W. et al. (2015). "T cells expressing CD19 chimeric antigen receptors for acute lymphoblastic leukaemia in children and young adults: a phase 1 dose-escalation trial". In: *Lancet* 385.9967, pp. 517–528. DOI: 10.1016/S0140-6736(14)61403-3.

Lewin, T.D. et al. (2018). "The Evolution of Tumour Composition During Fractionated Radiotherapy: Implications for Outcome". In: *Bull Math Biol* 80.103, pp. 1207–123. DOI: 10.1007/s11538-018-0391-9.

Liadi, I. et al. (2015). "Individual motile $CD4^+$ T cells can participate in efficient multikilling through conjugation to multiple tumor cells". In: *Cancer Immunol Res* 3.5, pp. 473–482. DOI: 10.1158/2326-6066.CIR-14-0195.

Liu, Q. et al. (2017). "Factors involved in cancer metastasis: a better understanding to "seed and soil" hypothesis". In: *Molecular Cancer* 16.1. DOI: 10.1186/s12943-017-0742-4.

Liu, Y. et al. (2020). "Single-cell transcriptome analysis demonstrates inter-patient and intra-tumor heterogeneity in primary and metastatic lung adenocarcinoma". In: *Aging* 12.21, pp. 21559–21581. DOI: 10.18632/aging.103945.

L.LChen et al. (2009). "Cancer metastasis networks and the prediction of progression patterns." In: *Br J Cancer* 101.5, pp. 749–758. DOI: 10.1038/sj.bjc.6605214.

López, A.G., J.M. Seoane, and M.A.F. Sanjuán (2017). "Destruction of solid tumors by immune cells". In: *Commun Nonlinear Sci Numer Simulatl* 44, pp. 390–403. DOI: 10.1016/j.cnsns.2016.08.020.

Lorenzo, G. et al. (2019). "Mechanistic modelling of prostate- specific antigen dynamics shows potential for personalized prediction of radiation therapy outcome". In: *J. R. Soc. Interface.* 16, p. 201901957. DOI: 10.1098/rsif.2019.0195.

Ma, S. et al. (2017). "Current Progress in CAR-T Cell Therapy for Solid Tumors". In: *Int. J. Biol. Sci.* 15.12, pp. 2548–2560. DOI: 10.7150/ijbs.34213.

Macklin, P. et al. (2009). "Multiscale modelling and nonlinear simulation of vascular tumour growth". In: *J Math Biol* 58.4-5, pp. 765–98. DOI: 10.1007/s00285-008-0216-9.

Mahlbacher, G.E., K.C. Reihmer, and H.B. Frieboes (2019). "Mathematical modeling of tumor-immune cell interactions." In: *Journal of Theoretical Biology* 469, pp. 47–604. DOI: 10.1016/j.jtbi.2019.03.002.

Mahlbachera, G.E., K.C. Reihmera, and H.B. Frieboes (2019). "Mathematical modeling of tumor-immune cell interactions". In: *J Theor Biol* 469, pp. 47–60. DOI: 10.1016/j.jtbi.2019.03.002.

Mandonnet, E. et al. (2003). "Continuous growth of mean tumor diameter in a subset of grade II gliomas". In: *Ann Neurol* 53.4, pp. 524–528. DOI: 10.1002/ana.10528.

Marciniak-Czochra, A. et al. (2009). "Modeling of asymmetric cell division in hematopoietic stem cells: regulation of self-renewal is essential for efficient repopulation". In: *Stem Cells Dev* 18, pp. 377–385. DOI: 10.1089/scd.2008.0143.

Martínez, M. and E.K. Moon (2019). "CAR T Cells for Solid Tumors: New Strategies for Finding, Infiltrating, and Surviving in the Tumor Microenvironment". In: *Front. Immunol.* 10, p. 128. DOI: 10.3389/fimmu.2019.00128.

Maude, S.L. et al. (2014). "Chimeric antigen receptor T cells for sustained remissions in leukemia". In: *N Engl J Med* 371, pp. 1507–1517. DOI: 10.1056/NEJMoa1407222.

McGowan, E. et al. (2019). "PD-1 disrupted CAR-T cells in the treatment of solid tumors: Promises and challenges". In: *Biomed. Pharmacother* 121.109625, pp. 45–56. DOI: 10.1016/j.biopha.2019.109625..

Miliotou, A.N. and L.C. Papadopoulou (2018). "CAR T-cell Therapy: A New Era in Cancer Immunotherapy". In: *Curr Pharm Biotechnol* 19.1, pp. 5–18. DOI: 10.2174/1389201019666180418095526.

Milo, R. et al. (2009). "BioNumbers—the database of key numbers in molecular and cell biology". In: *Nucleic Acids Research* 38.Database Issue, D750–D753. DOI: 10.1093/nar/gkp889.

Mollard, S. et al. (2017). "Model driven optimization of antiangiogenics + cytotoxics combination: application to breast cancer mice treated with bevacizumab + paclitaxel doublet leads to reduced tumor growth and fewer metastasis." In: *Oncotarget* 8.14, pp. 23087–23098. DOI: 10.18632/oncotarget.15484.

Mostolizadeh, R., Z. Afsharnezhad, and A. Marciniak-Czochra (2018). "Mathematical model of Chimeric Anti-gene Receptor (CAR) T cell therapy with presence of cytokine". In: *Numerical Algebra, Control & Optimization* 8.1, pp. 63–80. DOI: 10.3934/naco.2018004.

Nayar, S., P. Dasgupta, and C. Galustian (2015). "Extending the lifespan and efficacies of immune cells used in adoptive transfer for cancer immunotherapies. A review". In: *Oncoimmunology* 4, e1002720. DOI: 10.1080/2162402X.2014.1002720.

Neelapu, S.S. et al. (2018). "Chimeric antigen receptor T-cell therapy - assessment and management of toxicities". In: *Nat Rev Clin Oncol* 15.1, pp. 47–62. DOI: 10.1038/nrclinonc.2017.148.

Newton, P.K. et al. (2012). "A stochastic Markov chain model to describe lung cancer growth and metastasis". In: *PLoS ONE* 7.4, e34637. DOI: 10.1371/journal.pone.0034637.

Newton, P.K. et al. (2013). "Spreaders and sponges define metastasis in lung cancer: a Markov chain Monte Carlo mathematical model". In: *Cancer Res* 173.9, pp. 2760–2769. DOI: 10.1158/0008-5472.CAN-12-4488.

Nguyen, D.X. et al. (2009). "WNT/TCF signaling through LEF1 and HOXB9 mediates lung adenocarcinoma metastasis". In: *Cell* 138.1, pp. 51–62. DOI: 10.1016/j.cell.2009.04.030.

Niklas, K.J. and U. Kutschera (2015). "Kleiber's Law: How the Fire of Life ignited debate, fueled theory, and neglected plants as model organisms". In: *Plant Signal Behav* 10.7, e1036216. DOI: 10.1080/15592324.2015.1036216.

Niranjan, A. et al. (2019). "Guidelines for Multiple Brain Metastases Radiosurgery". In: *Prog Neurol Surg* 34, pp. 100–109. DOI: 10.1159/000493055.

Ocaña-Tienda, B. et al. (2021). "The Growth Laws of Brain Metastases". In: *PNAS (Submitted)*.

O'Rourke, D.M. et al. (2017). "A single dose of peripherally infused EGFRvIII-directed CAR T cells mediates antigen loss and induces adaptive resistance in patients with recurrent glioblastoma." In: *Sci. Transl. Med.* 9.399, eaaa0984. DOI: 10.1126/scitranslmed.aaa0984.

Oshime, Y. (2003). "Asymptotic expression of the period of the Lotka-Volterra system". In: *Japan J Indust App Math* 20, pp. 353–78.

Ostrom, Q.T. et al. (2020). "CBTRUS Statistical Report: Primary Brain and Other Central Nervous System Tumors Diagnosed in the United States in 2013-2017". In: *Neuro Oncol* 22.12, pp. iv1–iv96. DOI: 10.1093/neuonc/noaa200.

Pallud, J. et al. (2006). "Prognostic value of initial magnetic resonance imaging growth rates for World Health Organization grade II gliomas". In: *Ann Neurol* 60.3, pp. 380–383. DOI: 10.1002/ana.20946.

Pérez-García, V.M et al. (2016). "Applied mathematics and nonlinear sciences in the war on cancer". In: *App Math Nonlin Sci* 1.2, pp. 423–436. DOI: 10.21042/AMNS.2016.2.00036.

Perus, L.J.M. and L.A Walsh (2019). "Microenvironmental heterogeneity in brain malignancies". In: *Front Immunol* 10, p. 2294. DOI: 10.3389/fimmu.2019.02294.

Pérez-Beteta, J. et al. (2018). "Tumor Surface Regularity at MR Imaging Predicts Survival and Response to Surgery in Patients with Glioblastoma". In: *Radiology* 288.1, pp. 218–225. DOI: 10.1148/radiol.2018171051.

Pérez-García, V.M. et al. (2015). "Delay effects in the response of low-grade gliomas to radiotherapy: A mathematical model and its therapeutical implications". In: *Mathematical Biology and Medicine* 32, pp. 307–329. DOI: 110.1093/imammb/dqu009.

Pérez-García, V.M. et al. (2020). "Universal scaling laws rule explosive growth in human cancers". In: *Nature Physics* 16, pp. 1232–1237. DOI: 10.1038/s41567-020-0978-6.

Radunskaya, A., R. Kim, and T. Woods (2018). "Mathematical Modeling of Tumor Immune Interactions: A Closer Look at the Role of a PD-L1 Inhibitor in Cancer Immunotherapy". In: *Spora: a Journal of Biomathematics* 4.1, pp. 25–41. DOI: 10.30707/SPORA4.1Radunskaya.

Rafiq, S., C.S. Hackett, and R.J. Brentjens (2020). "Engineering strategies to overcome the current roadblocks in CAR T cell therapy". In: *Nature Reviews Clinical Oncology* 17.3, pp. 147–167. DOI: 10.1038/s41571-019-0297-y.

Reardon, D.A. et al. (2020). "Effect of Nivolumab vs Bevacizumab in Patients With Recurrent Glioblastoma: The CheckMate 143 Phase 3 Randomized Clinical Trial". In: *JAMA Oncol.* 6.7, pp. 1003–1010. DOI: 0.1001/jamaoncol.2020.1024.

Rejniak, K.A. and A.R.A. Anderson (2011). "Hybrid models of tumor growth". In: *Systems biology and medicine* 3.1, pp. 115–125. DOI: 10.1002/wsbm.102.

Ribba, B. et al. (2012). "A tumor growth inhibition model for low-grade glioma treated with chemotherapy or radiotherapy". In: *Clin Cancer Res* 15, pp. 5071–5080. DOI: 10.1158/1078-0432.CCR-12-0084.

Robert, C. (2020). "A decade of immune-checkpoint inhibitors in cancer therapy." In: *Nat Commun* 11.1, p. 3801. DOI: 10.1038/s41467-020-17670-y.

Rock, K.L. and H. Kono (2008). "The inflammatory response to cell death". In: *Annu Rev Pathol* 3, pp. 99–126. DOI: 10.1146/annurev.pathmechdis.3.121806.151456.

Rockne, R. et al. (2009). "A mathematical model for brain tumor response to radiation therapy. Journal of Mathematical Biology". In: *Journal of Mathematical Biology* 59, p. 561. DOI: 10.1007/s00285-008-0219-6.

Rockne, R. et al. (2010). "Predicting the efficacy of radiotherapy in individual glioblastoma patients in vivo: A mathematical modeling approach". In: *Phys Med Biol* 55, pp. 3271–3285. DOI: 10.1088/0031-9155/55/12/001.

Rockne, R.C. et al. (2015). "A patient-specific computational model of hypoxia-modulated radiation resistance in glioblastoma using 18F-FMISO-PET". In: *J. R. Soc. Interface* 12.103, p. 20141174. DOI: 10.1098/rsif.2014.1174.

Rodrigues, B.J., Luciana R. Carvalho Barros, and Regina C. Almeida (2019). "Three-Compartment Model of CAR T-cell Immunotherapy". In: *bioRxiv*. DOI: 10.1101/779793.

Rolink, A.G., J. Andersson, and F. Melchers (1998). "Characterization of immature B cells by a novel monoclonal antibody, by turnover and by mitogen reactivityt". In: *Eur J Immunol* 28.11, pp. 3738–3748. DOI: 10.1002/(SICI)1521-4141(199811)28:11<3738::AID-IMMU3738>3.0.CO;2-Q.

Roybal, K.T. et al. (2016). "Precision Tumor Recognition by T Cells With Combinatorial Antigen-Sensing Circuits". In: *Cell* 164.4, pp. 770–779. DOI: 10.1016/j.cell.2016.01.011.

Sadelain, M. (2015). "CAR therapy: the CD19 paradigm". In: *J Clin Invest* 125.9, pp. 3392–3400. DOI: 10.1172/JCI80010.

— (2017). "CD19 CAR T Cells". In: *Cell* 171.7, p. 1471. DOI: 10.1016/j.cell.2017.12.002.

Sahoo, P. et al. (2020). "Mathematical deconvolution of CAR T-cell proliferation and exhaustion from real-time killing assay data". In: *J. R. Soc. Interface* 17.162, p. 20190734. DOI: 10.1098/rsif.2019.0734.

Salkeld, A.L. et al. (2018). "Changes in Brain Metastasis During Radiosurgical Planning". In: *Int J Radiat Oncol Biol Phys* 102.4, pp. 727–733. DOI: 10.1016/j.ijrobp.2018.06.021.

Saltelli, A. et al. (2010). "Variance based sensitivity analysis of model output. Design and estimator for the total sensitivity index". In: *Computer Physics Communications* 181, pp. 259–270. DOI: 10.1016/j.cpc.2009.09.018.

Schuster, S.J. et al. (2019). "Tisagenlecleucel in Adult Relapsed or Refractory Diffuse Large B-Cell Lymphoma". In: *N Engl J Med* 380.1, pp. 45–56. DOI: 110.1182/bloodadvances.2019000151.

Scott, J.G. et al. (2013). "A mathematical model of tumour self-seeding reveals secondary metastatic deposits as drivers of primary tumour growth". In: *J R Soc Interface* 10.82, p. 20130011. DOI: 10.1098/rsif.2013.0011.

Shahaf, G. et al. (2016). "B Cell development in the bone marrow is regulated by homeostatic feedback exerted by mature B cells". In: *Front Immunol* 7, p. 77. DOI: 10.3389/fimmu.2016.00077.

Sharma, P. and J.P. Allison (2015). "The future of immune checkpoint therapy". In: *Science* 348.6230, pp. 56–61. DOI: 10.1126/science.aaa8172.

Shepard, D.M. et al. (2008). "Treatment Planning for Stereotactic Radiosurgery. In: Chin L.S. and Regine W.F. (eds)". In: *Principles and Practice of Stereotactic Radiosurgery*. Springer, New York, NY. DOI: 10.1007/978-0-387-71070-9_7.

Shih, D.J.H. et al. (2020). "Genomic characterization of human brain metastases identifies drivers of metastatic lung adenocarcinoma". In: *Nat Genet* 52.21, pp. 371–377. DOI: 10.1038/s41588-020-0592-7.

Shih, S.D. (1997). "The period of a Lotka-Volterra system". In: *Taiwanese J Math* 1, pp. 451–470.

Siegler, E.L. and S.S. Kenderian (2020). "Neurotoxicity and Cytokine Release Syndrome After Chimeric Antigen Receptor T Cell Therapy: Insights Into Mechanisms and Novel Therapies." In: *Front. Immunol.* 11, p. 19739. DOI: 10.3389/fimmu.2020.01973.

Skipper, H.E. and S. Perr (1970). "Kinetics of Normal and Leukemic Leukocyte Populations and Relevance to Chemotherapy". In: *Cancer Research* 30.6, pp. 1883–1897.

Smart, D. et al. (2015). "Analysis of radiation therapy in a model of triple-negative breast cancer brain metastasis". In: *Clin Exp Metastasis* 32.7, pp. 717–27. DOI: 10.1093/neuonc/nox043.

Soffietti, R. et al. (2020). "Management of brain metastases according to molecular subtypes". In: *Nat Rev Neurol* 16.10, pp. 557–574. DOI: 10.1038/s41582-020-0391-x.

Sperduto, P.W. et al. (2020). "Survival in Patients With Brain Metastases: Summary Report on the Updated Diagnosis-Specific Graded Prognostic Assessment and Definition of the Eligibility Quotient". In: *J Clin Oncol* 38.32, pp. 3773–3784. DOI: 10.1200/JCO.20.01255.

Starkov, K.E. and A.P. Krishchenko (2014). "On the global dynamics of one cancer tumour growth model". In: *Commun Nonlinear Sci Numer Simulat* 19, pp. 1486–1495. DOI: 10.1016/j.cnsns.2013.09.023.

Stein, A.M. et al. (2018). "Optimization of IL13Ra2-targeted chimeric antigen receptor T cells for improved anti-tumor efficacy against glioblastoma". In: *Mol. Ther* 26.5309, pp. 31–44. DOI: 10.1016/j.ymthe.2017.10.002.

Stein, A.M. et al. (2019). "Tisagenlecleucel Model-Based Cellular Kinetic Analysis of Chimeric Antigen Receptor-T Cells". In: *CPT Pharmacometrics Syst Pharmacol* 8.5, 285-295. DOI: 10.1002/psp4.12388.

Stella, G.M. et al. (2019). "Brain metastases from lung cancer: Is MET an actionable target?" In: *Cancers (Basel)* 11.3, p. 271. DOI: 10.3390/cancers11030271.

Stensjøen, A.L. et al. (2015). "Growth dynamics of untreated glioblastomas in vivo." In: *Neuro Oncology* 17.10, pp. 1402–1411. DOI: 10.1093/neuonc/nov029.

Stollar, D. (1998). *Encyclopedia of immunology. 2nd edition.* Academic Press PJ Delves Ed.

Stupp, R. et al. (2005). "Radiotherapy plus concomitant and adjuvant temozolomide for glioblastoma". In: *N Engl J Med* 352.10, pp. 987–96. DOI: 10.1056/NEJMoa043330.

Sung, H. et al. (2021). "Global Cancer Statistics 2020: GLOBOCAN Estimates of Incidence and Mortality Worldwide for 36 Cancers in 185 Countries". In: *CA Cancer J Clin* 71.3, pp. 209–249. DOI: 10.3322/caac.21660.

Sánchez-Martínez, D. et al. (2019). "Fratricide-resistant CD1a-specific CAR T cells for the treatment of cortical T-cell acute lymphoblastic leukemia". In: *Blood* 133.21, pp. 2291–2304. DOI: 10.1182/blood-2018-10-882944.

Talkington, A. and R. Durrett (2015). "Estimating Tumor Growth Rates In Vivo". In: *Bull Math Biol* 77.10, pp. 1934–1954. DOI: 10.1007/s11538-015-0110-8.

Toma-Dasu, I. and A. Dasu (2013). "Modelling Tumour Oxygenation, Reoxygenation and Implications on Treatment." In: *Computational and Mathematical Methods in Medicine* 26.3, p. 141087. DOI: 10.1155/2013/141087.

Tough, D.F. and J. Sprent (2018). "Life span of naive and memory t cells". In: *Stem Cells* 13.3, pp. 242–249. DOI: 10.1002/stem.5530130305.

Turtle, C.J. et al. (2017). "Durable molecular remissions in chronic lymphocytic leukemia treated with CD19-specific chimeric antigen receptor-modified T cells after failure of Ibrutinib". In: *J Clin Oncol* 35, pp. 3010–3020. DOI: 10.1200/JCO.2017.72.8519.

Valiente, M. et al. (2014). "Serpins promote cancer cell survival and vascular co-option in brain metastasis". In: *Cell* 156.5, pp. 1002–1016. DOI: 10.1016/j.cell.2014.01.040.

Vellayappan, B. et al. (2018). "Diagnosis and Management of Radiation Necrosis in Patients With Brain Metastases". In: *Front Oncol* 8.395, pp. 1521–1530. DOI: 10.3389/fonc.2018.00395.

Voglstaetter, M. et al. (2019). "Tspan8 is expressed in breast cancer and regulates E-cadherin/catenin signalling and metastasis accompanied by increased circulating extracellular vesicles". In: *J Pathol* 248.4, pp. 421–437. DOI: 10.1002/path.5281.

Wagner, S. et al. (2020). "Effects of effective stereotactic radiosurgery for brain metastases on the adjacent brain parenchyma". In: *Br J Cancer* 123.1, pp. 54–60. DOI: 10.1038/s41416-020-0853-3.

Wang, J.C. and J.E. Dick (2005). "Cancer stem cells: lessons from leukemia". In: *Trends Cell Biol* 15.9, pp. 494–501. DOI: 10.1016/j.tcb.2005.07.004.

Watanabe, Y. et al. (2016). "A mathematical model of tumor growth and its response to single irradiation". In: *Theor Biol Med Model* 13.6, pp. 362–375. DOI: 10.1186/s12976-016-0032-7.

West, G.B., J.H. Brown, and B.J. Enquist (1997). "A general model for the origin of allometric scaling laws in biology". In: *Science* 276.5309, pp. 122–126. DOI: 10.1126/science.276.5309.122.

— (2001). "A general model for ontogenetic growth". In: *Nature* 413.6856, pp. 628–631. DOI: 10.1086/401873.

West, J. and P.K. Newton (2013). "Cellular interactions constrain tumor growth". In: *Proceedings of the National Academy of Sciences* 116.6, pp. 1918–1923. DOI: 10.1073/pnas.1804150116.

WHO, World Health Organization (2020). "Global Health Estimates 2020: Deaths by Cause, Age, Sex, by Country and by Region, 2000-2019". In: *WHO* Accessed December 11, 2020. URL: who.int/data/gho/data/themes/mortality-and-global-health-estimates/ghe-leading-causes-of-death.

Xu, X. et al. (2019). "Mechanisms of Relapse After CD19 CAR T-Cell Therapy for Acute Lymphoblastic Leukemia and Its Prevention and Treatment Strategies". In: *Frontiers in Immunology* 10, p. 2664. DOI: 10.3389/fimmu.2019.02664.

Yasuyuki, A. et al. (2018). "Myeloid conditioning with c-kit-targeted CAR-T cells enables donor stem cell engraftment". In: *Molecular Therapy* 26.5, pp. 1181–1197. DOI: 10.1016/j.ymthe.2018.03.003.

Yu, V.Y. et al. (2015). "Incorporating cancer stem cells in radiation therapy treatment response modeling and the implication in glioblastoma multiforme treatment resistance". In: *Int J Radiat Oncol Biol Phys* 91.4, pp. 866–875. DOI: 10.1016/j.ijrobp.2014.12.004.

Zinn, K.R. et al. (2008). "Noninvasive bioluminescence imaging in small animals". In: *ILAR J* 49.1, pp. 103–115. DOI: 10.1093/ilar.49.1.103.